UNIVERSITÀ DI TRENTO

UNIVERSITÀ DEGLI STUDI FIRENZE

Dipartimento di Scienze della Terra

Eccellenza 2023-2027

**Doctorate of National Interest**

**on**

**Space Science and Technology**

# NATURAL ANALOGUES OF PLANET MERCURY'S SURFACE: MINERALOGICAL AND SPECTROSCOPIC ASPECTS


Anna-Irene Landi

Supervisor

Prof. Giovanni Pratesi

Dipartimento di Scienze della Terra, Università degli studi di Firenze

Co-Supervisor

Dr. Cristian Carli

INAF/IAPS, Roma



October, 2025

# Abstract

Understanding the nature and evolution of Mercury's surface materials is crucial to constrain the planet's formation processes. Data from NASA's MESSENGER (MErcury Surface, Space ENvironment, GEochemistry, and Ranging) mission indicate that the surface is dominated by Na-rich plagioclase, FeO-poor enstatite and forsterite, and Mg–Ca–Fe sulphides, suggesting that Mercury formed in the inner part of the protoplanetary disk from highly reduced precursor materials. However, the interpretation of Mercury's spectral properties remains complex due to the effects of space weathering (SpWe) and extreme temperature variations affecting the surface. Since it is not possible to have direct information on the surface, from meteorites from Mercury nor from returned samples, the study of analogous materials becomes crucial to prepare for the interpretation of the upcoming data form the ongoing ESA-JAXA BepiColombo mission.
Therefore, I conducted a comprehensive minero-petrological and spectroscopic investigation on highly reduced meteorites and terrestrial analogues. The investigated meteorites include five aubrites (Rantila, Tiglit, Peña Blanca Spring, Norton County, NWA 14185) and four enstatite chondrites, achondrites and melt rocks (Itqiy, NWA 4945, NWA 13266, NWA 13210). SEM (Scanning Electron Microscope) and EPMA (Electron Probe Micro Analyzer) analyses revealed that the samples are mainly composed of nearly FeO-free enstatite, with variable amounts of forsterite, diopside, and Na-rich plagioclase. Sulphides and metals, particularly abundant in enstatite chondrites and achondrites, include troilite, daubréelite, oldhamite, alabandite, keilite, and kamacite with variable Si contents. The mineralogical and compositional features indicate that these meteorites come from multiple parent bodies. The visible–near infrared (VNIR) reflectance spectra show diagnostic features that reflect both the very low FeO content (<0.4 wt%) in silicates and the minero-chemical variations among the samples. Aubrites exhibit weak mafic-related absorption bands at 0.9 μm, attributed to $Fe^{2+}$ electronic transitions in low-Ca pyroxenes and olivine, with an additional minor absorption feature around 0.5 μm in olivine-rich portions, due to spin-forbidden $Fe^{2+}$ transitions. Enstatite chondrites and achondrites show nearly flat, featureless spectra with only weak or no absorptions, and in some cases a slight red slope likely related to the higher abundance of metal and sulphides. Minor features at 1.4 μm and 1.9 μm are occasionally observed, indicating incipient terrestrial weathering. Rantila aubrite presents slightly higher FeO contents in silicates, which are observable in VNIR spectra: the potential detection limit of mafic minerals from crystal field absorptions in VNIR reflectance spectra could be placed between the composition of Rantila and that of the other reduced meteorites. For Rantila aubrite Laser-Induced Time-Resolved Luminescence (LITRL) analysis was conducted, revealing the presence of different activators in different mineral phases, giving us additional information on the mineralogy and chemistry of the sample.
To simulate SpWe processes on Mercury's surface, particularly the effects of solar wind irradiation, ion irradiation experiments with $He^+$ (20 keV) and $C^+$ (30 keV) were performed on aubrite powders and rock fragments. The observed spectral effects are darkening and reddening in VNIR spectra, accompanied by a reduction in spectral contrast and shifts of Christiansen Features (CFs) and Reststrahlen Bands (RBs) positions toward longer wavelengths in MIR spectra. $C^+$ irradiation produces stronger darkening effects than $He^+$, and the presence of carbon in the sample prior to irradiation appears to cause more pronounced spectral darkening. Different responses to ion irradiation are observed between powders and rock fragments. Therefore, the extent of the spectral changes induced by ion irradiation depends on both the nature of the ion species and the physical state of the target (powder vs rock), revealing that surface mineralogy and texture play a key role in spectral alteration under solar wind exposure.
The study of boninites provided several insights relevant to Mercury's surface exploration. First of all, their mineralogy and bulk composition generally match Mercury's surface. The primary compositional difference is the higher FeO content in the terrestrial samples (~8 wt% compared to estimated <2 wt% on Mercury). Major mineralogical discrepancies include the presence of hydrated alteration minerals, which are absent on Mercury, and the absence of sulphides typical of highly reduced environments such as Mercury's surface. Reflectance spectra show a red slope in the ultra-violet (UV) region and a subtle red slope in the visible (VIS) region. The main absorption feature is in the VNIR range, at ~1 μm, associated with mafic minerals. CFs are located at lower wavelengths for the samples with higher plagioclase content. Increasing grain size leads to spectral flattening and reduced reflectance and absorption band intensities. Heating to Mercury-like temperatures (up to 450°C) induces a reddening of the VIS slope, disappearance of the band linked to aqueous alteration, a decrease in the MIR spectral contrast, and shifts of RBs positions. The emissivity spectra show three changes occurring for all the samples as the temperature increases from 150°C to 450°C: CFs positions shift, emissivity minima shift, and the spectral contrast between CFs and RBs increases. An opposite trend is observed for the emissivity minima shifting between mafic-richer and felsic-richer samples. Still, the minima positions remain distinct, suggesting that mafic-richer and felsic-richer terranes should be easily identifiable with the MERTIS instrument.
By integrating mineralogical, chemical, and spectroscopic data from natural analogues of Mercury's surface, we can better constrain how composition, reduction state, and space weathering can influence spectral properties, highlighting the value of a multi-methodological approach. Moreover, this study provides a detailed analogues spectral library that could help in the interpretation of Mercury's surface spectra from BepiColombo SIMBIO-SYS (Spectrometer and Imagers for MPO BepiColombo Integrated Observatory SYStem) and MERTIS (MErcury Radiometer and Thermal Infrared Spectrometer) instruments.

**Keywords (max 5)**
Mercury's surface
Highly reduced meteorites
Boninites
Experimental techniques
Space weathering

# Contents

# 1. Introduction

Mercury is the innermost and smallest planet of the Solar System. It is one of the four rocky planets, along with Earth, Venus, and Mars. Mercury's surface appears dark, it is heavily cratered and covered with regolith, and it presents only a tenuous exosphere (e.g., ***Rothery et al., 2015; Solomon et al., 2018***). Mercury has the shortest and most eccentric orbit among the planets of the Solar System. The sidereal year (87.969 Earth days) and sidereal day (58.65 Earth days) are in a 3:2 ratio, in a spin–orbit resonance. The planet rotates three times for every two revolutions around the Sun. Considering the orbit and the lack of a thick atmosphere, Mercury's surface undergoes extreme temperature variations, from −170 °C to 420 °C at the equator. Moreover, the planet has nearly zero axial tilt, meaning that the polar regions are permanently shadowed, suggesting the presence of water ice on craters' floors (e.g., ***Lawrence et al., 2013; Slade et al., 1992***). Moreover, Mercury presents an internal magnetic field. Studying the processes that led to the formation of Mercury is essential to understanding the formation and evolution of rocky planets (e.g., ***Rothery et al., 2015; Solomon et al., 2018***).

In this chapter, I primarily focus on Mercury's surface composition and mineralogy. Therefore, the following sections review the main findings from past space missions to Mercury that have contributed to our current knowledge of these aspects of the planet.

## 1.1. Mercury's Exploration - Current Knowledge of the Planet and Future Prospects

### 1.1.1. Mariner 10 mission

Besides ground-based observations, the first information about planet Mercury comes from NASA's Mariner 10 mission (launch 1973 – end 1975) (***Dunne & Burgess, 1978***). Mariner 10 was the first mission to launch a spacecraft to Mercury (and Venus). It observed 45 % of the planet's surface, revealing its intense cratering (**Fig. 1.1**). Mariner 10's camera observed basins (including the biggest, Caloris basin, about 1,500 km in diameter), craters, ridges, highlands, and plains. This mission also enabled the discovery and study of the planet's internal magnetic field and its exosphere.

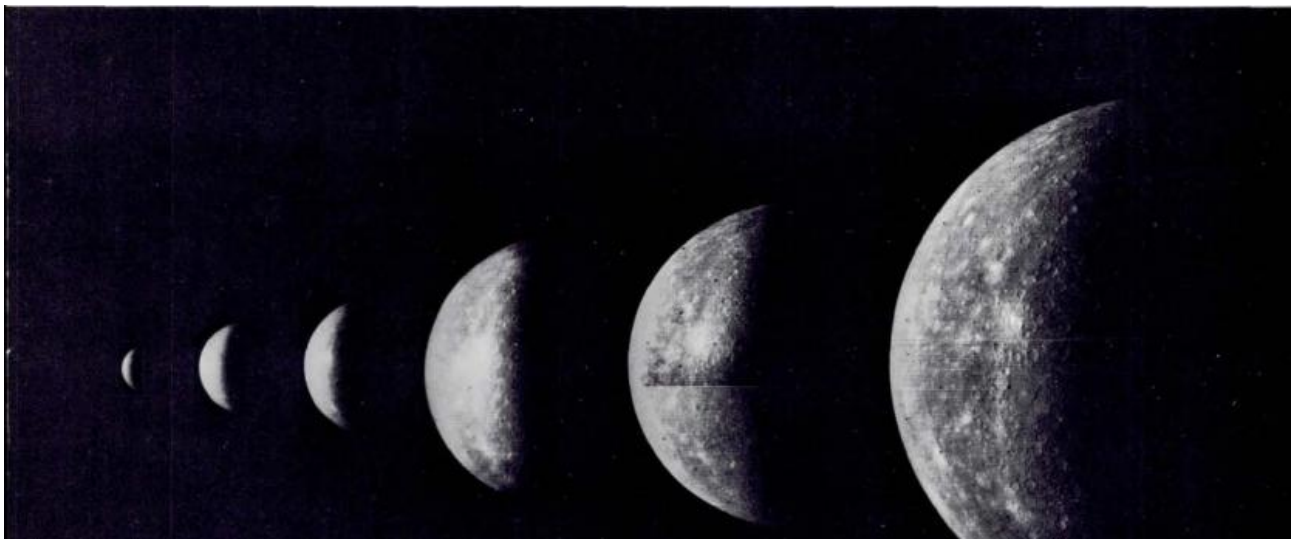

Figure 1.1. Craters identification in one of the first images of Mercury from Mariner 10. The last view in this picture was taken on 28 March 1974, at 952,000 km from the planet. Picture from **Dunne & Burgess, 1978**.

### 1.1.2. MESSENGER mission

Mariner 10 crucially expanded our knowledge of Mercury. Nevertheless, several questions remained unanswered or were newly raised after the end of the mission, including the surface composition, which was not investigated. These issues were further investigated by NASA's MESSENGER (MErcury Surface, Space ENvironment, GEochemistry, and Ranging) mission (launch 2004 - end 2015) (***Solomon et al., 2001; 2018***). The mission provided comprehensive, global insights into Mercury's surface, interior, exosphere, and magnetosphere. Seven instruments were present on board the mission. Among them, the instruments investigating various aspects of the surface were: X-Ray Spectrometer (XRS; ***Schlemm et al., 2007***) and Gamma-Ray and Neutron Spectrometer (GRNS; ***Goldsten et al., 2007***) for the chemical composition, Mercury Dual Imaging System (MDIS; ***Hawkins et al., 2007***) and Mercury Atmospheric and Surface Composition Spectrometer (MASCS; ***McClintock & Lankton, 2007***) for imaging and spectral information, and Mercury Laser Altimeter (MLA; ***Cavanaugh et al., 2007***) for topographic studies.

#### 1.1.2.1.Chemical composition and mineralogy

XRS and GRNS instruments measured the elemental abundance in the northern hemisphere; the southern hemisphere was also investigated, although with a poorer spatial resolution. Mercury differs from the other rocky planets of the inner solar system. The overall elemental distribution evidenced that it presents high Mg/Si ratio, variable Al/Si and Ca/Si, and very low Fe; it is not depleted in moderately elements (Na, K, S) which are widespread and abundant, and highly volatile species (H included) are detected and confined to the permanently shadowed polar regions

(***Evans et al., 2012, 2015***; ***Nittler et al., 2011, 2018***; ***Nittler & Weider, 2019***; ***Peplowski et al., 2012a, 2012b, 2014, 2015, 2016***; ***Weider et al., 2012, 2014, 2015, 2016***). XRS was able to detect Mn, Cr, and Ti during solar flares, evidencing averaged low abundances (<0.1 wt%, ***Nittler et al., 2011***). Carbon is also present on the planet's surface with an estimated average concentration of 1.4 ±0.9 wt% (***Peplowski et al., 2015***). It is suggested in the literature that it could be in the form of graphite that formed from the C that was not trapped in the core during the cooling of the magma ocean, creating a primary graphite flotation crust (***Vander Kaaden & McCubbin, 2015***). Fe quantity is maximum 1-2 wt%, and reflectance spectroscopy data suggest that FeO on silicates must be < 1 wt% (***Murchie et al., 2015***). This low Fe concentration and the high S content (~4 wt%, compared to the <0.1 wt% in Earth's crust; ***Nittler et al., 2011***) suggest that that Mercury formed from highly reduced precursor materials, such as the asteroidal parent bodies of enstatite chondrite meteorites, in the inner part of the Sun's protoplanetary disk (***Nittler & Weider, 2019***). The estimated oxygen fugacity ($fO_2$) is in the range 2.6-7.3 log units below the iron-wüstite buffer (***McCubbin et al., 2012; Namur et al., 2016; Zolotov et al., 2013***).

The elemental distribution is not homogeneous across the surface, and the presence of different "geochemical terranes" (areas with chemical compositions distinct from their surroundings) was also proposed (***Weider et al., 2015***; ***Vander Kaaden et al., 2017***) (**Fig. 1.2**).

The inferred mineralogy is thought to be composed of Na-rich plagioclase, FeO-poor pyroxene and olivine, and Mg-Ca-Fe sulphide assemblages (***Namur & Charlier, 2017; Nittler & Weider, 2019***).

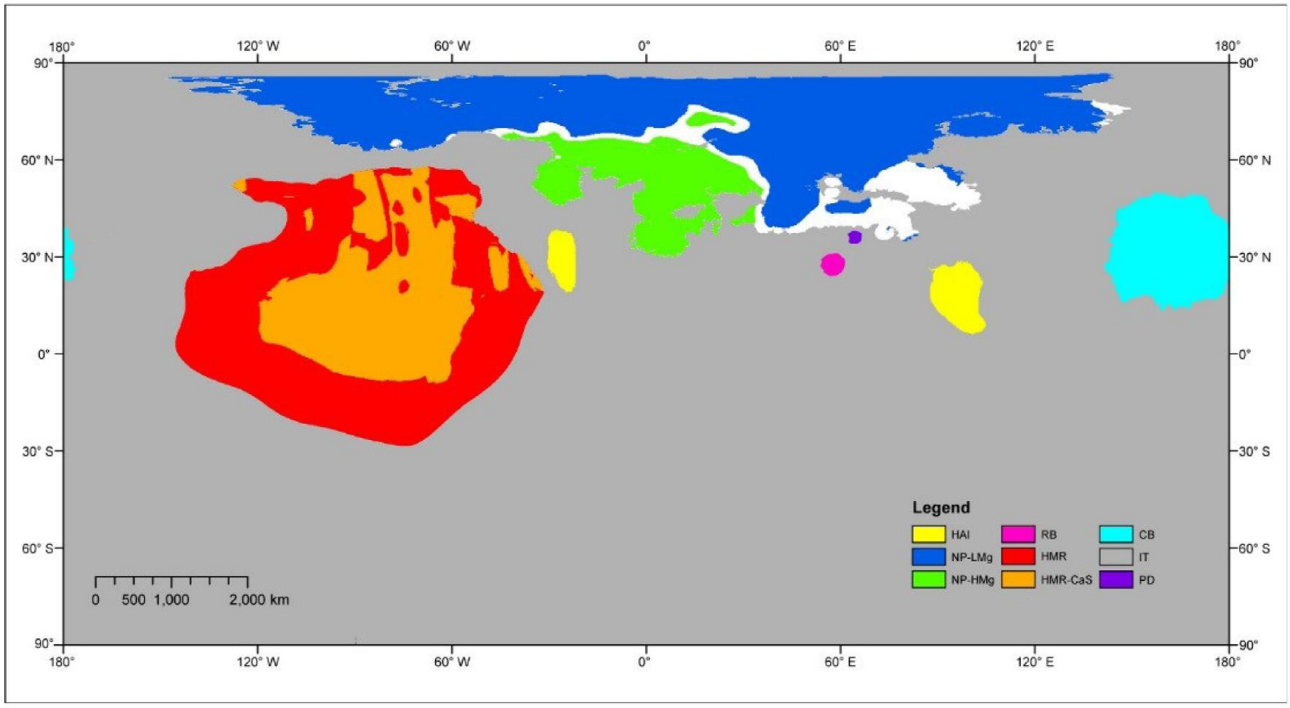


Figure 1.2. Mercury's geochemical terranes proposed by **Vander Kaaden et al. (2017)**. HAI= high-Al region; NP-LMg= northern volcanic plains with low Mg; NP-HMg= northern volcanic plains with high Mg; RB= Rachmaninoff Basin (RB); HMR= high-Mg region; HMR-CaS= high-Mg region with highest Ca and S; CB= Caloris Basin; IT= intermediate terrane; PD= pyroclastic deposits.

1.1.2.2. Imaging and spectral data

MDIS images show the morphology of the surface modelled by volcanism and cratering. Effusive volcanism initially formed the plains, which were later modified by impact processes that created cratering. Different geomorphic units, with different ages of formation and cratering degrees, have been proposed in the literature (e.g., ***Denevi et al., 2013***). Features related to the presence of explosive volcanism have also been observed. Pyroclastic deposits, called Faculae, presenting higher reflectance and redder spectral slope than the surrounding materials were detected (***Barraud et al., 2021; Blewett et al., 2009; Galiano et al., 2022; Goudge et al., 2014; Head et al., 2008; Kerber et al., 2009, 2011; Thomas et al., 2014***).

MDIR and MASCS-VIRS (Visible-Infrared Spectrograph) and UVVS (Ultraviolet and Visible Spectrometer) spectra evidenced different reflectance and spectral slope values across the surface. Therefore, similarly to the identification of distinct geochemical terranes representing the chemical heterogeneity of Mercury's surface, different spectral units have also been proposed (***Murchie et al., 2015***) (**Fig. 1.3**). The major spectral units are divided into:

- low-reflectance material (LRM), having the lowest reflectance and spectral slope. It is suggested that C content can be high in this region (***Peplowski et al., 2016***), influencing the dark albedo;

- low-reflectance blue plains (LBP), having lower reflectance and spectral slope than the average, but higher than the LRM;
- intermediate plains (IP), having intermediate reflectance and spectral slope values, most of the surface is represented by IP;
- high-reflectance red plains (HRP), having the highest reflectance and slope values.

Three additional units are also suggested:
- red unit, with higher reflectance and slope than HRP, corresponding to faculae;
- fresh crater material, with high reflectance but a bluer slope than Mercury's average;
- hollows, bright, fresh, rimless, shallow depressions, having higher reflectance but bluer slope than surroundings (***Blewett et al., 2011, 2013; Barraud et al., 2020, 2023***).

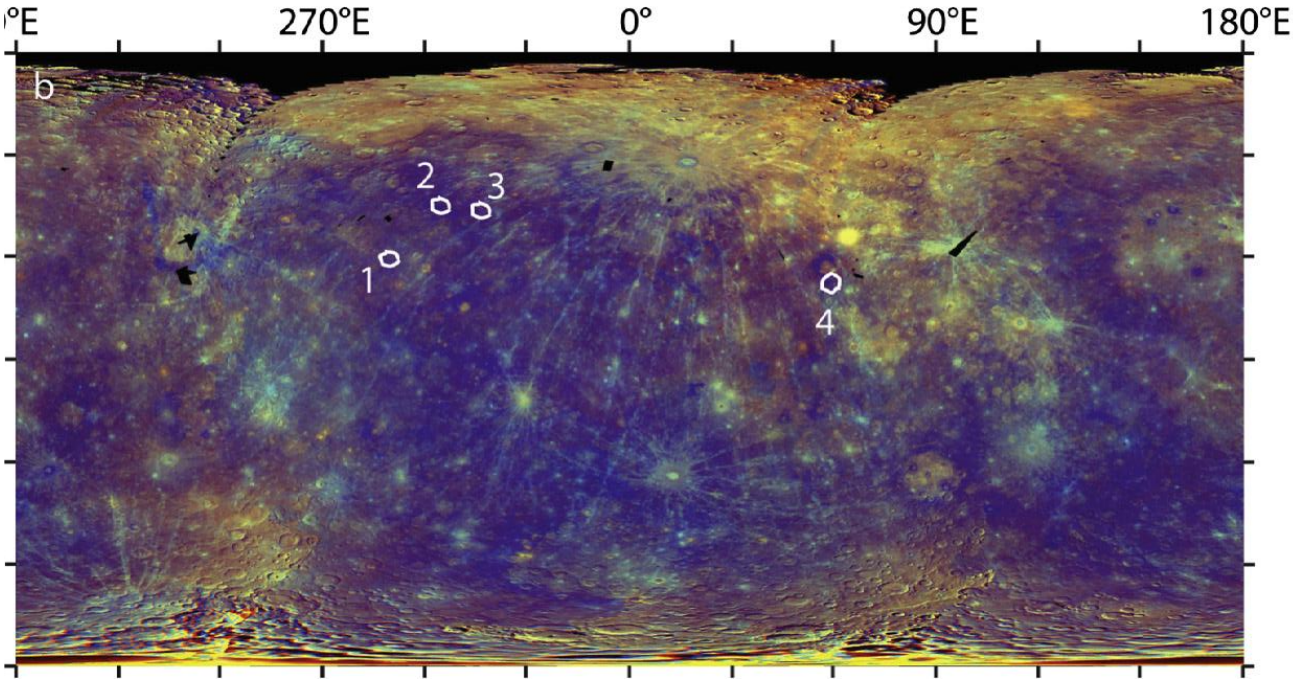


*Figure 1.3. Enhanced colour map of Mercury' surface from **Murchie et al. (2015)**. Orange= HRP; blue= LRM.*

Mercury's average spectrum from MASCS presents low reflectance, the surface appears darker than any laboratory mixture of analogues minerals, a clear red slope, and no evidence of absorption band at 1 μm (***Izenberg et al., 2014***) (**Fig. 1.4**). The 1 μm absorption is associated with $Fe^{2+}$ in mafic minerals (pyroxene and olivine) (e.g., ***Burns, 1993***; ***Cloutis et al., 1986***; ***Dunn et al., 2010***; ***Gaffey et al., 1993***; ***Klima et al., 2007, 2011; Sunshine & Pieters, 1998***), the lack of it in Mercury's spectra is consistent with the very low FeO present on the surface. The dark albedo could be explained by the presence of graphite, by extreme thermal variations (***Helbert & Maturilli, 2009; Maturilli et al., 2014***), and by additional different processes affecting the surface that could

lead to the darkening of the reflectance spectra (see **Section 1.1.3**). Moreover, MASCS spectra show a UV-downturn and concave curvature of the spectrum in the UV range (***Goudge et al., 2014***), particularly for hollows and pyroclastic deposits (***Barraud et al., 2020, 2021***).

MDIS spectra, on the other hand, revealed the presence of an absorption feature around 1 µm for some hollows (***Lucchetti et al. 2018***), along with a ~0.6 µm feature associated with higher concentrations of sulphides (***Vilas et al., 2016***) or transitional elements different from iron on mafic mineral (***Lucchetti et al. 2018***).

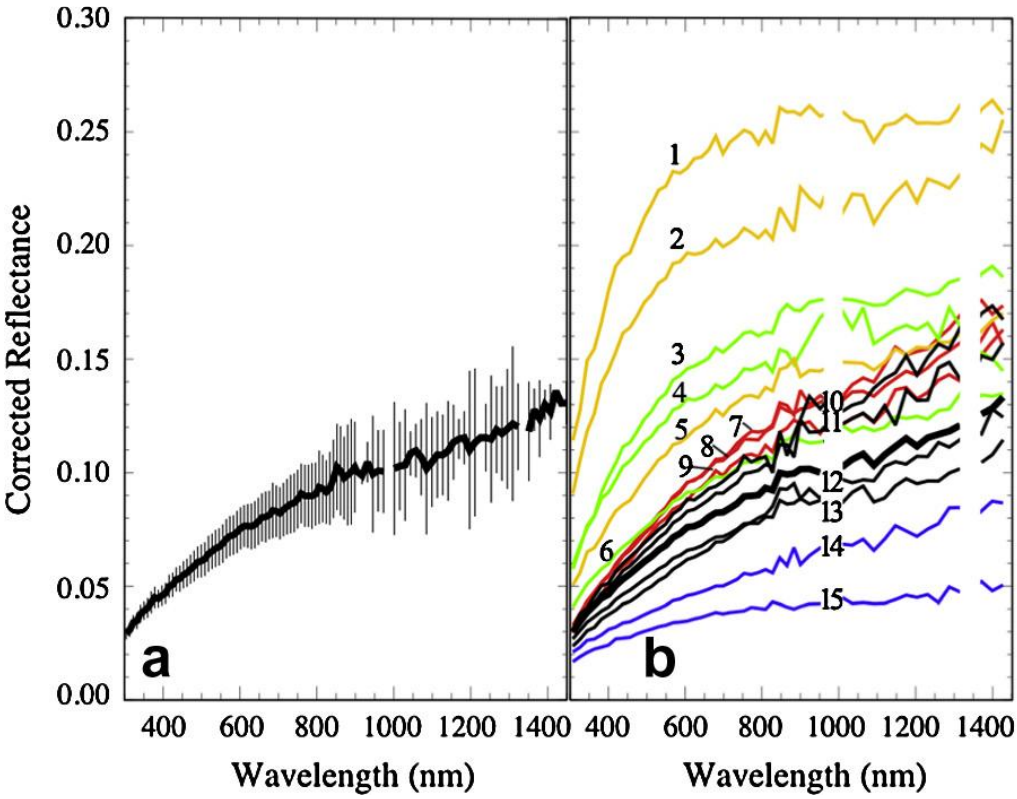


Figure 1.4. Mercury's surface MASCS spectra from **Izenberg et al., (2014)**. a) average spectrum. b) spectra for the identified VIRS spectral units.

1.1.2.3. Unresolved questions

MESSENGER delivered new key information on Mercury, yet some questions still need to be further investigated. For example, concerning only the surface, more information is required on the chemical composition of the southern hemisphere, the permanently shadowed regions, the processes of volatile loss, and the effects of space weathering.

The collected reflectance spectra interpretation is complicated by three factors that can influence the spectral features. Firstly, we do not know the precise grain size of the regolith covering the surface that could influence the intensity of the absorptions. Subsequently, the acquisition geometry (e.g., ***Domingue et al., 2017***) and spatial resolution (e.g., ***McClintock et al., 2008***) play

important roles in the reflectance intensity, detection of spectral features, and small variabilities across the surface. Finally, the effect of Space Weathering (SpWe, see **Section 1.1.3**) leads to darkening and reddening of the surface spectra. Moreover, no mid-infrared (MIR) data were acquired by the MESSENGER mission. To date, the MIR spectra available for Mercury's surface come from ground-based observations (***Sprague et al., 2000***).
The ESA-JAXA BepiColombo mission is expected to address these unresolved questions (**Section 1.1.4**).

### 1.1.3. Space weathering affecting Mercury's surface

Like other airless bodies, Mercury's surface is affected by Space Weathering (SpWe), which produces alteration in the physical and chemical properties of the uppermost layers (***Domingue et al., 2014; Killen et al., 2001***). SpWe involves multiple processes: solar wind irradiation, cosmic ion irradiations, and micrometeoroid bombardment (e.g., ***Chapman, 2004; Hapke, 2001; Pieters & Noble, 2016***). SpWe can be shielded by a planet's magnetic field, but in the case of Mercury's weak magnetic field, it is only slightly moderated (***Domingue et al., 2014***). SpWe in the inner solar system has been extensively studied for the Moon (e.g., ***Hapke, 1973; Keller & McKay, 1993; Pieters et al., 1993***). The literature suggests that since Mercury is closer to the Sun and has a greater mass than the Moon, this leads to frequent impacts occurring at high speeds, exceeding those on the Moon (***Cintala, 1992***), and to a stronger irradiation (***Domingue et al., 2014***). One of the effects of SpWe on airless bodies' surfaces is the formation of small particles of metallic iron, called "nanophase iron" (npFe$^0$) (e.g., ***Cassidy & Hapke, 1975; Hapke, 2001; Vilas & Hendrix, 2015***). On Mercury, the high rate and efficiency of SpWe processes on the surface might have led to the formation of npFe$^0$ particles in greater amounts than on the Moon, and in different abundances across the surface, depending on the original quantity of FeO in the various geochemical units (***Domingue et al., 2014***).
SpWe induced physical and chemical modifications that complicate the interpretation of remote sensing information from the body's surface, as they can alter the reflectance spectra. The main effects in the VNIR spectral range, as observed in laboratory SpWe simulations experiments through ion irradiation and laser irradiation, are an albedo decrease (darkening) and a spectral slope increase (reddening) (***Brunetto & Strazzulla, 2005***; ***Brunetto et al., 2014; Fulvio et al., 2012; Hapke, 1973***; ***Hapke, 2001***; ***Marchi et al., 2005***; ***Penttilä et al., 2020; Weber et al., 2020***). In some cases, an albedo increase (brightening) and slope decrease (blueing) have also been observed (e.g., ***Lantz et al., 2013, 2015, 2017; Moroz et al., 2004; Nesvorný et al., 2005; Vernazza et al., 2013***). Moreover, the intensity of the absorption bands can be reduced (***Fulvio et al., 2012;***

***Hapke, 2001; Marchi et al., 2005; Penttilä et al., 2020; Strazzulla et al., 2005; Vernazza et al., 2009***). In the MIR spectral range, SpWe can induce spectral contrast attenuation, modifications of band shapes, and shifts of the Christiansen Feature (CF), Reststrahlen Bands (RBs), and Transparency Feature (TF) positions (***Brunetto et al., 2014; Brunetto et al., 2018; Chrbolková et al., 2021; Lantz et al., 2015; 2017; Rubino et al., 2024***). The spectral variations can also be induced by the partial amorphization of the SpWe exposed surface (e.g., ***Brucato et al., 2004***). Simulating SpWe processes with different laboratory techniques, ion irradiation to simulate solar wind irradiation, and laser irradiation to simulate micrometeorite impacts, lead to different microstructural modifications of the surface, but the spectral effects are similar (***Weber et al., 2020***), i.e., mostly darkening and reddening. Additionally, SpWe simulations through ion irradiation evidenced that the spectral modifications are strongly dependent on the composition and mineralogy of the material. On Mercury's surface, the creation of $npFe^0$ could lead to darkening and reddening of the spectra. It was proposed in the literature that most of the surficial iron might have been converted into $npFe^0$ of different sizes (***Lucey & Riner, 2011***), with smaller $npFe^0$ (<10 nm) leading to darkening and reddening, and larger $npFe^0$ (>40 nm) producing darkening alone (***Noble et al., 2007***). Nevertheless, other darkening agents must be taken into account to explain such a dark albedo. These agents could be amorphous carbon (***Bruck Syal et al., 2015; Trang et al., 2015***) and opaque compounds containing S (***Domingue et al., 2014***), considering the presence of C and S on the surface. Since different minerals are thought to respond differently to irradiation (e.g., ***Chrbolková et al., 2021***) and that iron amount can influence the spectral effects (materials containing less iron are more sensitive to darkening and reddening, e.g., ***Caminiti et al., 2024***), it can be hypothesized that SpWe-induced spectral modifications can be different in distinct Mercury's geochemical terranes (***Caminiti et al., 2024***).

### 1.1.4. BepiColombo mission

The ESA-JAXA BepiColombo mission (***Benkhoff et al., 2021; Rothery et al., 2020***) was launched in 2018 and is expected to enter Mercury's orbit in November 2026. The mission is composed of two spacecraft, the Mercury Planetary Orbiter (MPO) and the Mercury Magnetospheric Orbiter (MMO), traveling together. MMO instruments will focus on Mercury's environment, including the exosphere and interactions with solar wind, and the magnetosphere. MPO instruments will focus on the planet's surface, exosphere, and interior. Concerning the surface, this mission will map it with a higher spatial resolution than MESSENGER and will also investigate the southern hemisphere and the polar deposits. The spectral studies will be at a higher resolution and extended to the MIR range. Moreover, the detailed study of the exosphere will help understand the complex

interaction processes between the surface and the surrounding environment that led to its formation (***Milillo et al., 2023***).

The MPO instruments that will retrieve information on these topics are listed below:
- Spectrometer and Imagers for MPO BepiColombo-Integrated Observatory SYSstem (SIMBIO-SYS, ***Cremonese et al., 2020***). It is composed of the Stereo Channel (STC), the High spatial Resolution Imaging Channel (HRIC), and the Visible Infrared Hyperspectral Imager Channel (VIHI). STC will provide images of the surfaces defining geological units and impact, volcanic, and tectonic features. HRIC will provide high-resolution images of special targets. VIHI will map the surface to provide the mineralogy, operating in the VNIR range between 0.4 and 2 μm.
- Mercury Thermal Infrared Spectrometer (MERTIS, ***Hiesinger et al., 2020***). It will map the surface to provide the mineralogy, operating in the MIR range between 7 and 14 μm. It will also investigate the surface temperatures.
- Mercury Imaging X-ray Spectrometer (MIXS, ***Fraser et al., 2010***). It will map the elemental composition of the entire surface.
- Mercury Gamma-ray and Neutron Spectrometer (MGNS, ***Mitrofanov et al., 2021***). It will study the volatiles.
- Search for Exosphere Refilling and Emitted Neutral Abundances (SERENA, ***Orsini et al., 2010***). It will study the interaction processes among the surface, exosphere, solar wind, and magnetosphere.
- Probing of Hermean Exosphere by Ultraviolet Spectroscopy (PHEBUS, ***Chassefière et al., 2010***). It will study the exosphere composition.

Based on the above, BepiColombo mission is going to provide an unprecedented investigation of the planet, offering new and valuable insights into its formation and evolution.

### 1.2. The Importance of Analogues

It is not possible to have direct information on Mercury's surface, since meteorites coming from Mercury are extremely unlikely to be found on Earth (***Love & Keil, 1995***), and no samples are currently available for study. Therefore, the investigation of potential analogues is crucial to obtain insights into the formation and evolution processes of the surface. The natural analogues proposed so far for the Mercury's surface can be divided into extraterrestrial (highly reduced meteorites such

as aubrites, enstatite chondrites, and related melt rocks) and terrestrial (high-Mg rocks such as boninites and komatiites) analogues.

### 1.2.1. Aubrites, enstatite chondrites and related melt rocks

Highly reduced meteorites, including enstatite chondrites, achondrites, aubrites and related melt rocks are the most reduced natural objects at our disposal. Their oxygen fugacity ($fO_2$) values are calculated to be lower than the iron-wüstite (IW) buffer (***McCoy & Bullock, 2017***), comparable to those inferred for Mercury (**Fig. 1.5**). Aubrites are a rare group of achondrites. They are igneous rocks, usually presenting a brecciated texture (***Keil, 2010***). They are mostly composed of FeO-poor enstatite, followed by forsterite, diopside, and plagioclase. Minor Fe,Ni metals, troilite, and exotic sulphides of typically lithophile elements (Mg, Ca, Mn, Na) are also present (e.g., ***Barrat et al., 2016; Keil, 2010; Okada et al., 1988; Watters & Prinz, 1979; Wheelock et al., 1994***). Enstatite chondrites are mostly composed of FeO-poor enstatite with variable amounts of Si-bearing metals, troilite, and exotic sulphides (e.g., ***Keil, 1989***). Plagioclase may occur in minor amounts, while it is more abundant in enstatite achondrites and melt rocks (***Burbine et al., 2000***; ***Lin & Kimura, 1998; McCoy et al., 1995; Udry et al., 2019***).

Considering the mineral assemblages and spectral features, aubrites are proposed in the literature as promising analogues of Mercury's surface (e.g., ***Burbine et al., 2002; Morlok et al., 2020; Wilbur et al., 2022***). However, it should be noted that despite the good mineralogical and spectral similarities, aubrites do not represent a perfect petrological analogue of Mercury's surface. For example, plagioclase and sulphides are expected to be much more abundant on the planet's surface (***Vander Kaaden et al., 2017; Wilbur et al., 2022***), which is also expected to present higher Fe content. More abundant plagioclase, sulphides, and Fe content can be observed in enstatite chondrite melt rocks, although in this type of meteorites, less, if none, forsterite and diopside are observed. Nonetheless, enstatite chondrite impact melts can be considered as valuable petrological natural analogues for the study of impact and high temperature processes on Mercury (***Udry et al., 2019***).

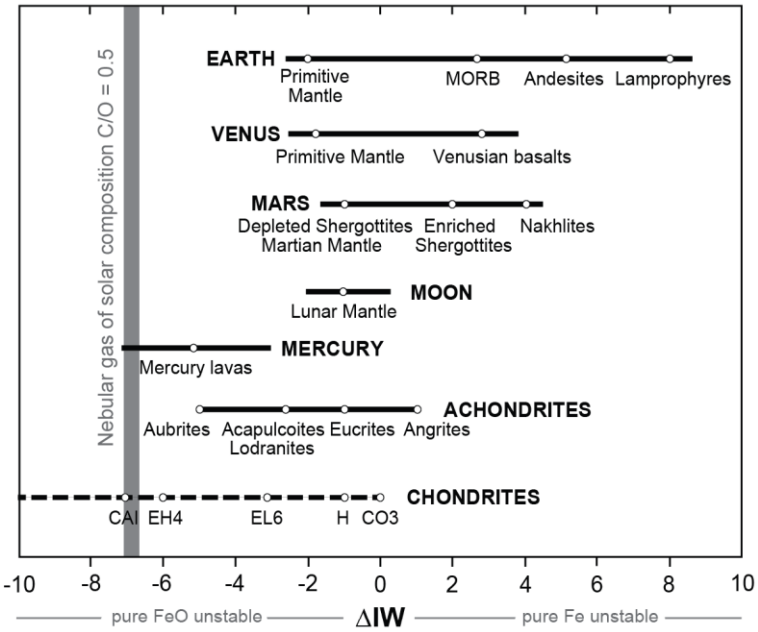


Figure 1.5. Oxygen fugacity ($fO_2$) values of several objects of the Solar System from **Cartier & Wood (2019)**.

### 1.2.2. Boninites and komatiites

Petrologic modelling of Mercury's surface shows that the mineralogy is dominated by plagioclase and orthopyroxene, suggesting similarities with terrestrial norites (***McCoy et al., 2018; Stockstill-Cahill et al., 2012***). At the same time, the high Mg/Si ratio indicates a better fit with terrestrial komatiites (***Charlier et al., 2013***), and the higher $SiO_2$ values of the same regions denote a more accurate similarity with boninites (***Vander Kaaden & McCubbin, 2015***). ***Vander Kaaden et al. (2017)*** propose that Mercury's geochemical terranes can be considered as boninites or komatiites depending on their estimated bulk composition. Boninites are porphyritic rocks with a typical chemical composition characterized by $SiO_2$> 52%, MgO> 8% and $TiO_2$< 0.5% (***Le Bas, 2000***). They are composed of olivine, orthopyroxene, and clinopyroxene phenocrysts in a glassy or finely crystalline groundmass (***Crawford et al., 1989***). Plagioclase can be present in certain boninitic lavas (***Taylor et al., 1994***) or in the groundmass of slowly cooled boninites (***Crawford et al., 1989***). Komatiites are defined by higher Mg contents, MgO > 18 %, minor Si contents, $SiO_2$< 52%, and $TiO_2$< 1% (***Le Bas, 2000***). Their mineralogy includes olivine and spinel phenocrysts in a groundmass of glass and pyroxene. They are characterized by the typical spinifex texture, resulting from their fast cooling (***Kerr & Arndt, 2001***). These terrestrial rocks display higher FeO contents than what we expect from Mercury; they do not present as much sulphides and metals as the planet's surface, and they are affected by intense aqueous alteration. However, despite the mineralogical and chemical differences intrinsic in the different conditions of formation, they represent promising analogues for the bulk chemical composition of Mercury's terranes (***Mari et al., 2023***).

### 1.2.3. Mercury's analogues: State of the art

The study of Mercury analogues is essential for the interpretation of the data that will be retrieved by BepiColombo. To date, several studies have been conducted on different types of analogues, natural and synthetic, focusing on various aspects.

There are relatively few spectral studies available on highly reduced meteorites. The latter include reflectance investigations on aubrites and enstatite chondrites in the VNIR range (e.g., ***Burbine et al., 2002***; ***Cantillo et al., 2024; Cloutis & Gaffey, 1993***; ***Cloutis et al., 2016; Dibb et al., 2022; Vernazza et al., 2009; Zhang et al., 2023***), MIR range (e.g., ***Markus et al., 2018; Morlok et al., 2020***), and in the VNIR-MIR range on ungrouped meteorites exhibiting similarities with Mercury (***Cloutis et al., 2018***; ***Rider-Stokes et al., 2025***). These studies evidenced a good spectral correlation between the relatively featureless spectra of reduced meteorites and Mercury's spectra. Still, some differences can be observed, and increasing the spectral database on these reduced materials is crucial. SpWe processes affecting Mercury's may contribute to these differences. Therefore, SpWe simulations can give us information on how these processes modify the spectral features of reduced materials. On this matter, only two SpWe simulations have been conducted on highly reduced meteorites so far: ion irradiation on an enstatite chondrite (***Vernazza et al., 2009)*** and laser irradiation on one aubrite and two enstatite chondrites (***Zhang et al., 2022***). Ion irradiation has also been conducted on boninites and komatiites by ***Caminiti et al. (2024)***, and their reflectance properties in the VNIR and MIR spectral ranges have been investigated. Other reflectance studies have been conducted in the VNIR by ***Carli et al. (2013)*** and ***Mari et al. (2023)***. The investigation is expanded to the MIR range by ***Maturilli et al. (2014)***, along with the study of the effects of thermal variations on the reflectance spectra. To date, no direct measurement of the emissivity of the terrestrial analogues has been performed. Emissivity studies have only been conducted on minerals expected to be present on Mercury's surface (***Ferrari et al., 2014; Helbert et al., 2013***), although the minerals used in those studies present a higher FeO content than the planet's surface, and on synthetic mixtures of varying composition, including sulphides (***Bott et al., 2023; Carli et al., 2024a; Ferrari et al., 2020***). Reflectance studies on synthetic materials have focused on synthetic glasses and mixtures (e.g., ***Bruschini et al., 2022; Carli et al., 2025; Izawa et al., 2013; Markus et al., 2018, 2024; Morlok et al., 2017, 2021, 2023, 2024; Pisello et al., 2023; Reitze et al., 2021; Renggli et al., 2023; Weber et al., 2023***).

Experimental petrology studies have been conducted, at reducing conditions, to understand igneous processes at low $fO_2$ starting from natural samples (e.g., Indarch EH4 meteorite, ***Berthet et al., 2009; McCoy et al., 1999;*** Hvittis EL6 meteorite, ***Cartier et al., 2014***). Experiments have also

been carried out to infer the possible mineralogy of Mercury's surface, starting from synthetic materials (***Charlier et al., 2013; Namur et al., 2016; Namur & Charlier, 2017***), and to study the formation of sulphides in reducing conditions (***Renggli et al., 2022***). Moreover, to support the interpretation of future data from BepiColombo, a blind sample simulating Mercury's regolith has been developed to be investigated using multiple analytical techniques (***Barraud et al., 2025***).

### 1.3. Objectives and Methodological Approach of This Work

The aim of this work is to improve our understanding of Mercury's surface through the investigation of analogous materials using a wide range of analytical techniques, in preparation for the interpretation of the upcoming data from the BepiColombo mission.

The natural analogues selected to reach these goals are both extraterrestrial and terrestrial. The extraterrestrial analogues are represented by five aubrites (Rantila, Tiglit, Norton County, Peña Blanca Spring, and NWA 14185), two enstatite chondrites of high petrologic type (Itqiy and NWA 4945), one enstatite achondrite (NWA 13266), and one enstatite chondrite melt (NWA 13210). These meteorites have been characterized using the analytical techniques illustrated below:

- Scanning Electron Microscope (SEM); for backscattered electron (BSE) and energy-dispersive spectroscopy (EDS) maps collection for textural and mineralogical analysis;
- Electron Probe Microanalysis (EPMA); for the quantitative chemical analysis of minerals;
- Reflectance spectroscopy in the visible and near-infrared (VNIR) and mid-infrared (MIR) spectral range; for the collection of reflectance spectra in the spectral ranges that will be investigated by SIMBIO-SYS/VIHI (0.4-2 μm) and MERTIS (7-14 μm) on board the BepiColombo mission;
- Laser Induced Time Resolved Luminescence (LITRL); on the Rantila aubrite, to study the luminescence behaviour and activator elements.

The correlation between the spectral properties and mineralogy/mineral chemistry of these highly reduced materials could help prepare for the interpretation of the upcoming spectral data from SIMBIO-SYS/VIHI and MERTIS instruments and chemical data coming from the MIXS instrument.

The five aubrites have also been used for ion irradiation experiments, with $He^+$ and $C^+$, simulating solar wind exposure. Studying how ion irradiation changes the reflectance spectra and physical properties of the uppermost layers of the material most like Mercury's surface currently available, can provide insights into how reduced surfaces like Mercury's ones are affected.

The chosen terrestrial analogues are boninites' samples coming from different localities of the Troodos Massif in Cyprus. These specific boninites were chosen because of their relatively low

degree of aqueous alteration. The boninites were investigated using the same analytical techniques as the meteorites, except for LITRL. X-ray Fluorescence (XRF) analysis was also performed to investigate the bulk composition and to compare it with the composition of Mercury's geochemical terranes. Moreover, the emissivity behaviour of these materials at Mercury-like surface temperatures (up to 450 °C) was studied, in order to obtain insights into what the MERTIS instrument might observe on the planet's surface.

### 1.4. Thesis Structure and Content Overview

This thesis is composed of six chapters, including the introduction (Chapter 1) and the conclusions (Chapter 6). Chapters 2 through 5 present the main scientific achievements obtained during my Ph.D. project. Each of these chapters is dedicated to a specific topic and is structured as a scientific paper (i.e., introduction, materials and methodologies, results, discussion, and conclusions). In detail, Chapter 2 reports a published article about the mineralogical and spectroscopic characterization of three fragments, each presenting distinct characteristics, of the Rantila aubrite (***Landi et al., 2025***). This work also includes the first LITLR investigation on this type of meteorites. Compared to the version presented in the published article, the content of Chapter 2 has been expanded and improved following the valuable suggestions of the thesis referees. Chapter 3 presents a work, about to be submitted for publication, on the mineralogical and spectroscopic characterization of different types of highly reduced meteorites, highlighting their differences and suggesting the origin from multiple distinct parent bodies. Chapter 4 collects ion irradiation studies on aubrites, about to be submitted for publication. At the time of writing, this represents the first ion irradiation investigation performed on this group of meteorites. Chapter 5 accounts for a published article about the mineralogical characterization and spectroscopic investigation, both reflectance and emissivity, of terrestrial boninites. At the time of writing, the latter represents the first paper on emissivity measurements of these materials. Similarly to Chapter 2, additional details suggested by the thesis referees have been included in the chapter.

The supportive information of the works presented in each chapter, published, submitted, and in preparation, is reported in the Appendices, along with additional investigation carried out during my Ph.D. project.

# 2. Insights into the Mineralogy of the Rantila Aubrite: A Luminescence and VNIR Reflectance Spectroscopy Study

This chapter is a published paper in the Icarus journal by A.I. Landi, M. Gaft, C. Carli, F. Capaccioni, and G. Pratesi.

Authors contribution
Writing – original draft: A.I.L., M.G., C.C.; Methodology: A.I.L., M.G., C.C.; Investigation: A.I.L., M.G., C.C., Formal analysis: A.I.L., M.G., C.C.; Conceptualization: A.I.L., C.C., F.C., G.P.; Writing – review & editing: C.C., F.C., G.P.; Supervision: C.C., G.P.; Funding acquisition: F.C.; Resources: G.P.; Project administration: G.P.

**Abstract**
Rantila aubrite fell in Rantila, Gujarat, India, in August 2022. This study aims to investigate the mineralogy and mineral-chemistry of three fragments of this meteorite and correlate them with reflectance spectroscopy in the visible and near-infrared spectral range (VNIR) and Laser-Induced Time-Resolved Luminescence (LITRL). The very low $Fe^{2+}$ content of aubrites prevents luminescence quenching under UV light exposure, allowing these meteorites to exhibit well-defined luminescence. The investigated samples have different appearances. One consists of a light-coloured portion primarily composed of FeO-free enstatite, along with forsterite, diopside, plagioclase, minor sulphides (troilite, alabandite, daubréelite, and (Fe,Ca,Mn,Mg)S), and kamacite. The second sample is composed mainly of the same light-coloured portion and hosts a dark forsterite clast. The third sample is mainly made of dark glass. Minor terrestrial weathering is observed, with the detection of sporadic iron oxides/hydroxides. The chemical composition of the detected phases indicates highly reducing conditions during the formation, as expected for an aubrite. The mineral chemistry is similar between the different fragments in terms of major elements concentrations; some differences are observed for minor elements. Luminescence spectra indicate $Cr^{3+}$ and $Mn^{2+}$ as activators in diopside and forsterite, respectively, for two of the three samples. $Ce^{3+}$ is the activator in the third sample, which lacks forsterite and has lower $Cr_2O_3$ contents in diopside compared to the other two samples. Therefore, the differences in mineral chemistry observed through electron microprobe analysis (EPMA) are further emphasized by luminescence data. Investigating the luminescence behaviour could provide a valuable contribution to the mineralogical-petrological study of these materials. VNIR reflectance spectra are consistent with low Fe-Ca pyroxene and forsterite. The main absorption typical of mafic minerals (~0.9 μm) is deeper than what has previously been observed in aubrites: this can be related to the slightly higher FeO concentrations, which, despite being very low (<0.4 wt%), still contribute to the absorption. The absorption features at ~1.4 μm and ~1.9 μm, associated with $H_2O$ and OH, indicate low levels of terrestrial weathering. Increasing the knowledge of the correlation between spectral properties and mineralogy/mineral chemistry on highly reduced meteorites will be useful for future investigation of Mercury with the ESA's BepiColombo mission, specifically for the interpretation of the data expected from the Spectrometer and Imagers for MPO BepiColombo Integrated Observatory SYStem (SIMBIO-SYS)/Visible and near Infrared Hyperspectral Imager (VIHI) and Mercury Radiometer and Thermal Infrared Spectrometer (MERTIS) instruments.

## 2.1. Introduction

Aubrites are a rare group of achondrites. They are igneous rocks mostly composed of FeO poor (almost free) enstatite, followed by forsterite, diopside and plagioclase. Minor Fe,Ni metals, troilite, and peculiar Mg, Ca, Mn, Cr, Ti, Na sulphides are also present (e.g., ***Barrat et al., 2016; Keil, 2010; Watters & Prinz, 1979; Wheelock et al., 1994***). Aubrites are typically brecciated, with some exceptions of unbrecciated meteorites (e.g., ***Keil, 2010; Okada et al., 1988; Watters & Prinz, 1979***). The extremely low amount of FeO in silicates and the presence of sulphides composed of typically lithophile elements are indicative of a formation under extremely reducing conditions (e.g., ***Fogel, 1997; Keil, 1989; Keil, 2010; Okada et al., 1988; Wilbur et al., 2022***): the oxygen fugacity (fO2) values during the formation are calculated to be lower than the iron-wüstite (IW) buffer (***McCoy & Bullock, 2017***). Therefore, the experimental data suggest that aubrites formed from igneous processes on enstatite chondrite-like parent materials (e.g., ***Keil, 1989; Keil, 2010; McCoy & Bullock, 2017***).

The very low $Fe^{2+}$ content in aubrites prevents the suppression of luminescence when exposed to UV light, resulting in clear luminescence visible for these meteorites. This feature has been qualitatively observed, for example, in the Norton County aubrite, but no specific studies on aubrites' luminescence behaviour have been carried out. Very few studies, in the past, have been conducted on the luminescence spectra of enstatite achondrites under UV light exposure (e.g., ***Derham et al., 1964; Geake & Walker, 1966***) and no one has been able to explain the causes fully. Luminescence imaging is widely used for mineralogy and petrology studies, especially for the study of phase distribution, crystal growth and the detection of internal textures such as inclusions, zoning, and intergrowth (e.g., ***Finch et al., 2024; Götze et al., 2024***). Nevertheless, it does not provide any information on the luminescence activators that can be obtained with the less commonly used luminescence spectroscopy. For this purpose, ***Gaft et al. (2015)*** built up an exhaustive library of luminescence spectra in minerals by means of three types of laser-based spectroscopy: Laser-Induced Time-Resolved Luminescence, Laser-Induced Breakdown spectroscopy, and Raman Spectroscopy. These techniques are gaining attention in the planetary sciences field as they are used for the investigation of organic compounds that can be detected in meteorites and on planetary surfaces (e.g., ***Edgett et al., 2012; Sharma et al., 2012***). For instance, the Perseverance rover of NASA's Mars 2020 mission was equipped with instruments for the detection of bio-organic matter on the Martian surface (***Gaft et al., 2024; Maurice et al., 2021***). For this purpose, the meteorites studied with this technique are carbonaceous chondrites and Martian meteorites (e.g., ***Laurent et al., 2019; Lymer et al., 2020; Minitti & McCoy 2012***).

Aubrites, in recent years, have gained attention due to their compositional and spectral properties resembling those highlighted by remote investigation of Mercury's surface by Mercury Surface, Space Environment, Geochemistry, and Ranging (MESSENGER) mission (***Solomon et al. 2018***). The highly reduced nature and the mineralogy of aubrites led to the hypothesis that, along with enstatite chondrite impact melts (***Udry et al., 2019***), they represent promising natural analogues of Mercury's surface rocks (e.g., ***Burbine et al., 2002; Morlok et al.; 2020, Wilbur et al., 2022***) on the basis of MESSENGER results (e.g., ***McCoy et al., 2018; McCubbin et al., 2017; Namur & Charlier, 2017; Nittler & Weider, 2019; Vander Kaaden et al., 2017; Weider et al., 2012***). In fact, the inferred mineralogy of Mercury's surface is mostly composed of enstatite, forsterite, albitic plagioclase and Mg-Ca-Fe sulphide assemblages (e.g., ***Nittler & Weider, 2019***). Also, Mercury's surface presents a notably high S concentration, ~4 wt%, and a very low Fe concentration, 1-2 wt%, of which FeO is inferred to be <1 wt% from reflectance spectroscopy studies (***Murchie et al., 2015***). These S and Fe concentrations reflect the highly reduced nature of the planet with an oxygen fugacity ($fO_2$) estimated to be in the range 2.6-7.3 log units below iron-wüstite buffer (***McCubbin et al., 2012; Zolotov et al., 2013***). However, so far, there are few spectral studies specifically on aubrites in the visible and near-infrared (VNIR) range (e.g., ***Burbine et al., 2002; Cantillo et al., 2024; Cloutis & Gaffey, 1993; Cloutis et al., 2016; Dibb et al., 2022***), and mid-infrared (MIR) range (e.g., ***Markus et al., 2018; Morlok et al., 2020***). In particular, in the VNIR spectral range, aubrites are characterized by relatively featureless spectra, due to the extremely low FeO content in mafic minerals, with orthopyroxene, clinopyroxene, and olivine being the primary constituents. The typical absorption bands of pyroxene are generally in the range of 0.9-1.0 μm and 1.9-2.1 μm (e.g., ***Burns, 1993; Cloutis et al., 1986; Dunn et al., 2010; Gaffey et al., 1993; Klima et al., 2007, 2011***), whereas olivine shows a broader band around 1.0 μm (***Burns, 1993; Cloutis et al., 1986; Sunshine & Pieters, 1998***). Those absorptions are generally absent or very weak for the FeO content typical of aubrites. Nonetheless, the position and depth of these absorption features can provide insights regarding the FeO content and the relative abundances of orthopyroxene, clinopyroxene and olivine (***Burns, 1993; Cloutis et al., 2016***).

In this work, we investigate, through luminescence and reflectance spectroscopy, some fragments of Rantila aubrite, a fall in Rantila, Gujarat, India, in August 2022 (see *The Meteoritical Bulletin n.112,* ***Gattacceca et al., 2024***). The fragments show different lithologies: the main portions show the mineralogy and petrology typical of aubrites (e.g., ***Keil, 2010; Watters & Prinz, 1979***), one fragment presents a dark forsterite clast embedded in the light-coloured aubritic portion, and another fragment is composed of a dark glassy portion, diopside phenocrysts, and only one enstatite phenocryst. We investigated the texture, the mineralogy, and the mineral-chemistry of the different

fragments. Then, we investigated the luminescence behaviour of this meteorite, which shows well visible luminescence colours under UV light, even stronger than those observed in other aubrites. Therefore, laser-induced time-resolved luminescence was performed for the first time on this type of meteorites, with the aim of correlating the luminescence spectra with the mineralogy, petrology, and geochemistry (minor and trace elements). We also studied the spectral properties of the different fragments in the visible and near-infrared (VNIR) spectral range to derive information on the mineralogy of such a fresh and highly reduced meteorite. We then discussed those results in the light of the potential correlation of aubrites with Mercury-like reduced objects from the inner Solar System. This work is particularly useful to increase the knowledge of the correlation between spectral properties and mineralogy/mineral chemistry of highly reduced meteorites in view of the future investigation of Mercury with the ESA's BepiColombo mission (***Benkhoff et al., 2021; Rothery et al., 2020***).

## 2.2. Samples and Analytical Methods

### 2.2.1. Samples

We investigated three centimetric fragments of the Rantila meteorite showing some differences in their appearance and not presenting fusion crust (**Fig. 2.1**). The biggest fragment (0.98 g), referred to as Ran_01, is composed of a predominant light-coloured portion typical of aubrites with a dark millimetric clast embedded in the main lithology. A second, smaller fragment (0.82 g), referred to as Ran_02, presents the same light-coloured portion typical of aubrites. The third fragment (0.88 g), referred to as Ran_03, appears darker with a black glassy portion on one side which does not resemble the light brown fusion crust typical of aubrites that was found in this meteorite (***Srivastava et al., 2023***).

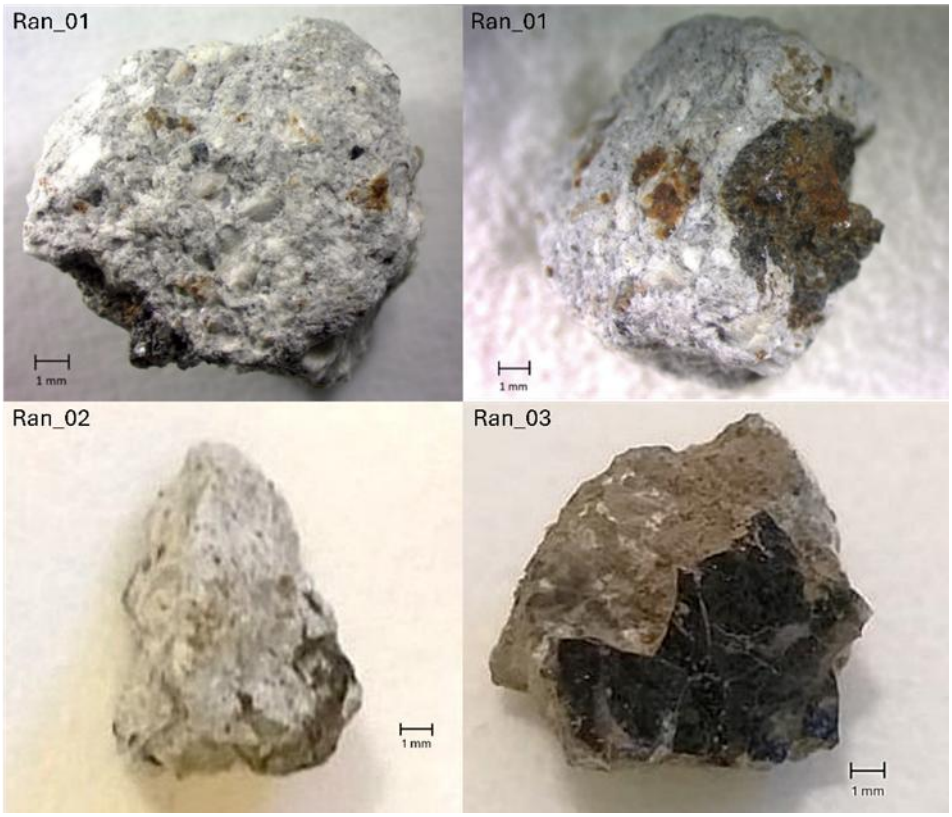


Figure 2.1. Hand specimens: upper left, Ran_01; upper right, Ran_01, view on the dark clast; c) lower left, Ran_02, d) lower right, Ran_03.

### 2.2.2. Analytical methods

We performed scanning electron microscope (SEM), electron probe microanalysis (EPMA), and laser-induced time-resolved luminescence (LITRL) on all samples. Reflectance spectroscopy in the visible and near-infrared spectral range (VNIR) was conducted on Ran_01 and Ran_02. Electron backscattered diffraction (EBSD) was performed on Ran_03. Ran_01 was cut into two pieces to obtain two sections for the study of both the aubritic portion and the dark clast, here referred to as Ran_clast. For SEM, EPMA, and LITRL analyses, the four fragments were singularly embedded in epoxy resin and their surfaces polished with diamond paste with a final particle size of 0.25 µm. EBSD analysis was conducted on Ran_03 to observe the characteristics of the glassy matrix: the previously polished sample was subsequently lapped to prepare it for the analysis. VNIR reflectance spectroscopy was acquired on rough surface of the meteorite fragment in its natural state, before the embedding in epoxy resin, for Ran_01 Ran_clast, and on the embedded and polished surface for Ran_02.

#### 2.2.2.1. SEM

SEM analyses were performed at the Centro di Servizi di Microscopia Elettronica e Microanalisi (MEMA) laboratory of the Università degli Studi di Firenze using a ZEISS EVO-MA15 equipped

with an Oxford ULTIM MAX 40 mm2 EDS detector and Oxford Symmetry EBSD detector. Backscattered electron (BSE) and energy-dispersive spectroscopy (EDS) maps were collected using an accelerating voltage of 15 kV, 10 s acquisition time. An accelerating voltage of 15 kV was used to collect point analyses; pure Co standard was used for calibration for semiquantitative chemical data.

Operation conditions for EBSD analysis were 15 kV accelerating voltage and 10 nA beam current. Modal abundances of the detected phases were obtained with XMapTools 4.1 (***Lanari et al., 2014***) starting from SEM-EDS maps of Mg, Fe, Ca, Na, Al, Si, S, Cr, Ti, Ni,O.

#### 2.2.2.2. EPMA

Quantitative analyses of the detected mineral phases were performed at "Filippo Olmi" laboratory, Dipartimento di Scienze della Terra of the Univerisità degli Studi di Firenze, using a JEOL JXA-8230 Electron Microprobe equipped with five wavelength-dispersive spectrometers (WDS).

The operating conditions (accelerating voltage, beam current, beam size, correction) and the used certified standards (Astimex, Smithsonian, MAC) are summarized in **Table 2.1**.

| | **Accelerating voltage (kV)** | **Beam current (nA)** | **Beam size (µm)** | **Correction** |
|---|---|---|---|---|
| Silicates | 15 | 20 | 3 | ZAF |
| Metals | 15 | 10 | 5 | ZAF |
| Sulphides | 20 | 10 | 3 | PRZ |
| Glasses | 15 | 10 | 10 | ZAF |

| **Investigated elements** | **Si** | **Mg** | **Fe** | **Ca** | **Na** | **K** | **Al** | **Mn** | **Cr** | **Ni** | **Ti** | **Cu** | **Co** | **V** | **S** | **P** | **Zn** |
|---|---|---|---|---|---|---|---|---|---|---|---|---|---|---|---|---|---|
| Silicates | Ab | Ol | Ilm | Di | Ab | San | Pl | Bus | Chr | Ni | Ilm | - | - | - | - | - | - |
| Metals | Si | - | Fe | - | - | - | - | Mn | Cr | Ni | Ti | Cu | Co | V | - | Ap | - |
| Sulphides | Ol | Mg | Ccp | Di | Ab | - | - | Mn | Chr | Pnt | Ti | Ccp | - | V | Ccp | Ap | Sph |
| Glasses | Ab | Ol | Ilm | Di | Ab | San | Pl | Bus | Chr | Ni | Ilm | - | Co | V | Cls | - | Wil |

Table 2.1. EPMA operating conditions and certified standards for every investigated element.
ZAF= Atomic Number (Z), Absorption (A), and Fluorescence (F) correction
PRZ= Phi-Rho-Z (φ(ρz)) correction, φ=ionization distribution, ρ=mass density, z=depth
Ab=albite, Ol=olivine, Di=diopside, Ilm=ilmenite, San=sanidine, Pl=plagioclase, Chr=chromite, Bus=bustamite, Ap=apatite, Ccp=chalcopyrite, Pnt=pentlandite, Sph=sphalerite, Cls=celestite, Wil=willemite

#### 2.2.2.3. Laser-induced time-resolved luminescence

Laser Induced Time Resolved Luminescence was performed to study the luminescence behaviour of the investigated samples, particularly to identify the activator elements. The analysis was conducted at the laboratory of the Department of Physics, Ariel University, Israel. The luminescence excitation source was pulsed neodymium-doped yttrium aluminium garnet (Nd-YAG) (266, 355, 532 nm) and tunable optical parametric oscillator (OPO) (200-800 nm) lasers, delivering 5-10 ns duration pulses. The spectra, observed at 90º, were detected by an intensified ANDOR iStar Charge-Coupled Device (CCD) camera synchronized to the laser pulses. It enables spectral

measurements in selectable time windows determined by a delay time, namely the time between the end of the laser pulse and the beginning of the measurement, and by gate width, that is the time between the beginning and the end of the measurement. Delay time and gate width may be changed from 1.5 ns to 19 ms. The spectral resolution is determined by the monochromator gratings (from 300 to 2400 lines/mm), and the minimal value was 0.1 nm. Decay times have been measured using a standard kinetic series method with different delays and gates. One hundred points have been measured in each kinetic series with different time intervals, namely 10 ms for long-lived components (with 100 μs steps), 1 ms (with ten μs steps), and 100 μs (with one μs steps) for short-lived components. This method has measured decay times without interference from closely spaced spectral features. Experiments were done at room temperature.

2.2.2.4. VNIR reflectance spectroscopy

Reflectance spectra on polished slab (Ran_02) and rock (Ran_01 and Ran_clast) were obtained with a Fieldspec Pro® spectrophotometer mounted on the goniometer at the S.LAB. laboratory at INAF (Istituto Nazionale di Astrofisica) Institute for Space Astrophysics and Planetology (IAPS), Rome. Measurements were made with illumination and collection field of view cones of ±3° which approximate a bidirectional measurement. The illumination and collection angles were 30° and 0°, respectively. The spectral range was 0.35-2.5 μm with a ~3 nm spectral resolution in the range 350-1000 nm and a ~10-12 nm spectral resolution in the range 1001-2500 nm. The illumination source is a quartz tungsten halogen lamp, and the illumination spot has a diameter of ~6 mm. The measurements were taken at room temperature and pressure. A Spectralon® optical standard 99% (registered trademark of Labsphere, Inc.) was used for the calibration. The spectra were acquired in three different areas for both samples: the final spectra are the average of three spectra taken in the same spot, slightly tilting the sample, to avoid systematic error derived from the relative unevenness of the surface. Each individual spectrum was an average of 200 scans. The spectral characteristics of Ran_03 will be investigated and analysed, along with the input from other analytical methods (e.g., micro-IR and Raman/EBSD) at a later stage.

The continuum line was determined by connecting the reflectance maxima in the spectrum with straight-line segments as a function of wavelength (***Clark & Roush, 1984***). The band center corresponds to the position of the minimum reflectance value of the band after the continuum removal. The band depth is calculated as 1-(R/C) after the continuum removal, in which R is the original reflectance and C is the continuum reflectance.

## 2.3. Results

### 2.3.1. Texture and mineralogy

Rantila appears to be a fragmental breccia as indicated by the brecciated texture and the presence of different components in the three analysed fragments: a principal light-coloured portion, an embedded dark clast mostly composed of forsterite, and a dark glassy portion.

#### 2.3.1.1. Light-coloured portion

Ran_01 and Ran_02 show the brecciated texture typical of aubrites (e.g., ***Keil, 2010; Watters & Prinz, 1979***), as shown in **Figure 2.2**.

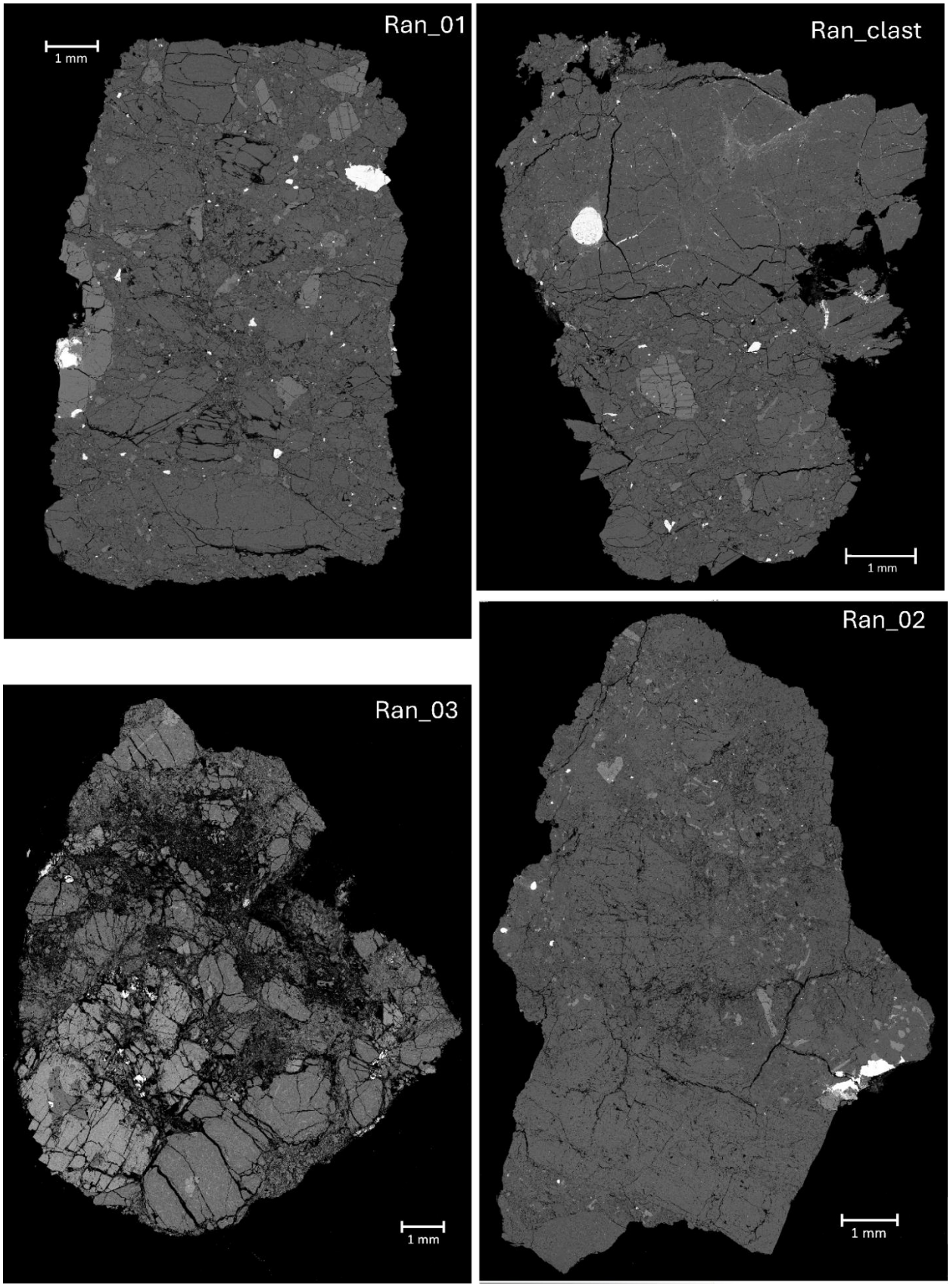


Figure 2.2. BSE maps of the investigated samples. Sample Ran_01 showing aubrites typical brecciated texture with heavily fractured phenocrysts and a finely grained matrix; sample Ran_01, view of the dark clast in the upper part, the clast is as heavily brecciated as the hosting light-coloured portion; sample Ran_02 showing the same textural characteristics of Ran_01; view on the very brittle nature of the glassy portion of sample Ran_03 causing the creation of many voids and missing fragments during the mount preparation.

Enstatite is the predominant phase (**Fig. 2.3 and Fig. 2.4, Table 2.2**), and it is present as phenocrysts of different sizes, up to 5 mm in length, and as fragments composing the matrix. We observed different types of enstatite grains (**Fig. 2.5**): 1) brecciated, free of inclusions or with diopside inclusions, 2) showing visible vesicles, 3) heavily fractured with vesicles and opaque minerals inclusions; in agreement with previous studies on aubrites (e.g., ***Lorenz et al., 2020; Okada et al., 1988***). Moreover, enstatite is present also as lamellae (<10 μm width) in diopside (**Fig. 5d**). Forsterite occur as phenocrysts, up to 5 mm in length, and as matrix in the brecciated veins. Diopside grains in Ran_02 have irregular and often elongated shapes. In Ran_01 millimetric phenocrysts are present often containing enstatite lamellae (**Fig. 5d**). Plagioclases typically have irregular shapes and are more abundant in Ran-01 than in Ran_02 (**Table 2.2**).

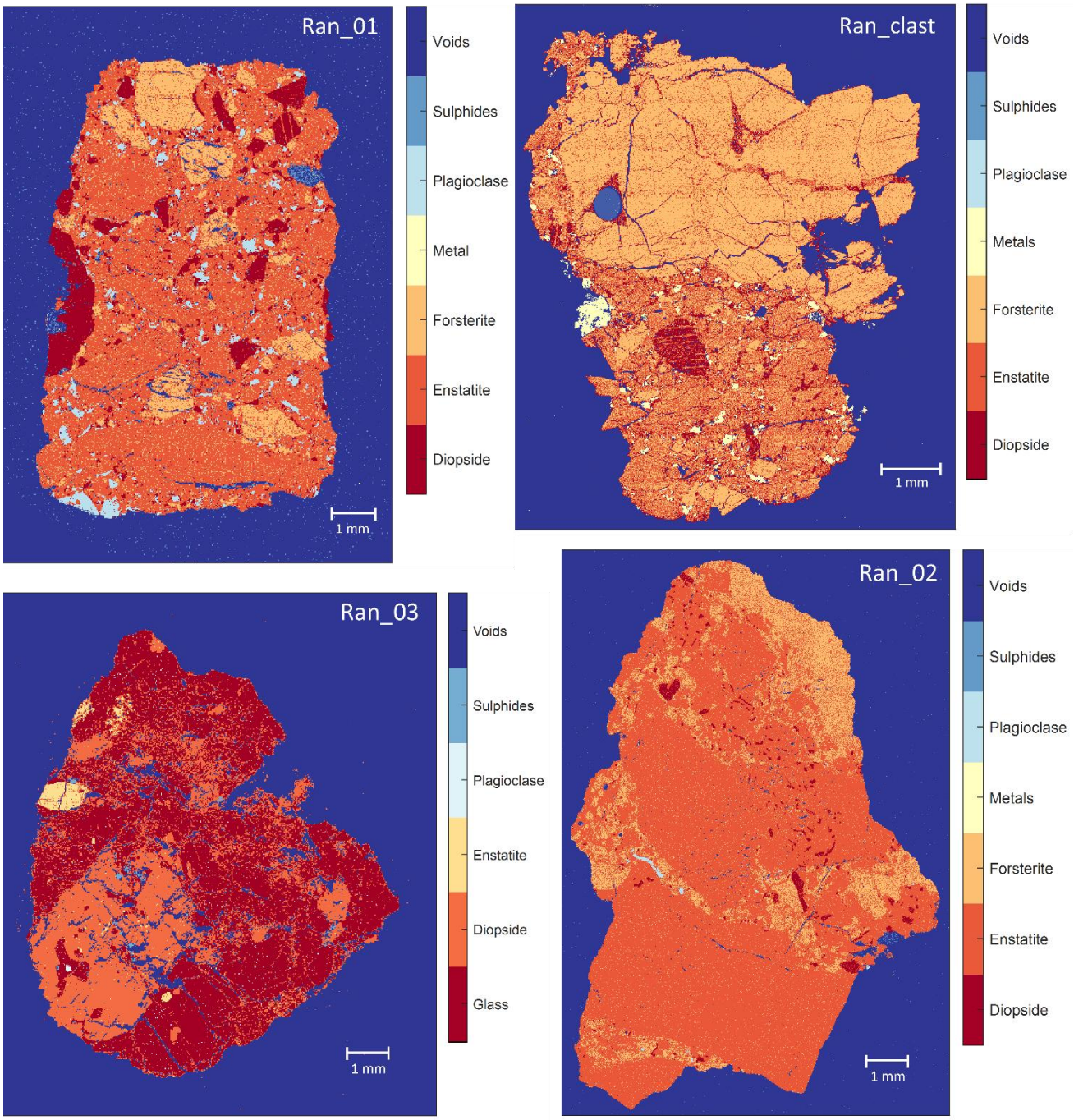


Figure 2.3. Phase maps of the investigated samples.

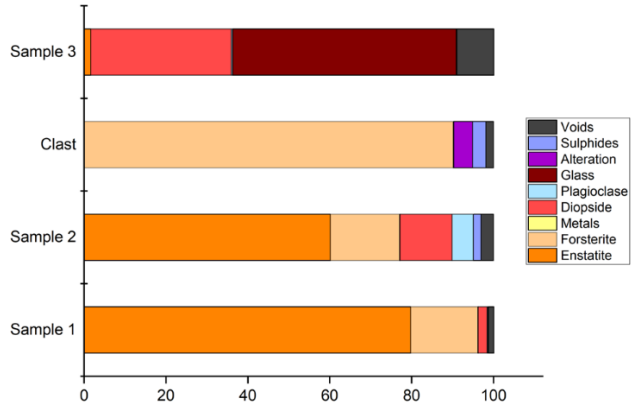


Figure 2.4. Modal mineralogy (%) of the investigated samples.

| | Enstatite | Forste-rite | Diopside | Plagioclase | Sulphi-des | Metals | Glass | Altera-tion | Voids |
|---|---|---|---|---|---|---|---|---|---|
| *Ran_01* | 60.2 | 16.9 | 12.7 | 5.2 | 1.9 | 0.1 | <0.1 | <0.1 | 3.0 |
| *Ran_02* | 79.8 | 16.4 | 2.2 | 0.2 | 0.1 | 0.1 | <0.1 | <0.1 | 1.3 |
| *Ran_03* | 1.6 | - | 34.4 | 0.3 | 0.2 | - | 54.6 | <0.1 | 9.0 |
| *Ran_clast* | - | 90.2 | - | - | 3.3 | 0.1 | <0.1 | 4.6 | 1.8 |

Table 2.2. Modal mineralogy of the investigated samples (%).

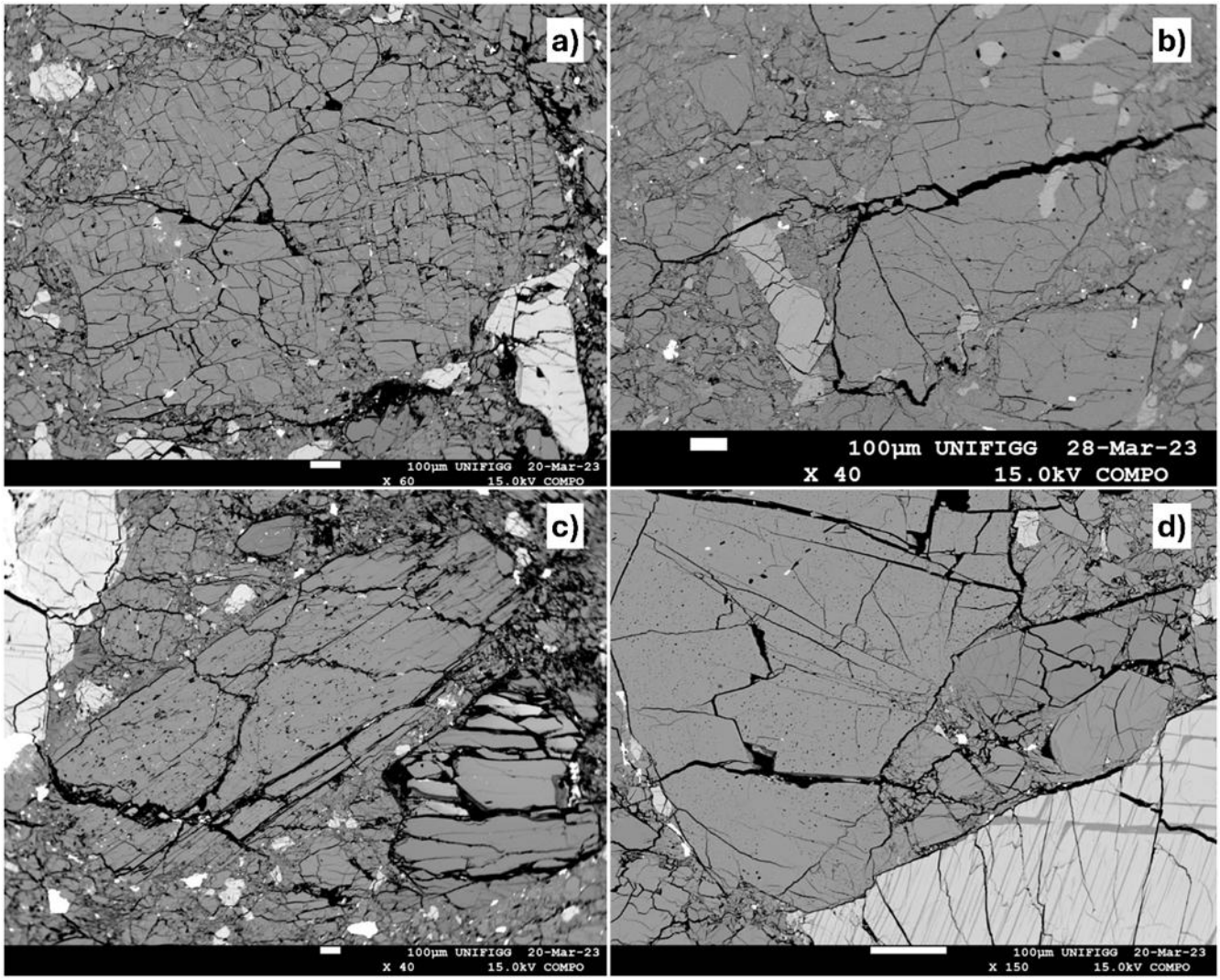


Figure 2.5. Different types of enstatite grains in the investigated samples, some examples from Ran_01 and Ran_02: a) brecciated; b) brecciated with diopside irregular inclusions (light grey); c) brecciated and porous with micrometric sulphide inclusions; d) brecciated and porous associated with forsterite, in the centre, and diopside with enstatite exsolution lamellae. BSE images acquired with the JEOL JXA-8230 Electron Microprobe. The white bar in each figure corresponds to 100 µm.

Metal and sulphide phases mostly occur as isolated objects. They can form irregular aggregates, from 30 µm up to 1 mm in size, composed of different sulphides or metal-sulphides aggregations (**Fig. 2.6**). Isolated objects are mostly represented by troilite, alabandite, and kamacite. Aggregates are typically composed of troilite/daubréelite and troilite/kamacite. Some sulphides, mostly troilite (<30 µm), are found enclosed in enstatite and forsterite (**Fig. 2.5c** and **Fig. 2.6d**). It has been observed that Rantila meteorite contains oldhamite as well (***Srivastava et al., 2023***), although no

occurrence of this sulphide was observed in any of the investigated samples. Some sporadic reddish areas can be observed on the surfaces of Ran_01 and Ran_02 (**Fig. 2.1**), they are composed of micrometric oxides/hydroxides, mostly iron-, and are linked to an incipient terrestrial weathering. There is no major evidence of weathering on opaque phases, except for one sulphide-metal aggregation with different phases surrounded by Fe-rich weathering rims (**Fig. 2.6e**).

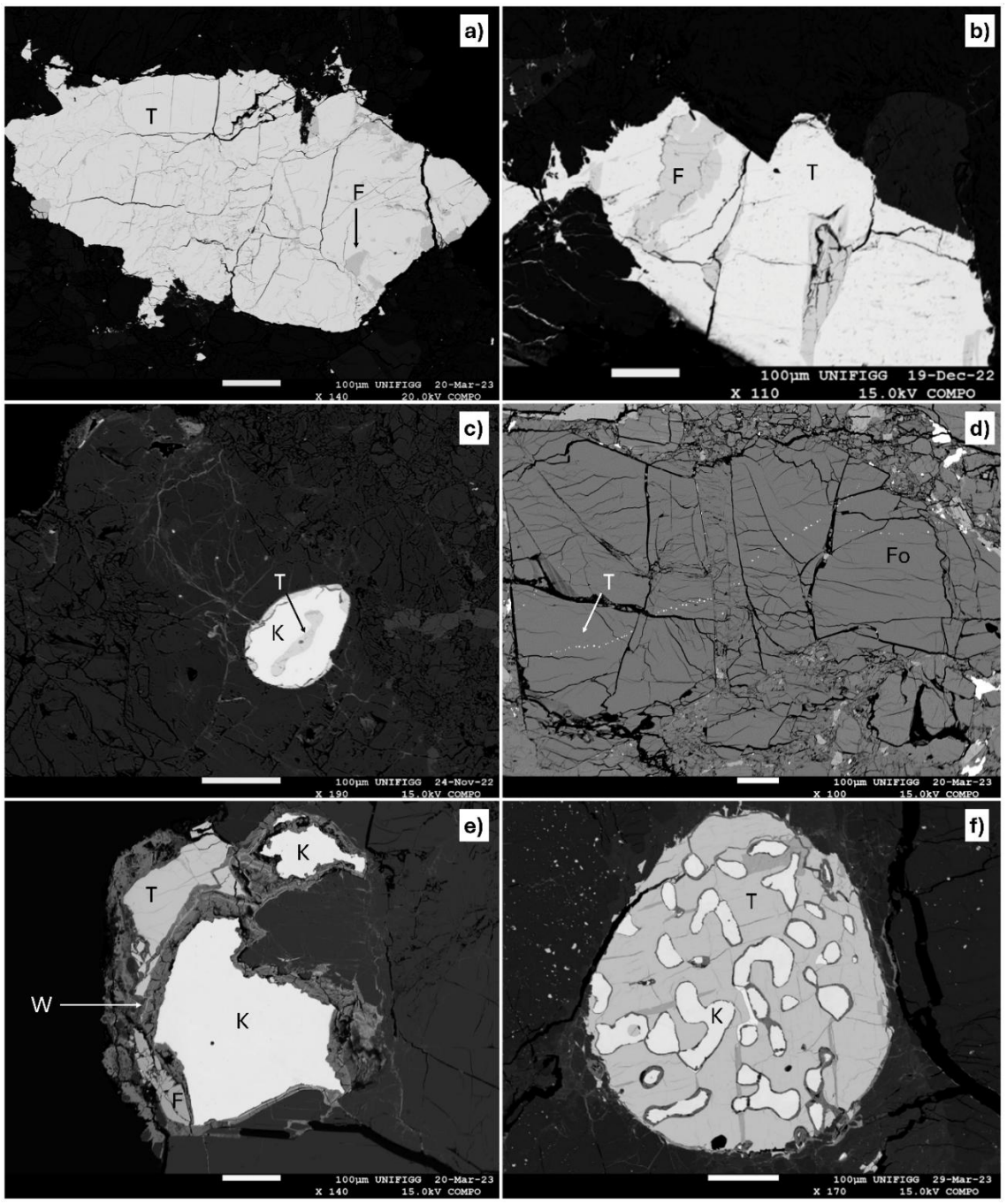


Figure 2.6. Examples of sulphides and sulphides/metals aggregations in the investigated samples. a) troilite-FeCr2S4 in Ran_01; troilite-FeCr2S4 in Ran_02; c) troilite-kamacite in Ran_02; d) micrometric troilite in forsterite phenocrystal in Ran_01; e) troilite-kamacite-FeCr2S4 surrounded by Fe-rich weathering rim in Ran_01; f) sulphides-metal aggregation and micrometric opaque minerals blebs in Ran_clast. BSE images acquired with the JEOL JXA-8230 Electron Microprobe. The white bar in each figure corresponds to 100 µm. T= troilite, F= FeCr2S4, K= kamacite, W= weathering, Fo= forsterite.

Evidence of melting processes is visible in Ran_01 and Ran_02. Two micrometric glass fragments with albitic composition were detected in Ran_02, while both samples present melts containing Fe-S spherules similar to those already found in other aubrites (e.g., ***Lorenz et al., 2020; Wilbur et al., 2022***) (**Fig. 2.7a**), or Fe-Cr-S spherules (**Fig. 2.7b**).

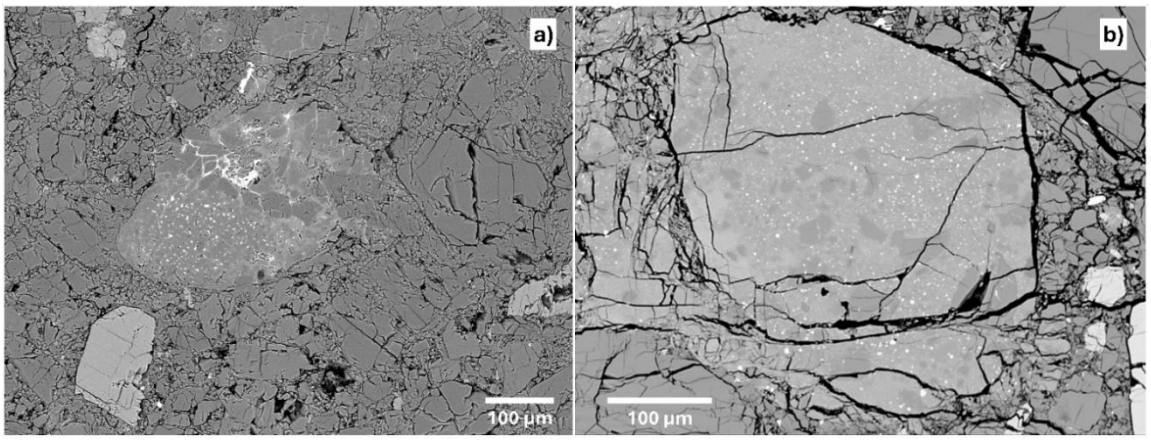


Figure 2.7. a) Example of melt in Ran_02, enstatite melt pocket containing Fe-S veins and spherules; b) example of melt in Ran_01, plagioclase grain containing Fe-Cr-S spherules. BSE images acquired with a ZEISS EVO-MA15 scanning electron microscope.

2.3.1.2. Forsterite dark clast

The clast has homogeneous forsterite composition. It is characterized by the presence of opaque mineral blebs scattered through the surface and filling fractures (**Fig. 2.6f** and **Fig. 2.8**). Those blebs are mostly represented by troilite. In addition, troilite is also present as a grain 500 µm in size containing dispersed micrometric kamacite and daubréelite, it is surrounded by a Ca-Fe-rich silicate phase (**Fig. 2.6f**) which also forms veins scattered through the surface (**Fig. 2.8**).

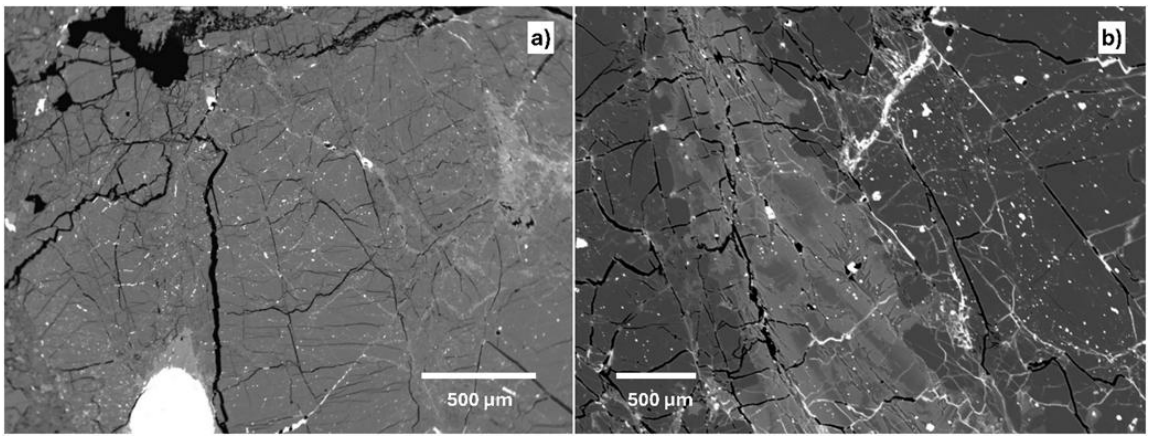


Figure 2.8. a) examples of Ca-Fe-rich veins in the forsterite clast, sample Ran_clast. Opaque mineral blebs scattered through forsterite and filling cracks are also visible; b) higher magnification on the weathering phase and opaque mineral blebs and veins. BSE images acquired with the JEOL JXA-8230 Electron Microprobe.

2.3.1.3. Glass portion

Ran_03 is completely different from the other specimens (**Fig. 2.2** and **Fig. 2.3**). It is mostly composed (**Fig. 2.4** and **Table 2.2**) of very brittle dark glass of albitic composition containing dispersed diopside, enstatite, and plagioclase microcrystals, elongated and often skeletal (**Fig. 2.9**). These crystals are generally a few microns in length. Some exceptions can be observed for some diopside crystals reaching up to 100 µm in length. The average glass composition is: $SiO_2$ 72.8 wt%, $Al_2O_3$ 15.7 wt%, $Na_2O$ 8.8 wt%, $K_2O$ 0.8 wt%, $SO_3$ 0.4 wt%, $TiO_2$ 0.3 wt%, CaO 0.2 wt%. Fe and all the other transition elements are below the detection limit, as well as P and Cl. Diopside is also present as phenocrysts (500 µm) embedded in the glass and as a single 5 mm phenocryst beside the glass containing glass inclusion. Enstatite is observed as one millimetric crystal. Alabandite is the only observed sulphide, and it occurs as isolated grains up to 200 µm in size. Forsterite and metals are not detected.

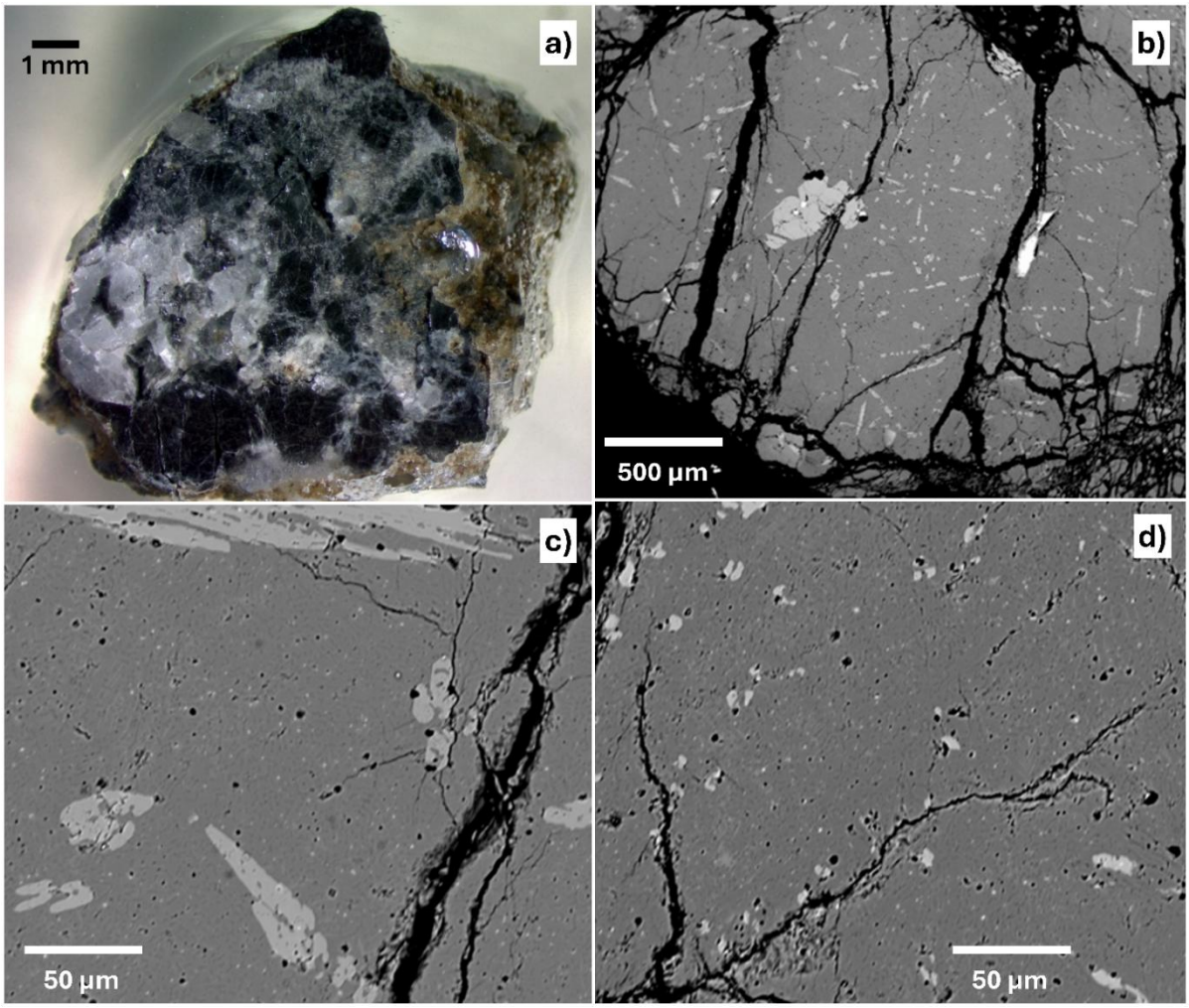


Figure 2.9. a) Ran_03 embedded in resin, black=glass, light gray= diopside, one enstatite phenocryst on the edge of the left upper side; b) glass texture with skeletal microcrystals; c, d) glass texture higher magnification. BSE images acquired with the JEOL JXA-8230 Electron Microprobe.

#### 2.3.1.4. Terrestrial weathering

Due to their highly reduced nature, aubrites tend to be easily affected by terrestrial alteration (***Wilbur et al., 2022***). Even falls can present an incipient weathering as in the case of Rantila: sporadic oxides/hydroxides, mostly iron-, can be observed. Metal and sulphides are usually the first phases to be altered, and the weathering is sporadically present but not pervasive on these phases. Silicates can be affected by the presence of iron oxides/hydroxides in veins (e.g., **Fig. 2.6c**). Still, they are not affected by other forms of weathering (such as the formation of clay minerals). So, we can assume this meteorite's weathering grade is low.

### 2.3.2. Mineral chemistry

Despite the textural and modal mineralogy differences between the investigated samples, the chemical compositions of silicates are quite similar regarding the major elements; some differences were observed only in minor elements concentrations (**Table 2.3**).

Enstatite grains are nearly FeO-free with average composition $En_{98.7}Wo_{0.9}Fs_{0.4}$. There are no substantial differences between the compositions of the different enstatite types in terms of major and minor elements. Enstatite lamellae in diopside have average composition $En_{97.5}Wo_{1.2}Fs_{1.3}$. Forsterite is nearly FeO-free with average composition $Fo_{99.7}$.

Diopside phenocrysts have average composition $En_{56.8}Wo_{43.0}Fs_{0.2}$ while acicular crystals in glass matrix of Ran_03 are represented by average composition $En_{54.8}Wo_{45.2}$.

Plagioclases present a wider range of chemical composition. Average composition in Ran_02 and Ran_03 is $Ab_{83.4}Or_{0.1}An_{16.4}$ and $Ab_{95.0}Or_{4.4}An_{0.6}$ respectively. Plagioclase in Ran_01 are represented by three different average compositions associated with different fragments: the most common is $Ab_{94.0}Or_{4.3}An_{1.8}$, then $Ab_{82.2}Or_{1.8}An_{16.0}$ and $Ab_{89.2}Or_{10.0}An_{0.8}$. No zoning is present within the same plagioclase crystal of a single individual.

| | *Forsterite* | | | *Enstatite* | | | |
|---|---|---|---|---|---|---|---|
| | ***Ran_01*** | ***Ran_02*** | ***Ran_clast*** | ***Ran_01*** | ***Ran_01**** | ***Ran_02*** | ***Ran_03*** |
| *n* | *65* | *28* | *26* | *40* | *3* | *47* | *5* |
| $SiO_2$ | 42.98 (0.14) | 41.96 (0.07) | 42.57 (0.30) | 59.68 (0.22) | 59.67 (0.19) | 58.65 (0.37) | 57.53 (0.24) |
| $TiO_2$ | 0.03 (0.01) | 0.02 (<0.01) | 0.06 (0.02) | 0.06 (0.03) | 0.05 (<0.01) | 0.06 (0.02) | 0.07 (0.01) |
| $Al_2O_3$ | b.d. | b.d. | b.d. | 0.09 (0.02) | 0.08 (0.01) | 0.04 (0.03) | 0.09 (0.01) |
| $Cr_2O_3$ | b.d. | 0.03 (0.02) | b.d. | 0.06 (0.02) | 0.04 (0.01) | 0.05 (0.01) | b.d. |
| FeO | 0.28 (0.07) | 0.32 (0.04) | 0.36 (0.07) | 0.23 (0.04) | 0.27 (0.01) | 0.20 (0.04) | b.d. |
| MnO | 0.26 (0.01) | 0.28 (0.02) | 0.29 (0.02) | 0.20 (0.11) | 0.69 (<0.01) | 0.23 (0.07) | 0.05 (0.01) |
| NiO | b.d. | b.d. | b.d. | b.d. | b.d. | b.d. | b.d. |
| MgO | 56.19 (0.13) | 57.11 (0.27) | 56.35 (0.25) | 39.20 (0.47) | 38.33 (0.21) | 39.62 (0.33) | 39.74 (0.06) |
| CaO | 0.04 (<0.01) | 0.03 (<0.01) | 0.02 (<0.01) | 0.47 (0.12) | 0.64 (0.08) | 0.50 (0.03) | 0.58 (0.02) |
| $Na_2O$ | n.a. | n.a. | n.a. | b.d. | b.d. | b.d. | b.d. |
| $K_2O$ | n.a. | n.a. | n.a. | b.d. | b.d. | b.d. | b.d. |
| Total | 99.79 (0.21) | 99.76 (0.27) | 99.68 (0.30) | 100.01 (0.47) | 99.78 (0.54) | 99.40 (0.67) | 98.08 (0.20) |
| Fo | 99.7 | 99.7 | 99.6 | - | - | - | - |
| En | - | - | - | 98.8 | 97.5 | 98.6 | 98.9 |
| Wo | - | - | - | 0.7 | 1.2 | 0.9 | 1.0 |
| Fs | - | - | - | 0.5 | 1.3 | 0.5 | 0.1 |

(…) = standard deviations
b.d.= below detection limit
n.a.= not analyzed
*=lamellae in diopside
°=microcrystals

Table 2.3. Silicates average chemical compositions (wt%)

| | *Diopside* | | | | *Plagioclase* | | |
|---|---|---|---|---|---|---|---|
| | ***Ran_01*** | ***Ran_02*** | ***Ran_03*** | ***Ran_03°*** | ***Ran_01*** | ***Ran_02*** | ***Ran_03*** |
| *n* | *18* | *14* | *20* | *2* | *15* | *4* | *3* |
| $SiO_2$ | 55.52 (0.14) | 55.71 (0.18) | 55.0 (0.15) | 54.59 (0.12) | 66.39 (2.16) | 63.03 (0.28) | 67.73 (0.63) |
| $TiO_2$ | 0.29 (0.01) | 0.32 (0.03) | 0.44 (0.04) | 0.74 (0.08) | 0.05 (0.02) | 0.04 (0.01) | 0.03 (0.02) |
| $Al_2O_3$ | 0.20 (0.01) | 0.37 (0.01) | 0.50 (0.04) | 1.66 (0.24) | 20.27 (1.53) | 22.23 (0.09) | 18.89 (0.16) |
| $Cr_2O_3$ | 0.04 (0.01) | 0.05 (0.02) | b.d. | b.d. | n.a. | n.a. | n.a. |
| FeO | 0.13 (0.08) | 0.12 (0.01) | b.d. | b.d. | b.d. | b.d. | b.d. |
| MnO | 0.23 (0.03) | 0.10 (0.01) | b.d. | b.d. | b.d. | b.d. | b.d. |
| NiO | b.d. | b.d. | b.d. | b.d. | n.a. | n.a. | n.a. |
| MgO | 20.20 (0.10) | 20.41 (0.29) | 21.46 (0.79) | 19.37 (0.12) | b.d. | b.d. | b.d. |
| CaO | 22.60 (0.25) | 22.34 (0.06) | 21.47 (0.74) | 22.24 (0.24) | 1.47 (1.37) | 3.32 (0.05) | 0.13 (0.02) |
| $Na_2O$ | 0.19 (0.01) | 0.20 (0.01) | 0.36 (0.03) | 0.30 (0.06) | 10.40 (0.75) | 9.37 (0.12) | 10.75 (0.33) |
| $K_2O$ | b.d. | b.d. | b.d. | b.d. | 0.59 (0.24) | 0.04 (0.01) | 0.76 (0.09) |
| Total | 99.40 (0.64) | 99.62 (0.45) | 99.29 (0.20) | 99.25 (0.40) | 99.03 (0.68) | 98.18 (0.38) | 98.40 (0.40) |
| En | 56.2 | 56.3 | 58.8 | 54.8 | - | - | - |
| Wo | 43.6 | 43.4 | 41.1 | 45.2 | - | - | - |
| Fs | 0.2 | 0.3 | 0.1 | 0.0 | - | - | - |
| Ab | - | - | - | - | 79.5-95.6 | 83.4 | 95.0 |
| Or | - | - | - | - | 1.5-10.0 | 0.2 | 4.4 |
| An | - | - | - | - | 0.2-18.6 | 16.4 | 0.6 |

(…) = standard deviations
b.d.= below detection limit
n.a.= not analyzed
*=lamellae in diopside
°=microcrystals

Table 2.3. continue.

Metals and sulphides chemical compositions are reported in **Table 2.4** and **Table 2.5**, respectively. Metal is composed of low-Ni (5-7 wt%) Fe-Ni phase with low Si (up to 0.28 wt%) and Co (0.34-0.64 wt%). Troilite is the most abundant sulphide and has low Ti (0.04-0.23 wt%) and Cr (0.5 wt%). Daubréelite has a Mn value of around 1 wt% and Zn content below detection limits in

Ran_01 and Ran_03, Ti (0.05 wt%) was detected only in crystals from Ran_01. Alabandite is Fe-bearing (Fe 11.4-15.3 wt%). One grain of heideite with Ti content of 26.35 wt% was detected in Ran_01.

| | ***Ran_01*** | ***Ran_02*** | ***Rantila_clast*** |
|---|---|---|---|
| *n* | *10* | *6* | *8* |
| Si | b.d. | 0.28 (0.01) | 0.07 (0.02) |
| Fe | 92.43 (0.33) | 90.42 (0.50) | 93.29 (0.32) |
| Cr | b.d. | b.d. | b.d. |
| Co | 0.37 (0.02) | 0.64 (0.01) | 0.34 (0.02) |
| P | b.d. | 0.06 (0.02) | 0.08 (0.02) |
| Cu | b.d. | b.d. | b.d. |
| Ni | 5.65 (0.19) | 6.96 (0.08) | 5.15 (0.09) |
| Mn | b.d. | b.d. | b.d. |
| Total | 98.50 (0.33) | 98.36 (0.64) | 98.96 (0.32) |

(…) = standard deviations
b.d.= below detection limit

Table 2.4. Metals average chemical composition (wt%)

| | ***Troilite*** | | | ***Alabandite*** | | ***Daubréelite*** | | ***Heideite*** |
|---|---|---|---|---|---|---|---|---|
| | ***Ran_01*** | ***Ran_02*** | ***Ran_clast*** | ***Ran_01*** | ***Ran_03*** | ***Ran_01*** | ***Ran_02*** | ***Ran_01*** |
| *n* | *15* | *12* | *9* | *4* | *4* | *4* | *4* | *1* |
| Si | b.d. | b.d. | b.d. | b.d. | b.d. | b.d. | b.d. | 0.19 |
| Fe | 62.27 (0.57) | 61.14 (0.17) | 61.96 (0.50) | 11.40 (3.08) | 15.32 (0.16) | 18.07 (0.25) | 18.60 (0.33) | 26.06 |
| Co | 0.05 (0.01) | 0.06 (0.01) | 0.04 (0.02) | b.d. | b.d. | b.d. | b.d. | 0.03 |
| Cr | 0.47 (0.10) | 0.54 (0.06) | 0.56 (0.14) | 0.10 (0.08) | 0.35 (<0.01) | 34.04 (0.74) | 34.14 (0.22) | 1.32 |
| Zn | b.d. | b.d. | b.d. | b.d. | b.d. | b.d. | b.d. | b.d. |
| S | 35.69 (0.22) | 35.63 (0.05) | 35.90 (0.25) | 36.51 (0.52) | 35.70 (1.01) | 43.62 (0.22) | 43.04 (0.11) | 41.04 |
| Ti | 0.23 (0.20) | 0.04 (0.01) | 0.06 (0.01) | b.d. | 0.08 (0.01) | 0.05 (0.02) | b.d. | 26.35 |
| Ca | b.d. | b.d. | b.d. | 0.13 (0.11) | 0.29 (0.02) | b.d. | b.d. | 0.06 |
| Cu | 0.05 (0.03) | b.d. | b.d. | 0.05 (0.04) | b.d. | 0.10 (0.09) | b.d. | 0.13 |
| Ni | b.d. | b.d. | b.d. | b.d. | b.d. | b.d. | b.d. | 0.06 |
| Mn | b.d. | b.d. | b.d. | 48.69 (3.48) | 42.96 (1.21) | 1.10 (0.16) | 0.81 (0.10) | b.d. |
| V | b.d. | b.d. | b.d. | b.d. | b.d. | b.d. | b.d. | 0.16 |
| Na | b.d. | b.d. | b.d. | b.d. | 0.10 (0.01) | b.d. | b.d. | b.d. |
| Mg | b.d. | b.d. | b.d. | 0.33 (0.12) | 1.75 (0.06) | b.d. | b.d. | 0.09 |
| Total | 98.80 (0.59) | 97.57 (0.16) | 99.11 (0.44) | 97.34 (0.99) | 96.60 (0.40) | 97.04 (0.78) | 96.13 (0.24) | 95.49 |

(…) = standard deviations
b.d.= below detection limit

Table 2.5. Sulphides average chemical composition (wt%)

### 2.3.3. Laser-Induced Time-Resolved Luminescence

Luminescence centres appear to be mainly connected to $Cr^{3+}$ (750 nm) in diopside and $Mn^{2+}$ (640 nm) in forsterite. $Ce^{3+}$ can also act as a luminescence centre in diopside. The luminescence spectra observed for Ran_01 and Ran_02 are different from those observed in Ran_03 that is mainly composed of glass.

#### 2.3.3.1. $Cr^{3+}$

**Figure 2.10a** presents the typical luminescence under excitation by 532 nm on the border between the red and IR parts of the spectrum. At 300 K it may be fitted by one broad Gaussian band with $\lambda_{max}$= 771 nm and half-width of $\Delta$=131 nm. The decay time of this luminescence is relatively short, $\tau$=16.2 μs.

Such luminescence is like the emission found in $CaMgSi_2O_6:Cr^{3+}$ artificial diopside (***Fang et al., 2022; Szymczak et al., 2024***). In both studies, the emission spectra obtained under blue excitation consist of a broad luminescence band associated with the $^4T_{2g} \rightarrow {}^4A_{2g}$ electronic transitions of $Cr^{3+}$, which confirms that $Cr^{3+}$ ions are in the weak crystal field structural position in diopside. The band's maximum is around 770-780 nm, with the FWHM increasing from 184.6 nm to 211.6 nm for 0.5% and 5% $Cr^{3+}$, respectively. The decay time was shortened from 37.5 to 6.82 μs for 0.5 % to 6 % of $Cr^{3+}$. The similarity of red-IR luminescence with that of artificial $CaMgSi_2O_6:Cr^{3+}$ allows us to ascribe it confidently enough to the $Cr^{3+}$ luminescence center in diopside. Such conclusion is confirmed by the presence in diopside of broad luminescence bands peaking at 760-770 nm in Raman spectra under 532 nm excitation (***Lafuente et al., 2016***). It may be attributed to a strong broadband quartet-quartet $^4T_2$ - $^4A_2$ transition in the weak crystal field site, which is only symmetry forbidden and has a relatively short decay time. A narrow, weak emission line near 693 nm is related to the $^2E_g \rightarrow {}^4A_{2g}$ electronic transition of $Cr^{3+}$ in the intermediate crystal field. A similar line in artificial $CaMgSi_2O_6:Cr^{3+}$ was detected under elevated pressures, indicating increased crystal field strength affecting $Cr^{3+}$ ions (***Szymczak et al., 2024***). The detection of luminescence spectra attributable to $Cr^{3+}$ and not $Cr^{2+}$, whose presence could be expected in such reducing conditions, is discussed in **Section 2.4.4**.

#### 2.3.3.2. $Mn^{2+}$

**Figure 2.10b** presents the luminescence in the orange-red part of the spectrum. Emission consists of two bands peaking at 587 and 651 nm, with a long decay time: 4.6 ms for the 587 nm and 4.0 ms for the 656 nm. The halfwidths of these bands are $\Delta_1$ = 38.7 and $\Delta_2$ = 92 nm. To detect this luminescence in the most straightforward form, a long delay of 100 μs was used to remove a short-

lived, strong competing red-IR luminescence of $Cr^{3+}$. Such luminescence is typical for forbidden d-d transitions in the $Mn^{2+}$ emission centre. The $3d^5$ system $Mn^{2+}$ with sextet (6S) ground state is a well-known activator of many calcium- and magnesium-bearing minerals (***Gaft et al., 2015***). Luminescence of artificial $CaMgSi_2O_6$:$Mn^{2+}$ is well studied, where two broad emission bands were found and ascribed to two distinct $Mn^{2+}$ ions located in two different crystal field environments corresponding to the substitution by $Mn^{2+}$ in $Mg^{2+}$ and $Ca^{2+}$ sites: at 590 nm ($Mn^{2+}_{Ca}$) and 680 nm ($Mn^{2+}_{Mg}$) (***Rosticher et al., 2015, 2016***). The first luminescence band in the meteorite sample is very similar to emission in $Mn^{2+}_{Ca}$, while the second one is situated at a lower wavelength compared to $Mn^{2+}_{Mg}$ centre (656 instead of 689 nm). This band may be preliminarily connected to $Mn^{2+}$ luminescence in forsterite peaking at 643 nm (***Green & Walker, 1985***). As for $Cr^{3+}$, those $Mn^{2+}$ luminescence bands often appear in Raman spectra of diopside and forsterite under 532 nm excitation (***Lafuente et al., 2016***).

### 2.3.3.3. $Ce^{3+}$

**Figure 2.10c** presents UV luminescence detected in Ran_03 diopside. It consists of a band with two maxima peaking at 355 and 377 nm and an extremely short decay time of 20-25 ns. Such luminescence is typical for the 5d-4f transition in $Ce^{3+}$ emission centres (***Gaft et al., 2015***). Such interpretation is supported by the known emission in synthetic $MgCaSi_2O_8$ activated by $Ce^{3+}$ (***Su et al., 2021***), which has very similar spectral-kinetic parameters.

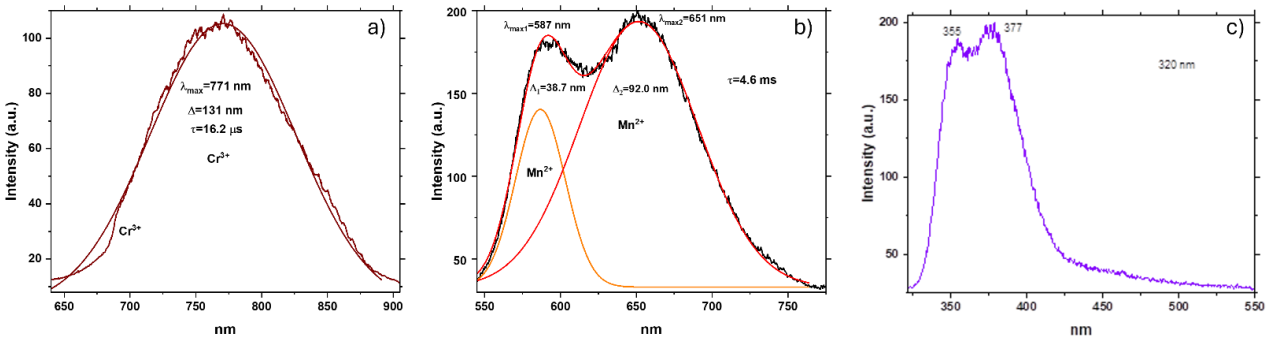


Figure 2.10. a) Time-resolved red-infrared luminescence emission spectrum of Ran_01 and Ran_02 at 300 K under 532 nm excitation associated with the presence of $Cr^{3+}$ in diopside; b) Time-resolved orange-red luminescence emission spectrum of Ran_01 and Ran_02 at 300 K under 532 nm excitation associated with the presence of $Mn^{2+}$ in forsterite; c) Time-resolved UV-violet luminescence emission spectrum of Ran_03 at 300 K under 320 nm excitation associated with $Ce^{3+}$ in diopside.

### 2.3.4. Reflectance spectra

Six reflectance spectra were acquired in different areas of Ran_01 and Ran_02. Spectra on Ran_02 were acquired on a polished, not mirror, section while those on Ran_01, the dark forsterite clast included, were acquired on a rougher surface. The measurement spots on the two samples are shown in **Figure 2.11**. All the spectra (**Fig. 2.12a**) have a blue slope, as expected with measurements on slabs and rock fragments (e.g., ***Carli & Sgavetti, 2011; Cloutis et al., 2013; Pompilio et al., 2007***). The spectrum acquired on the dark clast has a lower reflectance, ca 50%, compared to the other two spectra of Ran_01. Those spectra are brighter than the Ran_02 spectra due to partially different composition but also affected by the higher scattering on a rougher surface (***Harloff & Arnold, 2001***). The spectra show one main, relatively weak, absorption band around 1 μm (e.g., ***Burns, 1993***; **Figure 2.12**).

The 1 μm absorption (band I) could be accompanied by a broader absorption around 2 μm (band II) for pyroxenes (e.g., ***Burns, 1993***). In the investigated samples, the 2 μm band is present on Ran_02_3 and Ran_01_1, weaker than the 1 μm absorption and strongly affected by the contribution of terrestrial alteration products. In fact in almost all the spectra, apart from the one acquired on the Clast, we can see absorption features at ~1.4 μm and ~*1.9* μm, which are a combination of H-O-H and O-H overtone, and at 2.2-2.3 μm, attributable to M-OH overtone, on iron hydroxides due to terrestrial contamination (e.g., ***Burbine et al., 2002; Cantillo et al., 2024; Gaffey et al., 1993***).

Spectral positions (**Table 2.6**) of the 1 μm absorption, ranging from 0.901 and 0.920 μm, are consistent with low Fe-Ca pyroxene, as well as the absorption shapes (***Cloutis & Gaffey, 1991; Klima et al., 2008***) for the three spectra of Ran_02 and spectrum Ran_01_2. The spectrum Ran_01_1 shows a broader absorption band centred at 926 μm and with an asymmetry towards the longer wavelengths (see **Figure 2.12**), which could be caused by the presence of forsterite ($Fo_{99.7}$) or high-Ca pyroxene ($En_{56.2}Wo_{43.6}Fs_{0.2}$). In the clast spectrum we have a weaker absorption shifted at slightly longer wavelengths (920 nm) similar to the spectrum Ran_01_1, without the presence of a 2 μm, which is consistent with a forsterite $Fo_{99.6}$ being the dominant phase, even if the position is at relative low wavelengths with respect to more common olivine (e.g., ***Burns, 1993; Sunshine & Pieters, 1998***). It is possible to observe also very weak absorption features around 0.5 μm, 0.503 μm in spectrum Ran_01_1 and 0.497 μm in spectrum Ran_clast, that could be associated with the contribution of spin-forbidden $Fe^{2+}$ absorption in olivine (e.g., ***Burns, 1993; Carli et al., 2018***), underlining the presence of a considerable quantity of forsterite in these portions of the samples with respect to the others.

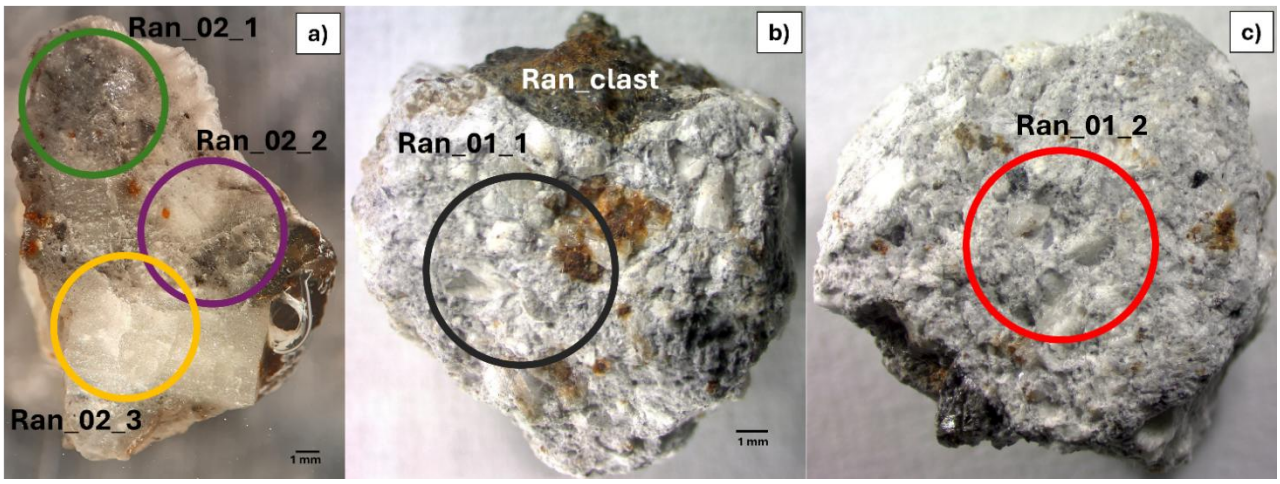


Figure 2.11. Measurement spots: a) the three spectra of sample Ran_02 acquired on a polished surface; b) spectrum Ran_01_1 and spectrum Ran_clast acquired on the rough surface of the light coloured portion and of the dark clast, respectively; c) spectrum Ran_01_2 acquired on the rough surface of the light coloured portion on the opposite side of the fragment.

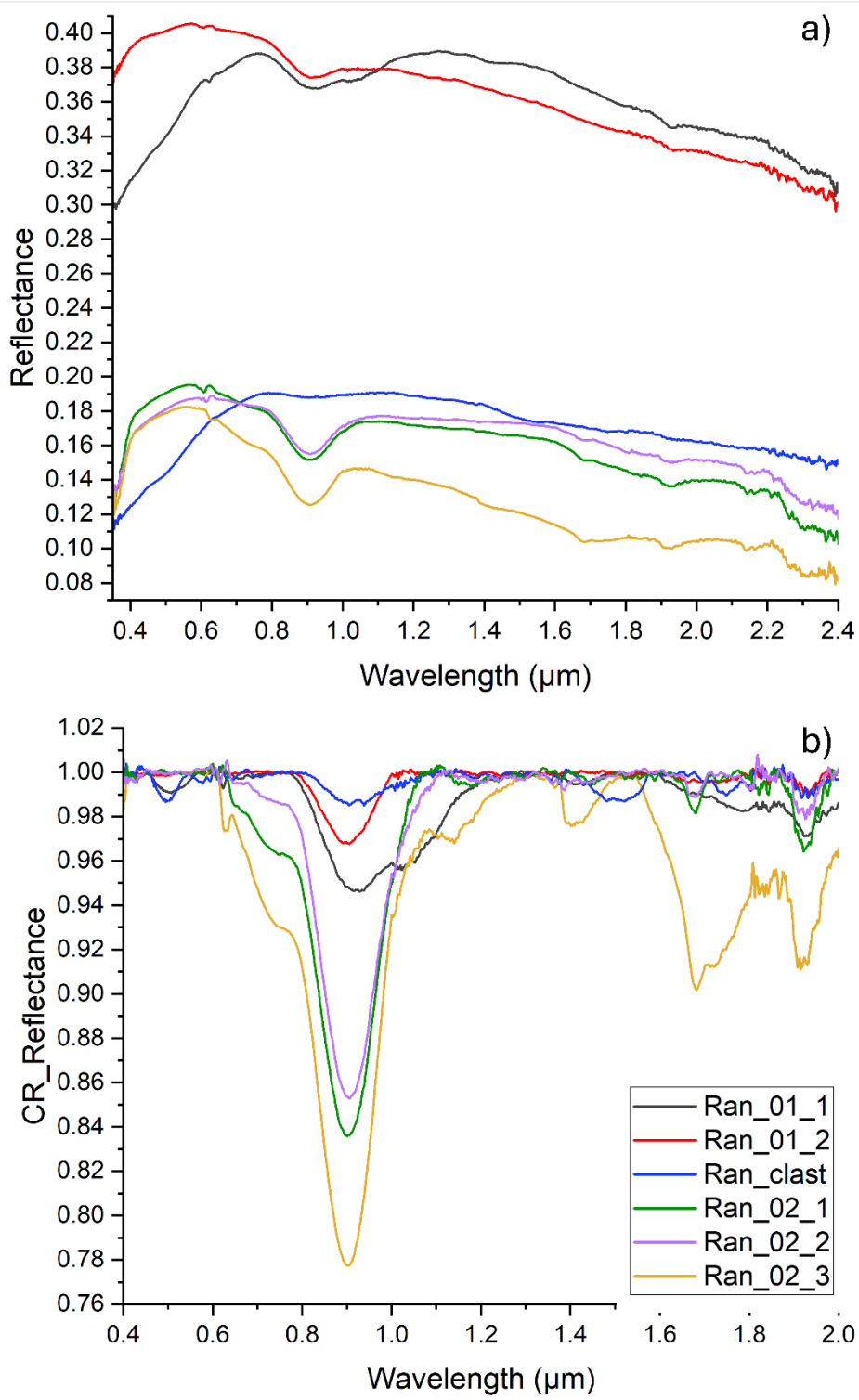


Figure 2.12. a) Reflectance spectra of Ran_01 and Ran_02 acquired in three different areas of the samples' surfaces. One of the points analyses for the sample Ran_01 was on the dark clast; therefore the spectrum is called Ran_clast. The sharp little peak visible in every spectrum at circa 0.64 μm is an instrumental feature due to the presence of a filter. b) Reflectance spectra continuum removed.

| | *Band center* | *Band depth* |
|---|---|---|
| Ran_01_1 | 926 | 0.05 |
| Ran_01_2 | 901 | 0.03 |
| Ran_02_1 | 902 | 0.16 |
| Ran_02_2 | 905 | 0.14 |
| Ran_02_3 | 902 | 0.22 |
| Ran_clast | 920 | 0.01 |

Table 2.6. Band center and band depth of reflectance spectra main absorption. The error for the band center is ± 5 nm, the resolution at those wavelengths being 10 nm. Band depth error is <0.01.

## 2.4. Discussion

### 2.4.1. Light-coloured portion

In the three samples, the main lithology is represented by the light-coloured portion showing a texture and a mineral chemistry of silicates and metals typical of aubrites (e.g., ***Keil 2010*** *and references therein*). The enstatite is the main phase, but with abundance (60.2-79.8 %) lower than the aubrite range (75–98 %, e.g., ***Keil 2010; Watters & Prinz 1979***). Forsterite is more abundant (16.4-16.9 %) than in other aubrites (0.3-10.0 %, e.g., ***Keil 2010; Watters & Prinz 1979***).

Diopside amount (2.2-12.7 %) and plagioclase amount (0.2-5.2 %) are in the range of aubrites (e.g., ***Keil 2010; Watters & Prinz 1979***): diopside 0.2-8.1 %, up to 20 % in Norton County (***Okada et al., 1988***), plagioclase 0.3-16.2 % (***Keil, 2010***). The plagioclase shows a limited chemical variability in Ran_02 (average $Ab_{83.4}Or_{0.2}An_{16.4}$) similar to what was observed in ten aubrites by ***Watters & Prinz (1979)***, but a wide chemical variability in Ran_01 ($Ab_{79.5\text{-}95.6}Or_{1.5\text{-}10.0}An_{0.2\text{-}18.6}$), similar to what observed for the aubrite ALH A78113 by ***Kimura et al. (1993)***.

Minor content (0.1 %) of Si-bearing metallic FeNi is present with a chemical composition consistent with the average for aubrites (e.g., ***Keil 2010; Watters & Prinz 1979***). Troilite contains lower Cr (0.5 wt%) and Ti (0.04-0.23 wt%) than what has been found for other aubrites (average 0.80 wt% Cr, ***Keil 2010***; average 2.76 wt% Ti, e.g., ***Keil 2010; Watters & Prinz 1979***). In particular, Ti contents are even lower than those typically observed in enstatite chondrites (0.27–0.77 wt%, e.g., ***Keil, 1968; Weyrauch et al., 2018***).

### 2.4.2. Forsterite dark clast

A peculiar component of this meteorite is the dark forsterite clast enclosed in the light-coloured portion of Ran_01. Forsterite ($Fo_{99.6}$) represents 90% of the clast, it is highly brecciated with major fractures (2%). The presence of macro but mostly micro to nano impurities represented by opaque minerals could explain why the entire clast is so dark. Mineral chemistry of forsterite, as well as sulphides and metals, is the same, in terms of major and minor elements, as in the light-coloured

portion (Ran_01 and Ran_02). In contrast, the 5 % of Ca-Fe-rich phase is present only in this portion.

### 2.4.3. Impact glass portion

Ran_03 is entirely different in mineral composition, as it is primarily composed of glass, compared to the other two samples and other described portions of any aubrites. Moreover, the mineral chemistry of enstatite and diopside is peculiar. The enstatite and diopside phenocrysts in this sample have FeO, $Cr_2O_3$, and MnO content below the microprobe detection limit. Diopside microcrystals dispersed in the glass show a different composition compared to the phenocrysts, with lower MgO content and higher $Al_2O_3$ and TiO contents, and even in this case, FeO, $Cr_2O_3$, and MnO content are below microprobe detection limit. The glass composition is like the composition measured for interstitial glasses in aubrite Y-793592 (***Kimura et al., 1993***) and for interstitial glass and glass pockets in the aubrite basalt vitrophyre from the LEW 87007 aubrite (***Fogel, 2005***). The high values of dissolved S ($SO_3$ 0.4 wt%) and the FeO amount under detection limit are caused by the highly reducing conditions of formation (***Fogel, 2005***).

### 2.4.4. Luminescence

The different mineral chemistry between Ran_03 and the other two samples is also underlined by luminescence behaviour. Luminescence in Ran_01 and Ran_02 appears to be connected to diopside and forsterite, and the activator elements are $Cr^{3+}$ and $Mn^{2+}$.

The luminescence related to $Cr^{3+}$ in weak crystal field sites may be ascribed to a strong broadband quartet-quartet $^4T_2$ - $^4A_2$ transition, which is only symmetry forbidden and has a relatively short decay time. The spectral-kinetic characteristics of the luminescence in these samples are very similar to those found for $CaMgSi_2O_6:Cr^{3+}$ artificial diopside recently studied as an NIR phosphor-converted light-emitting diode (***Fang et al., 2022***).

The highly reducing conditions of formation of this meteorite could have suggested the presence of $Cr^{2+}$ rather than $Cr^{3+}$. However, the presence of $Cr^{3+}$ in clinopyroxene in another highly reduced meteorite (Ungrouped Achondrite NWA 7325) has been detected by ***Sutton et al. (2017)*** by means of XANES spectroscopy. The suggested hypothesis is that $Cr^{3+}$ presence in pyroxene might be caused by secondary reheating, likely shock heating (***Sutton et al., 2017***).

The luminescence related to $Mn^{2+}$ is typical for forbidden d-d transitions in the $Mn^{2+}$ emission centre and like emission found in $CaMgSi_2O_6:Mn^{2+}$ (***Rosticher et al., 2015, 2016***).

In Ran_03, the orange-red luminescence is not detected, while $Ce^{3+}$ presents, which is absent in the first two samples. This agrees with the lower Cr and Mn contents, which are under the EPMA detection limit, with respect to the other two samples (**Table 2.3**).

### 2.4.5. Reflectance spectra

Ran_01, Ran_02 and Ran_clast present FeO content: 0.28-0.36 wt% in forsterite ($Fo_{99.7}$, $Fo_{99.7}$ and $Fo_{99.6}$ respectively), 0.20-0.27 wt% in enstatite ($En_{98.8}Wo_{0.8}Fs_{0.5}$ and $En_{98.6}Wo_{0.9}Fs_{0.5}$ Ran_01 and Ran_02, respectively), 0.12-0.13 wt% in diopside ($En_{56.2}Wo_{43.6}Fs_{0.2}$ and $En_{56.3}Wo_{43.4}Fs_{0.3}$ in Ran_01 and Ran_02, respectively). Despite these low values, an absorption band centred around 0.902-0.926 μm attributed to mafic minerals is present in the VNIR reflectance spectra. In particular, absorption bands are located at at 0.901 and 0.926 μm for two different spots on Ran_01 and at 0.902 and 0.905 μm for three different spots on Ran_02. Moreover, we can clearly see a different shape between the spectrum Ran_01_1, as well as for the weaker absorption centred at 920 μm of the spectrum Ran_clast, and the other spectra. These absorptions are attributed to crystal field transitions in $Fe^{2+}$ that preferentially occupies the M2 crystallographic site on pyroxene (***Cloutis 2002*** and references therein). The main phase on those samples is enstatite; in fact, the spectra show wavelength position typical of orthopyroxene, but in the portions containing higher abundances of olivine (spectrum Ran_01_1 and spectrum Ran_clast), the absorption is wider than in the other spectra, with a shifting towards longer wavelengths (***Burns, 1993***). In addition, in olivine rich portions (spectrum Ran_01_1 and spectrum Ran_clast), we can observe weak and narrow absorptions around 0.5 μm which can be attributed to a spin-forbidden $Fe^{2+}$ absorption in olivine (e.g., ***Burns, 1993; Carli et al., 2018***).

Conversely, none of the spectra of these three samples show appreciable absorption around 2 μm, which is, in general, associated with pyroxene. This could be because even where low-Ca pyroxene is the dominating mafic phase, crystal field absorptions are not favoured at such wavelengths due to the high enstatite values and the low FeO values, and they could be made up by the weathering absorption due to H-O-H overtone around 1.9 μm (e.g., Ran_02_3).

The observed mafic absorptions were not highlighted on spectra of other aubrite from the literature (e.g., Norton County, ***Cloutis et al., 2016***; Mayo Belwa, Norton County, Aubres, Shallowater, ***Dibb et al., 2022***; Ribbeck***, Cantillo et al., 2024***). In those aubrites, mafic minerals have in general lower amounts of FeO: <0.02-0.08 wt% in enstatite, <0.02-0.12 wt% in diopside, <0.02-0.16 wt% in forsterite (***Cantillo et al., 2024; Watters & Prinz, 1979***) with respect to Rantila. This indicates that the potential detection limit of mafic minerals from crystal field absorptions in the VNIR reflectance spectra should be placed between the composition from Mayo Belwa, Norton County,

Aubres, Shallowater, and Ribbeck meteorites and the composition of Rantila. A direct comparison between the spectra of the investigated Rantila samples and the spectra of aubrites Mayo Belwa, Peña Blanca Spring, Khor Temiki and Bishopville (data from the RELAB, Reflectance Experiment Laboratory, database), can be observed in **Figure 2.13**. Those spectra are acquired on particulate material, with a better spectral contrast and higher reflectance, with respect to the spectra acquired in this manuscript. Considering these four aubrites, the spectrum shapes are relatively featureless, even if a weak absorption can be seen around 1 μm. In particular, the spectrum of Peña Blanca Spring shows a weak but defined band I absorption. Band I in Rantila spectra is deeper, in agreement with the higher FeO content in mafic minerals (0.12-0.36 wt%) compared to Peña Blanca Spring (<0.02 -0.07 wt%, ***Watters & Prinz, 1979***), Khor Temiki (<0.02-0.03 wt%, ***Watters & Prinz, 1979***) and Bishopville (<0.02 -0.08 wt%, ***Watters & Prinz, 1979***). Also, these three aubrites present minor bands (1.4 and 1.9 μm) associated with the presence of iron hydroxides, more pronounced than those observed in Rantila, suggesting the relatively low weathering grade of this fall. Mayo Belwa spectrum, on the other hand, is featureless, suggesting lower FeO content in mafic minerals at least in this specific sample (FeO content reported ranging from 0.02 to 0.07 wt%, ***Watters & Prinz, 1979***). ***Cloutis et al. (2016)*** compared some aubrites spectra, showing a very weak band I absorption, with an orthopyroxene having 0.59 wt% FeO showing, on the contrary, a clear band I absorption (up to 40 % deep). The samples studied here have FeO composition between the other aubrites and the pyroxene studied by ***Cloutis et al. (2016)***, permitting to move the potential detection limit at lower values of FeO in pyroxene or olivine. ***Cloutis et al. (2016)*** also highlighted for the terrestrial pyroxene that band II was weaker than band I, which supports the idea that with such low $Fe^{2+}$ content pyroxene should have no, or easily made up, absorptions around 2 μm.

An asymmetry can be observed in band I of the three spectra of Ran_02, marked by a shoulder around 700 nm. This phenomenon could be attributed to the presence of small amounts of $Fe^{3+}$ in iron hydroxides resulting from terrestrial alteration. For example, goethite exhibits an absorption band around 700 nm (***Burns, 1993; Clark, 1999; Cloutis et al., 2008; Crowley et al., 2003; Sherman et al., 1982; Sherman & Waite, 1985***). The minor bands visible in the region between 1.4 and 1.9 μm are consistent with the presence of iron hydroxides, as this is where the OH absorptions occur (***Clark, 1999; Crowley et al., 2003; Sherman et al., 1982***).

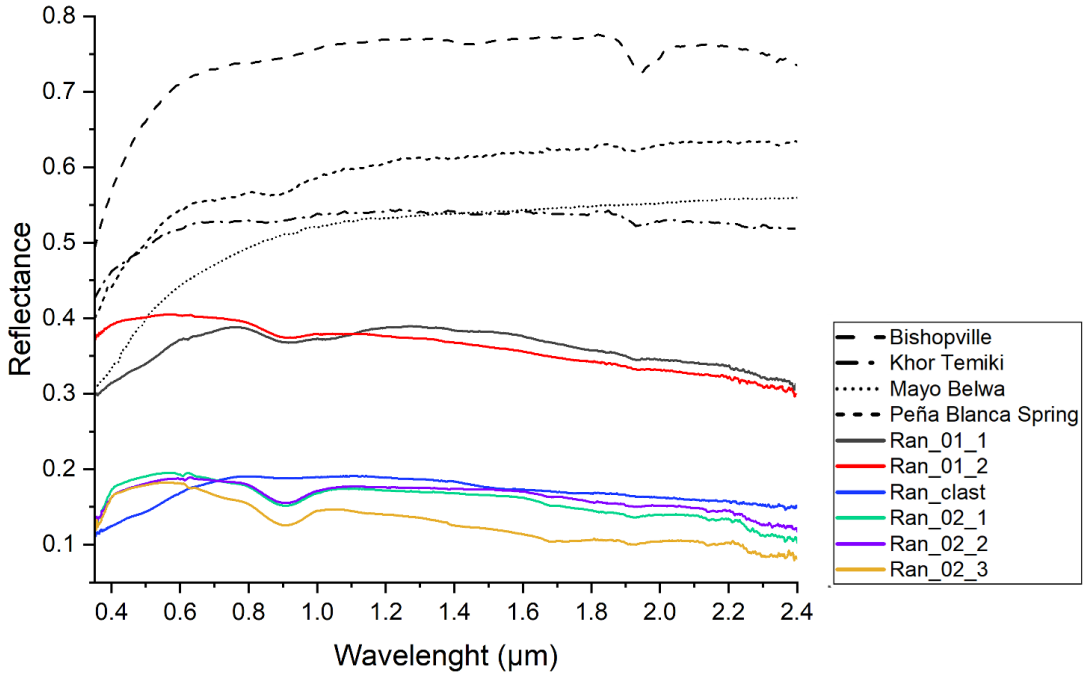


Figure 2.13. Reflectance spectra of investigated Rantila samples and aubrites from literature: grain size <125 µm, data from the RELAB database. Bishopville specimen ID TB-TJM-047 (see also **Clark et al., 2004; Reddy et al., 2016**), Khor Temiki TB-TJM-048, Mayo Belwa TB-TJM-046 (see also **Clark et al., 2004; Reddy et al., 2016**), Peña Blanca Spring TB-TJM-045 (see also **Clark et al., 2004; Reddy et al., 2016**).

### 2.4.6. Implications for Mercury

Studying the reflectance properties of highly reduced meteorites, including aubrites, provides valuable insights for comparing their spectroscopic properties with those of Mercury's surface and Near-Earth asteroids. In particular, recent spectral studies have been conducted on the VNIR spectral range of aubrites (e.g., ***Burbine et al., 2002; Cantillo et al., 2024; Cloutis et al., 2016; Dibb et al., 2022***). Unlike previously studied samples, the Rantila samples analysed in this work highlighted a very weak absorption feature associated with the primary mafic mineralogy. The spectral signature varies from almost featureless (Ran_clast spectrum) to broader and weaker absorption (Ran_01_spectra) up to a narrow-deeper absorption (Ran_02_spectra).

These absorption bands attributable to FeO in mafic minerals, allow us to extend the potential FeO detection limit on silicates, as we can detect the absorption features around 1 µm in $En_{98.6}Wo_{0.9}$ (dominating in Ran_02), as well as in $En_{98.8}Wo_{0.7}$ with the association of $En_{56.2}Wo_{43.4}$ and $Fo_{99.7}$. Additionally, we can highlight that mafic minerals with this composition do not exhibit an absorption band around 2 µm (or it is very weak, especially where low-Ca pyroxene dominates, although in these samples, it is affected by weak terrestrial alteration). The absorption around 1 µm can be observed also in the spectra of some of the Hollows fields of Mercury observed by MESSENGER Mercury Dual Imaging System (MDIS) Camera with filters covering the range 898-996 nm (***Carli***

***et al., 2024b; Luchetti et al. 2018***). For instance, observations of the Hollow field of the Dominici crater, as highlighted in ***Vilas et al. (2016)*** and ***Lucchetti et al. (2018)***, and Warhol crater (***Carli et al., 2024b***) indicate the exposure of relatively fresh mafic minerals in those terrains. As it is possible to observe in **Figure 2.14**, despite a similar intensity, the absorption features in the Rantila aubrite spectra are located around 0.9 μm, while the hollows spectra show a downward deflection from 0.8 μm, resulting in an absorption located around 1 μm, suggesting possible assemblages with higher Ca-Pyroxene or olivine on Hollows material. Moreover, the reflectance spectroscopy of the investigated samples highlights that the olivine-rich clast with $Fo_{99.7}$ shows the weakest, almost featureless, absorption, suggesting that olivine could be more difficult to detect compared to low-Ca pyroxene. Additionally, the narrow-weak features at ~500 nm could be attributed to iron spin-forbidden absorptions. However, such mineralogy does not show any other absorptions, such as those at ~0.628-0.748 μm, which are typically associated with either a higher concentration of sulphides (as suggested by ***Vilas et al., 2016***) or with the presence of other transitional elements (e.g., ***Lucchetti et al., 2018***) with higher concentration than those found in Rantila mafic minerals. In fact, it is possible to observe the ~0.6 μm feature in the hollows spectra and not in Rantila spectra (**Fig. 2.14**).

MASCS reflectance spectra show an evident UV-downturn, concave curvature of the spectrum in the UV range (***Goudge et al., 2014***), particularly for hollows and pyroclastic deposits (***Barraud et al., 2020, 2021***). This feature is thought to be influenced by three factors (***Barraud et al., 2020***): the space weathering, strongly affecting the planet's surface (***Domingue et al., 2014***); the size of the particles, UV-downturn increasing with decreasing grain size (***Cloutis et al., 2008***); the presence of sulphides. We do not observe UV-downturn in the investigated Rantila samples (**Fig. 2.14**), which can be linked to the acquisition on slab and not on fine-grained powders and to the presence of sulphides only as minor phases in the mineralogical assemblage. The effect of space weathering on aubrite, simulated through pulsed laser by ***Zhang et al. (2022)***, shows a spectral darkening and reddening, but no specific effects on the UV-downturn are observed.

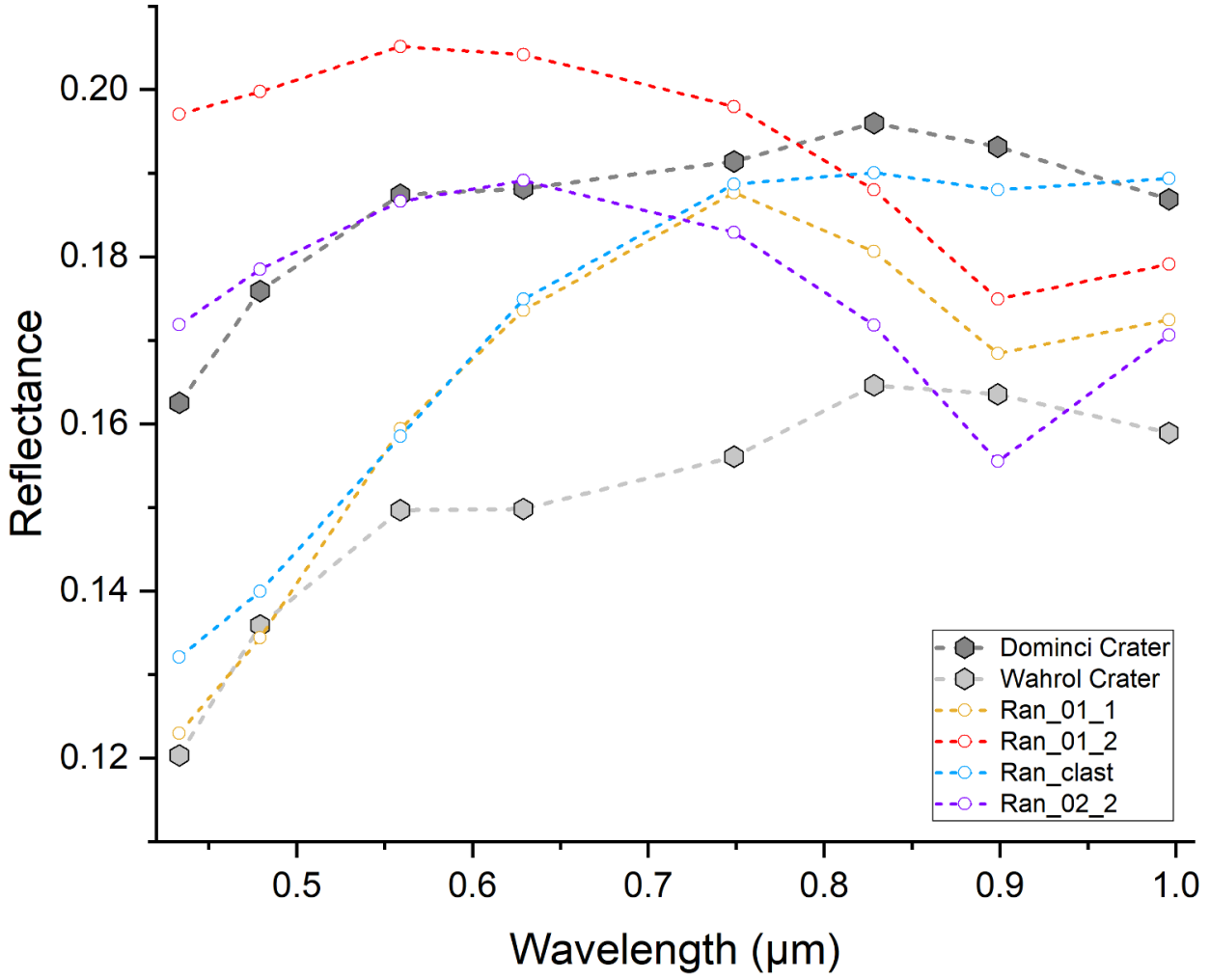


Figure 2.14. Comparison between two Hollows spectra (Dominici crater and Warhol crater) (**Carli et al., 2024b**) and Rantila spectra. Hollows spectra were acquired on a MDIS mosaic at 665 m per pixel, which was produced following the procedure explained in **Zambon et al. (2022).** For sample Ran_02, only one spectrum (Ran_02_2) is reported, considering the high similarity of the other spectra (see figure 2.12a). Ran_01_2 spectrum was vertically shifted (-0.2) for figure clarity.

Although aubrites are considered one of the best analogues of Mercury's surface at our disposal (***Burbine et al., 2002***; ***Morlok et al., 2020***; ***Udry et al., 2019***; ***Wilbur et al., 2022***), some differences must be taken into account. They share with Mercury's surface the highly reducing conditions of formation and highly reduced mineralogy, but they do not represent a perfect petrological analogue: for example the plagioclase modal abundance on Mercury is expected to be likely double than in aubrites (***Wilbur et al., 2022***), sulphides are expected to be more abundant on the planet surface as well, up to 10.1 % in some specific areas of hollows (***Barraud et al., 2023***), aubrites present metallic Fe,Ni (***Casanova et al., 1993***). In particular, the presence of these primitive metals indicates an incomplete core formation in the aubrite parent body/bodies, suggesting that they cannot have originated from Mercury (***Keil et al., 2010***). Also, the reddening of Mercury spectra, influenced by space weathering (***Domingue et al., 2014***), is linked to the presence of metallic iron

nanophase that needed a few percent of FeO in the pristine material. That quantity of FeO exceeds the one observed in aubrites, again suggesting the inconsistency of their origin from Mercury (***Keil et al., 2010***). Moreover, considering delivery mechanisms of ejected materials from another planet to the Earth (ejection of the materials at escape speed or higher and Earth-crossing orbital evolution), ***Love and Keil (1995)*** suggested that the probability of collecting a Mercurian meteorite is extremely low, and the number of recognized aubrites exceeds, hundreds of times, the number of possible meteorites from Mercury. Nonetheless, increasing the existing spectral data set on aubrites and, on a large scale, highly reduced meteorites will be useful for future comparison with the data expected to arrive from the ESA's BepiColombo mission. In fact, new VNIR data will be provided by the SIMBIO-SYS/VIHI imaging spectrometer (0.4-2.0 μm, ***Cremonese et al., 2020***). In this study, we focused on the connection between the reflectance spectra and the mineralogy and mineral chemistry of this aubrite, with a focus on the iron contents and on the presence of hydrous alteration, which produce spectral features not expected in the spectra of Mercury's surface. Having a clear picture of the mineralogy and mineral chemistry of these meteorites viewed as Mercury's analogues, considering the differences as well, will help in understanding how to correlate the reflectance spectroscopy information with the compositional information, which will be given by the BepiColombo mission MIXS spectrometer (***Fraser et al., 2010***).

### 2.5. Conclusions

The Rantila aubrite fragments under investigation are composed of different features: a principal light-coloured portion; a dark forsteritic inclusion embedded in the light-coloured portion; a dark glassy portion mainly composed of glass containing microcrystals of diopside, enstatite, and plagioclase, diopside phenocrysts, and only one enstatite phenocryst. The mineral chemistry of the detected phases is similar among the fragments, especially in terms of major elements contents, despite their textural and modal mineralogy differences. The mineralogy is indicative of highly reducing conditions of formation, as it can be inferred from the very low FeO contents, from below EPMA detection limit to 0.36 wt%, and from the relatively high values of dissolved S ($SO_3$ 0.4 wt%) in the glass of Ran_03. Due to this highly reduced nature, aubrites tend to be quickly subject to terrestrial weathering: even Rantila, despite being a fall, presents sporadic iron oxides/hydroxides and visible reddish portions. Still, there is no evidence of pervasive weathering on opaque phases, which are usually the first to be altered so that we can consider a low weathering grade for this meteorite.

The substantial lack of iron makes this meteorite very interesting for laser-induced time-resolved luminescence. The results indicate that $Cr^{3+}$ (750 nm) is present in diopside as a luminescence activator, and $Mn^{2+}$ (587 and 640 nm) is present in both diopside and forsterite, within the aubritic portions of Ran_01 and Ran_02. $Ce^{3+}$ is the luminescence activator present in diopside of Ran_03. This is consistent with the absence of forsterite in this sample and the lower $Cr_2O_3$ content (below the EPMA detection limit), compared to the others. Investigating the luminescence behaviour could give a valuable contribution to the minero-petrological study of these materials, providing information on the luminescence activator elements present in the diverse mineralogical phases, even at very low concentrations.

Reflectance spectra acquired on different portions of Ran_01 and Ran_02, including the dark clast, show some differences (i.e. band I positions and shapes, the presence of an additional band around 0.5 μm in two of the spectra), reflecting the different mineralogy. The spectra acquired on Ran_02 are consistent with low Fe-Ca pyroxene. The lack of the broader absorption around 2 μm typical of pyroxenes is attributed to the low $Fe^{2+}$ content and to the presence of absorption features at ~1.4 μm and ~1.9 μm produced by the presence of low terrestrial contamination. The same can be said for Ran_01, but, in this case, there is a higher variability between the two acquired spectra ascribed to a higher abundance of forsterite in some portions of the sample. The Ran_clast spectrum is consistent with nearly FeO-free forsterite being the dominant phase. This study highlights the extent to which spectral features can vary according to mineralogy and mineral-chemistry. In particular, $Fe^{2+}$ serves as a critical indicator of the mineral phases in which it is present, even at very low concentrations, influencing the presence, position, and shape of absorption bands. Moreover, the depth of the mafic mineral band I absorption varies significantly with increasing $Fe^{2+}$ concentrations, even at very low levels (e.g., from 0.03 to 0.3 wt%). The correlation between the results of the various analytical techniques provides a thorough understanding of the mineralogy and mineral chemistry of this aubrite, pointing out its mineralogical diversity, which is a characteristic feature of aubrites.

Given that aubrites are considered promising analogues for Mercury's surface, this study, by increasing the knowledge of the correlation between spectral properties and mineralogy/mineral chemistry of these highly reduced meteorites, could provide a valuable spectral baseline for future investigation of Mercury. In particular, it could be useful for the interpretation of the data expected from ESA's BepiColombo mission, specifically from the SIMBIO-SYS/VIHI imaging spectrometer.

# 3. Highly reduced meteorites: mineralogical and VNIR reflectance spectroscopy investigation

This chapter is a manuscript in preparation for publication by A.I. Landi, C. Carli, F. Capaccioni, and G. Pratesi.

**Abstract**

In this work, we investigated the mineralogy, chemical composition, and VNIR reflectance spectroscopy of eight highly reduced, enstatite-rich meteorites belonging to different groups, including aubrites, enstatite chondrites and achondrites, and enstatite melt rocks. Enstatite is the dominant phase in all the samples, although with variable modal abundances, while metals and sulphides are more abundant in enstatite chondrites and achondrites than aubrites. Aubrites display the highest mineralogical heterogeneity. The enstatite melt rock shows heterogeneity as well, although in this case it is induced by terrestrial weathering. The other samples are affected by just an incipient terrestrial weathering. Three aubrites, the enstatite achondrite and the enstatite melt rock show textural and mineralogical evidence of partial melting processes. Enstatite and forsterite compositions are overall homogeneous among the samples from different groups, with very low FeO contents (<0.4 wt%). Plagioclase shows a wider compositional range in aubrites than in enstatite chondrites and achondrites. Metals and sulphides compositions are different among samples of different meteorite groups. Kamacite presents higher Si contents in enstatite chondrites than in aubrites and enstatite achondrites. Troilite contains variable amounts of Cr and Ti across the investigated samples. Oldhamite is present across all the meteorite groups, while alabandite is detected in aubrites and in one enstatite chondrite, keilite is present in one enstatite chondrite and in the enstatite achondrite, which is also the only sample presenting niningerite. These mineralogical and chemical differences suggest that these samples derive from multiple distinct enstatite chondrite–like parent bodies.

VNIR reflectance spectra of enstatite chondrites and achondrites are generally flat and almost featureless, reflecting the low FeO content in silicates. Aubrite spectra, on the other hand, exhibit weak 0.9 μm mafic absorption features accompanied by a weak 0.5 μm band in olivine-rich portions. Minor features at 1.9 μm are attributed to hydrated phases from terrestrial aqueous alteration. Overall, the correlation between mineralogical and spectral properties of these highly reduced materials can provide additional information for the interpretation of upcoming data of Mercury's surface from ESA's BepiColombo mission.

### 3.1. Introduction

Enstatite-rich meteorites, including aubrites, enstatite chondrites, achondrites, and related melt rocks, are the most reduced natural materials at our disposal (e.g., ***Fogel, 1997; Keil, 1989***; ***Keil, 2010; Okada et al., 1988; Wilbur et al., 2022***), with oxygen fugacity ($fO_2$) values lower than the iron-wüstite (IW) buffer (***McCoy & Bullock, 2017***). Enstatite chondrites are mostly composed of FeO-free enstatite with variable amounts of Si-bearing metals, troilite, and exotic sulphides composed of typically lithophile elements, indicating the highly reducing conditions (e.g., ***Keil, 1989***). Plagioclase may occur in minor amounts, while it is more abundant in enstatite achondrites and melt rocks (***Burbine et al., 2000***; ***Lin & Kimura, 1998; McCoy et al., 1995; Udry et al., 2019***). Aubrites are a rare group of achondrites of igneous origin composed of FeO-poor enstatite, followed by forsterite, diopside and plagioclase, and minor Fe,Ni metals, troilite and exotic sulphides (e.g., ***Barrat et al., 2016; Keil, 2010; Okada et al., 1988; Watters and Prinz, 1979; Wheelock et al., 1994***). These highly reduced meteorites are thought to have formed in the innermost part of the protoplanetary disk (e.g., ***Kallemeyn & Wasson; 1986***), from multiple parent bodies (e.g., ***Keil, 2010; Weyrauch et al., 2018***). Enstatite chondrites are divided into two groups: the high-Fe, high siderophile EHs and the low-Fe, low-siderophile ELs (***Sears et al., 1982***). ***Weyrauch et al. (2018)*** propose the additional division of EHs and ELs into two subgroups "a" and "b", on mineral chemistry basis. These subgroups are suggested to come from different parent bodies, increasing the number of enstatite chondrite source materials to at least four. Moreover, it is hypothesized that aubrites formed from igneous processes on enstatite chondrite-like parent materials (e.g., ***Keil, 1989; Keil, 2010; McCoy and Bullock, 2017***), but not from one of the EHs/ELs parent bodies (***Keil, 1989; Keil, 2010***). There is also evidence that aubrites come from at least two distinct parent materials (***Keil, 1989; Keil, 2010***). The occurrence of anomalous enstatite-rich/reduced meteorites, e.g., Itqiy (***Patzer et al., 2001***), QUE 94204 (***Van Niekerk et al., 2014***), Zakłodzie (***Przylibski et al., 2005***), NWA 15915 and Ksar Ghilane 022 (***Rider-Stokes et al., 2025***), suggests that they may come from further distinct source materials.

Highly reduced meteorites, specifically aubrites (e.g., ***Burbine et al., 2002***; ***Morlok et al., 2020***, ***Wilbur et al., 2022***) and enstatite chondrite melts (***Udry et al., 2019***), have been proposed as potential analogues of Mercury's surface due to the similarity with retrieved $fO_2$ and mineralogy of the hermean surface. According to data from MErcury Surface, Space ENvironment, GEochemistry, and Ranging (MESSENGER) mission (***Solomon et al. 2018***), the $fO_2$ is estimated to be in the range 2.6-7.3 log units below iron-wüstite buffer (***McCubbin et al., 2012; Namur et al., 2016; Zolotov et al., 2013***) and the inferred mineralogy is composed of enstatite, plagioclase (suggested as albitic), forsterite and Mg-Ca-Fe sulphides (e.g., ***Namur & Charlier, 2017; Nittler & Weider,***

***2019***). Investigations on reflectance spectra properties in the visible and near-infrared (VNIR) range on aubrites and enstatite chondrites (e.g., ***Burbine et al., 2002***; ***Cantillo et al., 2024; Cloutis & Gaffey, 1993***; ***Cloutis et al., 2016; Dibb et al., 2022; Landi et al., 2025; Vernazza et al., 2009; Zhang et al., 2023***) evidenced that their spectra are relatively featureless, due to extremely low FeO content in mafic minerals. When weak absorption features related to mafic minerals (between 0.9-1.0 μm and 1.9-2.1 μm for pyroxenes, e.g., ***Burns, 1993***; ***Cloutis et al., 1986***; ***Dunn et al., 2010***; ***Gaffey et al., 1993***; ***Klima et al., 2007, 2011***, and around 1.0-1.06 μm for olivine, ***Burns, 1993***; ***Cloutis et al., 1986***; ***Sunshine & Pieters, 1998***) are observed, their position and depth can provide insights regarding the FeO content and the relative abundances of mafic phases (***Burns, 1993; Cloutis et al., 2016***). Therefore, they are proposed to be the best natural analogue for comparison with Mercury's surface spectra derived from Mercury Atmospheric and Surface Composition Spectrometer (MASCS) and Mercury Dual Imaging System (MDIS) Camera instruments on board of MESSENGER mission.

In this work, we investigated the mineralogy, chemical composition, and VNIR reflectance spectra properties of eight highly reduced meteorites of different groups, including the first detailed mineralogical characterization of four meteorites: Tiglit (aubrite), NWA 14185 (aubrite), NWA 4945 (EL6), and NWA 13266 (enstatite achondrite). Correlating the spectral properties and mineralogy of these highly reduced materials could help prepare for the interpretation of the upcoming spectral data from SIMBIO-SYS/VIHI (Spectrometer and Imaging for MPO BepiColombo Integrated Observatory SYStem/Visible and near-Infrared Hyperspectral Imaging channel) and chemical data from MIXS (Mercury Imaging X-ray Spectrometer) instruments (***Cremonese et al., 2020; Fraser et al., 2010***) onboard the ESA's BepiColombo mission (***Benkhoff et al., 2021; Rothery et al., 2020***).

## 3.2. Samples and Analytical Methods

### 3.2.1. Samples

The samples chosen for this work are different types of highly reduced meteorites: four aubrites (Rantila, Norton County, Tiglit, NWA 14185); two enstatite chondrites of high petrologic type (Itqiy and NWA 4945); one enstatite achondrite (NWA 13266); and one enstatite melt rock (NWA 13210).

The aubrites Norton County, Tiglit and Rantila are confirmed fall (***LaPaz, 1948; Gattacceca et al., 2023***; ***Gattacceca et al., 2024***), while NWA 14185 is a find (***Gattacceca et al., 2022***). They appear light coloured, except for Tiglit, which presents white phenocrysts in a darker matrix, with a brecciated aspect (**Figure S3.1**). Among the aubrite fragments under investigation, Tiglit is the

only one showing the light-coloured fusion crust (**Figure S3.1**). In the Rantila, Norton County, and NWA 14185 fragments, sporadic dark sulphide grains are visible, along with occasional reddish areas resulting from minor terrestrial weathering (**Figure S3.1**).

Itqiy is classified as an EH7-anomalous (***Grossman & Zipfel, 2001, revised in 2006***). NWA 4945 is classified as an EL6 (***Ruzicka et al., 2014***). NWA 13266 is classified as an enstatite achondrite (***Gattacceca et al., 2021***). NWA 13210 is classified as an EL-melt rock (***Gattacceca et al., 2021***) and suggested as a paired of Al Haggounia 001 (***Leili et al., 2024***). Itqiy, NWA 4945, and NWA 13266 appear dark with well-visible grey enstatite grains, darker sulphides, and metals showing the typical metallic luster (**Figure S3.2**). NWA 13210 appears lighter with well-visible voids and reddish-yellowish weathering products, testifying to the higher weathering grade of this meteorite compared to the others (**Figure S3.2**).

### 3.2.2. Analytical methods

We performed scanning electron microscope (SEM) and electron probe microanalysis (EPMA) on all the investigated meteorites. From each meteorite sample, a portion was selected and cut, then embedded in epoxy resin and polished with diamond paste down to a final particle size of 0.25 μm. Reflectance spectroscopy in the visible and near-infrared spectral range (VNIR) was performed, acquiring spectra on the rough surface of the meteorite fragments in their natural state, before the cutting and embedding in epoxy resin of the chosen fragments.

#### 3.2.2.1. SEM

SEM analyses were performed at the Centro di Servizi di Microscopia Elettronica e Microanalisi (MEMA) laboratory of the Università degli Studi di Firenze using a *ZEISS EVO-MA15* equipped with an Oxford ULTIM MAX 40 $mm^2$ EDS detector and Oxford Symmetry EBSD detector. Backscattered electron (BSE) and energy-dispersive spectroscopy (EDS) maps were collected using an accelerating voltage of 15 kV, 10 s acquisition time. An accelerating voltage of 15 kV was used to collect point analyses; a pure Co standard was used for calibration for semiquantitative chemical data.

Modal abundances of the detected phases were obtained with *XMapTools 4.1* (***Lanari et al., 2014***) starting from SEM-EDS maps of Mg, Fe, Ca, Na, Al, Si, S, Cr, Ti, Ni,O.

3.2.2.2. EPMA

Quantitative analyses of the detected mineral phases were performed at "Filippo Olmi" laboratory, Dipartimento di Scienze della Terra of the Università degli Studi di Firenze, using a *JEOL JXA-8230* Electron Microprobe equipped with five wavelength-dispersive spectrometers (WDS).

The operating conditions (accelerating voltage, beam current, beam size, correction) and the used certified standards (Astimex, Smithsonian, MAC) are summarized in **Table S3.1**.

3.2.2.3. VNIR reflectance spectroscopy

Reflectance spectra were obtained with a Fieldspec Pro® spectrophotometer mounted on a goniometer at the S.LAB. laboratory at INAF (Istituto Nazionale di Astrofisica) Istituto di Astrofisica e Planetologia Spaziali (IAPS), Rome. Measurements were made with illumination and collection field of view cones of ±3°, which approximate a bidirectional measurement. The illumination and collection angles are 30° and 0°, respectively. The spectral range is 0.35-2.5 μm with a ~3 nm spectral resolution in the range 350-1000 nm and a ~10-12 nm spectral resolution in the range 1001-2500 nm. The illumination source is a quartz tungsten halogen lamp, and the illumination spot has a diameter of ~6 mm. The measurements were taken at room temperature and pressure. A Spectralon® optical standard 99% (registered trademark of Labsphere, Inc.) was used for the calibration. The number of spectra collected varied for each sample to capture the heterogeneity of the fragments: for smaller and less heterogeneous fragments, a minimum of three-point analyses were taken, while up to ten-point analyses were selected for larger and more heterogeneous fragments. Each final spectrum is the average of three spectra taken in the same spot, slightly tilting the sample, to avoid systematic error derived from the relative unevenness of the surface. Additionally, three aubrites (Rantila, Norton County and NWA 14185) were studied as powders with grain sizes below 100 μm. Three measurements were performed for each sample, with the powder being redistributed between each measurement. Each individual spectrum is an average of 200 scans.

The continuum line was determined by connecting the reflectance maxima in the spectrum with straight-line segments as a function of wavelength (***Clark & Roush, 1984***). The band center corresponds to the position of the minimum reflectance value of the band after the continuum removal. The band depth is calculated as 1-(R/C) after the continuum removal, in which R is the reflectance value at the band center wavelength and C is the continuum reflectance.

## 3.3. Results

### 3.3.1. Texture and mineralogy

3.3.1.1. Aubrites

The four aubrite samples show the brecciated texture (**Fig. 3.1**) typical of aubrites (e.g., ***Keil, 2010; Watters & Prinz, 1979***).

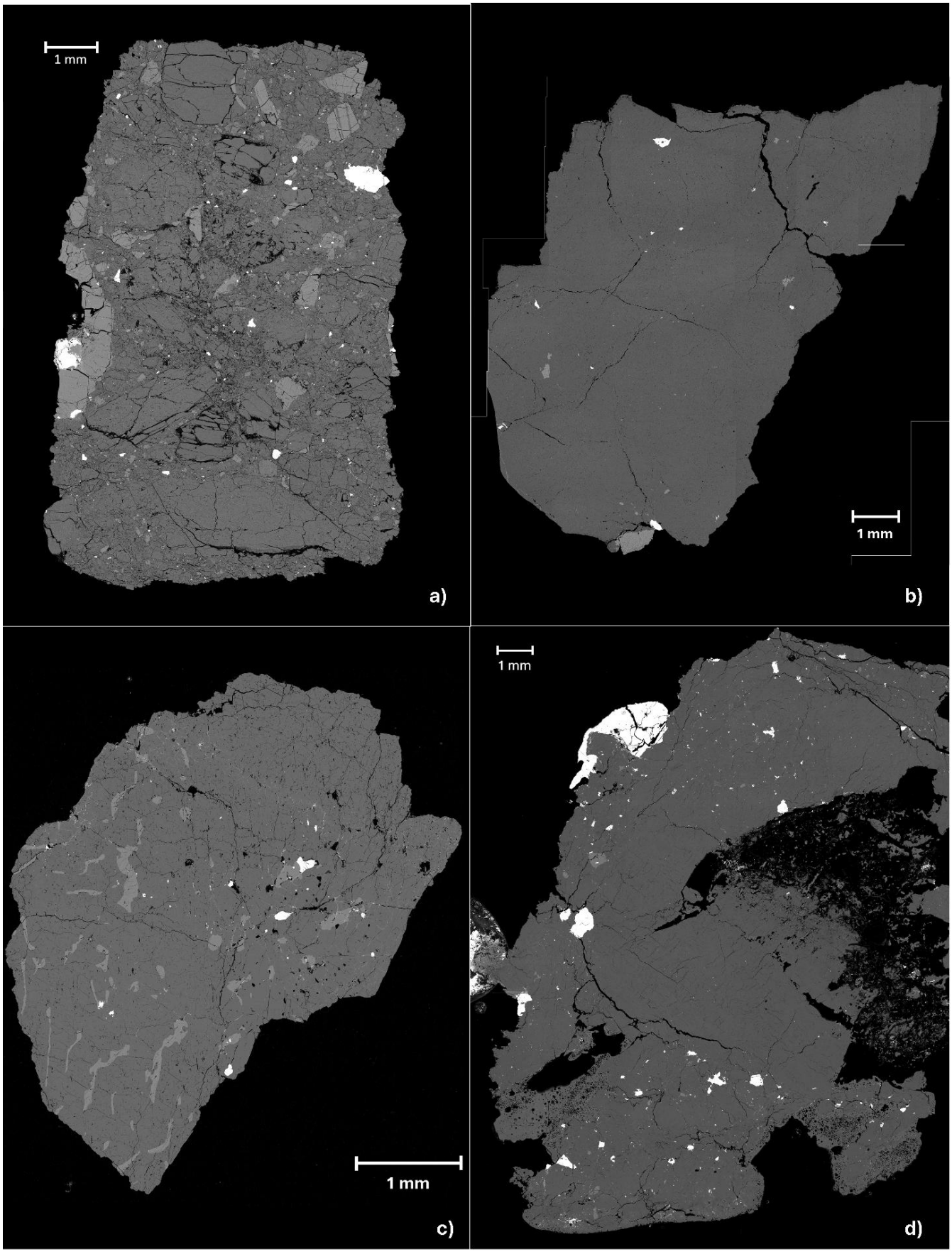


Figure 3.1. BSE maps of the four investigated aubrites showing a highly brecciated texture. a) Rantila; b) NWA 14185; c) Norton County; d) Tiglit. Rantila map from **Landi et al, 2025.**

Enstatite is the predominant phase (**Fig. 3.2** and **Table 3.1**). It is present as phenocrysts of different sizes, up to centimetric dimensions, and as micrometric fragments composing the matrix. Different types of enstatite were found in Rantila (***Landi et al., 2025***): brecciated, free of inclusions or with diopside inclusions, showing visible vesicles, heavily fractured with vesicles and opaque minerals inclusions, as lamellae (<10 μm width) in diopside. These different enstatite features were described for other aubrites (e.g., ***Lorenz et al., 2020; Okada et al., 1988***) and can be observed in the Norton County fragment as well. Heavily brecciated enstatite without vesicles and inclusions seems to be the predominant type in NWA 14185 and Tiglit. Forsterite is present in very different amounts among the investigated samples (**Table 3.1**): from no detection to 16.9 % in Rantila. The presence and quantity of forsterite in these fragments can be influenced by sampling. For example, forsterite is not detected in the first investigated Norton County fragment, although it can be abundant in this meteorite (up to 10 %; ***Watters & Prinz, 1979***). A second fragment was studied, and 5.6 % forsterite was detected along with plagioclase (**Fig. 3.3**). In Rantila, forsterite appears as phenocrysts up to millimetric dimensions and as smaller fragments composing the matrix (***Landi et al., 2025***), while in the second fragment of Norton County, the phenocrysts maximum length is smaller than 500 μm. Diopside occurs in different amounts among the samples as well (**Table 3.1**): it can be present in small amounts, mainly as micrometric irregular grains, in higher amounts as irregular and often elongated grains, or as phenocrysts up to millimetric dimensions and often hosting enstatite lamellae and inclusions. Plagioclases are typically less abundant than other silicates in aubrites, with some exceptions: for instance, in this Tiglit fragment, they are more abundant than forsterite and diopside (**Table 3.1**). They are usually present as microscopic grains, occasionally bigger than 500 μm, and sometimes appear as irregular fragments. Metal and sulphide phases can occur as isolated objects or as irregular aggregates of different sulphides or metal-sulphides (***Landi et al., 2025***). Troilite represents the principal sulphide, mostly occurring as isolated objects and as inclusions in silicates, sometimes associated with daubréelite. Alabandite is observed in Rantila and Tiglit, oldhamite in Norton County and Tiglit, heideite in Rantila and Tiglit. Oldhamite was observed in Rantila (***Srivastava et al., 2023***) but not in this fragment. Metals are present in trace amounts (**Table 3.1**) and are represented by kamacite. Schreibersite, a phosphide, is observed in Tiglit.

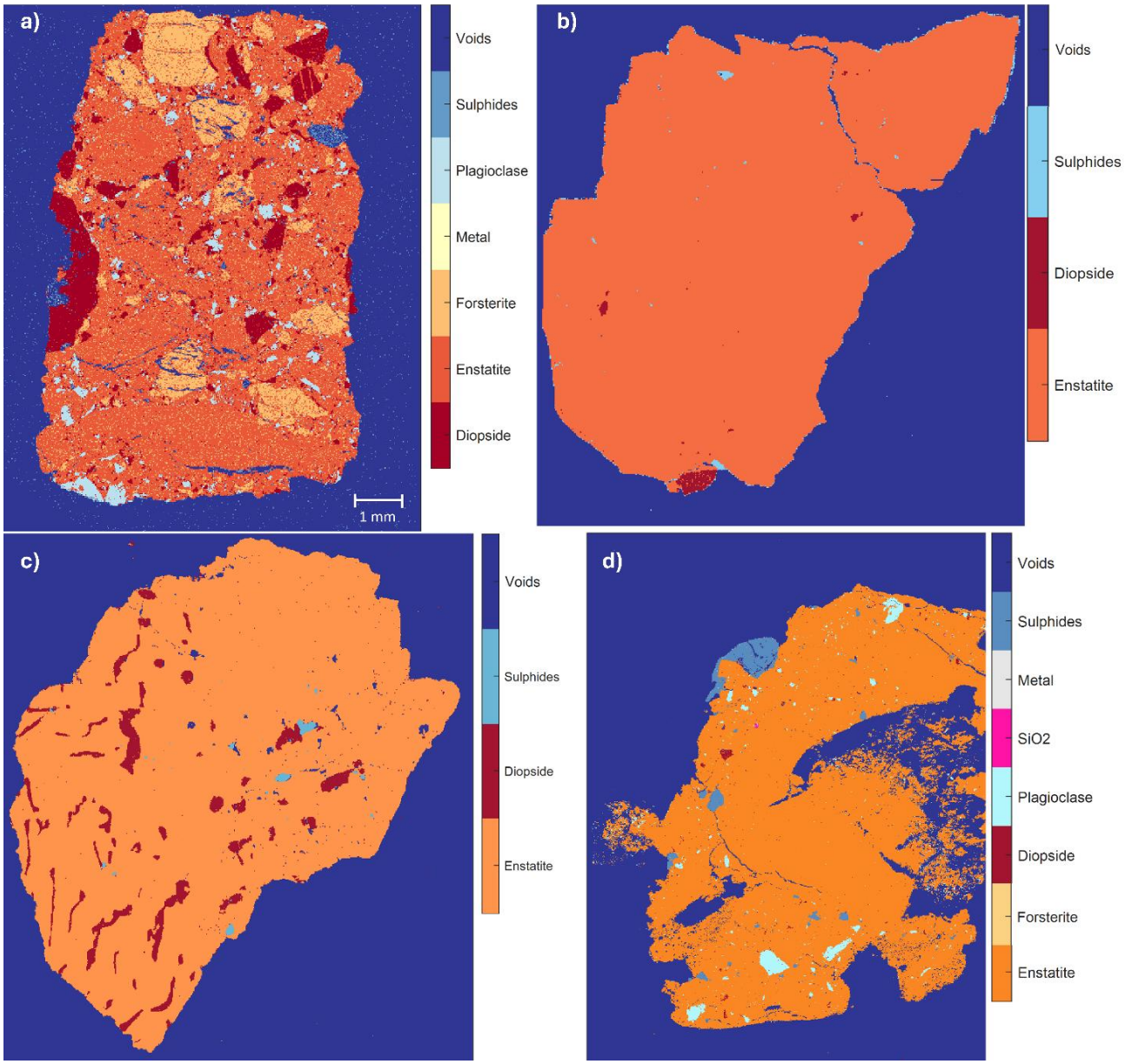


Figure 3.2. Phase maps of the investigated aubrites. a) Rantila; b) NWA 14185; c) Norton County; d) Tiglit. Rantila map from **Landi et al, 2025.**

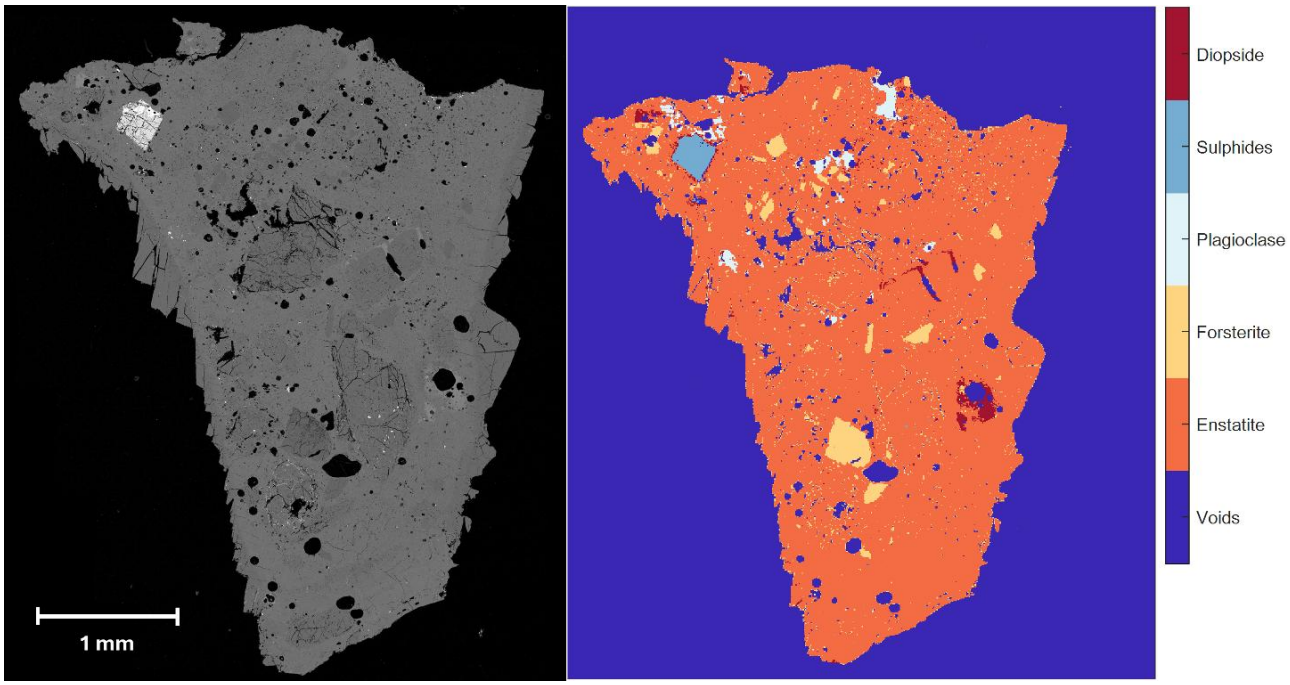


Figure 3.3. BSE map and phase map of the second fragment of Norton County showing melt texture and the presence of forsterite and plagioclase.

| | Enstatite | Forsterite | Diopside | Plagioclase | Sulphides | Metals | Silica | Glass | Alteration | Voids |
|---|---|---|---|---|---|---|---|---|---|---|
| *Rantila*[1] | 60.2 | 16.9 | 12.7 | 5.2 | 1.9 | 0.1 | - | <0.1 | <0.1 | 3.0 |
| *Norton County*[1] | 93.5 | - | 5.5 | - | 0.4 | <0.1 | - | - | - | 0.6 |
| *Tiglit*[1] | 90.4 | 0.1 | 0.6 | 2.8 | 2.9 | <0.1 | - | <0.1 | - | 3.1 |
| *NWA 14185*[1] | 97.2 | - | 1.5 | - | 0.6 | <0.1 | - | - | - | 0.7 |
| *Itqiy*[2] | 89.4 | - | - | - | 0.4 | 7.0 | - | - | - | 3.2 |
| *NWA 4945*[2] | 71.9 | - | 1.3 | 8.6 | 9.0 | 7.8 | - | - | - | 1.4 |
| *NWA 13266*[3] | 63.5 | - | - | 4.5 | 7.9 | 10.9 | 5.2 | 7.3 | - | 0.7 |
| *NWA 13210*[4] | 66.8 | - | - | 13.2 | 0.8 | <0.1 | - | 1.2 | 8.5 | 9.5 |

Table 3.1. Modal mineralogy of the investigated meteorites (%).
[1]=aubrites, [2]=enstatite chondrites, [3]=enstatite achondrite, [4]=enstatite chondrite melt rock

3.3.1.2. Enstatite chondrites, achondrites and melt rocks

Itqiy and NWA 4945 are classified as enstatite chondrites of high petrologic type, 7 and 6, respectively, and experienced recrystallization with loss of chondritic texture and chondrules definition (e.g., ***Keil, 1989***). Itqiy texture (**Fig. 3.4**) is composed of big enstatite grains, up to 2 mm in length in this fragment, typically equigranular and subhedral (***Patzer et al., 2001)***, disposed in triple junctions. Metals occur as millimetric grains and occupy the interstitial spaces between enstatite grains. Sulphides occur in small amounts (**Table 3.1**), represented by troilite and by a millimetric grain of different Ca-Mn-Fe-Mg-Cr sulphide assemblages, including oldhamite (**Fig. 3.4**).

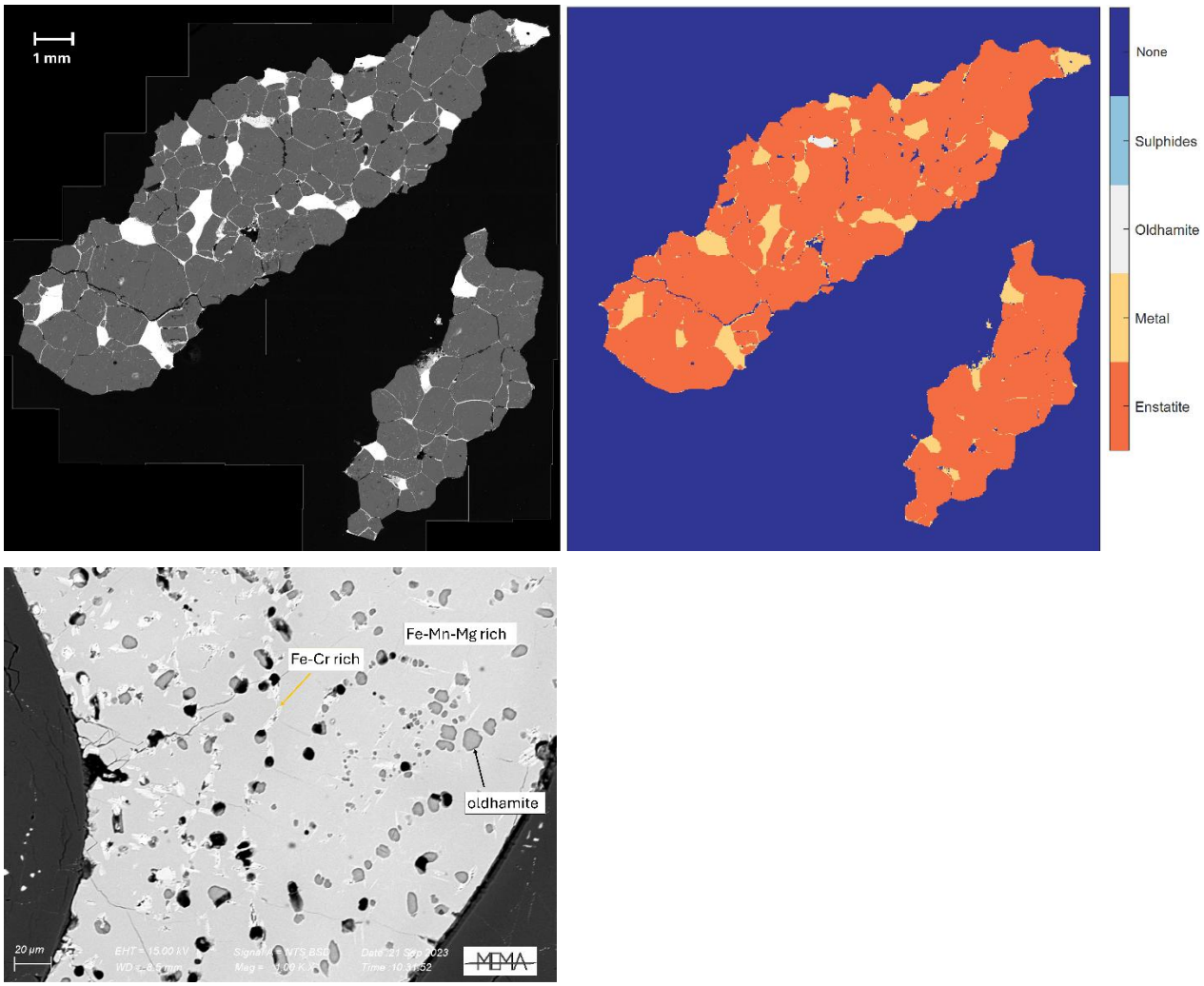


Figure 3.4. Itqiy BSE map and phase map. View of the millimetric sulphide in the lower left panel.

NWA 4945 has more complex mineral assemblage and texture, composed of micrometric enstatite grains mixed with abundant (**Table 3.1**) irregularly shaped metals and sulphides, and a relict chondrule can be observed (**Fig. 3.5**). Moreover, diopside is detected, as in some other EL6 (e.g., ***Floss et al., 2003; Fogel, 1997***) (**Fig. 3.5**). Metals are represented by kamacite. Troilite is the main sulphide, often containing keilite and kamacite (**Fig. 3.5**); oldhamite is also detected.

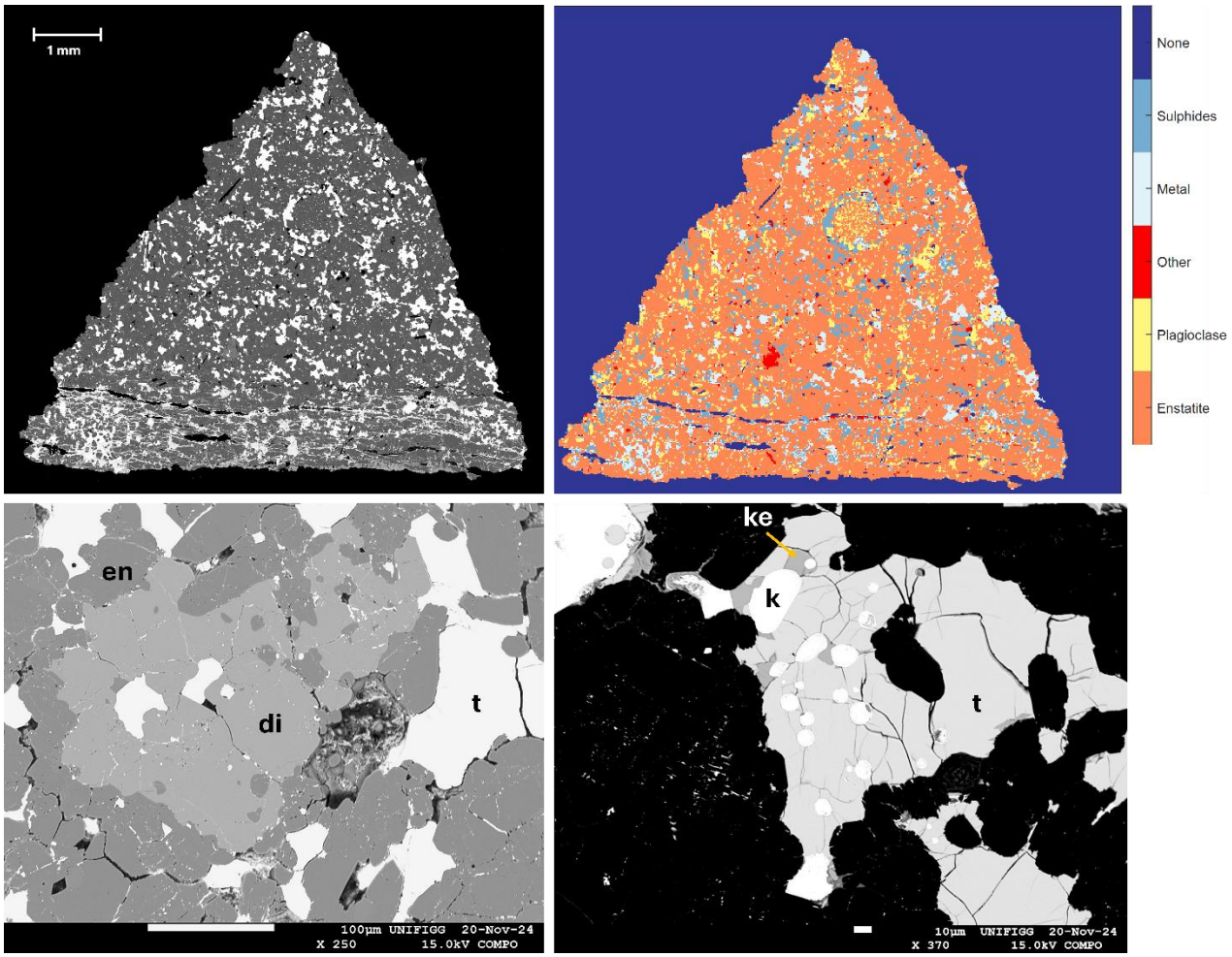


Figure 3.5. NWA 4945 BSE map and phase map. Example of observed diopside in the lower left panel; en=enstatite, di= diopside, t= troilite. Example of troilite (t) with kamacite (k) and keilite (ke) in the lower right panel.

NWA 13266 is an enstatite achondrite composed of poorly defined enstatite grains in a matrix of plagioclase, silica, and glass (**Fig. 3.6**). Abundant metals and sulphides (**Table 3.1**) are mostly present as irregularly shaped aggregates. Metal is represented by kamacite, the occurring sulphides are troilite, niningerite, minor keilite, and oldhamite. Niningerite contains irregularly shaped troilite and acicular microcrystals of Fe-sulphides rich in Zn (**Fig. 3.6**).

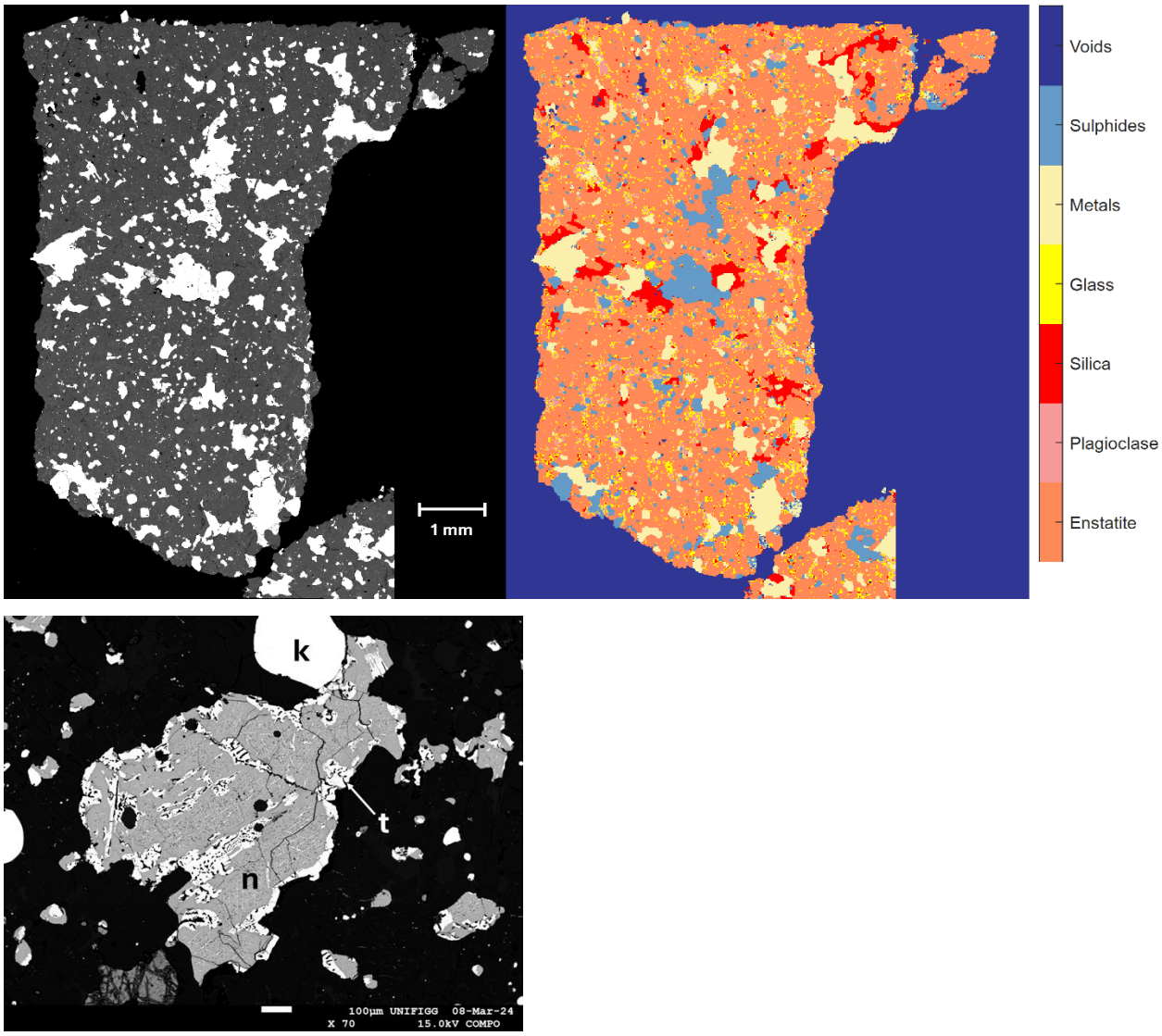


Figure 3.6. NWA 13266 BSE map and phase map. Example of sulphide-metal assemblage in the lower left panel. n= niningerite, k= kamacite, t= troilite.

NWA 13210 is a melt rock with a strongly recrystallized texture (**Fig. 3.7**). It is mostly composed of 100 µm enstatite grains and plagioclase grains (**Fig. 3.7** and **Table 3.1**). This fragment presents products of terrestrial weathering and a more scrambled nature compared to the other meteorites: alteration may have caused its brittle nature and the presence of voids. Minor sulphides were detected but no metals, maybe these phases have been replaced by oxides due to terrestrial weathering. Minor glass among enstatite grains was detected as well.

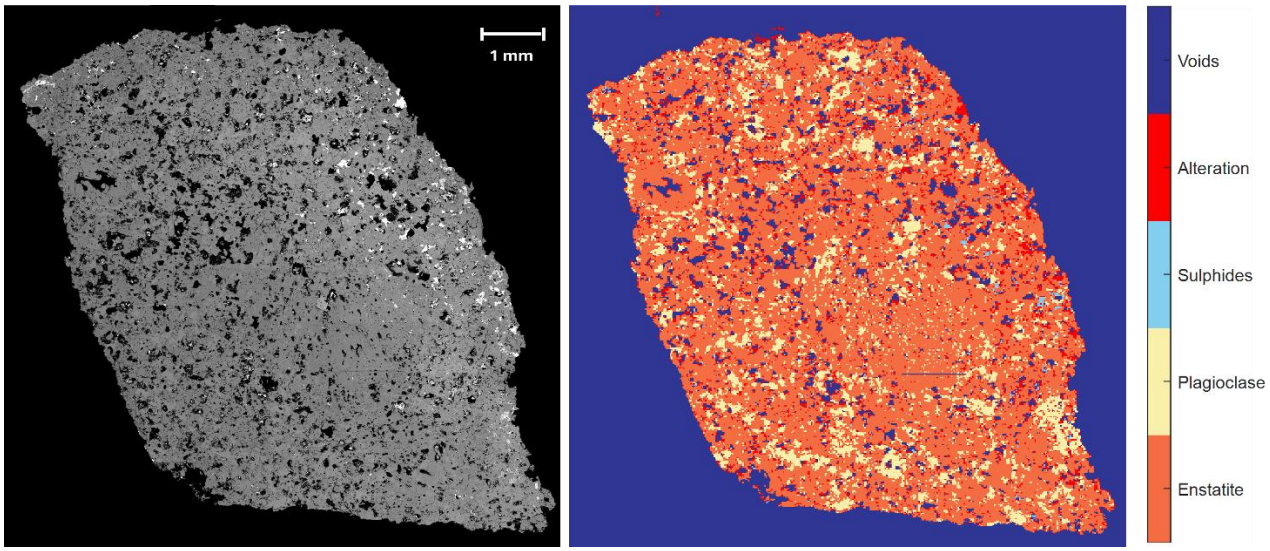


Figure 3.7. NWA 13210 BSE map and phase map. The high porosity of the fragment, a consequence of terrestrial weathering and already observed in the hand specimen, is here clearly visible.

3.3.1.3. Melt features

Evidence of melting processes is observed in all the investigated aubrites, except NWA 14185. Enstatite melt pockets containing Fe-S veins and spherules, and plagioclase grain containing Fe-Cr-S spherules were observed in Rantila (***Landi et al., 2025***). Norton County has been affected by local melting processes, as evidenced by the investigated millimetric fragment showing a melt matrix of enstatitic composition surrounding vesicles and enstatite, diopside, forsterite, plagioclase and sulphide phenocrysts (**Fig. 3.3**). The matrix texture is composed of enstatite microcrystals, and minor acicular forsterite crystals (**Fig. 3.8**). Melting features in Tiglit are represented by enstatite melt pockets containing opaque mineral spherules, as well as by a melt pocket with a matrix composed of acicular micro grains, elongated enstatite and forsterite phenocrystals, and troilite grains of different sizes, micrometric grains scattered through the whole pocket and submicrometric scattered on forsterite phenocrysts (**Fig. 3.8**). Among the investigated aubrites, Tiglit fragment is the only one showing fusion crust (**Fig. S3.3**). Melt features are observed in NWA 13266 and NWA 13210 with the presence of interstitial glass and curvilinear troilite trails in enstatite (**Fig. 3.8**).

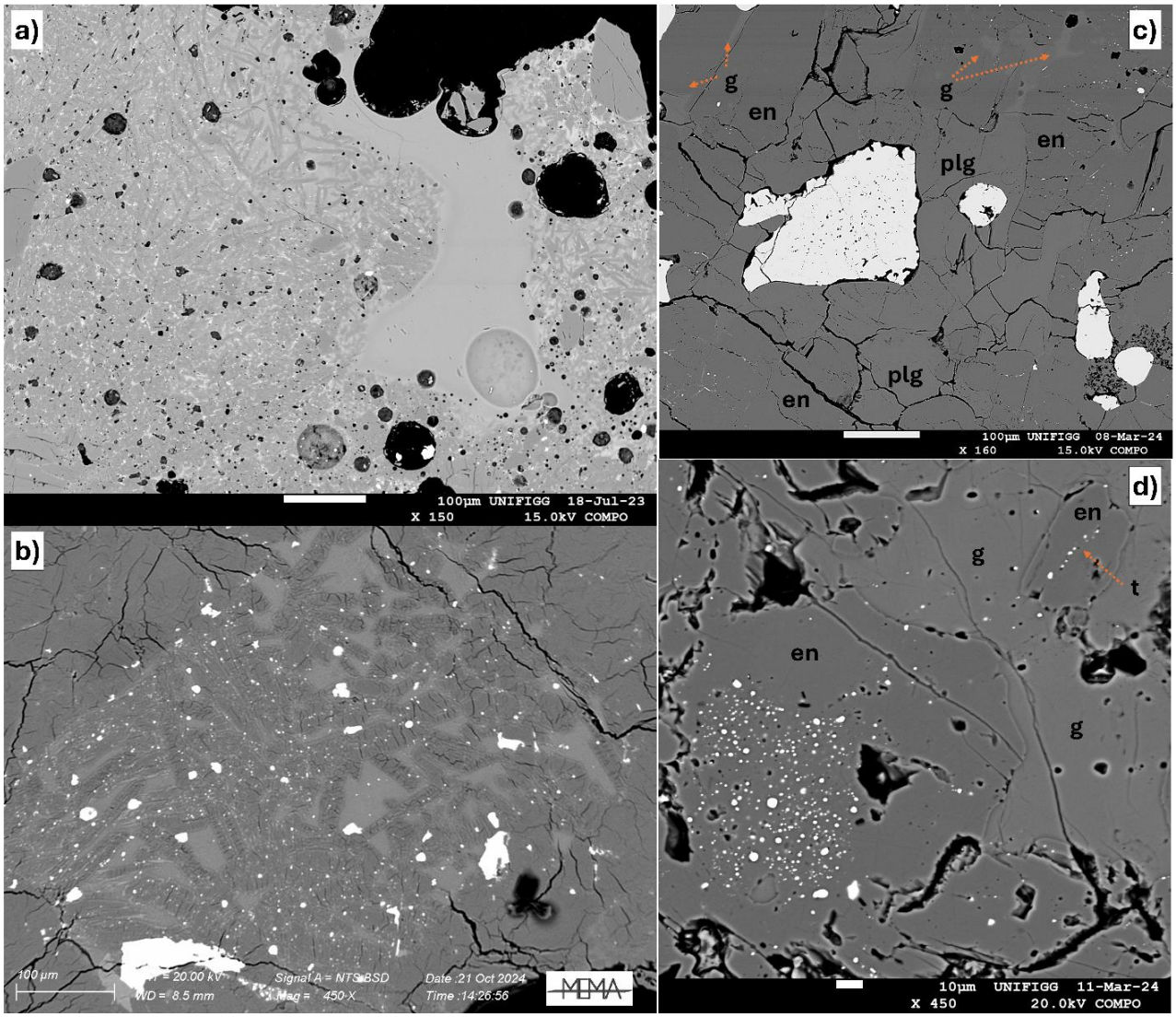


Figure 3.6. Evidences of melting in the investigated samples: a) melt texture in Norton County; b) melt pocket in Tiglit; c) glass in NWA 13266; d) glass and example of troilite trails in enstatite grains in NWA 13210.

### 3.3.1.4. Terrestrial weathering

Aubrites, enstatite chondrites, and achondrites are in general strongly affected by terrestrial alteration (***Wilbur et al., 2022***). The weathering grade is low in all the meteorites studied in this work, except NWA 13210. Sporadic oxides/hydroxides, mostly iron-, can be observed on the surface of some of the samples under investigation, even on the falls Rantila and Norton County. Metal and sulphides are usually the first phases to be altered, and in the case of these fragments, the weathering is sporadically present but not pervasive on these phases. Silicates are affected by the presence of iron oxides/hydroxides in veins. Still, other forms of weathering, such as the formation of clay minerals, are not observed. In the most weathered portion of the fragment of NWA 13210, enstatite presents higher FeO and CaO contents, and oxides are detected.

### 3.3.2. Mineral chemistry

In aubrites, the chemical composition of silicates is similar in terms of major elements, while minor elements show some variability among the different samples (**Table 3.2**). For example, FeO concentration falls below EPMA detection limit, on average, for Norton County, Tiglit, and NWA 14185, while in Rantila it is at least an order of magnitude higher (~0.2 wt%) (**Table 3.2**). It is to be noted that enstatite crystals in Tiglit melt pockets present higher FeO content (up to 0.8 wt%). Enstatite average composition is $En_{98.8}Wo_{0.7}Fs_{0.5}$ in Rantila, $En_{99.6}Wo_{0.3}Fs_{0.1}$ in Norton County, $En_{99.0}Wo_{0.9}Fs_{0.1}$ in Tiglit, and NWA 14185. Forsterite average composition is $Fo_{99.7}$ in Rantila and $Fo_{99.9}$ in Norton County and Tiglit. Diopside average composition is $En_{56.2}Wo_{43.6}Fs_{0.2}$ in Rantila, $En_{55.2}Wo_{44.6}Fs_{0.2}$ in Norton County, $En_{56.0}Wo_{43.9}Fs_{0.1}$ in Tiglit, and $En_{53.7}Wo_{46.2}Fs_{0.1}$ in NWA 14185. Plagioclase presents a wide range of chemical compositions in Rantila ($Ab_{79.5\text{-}95.6}Or_{1.5\text{-}10.0}An_{0.2\text{-}18.6}$) and Norton County ($Ab_{69.3\text{-}95.2}Or_{0.7\text{-}4.1}An_{0.7\text{-}30.0}$), while in Tiglit it is mostly albitic and less variable ($Ab_{89.6\text{-}95.8}Or_{3.8\text{-}4.9}An_{0.1\text{-}6.2}$) (**Table 3.2**).

| | ***Enstatite*** | | | | ***Diopside*** | | | |
|---|---|---|---|---|---|---|---|---|
| | ***Rantila*** | ***Norton County*** | ***Tiglit*** | ***NWA 14185*** | ***Rantila*** | ***Norton County*** | ***Tiglit*** | ***NWA 14185*** |
| *n* | *40* | *26* | *30* | *30* | *18* | *15* | *14* | *10* |
| $SiO_2$ | 59.68 (0.22) | 59.65 (0.27) | 59.45 (0.62) | 59.65 (0.27) | 55.52 (0.14) | 55.82 (0.16) | 54.98 (0.40) | 55.50 (0.43) |
| $TiO_2$ | 0.06 (0.03) | 0.04 (0.01) | 0.03 (0.01) | b.d. | 0.29 (0.01) | 0.22 (0.01) | 0.35 (0.23) | 0.30 (0.09) |
| $Al_2O_3$ | 0.09 (0.02) | 0.11 (0.02) | 0.10 (0.10) | 0.09 (0.03) | 0.20 (0.01) | 0.45 (0.04) | 0.40 (0.16) | 0.43 (0.12) |
| $Cr_2O_3$ | 0.06 (0.02) | b.d. | b.d. | 0.03 (0.01) | 0.04 (0.01) | b.d. | b.d. | b.d. |
| FeO | 0.23 (0.04) | b.d. | b.d. | b.d. | 0.13 (0.08) | b.d. | 0.04 (0.03) | b.d. |
| MnO | 0.20 (0.11) | b.d. | 0.06 (0.04) | 0.08 (0.04) | 0.23 (0.03) | b.d. | 0.04 (0.03) | b.d. |
| NiO | b.d. | b.d. | b.d. | b.d. | b.d. | b.d. | b.d. | b.d. |
| MgO | 39.20 (0.47) | 38.72 (0.32) | 39.92 (0.54) | 37.83 (0.13) | 20.20 (0.10) | 19.95 (0.23) | 20.17 (0.57) | 18.87 (0.53) |
| CaO | 0.47 (0.12) | 0.48 (0.17) | 0.48 (0.16) | 0.45 (0.10) | 22.60 (0.25) | 22.43 (0.28) | 22.02 (0.46) | 22.59 (0.87) |
| $Na_2O$ | b.d. | b.d. | b.d. | b.d. | 0.19 (0.01) | 0.21 (0.03) | 0.26 (0.11) | 0.32 (0.05) |
| $K_2O$ | b.d. | b.d. | b.d. | b.d. | b.d. | b.d. | b.d. | b.d. |
| Total | 100.01 (0.47) | 100.01 (0.47) | 100.14 (0.81) | 98.19 (0.14) | 99.40 (0.64) | 99.17 (0.36) | 98.29 (0.42) | 98.06 (0.53) |
| En | 98.8 | 99.6 | 99.0 | 99.0 | 56.2 | 55.2 | 56.0 | 53.7 |
| Wo | 0.7 | 0.3 | 0.9 | 0.9 | 43.6 | 44.6 | 43.9 | 46.2 |
| Fs | 0.5 | 0.1 | 0.1 | 0.1 | 0.2 | 0.2 | 0.1 | 0.1 |

(…) = standard deviations
b.d.= below detection limit

Table 3.2. Silicates average chemical compositions (wt%) of aubrites. Rantila chemical composition from **Landi et al. (2025)**.

| | *Forsterite* | | | *Plagioclase* | | |
|---|---|---|---|---|---|---|
| | ***Rantila*** | ***Norton County*** | ***Tiglit*** | ***Rantila*** | ***Norton County*** | ***Tiglit*** |
| *N* | *65* | *17* | *6* | *15* | *5* | *5* |
| $SiO_2$ | 42.98 (0.14) | 42.41 (0.45) | 41.96 (0.32) | 66.39 (2.16) | 63.07 (3.05) | 67.21 (0.62) |
| $TiO_2$ | 0.03 (0.01) | 0.03 (0.01) | 0.03 (0.01) | 0.05 (0.02) | b.d. | b.d. |
| $Al_2O_3$ | b.d. | b.d. | b.d. | 20.27 (1.53) | 22.39 (2.09) | 19.30 (0.55) |
| $Cr_2O_3$ | b.d. | b.d. | b.d. | n.a. | n.a. | n.a. |
| FeO | 0.28 (0.07) | b.d. | 0.26 (0.05) | b.d. | 0.09 (0.02) | b.d |
| MnO | 0.26 (0.01) | b.d. | b.d. | b.d. | b.d. | b.d. |
| NiO | b.d. | b.d. | b.d. | b.d. | b.d. | b.d. |
| MgO | 56.19 (0.13) | 58.09 (0.35) | 57.62 (0.79) | b.d. | b.d. | b.d. |
| CaO | 0.04 (<0.01) | 0.09 (0.06) | 0.09 (0.04) | 1.47 (1.37) | 4.11 (2.45) | 0.39 (0.49) |
| $Na_2O$ | n.a. | n.a. | n.a. | 10.40 (0.75) | 9.03 (1.22) | 10.25 (0.33) |
| $K_2O$ | n.a. | n.a. | n.a. | 0.59 (0.24) | 0.31 (0.24) | 0.72 (0.08) |
| Total | 99.79 (0.21) | 100.60 (0.33) | 99.99 (0.66) | 99.03 (0.68) | 99.05 (0.65) | 97.94 (0.70) |
| Fo | 99.7 | 99.9 | 99.9 | - | - | - |
| Ab | - | - | - | 79.5-95.6 | 69.3-95.2 | 89.6-95.8 |
| An | - | - | - | 0.2-18.6 | 0.7-30.0 | 0.1-1.7 |
| Or | - | - | - | 1.5-10.0 | 0.7-4.7 | 3.8-4.9 |

(…) = standard deviations
b.d.= below detection limit
n.a.= not analyzed

Table 3.2. continue.

Silicates chemical composition in enstatite chondrites and achondrites is similar among the samples for major elements, while some differences can be observed for minor elements (**Table 3.3**): in this case, the most variable minor elements are Ca in pyroxene and Fe in plagioclase. Enstatite average composition is $En_{96.9}Wo_{3.0}Fs_{0.1}$ in Itqiy, $En_{98.3}Wo_{1.4}Fs_{0.3}$ in NWA 4945, $En_{99.0}Wo_{0.9}Fs_{0.1}$ in NWA 13266, $En_{98.4}Wo_{1.5}Fs_{0.1}$ in NWA 13210. Diopside composition in NWA 4945 is $En_{53.7}Wo_{46.2}Fs_{0.1}$. Plagioclase composition is homogeneous within the sample: $Ab_{81.9}Or_{4.9}An_{13.2}$ in NWA 4945, $Ab_{82.3}Or_{2.5}An_{15.2}$ in NWA 13266, $Ab_{79.7}Or_{4.2}An_{16.1}$in NWA 13210.

| | *Enstatite* | | | | *Diopside* | *Plagioclase* | | | *Silica* |
|---|---|---|---|---|---|---|---|---|---|
| | ***Itqiy*** | ***NWA 4945*** | ***NWA 13266*** | ***NWA 13210*** | ***NWA 4945*** | ***NWA 4945*** | ***NWA 13266*** | ***NWA 13210*** | ***NWA 13210*** |
| *n* | *45* | *32* | *31* | *35* | *5* | *12* | *13* | *20* | *16* |
| $SiO_2$ | 58.85 (0.27) | 59.36 (0.39) | 59.70 (0.28) | 59.43 (0.28) | 55.46 (0.15) | 66.21 (0.74) | 65.01 (0.74) | 64.54 (0.37) | 95.43 (0.46) |
| $TiO_2$ | 0.06 (0.02) | b.d. | b.d. | b.d. | b.d. | b.d. | b.d. | b.d. | b.d. |
| $Al_2O_3$ | 0.60 (0.03) | 0.21 (0.05) | 0.10 (0.02) | 0.21 (0.02) | 0.44 (0.03) | 20.90 (0.19) | 20.79 (0.67) | 20.32 (0.29) | 2.58 (0.16) |
| $Cr_2O_3$ | b.d. | b.d. | b.d. | b.d. | b.d. | n.a. | n.a. | n.a. | n.a. |
| FeO | b.d. | 0.24 (0.14) | 0.06 (0.02) | 0.06 (0.03) | 0.11 (0.03) | 0.33 (0.17) | b.d. | b.d. | 0.18 (0.16) |
| MnO | 0.05 (0.01) | b.d. | b.d. | 0.08 (0.04) | b.d. | b.d. | b.d. | b.d. | b.d. |
| NiO | b.d. | b.d. | b.d. | b.d. | b.d. | n.a. | n.a. | n.a. | n.a. |
| MgO | 38.04 (0.35) | 39.91 (0.22) | 38.47 (0.54) | 38.07 (0.31) | 19.73 (0.15) | 0.03 (0.01) | b.d. | b.d. | b.d. |
| CaO | 1.65 (0.04) | 0.78 (0.06) | 0.14 (0.02) | 0.79 (0.04) | 23.61 (0.35) | 2.59 (0.53) | 3.10 (0.53) | 3.30 (0.10) | b.d. |
| $Na_2O$ | b.d. | b.d. | b.d. | b.d. | 0.17 (0.03) | 8.87 (0.18) | 9.27 (0.28) | 9.01 (0.12) | 1.37 (0.35) |
| $K_2O$ | b.d. | b.d. | b.d. | b.d. | b.d. | 0.81 (0.07) | 0.42 (0.07) | 0.72 (0.08) | b.d. |
| Total | 99.39 (0.49) | 100.56 (0.45) | 98.53 (0.34) | 98.60 (0.30) | 99.55 (0.34) | 99.77 (0.56) | 98.83 (0.26) | 98.01 (0.51) | 99.70 |
| En | 96.9 | 98.3 | 99.0 | 98.4 | 53.7 | - | - | - | - |
| Wo | 3.0 | 1.4 | 0.9 | 1.5 | 46.2 | - | - | - | - |
| Fs | 0.1 | 0.3 | 0.1 | 0.1 | 0.1 | - | - | - | - |
| Ab | - | - | - | - | - | 81.9 | 82.3 | 79.7 | - |
| An | - | - | - | - | - | 13.2 | 15.2 | 16.1 | - |
| Or | - | - | - | - | - | 4.9 | 2.5 | 4.2 | - |

(…) = standard deviations
b.d.= below detection limit
n.a.= not analyzed

Table 3.3. Silicates average chemical compositions (wt%) of enstatite chondrites and achondrites.

Metals composition is reported in **Table 3.4**. Ni concentrations are, on average, higher in enstatite chondrites and achondrites than in aubrites. Si contents in metals are under EPMA detection limits or in little amounts (0.1-0.2 wt%) in aubrites, around 0.4 wt% in the enstatite achondrite NWA 13266, and one order of magnitude higher, around 2-3 wt%, in enstatite chondrites.

| | ***Kamacite*** | | | | | | ***Schreibersite*** |
|---|---|---|---|---|---|---|---|
| | ***Rantila*** | ***Norton County*** | ***Tiglit*** | ***Itqiy*** | ***NWA 4945*** | ***NWA 13266*** | ***Tiglit*** |
| *n* | *10* | *1* | *3* | *21* | *26* | *25* | *1* |
| Si | b.d. | 0.22 | 0.14 (0.17) | 2.73 (0.36) | 2.48 (0.06) | 0.39 (0.02) | 0.03 |
| Fe | 92.43 (0.33) | 96.18 | 92.98 (1.41) | 89.45 (0.53) | 87.62 (0.27) | 88.48 (0.83) | 61.07 |
| Cr | b.d. | b.d. | 0.29 (0.48) | 0.25 (0.03) | 0.04 (0.01) | 0.05 (0.06) | 0.02 |
| Co | 0.37 (0.02) | 0.23 | 0.30 (0.17) | 0.46 (0.02) | 0.42 (0.02) | 0.45 (0.01) | 0.23 |
| P | b.d. | 0.05 | 0.04 (0.05) | 0.17 (0.02) | 0.27 (0.08) | 0.49 (0.03) | 13.15 |
| Cu | b.d. | 0.03 | 0.04 (0.03) | b.d. | 0.02 (0.02) | 0.03 (0.02) | 0.01 |
| Ni | 5.65 (0.19) | 2.57 | 3.29 (2.85) | 5.58 (0.10) | 6.33 (0.17) | 7.07 (0.15) | 23.45 |
| Mn | b.d. | b.d. | 0.25 (0.41) | b.d. | b.d. | b.d. | 0.03 |
| Total | 98.50 (0.33) | 99.30 | 97.32 (1.02) | 98.66 (0.48) | 97.14 (0.23) | 96.98 (0.74) | 98.00 |

(…) = standard deviations
b.d.= below detection limit

Table 3.4. Metals and phosphides compositions (wt%) of the investigated samples. Rantila chemical composition from **Landi et al. (2025)**.

Various sulphides are present with a wide range of chemical compositions (**Table 3.5**). Troilite most variable minor elements among the different samples are Cr and Ti: Cr amounts range from 0.4 to 4.1 wt% in aubrites and from 2.7 to 5.1 wt% in enstatite chondrites and achondrites; Ti amounts range from below detection limit to 3 wt% for aubrites and from 0.4 to 2.2. wt% for enstatite chondrites and achondrites. Fe, Mn, Mg, Ca sulphides present a wide range of chemical compositions: Mg-rich sulphides (Mg up to 15 wt%) are present only in the enstatite achondrite NWA 13266; Fe-dominant sulphides (Fe up to 37 wt%) are observed in enstatite chondrites and achondrites but not in aubrite; Mn-rich sulphides show Mn up to 49 wt% in aubrites and up to 23 wt% in enstatite chondrites and achondrites; Ca-rich sulphides are observed in all meteorite groups. Daubreélite composition does not vary among the different meteorites.

| | *Troilite* | | | | | | | |
|---|---|---|---|---|---|---|---|---|
| | ***Rantila*** | ***Norton County*** | ***Tiglit*** | ***NWA 14185*** | ***Itqiy*** | ***NWA 4945*** | ***NWA 13266*** | ***NWA 13266*** |
| *n* | 15 | *4* | *14* | *11* | 1 | *24* | *18* | *8* |
| Si | b.d. | b.d. | b.d. | b.d. | b.d. | b.d. | b.d. | b.d. |
| Fe | 62.27 (0.57) | 52.82 (2.14) | 59.30 (1.27) | 57.70 (0.73) | 56.15 | 57.20 (0.32) | 55.41 (0.44) | 53.30 (0.28) |
| Co | 0.05 (0.01) | 0.05 (0.01) | b.d. | b.d. | 0.06 | b.d. | b.d. | b.d. |
| Cr | 0.47 (0.10) | 4.05 (0.86) | 1.15 (0.70) | 0.42 (0.15) | 4.77 | 2.69 (0.15) | 4.84 (0.21) | 5.05 (0.04) |
| Zn | b.d. | b.d. | b.d. | b.d. | b.d. | b.d. | b.d. | b.d. |
| S | 35.69 (0.22) | 37.07 (0.87) | 34.47 (1.04) | 36.93 (0.42) | 37.22 | 34.43 (0.23) | 37.02 (0.25) | 37.44 (0.24) |
| Ti | 0.07 (0.02) | 2.81 (0.35) | b.d. | 2.98 (0.28) | 0.41 | 0.47(0.02) | 0.66 (0.09) | 2.22 (0.03) |
| Ca | b.d. | b.d. | b.d. | b.d. | b.d. | b.d. | b.d. | b.d. |
| Cu | 0.05 (0.03) | 0.09 (0.03) | 0.05 (0.04) | b.d. | 0.07 | 0.05 (0.02) | 0.06 (0.03) | b.d. |
| Ni | b.d. | 0.46 (0.19) | b.d. | b.d. | 0.21 | 0.15 (0.04) | 0.09 (0.03) | 0.20 (0.03) |
| Mn | b.d. | 0.64 (0.64) | b.d. | b.d. | 0.50 | 0.83 (0.09) | 0.08 (0.02) | 0.16 (0.03) |
| V | b.d. | 0.06 (0.03) | 0.06 (0.04) | 0.14 (0.03) | 0.10 | 0.06 (0.02) | 0.08 (0.02) | 0.21 (0.04) |
| Na | b.d. | b.d. | b.d. | b.d. | b.d. | b.d. | b.d. | b.d. |
| Mg | b.d. | b.d. | b.d. | b.d. | 0.03 | 0.03 (0.01) | b.d. | b.d. |
| Total | 98.80 (0.59) | 98.19 (0.74) | 96.25 (0.62) | 98.33 (0.67) | 99.53 | 95.93 (0.41) | 98.31 (0.45) | 98.66 (0.53) |

(…) = standard deviations
b.d.= below detection limit

Table 3.5. Sulphides compositions (wt%) of the investigated samples.

| | ***(Mn, Ca, Fe, Mg)S*** | | | | | |
|---|---|---|---|---|---|---|
| | ***Ca-rich*** | | | | | ***Mg-rich*** |
| | ***Norton County*** | ***Tiglit*** | ***Itqiy*** | ***NWA 4945*** | ***NWA 13266*** | ***NWA13266*** |
| *n* | *2* | *3* | *1* | *1* | *6* | *30* |
| Si | b.d. | 0.07 (0.03) | b.d. | 0.08 | 0.08 (0.04) | b.d. |
| Fe | 0.04 (0.02) | 0.15 (0.05) | 7.61 | 1.43 | 2.27 (1.30) | 27.19 (0.79) |
| Co | b.d. | b.d. | b.d. | b.d. | 0.10 (0.05) | b.d. |
| Cr | b.d. | b.d. | 2.44 | 0.04 | 0.14 (0.07) | 2.08 (0.12) |
| Zn | b.d. | 0.04 (0.02) | b.d. | 0.04 | 0.03 (<0.01) | 0.13 (0.03) |
| S | 40.09 (0.04) | 42.45 (0.93) | 40.45 | 40.81 | 42.79 (0.54) | 44.80 (0.45) |
| Ti | b.d. | b.d. | 0.12 | 0.01 | 0.04 (0.01) | 0.09 (0.02) |
| Ca | 58.40 (0.48) | 52.10 (1.19) | 39.81 | 47.62 | 51.61 (2.18) | 2.90 (0.22) |
| Cu | b.d. | b.d. | b.d. | 0.04 | b.d. | b.d. |
| Ni | b.d. | b.d. | 0.03 | 0.03 | b.d. | b.d. |
| Mn | 1.22 (0.04) | 0.88 (0.35) | 8.53 | 1.42 | 0.50 (0.07) | 4.66 (0.15) |
| V | b.d. | b.d. | b.d. | 0.03 | b.d. | 0.03 (0.02) |
| Na | 0.04 (<0.01) | 0.06 (0.02) | 0.12 | 0.17 | 0.17 (0.06) | 0.50 (0.05) |
| Mg | 0.11 (<0.01) | 0.17 (0.11) | 2.25 | 0.96 | 2.19 (0.29) | 15.37 (0.62) |
| Total | 99.97 (0.47) | 95.97 (1.61) | 101.37 | 92.68 | 99.88 (1.02) | 97.84 (0.41) |

(…) = standard deviations
b.d.= below detection limit

Table 3.5. continue.

| | *(Mn, Ca, Fe, Mg)S* | | | | | |
|---|---|---|---|---|---|---|
| | ***Mn-rich*** | | | | ***Fe-rich*** | |
| | ***Rantila*** | ***Tiglit*** | ***Norton County*** | ***Itqiy*** | ***NWA 4945*** | ***NWA13266*** |
| *n* | *4* | *9* | *1* | *8* | *5* | *2* |
| Si | b.d. | b.d. | b.d. | b.d. | b.d. | b.d. |
| Fe | 11.40 (3.08) | 15.17 (2.44) | 12.85 | 20.41 (1.13) | 27.27 (1.31) | 36.67 (0.65) |
| Co | b.d. | b.d. | b.d. | b.d. | b.d. | b.d. |
| Cr | 0.10 (0.08) | 0.19 (0.09) | 0.35 | 4.37 (0.47) | 0.88 (0.08) | 2.83 (0.06) |
| Zn | b.d. | b.d. | b.d. | b.d. | 0.10 (0.03) | 0.08 (0.03) |
| S | 36.51 (0.52) | 35.35 (0.44) | 37.95 | 41.24 (0.48) | 37.61 (0.45) | 41.72 (0.72) |
| Ti | b.d. | b.d. | 0.07 | 0.20 (0.08) | 0.04 (0.01) | 0.14 (0.03) |
| Ca | 0.13 (0.11) | 0.13 (0.04) | 10.51 | 3.61 (0.68) | 1.27 (0.44) | 2.86 (0.12) |
| Cu | 0.05 (0.04) | 0.04 (0.03) | 0.03 | b.d. | 0.03 (<0.01) | 0.06 (0.02) |
| Ni | b.d. | b.d. | b.d. | b.d. | 0.04 (0.07) | b.d. |
| Mn | 48.69 (3.48) | 42.25 (2.72) | 36.87 | 23.37 (1.29) | 20.86 (1.82) | 2.79 (0.08) |
| V | b.d. | b.d. | b.d. | 0.06 (0.03) | b.d. | 0.04 (0.02) |
| Na | b.d. | 0.07 (0.03) | 0.08 | 0.38 (0.15) | 0.18 (0.03) | 0.31 (0.04) |
| Mg | 0.33 (0.12) | 0.49 (0.44) | 1.68 | 6.56 (0.31) | 6.60 (0.31) | 10.02 (0.51) |
| Total | 97.34 (0.99) | 93.73 (0.58) | 100.41 | 100.38 (0.63) | 94.91 (0.59) | 97.52 (0.66) |

(…) = standard deviations
b.d.= below detection limit

Table 3.5. continue.

| | ***Daubreélite*** | | | | ***Heideite*** |
|---|---|---|---|---|---|
| | ***Rantila*** | ***Tiglit*** | ***NWA 14185*** | ***NWA 13210*** | ***Rantila*** |
| *N* | *4* | *6* | *10* | *10* | *1* |
| Si | b.d. | b.d. | b.d. | b.d. | 0.19 |
| Fe | 18.07 (0.25) | 17.29 (0.18) | 16.75 (0.28) | 17.16 (0.21) | 26.06 |
| Co | b.d. | b.d. | b.d. | b.d. | 0.03 |
| Cr | 34.04 (0.74) | 32.73 (0.29) | 34.65 (0.15) | 33.84 (0.44) | 1.32 |
| Zn | b.d. | b.d. | 0.29 (0.03) | b.d. | b.d. |
| S | 43.62 (0.22) | 42.39 (0.40) | 44.71 (0.42) | 44.26 (0.73) | 41.04 |
| Ti | 0.05 (0.02) | 0.06 (0.05) | 0.07 (0.01) | 0.09 (0.04) | 26.35 |
| Ca | b.d. | b.d. | b.d. | 0.10 (0.08) | 0.06 |
| Cu | 0.10 (0.09) | 0.14 (0.08) | 0.05 (0.02) | 0.18 (0.07) | 0.13 |
| Ni | b.d. | b.d. | 0.04 (0.03) | b.d. | 0.06 |
| Mn | 1.10 (0.16) | 1.08 (0.14) | 1.42 (0.27) | 1.30 (0.06) | b.d. |
| V | b.d. | b.d. | b.d. | b.d. | 0.16 |
| Na | b.d. | b.d. | b.d. | b.d. | b.d. |
| Mg | b.d. | b.d. | b.d. | b.d. | 0.09 |
| Total | 97.04 (0.78) | 93.82 (0.77) | 97.99 (0.53) | 97.00 (0.86) | 95.49 |

(…) = standard deviations
b.d.= below detection limit

Table 3.5. continue.

Glass composition is different among the various samples for both major and minor elements (**Table 3.6**). $SiO_2$ contents vary between 64 wt% and 79 wt%, $Al_2O_3$ 10-20 wt%, $Na_2O$ 5-9 wt%. CaO is a major element in Tiglit and NWA 13210, while it is present in minor amounts in Rantila and NWA 13266. Concerning minor elements, in Rantila and NWA 13210 Fe and the other transitional elements are below the detection limits, whereas a very small amount of FeO is detected in NWA 13266 (0.05 wt%) and in Tiglit (0.6 wt%), along with MgO (0.5 and 6.5 wt%, respectively), and $Cr_2O_3$ (0.08 wt%) and MnO (0.3 wt%) in Tiglit. High values of dissolved S are observed in Tiglit (0.6 wt%), in NWA 13266 (1.4 wt%), and in Rantila (0.4 wt%, ***Landi et al., 2025***).

| | *Glass* | | | |
|---|---|---|---|---|
| | ***Rantila*** | ***Tiglit*** | ***NWA 13266*** | ***NWA 13210*** |
| *n* | *2* | *5* | *15* | *20* |
| $SiO_2$ | 73.83 (1.07) | 70.20 (1.42) | 78.64 (0.71) | 64.53 (0.36) |
| $TiO_2$ | 0.04 (0.02) | 0.23 (0.02) | b.d. | b.d. |
| $Al_2O_3$ | 15.34 (0.48) | 9.89 (1.53) | 12.55 (0.29) | 20.30 (0.20) |
| FeO | b.d. | 0.60 (0.16) | 0.05 (0.02) | b.d. |
| $Cr_2O_3$ | b.d. | 0.08 (0.01) | b.d. | b.d. |
| $V_2O_3$ | b.d. | b.d. | b.d. | b.d. |
| CoO | b.d. | b.d. | b.d. | b.d. |
| NiO | b.d. | b.d. | b.d. | b.d. |
| CuO | b.d. | b.d. | b.d. | b.d. |
| ZnO | b.d. | b.d. | b.d. | b.d. |
| MnO | b.d. | 0.31 (0.08) | b.d. | b.d. |
| MgO | b.d. | 6.48 (1.70) | 0.49 (0.11) | b.d. |
| CaO | 0.08 (0.08) | 7.03 (1.15) | 0.11 (0.02) | 3.33 (0.07) |
| $Na_2O$ | 9.00 (0.51) | 4.87 (0.66) | 5.58 (0.20) | 9.01 (0.12) |
| $K_2O$ | 0.53 (0.16) | 0.92 (0.13) | 2.09 (0.04) | 0.71 (0.08) |
| $P_2O_5$ | b.d. | b.d. | b.d. | b.d. |
| $SO_3$ | b.d. | 0.62 (0.10) | 1.38 (0.08) | b.d. |
| Total | 98.91 (0.23) | 101.28 (0.33) | 100.99 (0.87) | 98.01 (0.46) |

(…) = standard deviations
b.d.= below detection limit

Table 3.6. Glass compositions (wt%) of the investigated samples. Rantila chemical composition from **Landi et al. (2025)**.

### 3.3.3. VNIR reflectance spectra

VNIR reflectance spectra of the investigated meteorites are shown in **Figure 3.9**.

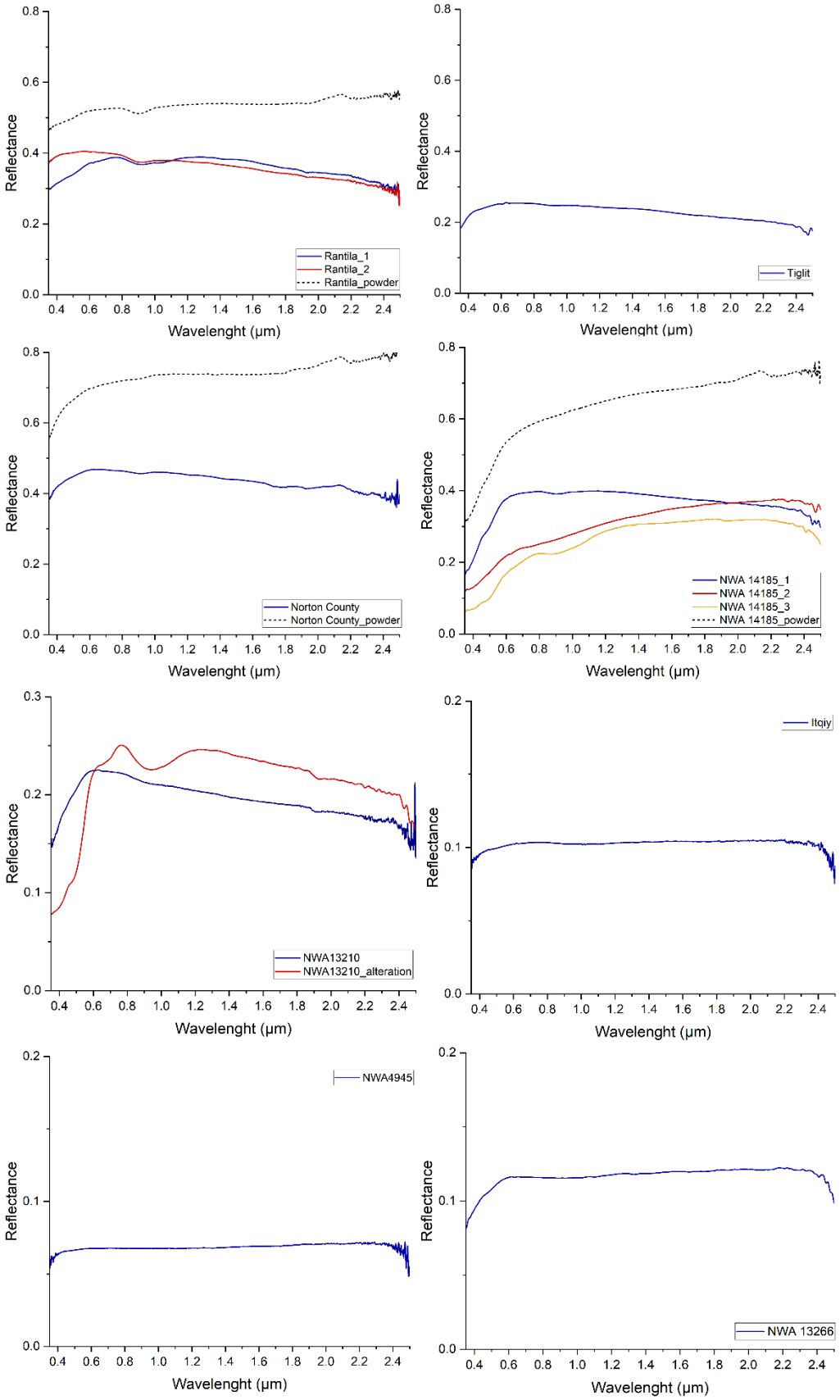


Figure 3.9. VNIR reflectance spectra of the investigated meteorites. The reported final spectra are the average of several point analysis taken in different areas of the sample surface: one point analysis for Rantila_1, Rantila_2, NWA 14185_3, NWA 13210_alteration; two point analysis for NWA 14185_2, Norton County; three point analysis for Tiglit, Rantila_powder, Norton County_powder, NWA 14185_1, NWA 14185_powder, NWA 13210; seven point analysis for Itqiy, NWA 13266; nine point analysis for NWA 4945.

Aubrites reflectance intensity and spectral features vary among the different meteorites, and, in the case of Rantila and NWA 14185, among different areas of the same fragment. The spectra show blue slopes in the IR region, as expected for measurements on slabs and rock fragments (e.g., ***Carli & Sgavetti, 2011; Cloutis et al., 2013; Pompilio et al., 2007***). The spectra acquired on powders (<100 µm grain size) show a higher reflectance intensity, of ca 25%, compared to the spectra acquired on the rocks, and a red slope. Enstatite chondrites and achondrites have lower reflectance intensity than aubrites, around 0.1 on average, for Itqiy and NWA 13266, below 0.1 for NWA 4945, and around 0.2 for NWA 13210, while aubrites maxima for rock spectra are around 0.4. Itqiy spectrum is substantially flat, NWA 4945 and NWA 13266 exhibit a slightly red slope, and NWA 13210 spectra exhibit a blue slope.

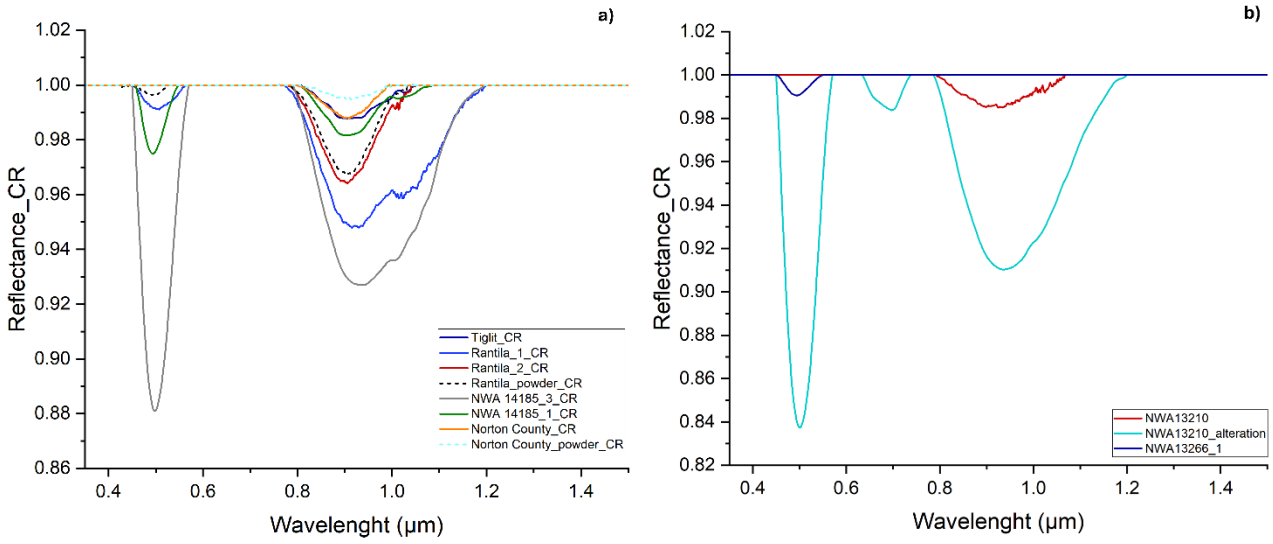


Figure 3.10. Reflectance spectra continuum removed. a) aubrites. b) enstatite achondrite and melt rock.

Absorption bands position (band center) and intensity (band depth) of the investigated samples are reported in **Table 3.10**. Enstatite chondrites and achondrites spectra tend to be featureless, with only minor absorption features around 0.9 µm and 1.9 µm for NWA 13210 (**Fig. 3.9** and **Fig. 3.10**). The 0.9 µm centered band is linked to enstatite (e.g., ***Burns, 1993***). The weak and narrow feature around 1.9 µm is attributable to a combination of H-O-H and O-H overtone on iron hydroxides originated from terrestrial contamination (e.g., ***Burbine et al., 2002, Cantillo et al., 2024; Gaffey et al., 1993***). Terrestrial contamination features are well visible in the NWA 13210_alteration spectrum, related to the most weathered portion of the sample, showing stronger absorption features centred at 0.501 µm, 0.697 µm and 0.938 µm (**Fig. 3.9** and **Fig. 3.10**), that could be attributed to charge transfer associated with $Fe^{3+}/Fe^{2+}$ in iron hydroxides, most likely goethite (***Burns, 1993; Crowley et al., 2003; Sherman et al., 1982***).

Aubrites spectra exhibit more defined absorption bands at 0.9 μm, except for Tiglit, NWA 14185_2, and NWA 14185_powder spectra, which are featureless. Rantila and NWA 14185 also exhibit a mild absorption feature at 0.5 μm, associated with spin-forbidden $Fe^{2+}$ absorption in olivine (e.g., ***Burns, 1993, Carli et al., 2018***). Minor absorption features at 1.9 μm, related to terrestrial weathering, are observed in Rantila, Norton County, and NWA 14185_3 spectra. The absorption band around 0.9-1 μm (band I) is attributable to olivine and/or pyroxenes. For pyroxenes, it could be associated with a broader absorption around 2 μm (e.g., ***Burns, 1993***), nevertheless, here the iron amount is closer to the detection limit (***Cloutis et al., 2016***). A very weak band II is visible in Rantila_1 and Norton County, but it is strongly affected by features linked to terrestrial alteration products.

The observed band I positions, ranging between 0.901 and 0.908 μm, and shapes are attributed to low Fe-Ca pyroxene (***Cloutis & Gaffey, 1991; Klima et al., 2008***). Band I shape and center at 0.926 μm for Rantila_1 could indicate the presence of forsterite and/or high-Ca pyroxene in larger amounts in that area of the sample. In this case, forsterite seems to be the cause for I positions and shapes: a weak absorption feature at 0.503 μm is visible, which could be attributed to spin-forbidden $Fe^{2+}$ absorption in olivine (e.g., ***Burns, 1993, Carli et al., 2018***), suggesting considerable amount of forsterite in this area of the sample (***Landi et al., 2025***). NWA 14185 is represented by three different spectra: NWA 14185_1 represents most of the surface, dominated by FeO-poor enstatite; NWA 14185_2 was acquired in a darker spot with many fractures, and, considering the red slope, maybe interested by the presence of metals; NWA 14185_3 spectral shape and absorption features, centered at 0.498 μm and at 0.939 μm, suggest the contribution of hydroxides from minor terrestrial weathering, underlined by the feature at 1.9 μm. The features at 0.49 μm and 1.9 μm are visible, even though much weaker, also in NWA 14185_1 and NWA 14185_powder, while they are not detected in NWA 14185_2, indicating that the incipient terrestrial weathering affected some areas of the sample more than others. The band at ~0.5 μm and ~1.4 μm, specifically at 0.501 μm and 0.938 μm, are also observed in the most weathered portion of sample NWA 13210, along with an additional feature at 0.697 μm, suggesting the contrbution of goethite.

| | *Band center* | *Band depth* | *Band center* | *Band depth* | *Band center* | *Band depth* |
|---|---|---|---|---|---|---|
| Tiglit | - | - | 0.904 | 0.01 | - | - |
| Rantila_1 | 0.503 | 0.01 | 0.926 | 0.05 | - | - |
| Rantila_2 | - | - | 0.901 | 0.03 | - | - |
| Rantila_powder | 0.492 | <0.01 | 0.904 | 0.03 | - | - |
| Norton County | - | - | 0.908 | 0.01 | - | - |
| Norton County_powder | - | - | 0.904 | <0.01 | - | - |
| NWA 14185_1 | 0.494 | 0.02 | 0.903 | 0.02 | - | - |
| NWA 14185_3 | 0.498 | 0.12 | 0.939 | 0.07 | - | - |
| NWA 13210 | - | - | 0.926 | 0.02 | - | - |
| NWA13210_alteration | 0.501 | 0.16 | 0.938 | 0.09 | 0.697 | 0.02 |

Table 3.10. Band center (μm) and band depth of reflectance spectra absorption features of the investigated samples. The error for the band center is ± 5 nm, the resolution at those wavelengths being 10 nm. Band depth error is <0.01.

## 3.4. Discussion

### 3.4.1. Mineral chemistry and origin

Enstatite is the predominant phase in all the investigated meteorite fragments, although with different percentages, from 60 to 97%, depending on the sample and on the selected fragment. Forsterite is present only in aubrites and in very different amounts (from no detection to 17 %). Diopside is a common phase in aubrites (from <1 to 13 wt%), while in enstatite chondrites its presence was evidenced only in EL6 (e.g., ***Fogel, 1997; Floss et al., 2003***). Diopside is not usually contained in equilibrated enstatite chondrites, because the low $fO_2$ values favour the formation of oldhamite, but at determined conditions, e.g., high temperature from metamorphic processes, diopside can be stable as well and coexist with oldhamite (***Fogel, 1997***). Plagioclase content is variable, even among meteorites of the same group, as already observed for aubrites (***Watters & Prinz, 1979***) and enstatite chondrites (***Keil, 1968***). Metals are much more abundant in enstatite chondrites and achondrites than in aubrites, <1 vs 7-11 wt%, respectively. Sulphides are generally a secondary or accessory phase in aubrites, while they are, on average, abundant in enstatite chondrites and achondrites. The modal mineralogy of the enstatite melt rock is different from the enstatite chondrites and achondrites, with metals and sulphides < 1 %. Nonetheless, it should be considered that these low quantities of sulphides and metals may be influenced by terrestrial weathering that could have altered them and favoured the formation of oxides and hydroxides. Moreover, it must be noted that sampling has a strong influence on the phase abundance described for these samples, especially for such heterogeneous meteorites as aubrites. For example, the two investigated Norton County fragments are quite different: the second one exhibits forsterite, plagioclase, and a melt texture, none of which are present in the first fragment. Also, Rantila aubrite presents at least three components: a light-coloured portion, a forsteritic dark clast, and a dark glassy fragment (***Landi***

***et al., 2025***). Enstatite chondrites and achondrites are more homogeneous, so the sampling effect is less significant for these meteorites.

Chemical composition of pyroxene and olivine is nearly FeO-free for all the samples, and there are no major differences between the distinct meteorite groups (**Fig. 3.11**). The albitic component is always predominant in plagioclases. Plagioclase composition is nearly the same for all the enstatite chondrites and achondrites, while aubrites show a wider compositional range (**Fig. 3.11**).

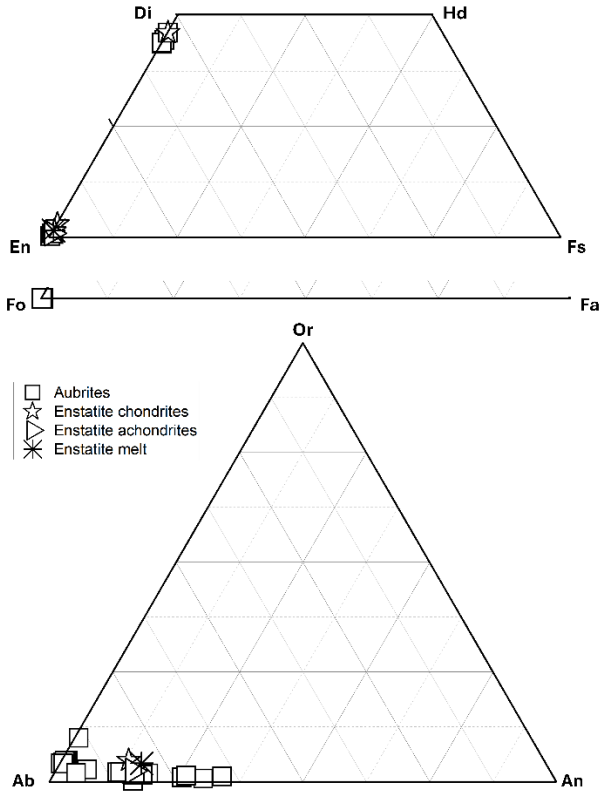


Figure 3.11. Silicates compositions of the investigated samples. From top to bottom: pyroxene, olivine, plagioclase.

Metals and sulphides composition, on the other hand, shows some variability among the different sample groups. Kamacite in the studied aubrites shows Si values <0.5 wt% (**Fig. 3.12**), which is in the range 0.12-2.44 wt% estimated by ***Watters & Prinz (1979)***. In enstatite chondrites, the detected Si values in the metallic phases are higher than in aubrites, between 2 and 3 wt% (**Fig. 3.12**), in agreement with data for EHs (***Keil, 1968; Weyrauch et al., 2018***). Enstatite achondrite NWA 13266, on the other hand, presents Si concentrations in metals more similar to aubrites than enstatite chondrites (**Fig. 3.12**), suggesting similar Si partitioning between silicates and metals during recrystallization.

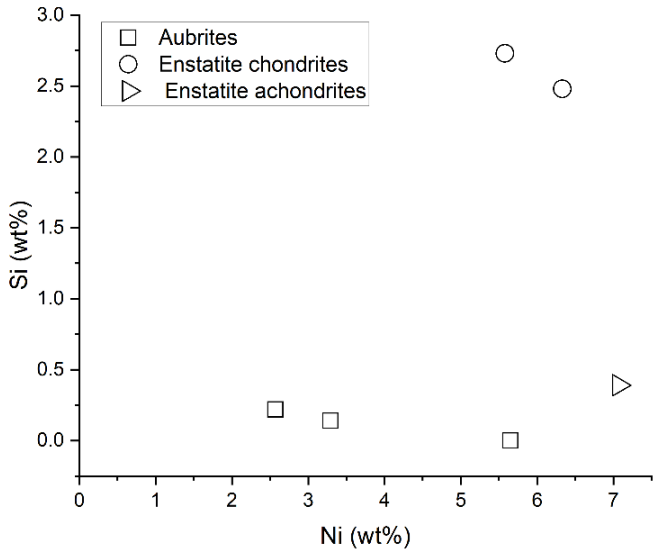


Figure 3.12. Ni and Si contents (wt%) in kamacite.

(Fe, Mg, Mn, Ca, Cr)S are present in all meteorites except the enstatite melt rock NWA 13210. Plotting their composition in the ternary diagram from ***Skinner & Luce (1971)*** (and following ***Keil, 2007***, and ***Udry et al., 2019***), it is possible to observe that they fall in different fields: alabandite field for aubrites and EH, keilite for EL, niningerite and keilite for enstatite achondrite (**Fig. 3.13**). Oldhamite and Ca-rich sulphide occur in all meteorite groups (**Fig. 3.13**). Sulphides composition dominated by Fe and Mn in EL is consistent with data from the literature (e.g., ***Weyrauch et al., 2018***), and ***Udry et al. (2019)*** suggested that the presence of alabandite indicates an EL parent body provenance. EH sulphides should be dominated by Mg and Fe with minor Mn. Nevertheless, high Mn content is observed in Itqiy: this meteorite presents some analogies with EH chondrites (e.g., metal composition) but sulphides compositions are different from those in EL and EH chondrites (***Patzer et al., 2001***), and it has been classified as an anomalous EH. Niningerite (***Keil, 1967***) is detected only in enstatite achondrite NWA 13266, suggesting an EH parent body origin (***Udry et al., 2019***). Fe content in (Fe, Mn, Mg)S is >20 wt% for all the investigated enstatite chondrites and achondrites, meaning that they could be classified in the subgroup "b" proposed by ***Weyrauch et al. (2018)***. Keilite is common in enstatite chondrites that appear to have been impact melted and in impact melt rocks (***Keil, 2007***; ***Rubin, 2015***; ***Weyrauch et al. 2018***), but it has not been detected in melt rock NWA 13210, in which daubréelite is the only detected sulphide. It is to be noted that the detection of these sulphides can be biased by sampling; therefore, it cannot be considered alone as a parameter for parent body origin. Other parameters should be considered, like the presence of daubréelite and troilite composition (***Weyrauch et al. 2018***). Daubréelite is observed in aubrites, but not in the enstatite chondrites and achondrites, again suggesting an affinity with the subgroup "b" (***Weyrauch et al. 2018***). Cr and Ti contents in troilite are variable in

these samples (**Fig. 3.13**). On average, Cr content in troilite is estimated to be 0.80 wt% and Ti content 2.76 wt% (***Keil, 2010; Watters & Prinz, 1979***) in aubrites, while in ELs and EHs Cr is up to 1.5 and 3.7 wt%, respectively, and Ti up to 0.8 and 0.5% respectively (***Keil, 1968***; ***Keil & Bischoff, 2008***). Therefore, for the investigated samples, we will expect, on average, higher Ti contents in aubrites and higher Cr contents in enstatite chondrites. However, some of the selected meteorites show peculiarities: aubrites Rantila and Tiglit show the Cr contents estimated for aubrites, but very low Ti contents, even lower than what expected for enstatite chondrites, on the other hand, Norton County presents the Ti content estimated for aubrites but very high Cr content; EL NWA 4945 and EH Itqiy show high Cr content but still in the range estimated by ***Weyrauch et al. (2018)*** for ELs and EHs of subgroup "b". Enstatite achondrite NWA 13266 troilite composition show similarities with Itqiy. These high Cr contents (>2 wt%), along with Fe >20 wt% in (Fe, Mn, Mg)S, and absence of daubréelite suggest Itqiy, NWA 4945 and NWA 13266 belong to the subgroup "b" (***Weyrauch et al. 2018***). Enstatite melt rock NWA 13210 presents higher Ti content (2.22 wt%) than what expected for enstatite chondrites, similarly to what has been observed for other enstatite impact melt rocks (***Udry et al., 2019***) and anomalous QUE meteorites (***Van Niekerk et al. 2014***).

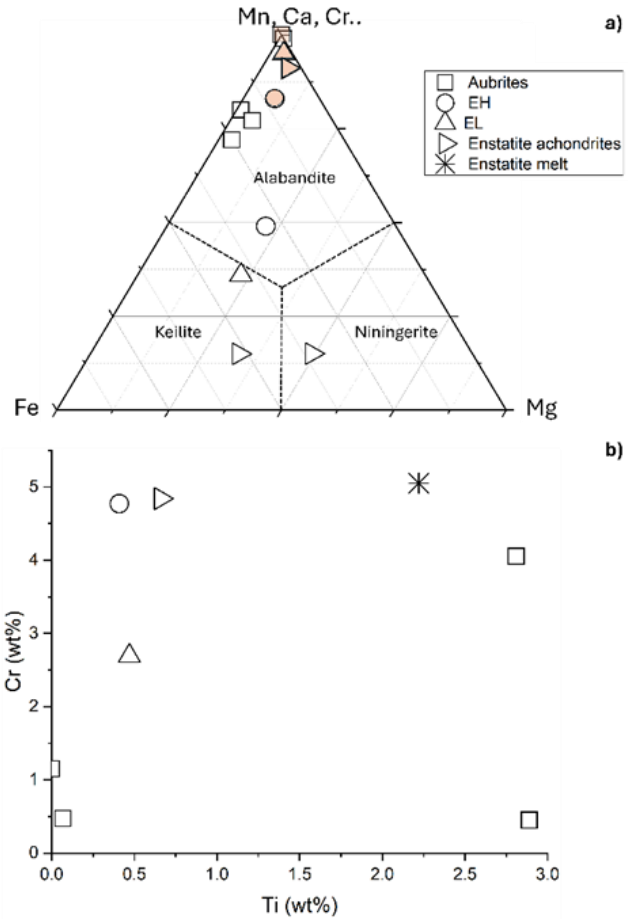


Figure 3.13. Sulphides composition of the investigated samples. a) sulphide ternary diagram (**Skinner & Luce, 1971**). Orange filled symbols represent oldhamite, found in all meteorite groups (except melt rock). b) Cr and Ti contents (wt%) in troilite.

Important textural differences can be observed between aubrites and enstatite chondrites and achondrites. The four aubrites show the typical highly brecciated texture (***Keil, 2010***). They also show coarse-grain sizes, with phenocrystals of centimetric dimensions, and exsolution features (e.g., enstatite lamellae in diopside), suggesting that they have formed at slow cooling rates (***Keil, 1968; Okada et al. 1988; Wilbur et al., 2022***). NWA 4945 texture does not indicate partial melting but high temperature metamorphic processes, as already suggested by diopside presence, and relict chondrules can be observed. Itqiy presents triple junctions between enstatite grains, which are indicative of extensive recrystallization from partial melting, also suggested by the absence of plagioclase and a low amount of sulphides, and subsequent slow cooling (***Patzer et al., 2001***). NWA 13210 presents a strongly recrystallized texture as well, following melting processes, likely from impact, as also suggested by the presence of curvilinear trails of sulphides (mostly troilite) and metal blebs in enstatite grains (***McCoy et al. 1995; Rubin, 2015; Van Niekerk et al. 2014***). They do not follow enstatite cleavage plains, so the hypothesis is that they could have formed by FeS and Fe,Ni shock mobilization and trapping in previous fractures before the melting (***Keil &***

***Bischoff, 2008***). This feature is observed in enstatite achondrite NWA 13266 as well, showing also high amount of silica (5 %) and glass. Enstatite chondrites can contain quartz, tridymite, and cristobalite, but in very small amounts (***Keil, 1968***). Therefore, the high silica percentage found in this meteorite may be a result of impact melting: reduced Si from kamacite may have reacted with FeO from melted enstatite, producing silica and Fe, or it may have been created during crystallization from the melt by enstatite sulfidation (***Rubin, 1983***), along with the production of niningerite (***Rubin, 2015***). Both scenarios are possible for this meteorite, since niningerite is present and kamacite is extremely Si-poor (0.4 wt%). Troilite and metal blebs are also observed in Rantila aubrite. Glass is detected in NWA 13210, NWA 13266, Rantila and Tiglit. On average, these glasses present high dissolved $SO_3$ values and very low FeO amounts, caused by the highly reducing conditions of formation. Also, silicate-rich melt pockets presenting small blebs of sulphides and metals, which are another indicator of impact melt processes (***Rubin, 2015***), are observed in these four meteorites.

The highly brecciated texture of aubrites suggests that their parent bodies were likely affected by collisions (***Keil, 2010***). Moreover, it was observed that aubrites derived from an enstatite chondrite-like parent body, but it cannot be either the EHs or ELs parent bodies, given the mineralogical differences observed between enstatite chondrites and aubrites that cannot be explained with igneous differentiation (***McCoy & Bullock, 2017; Udry et al., 2019; Wilbur et al., 2022***). Moreover, ***Weyrauch et al. (2018)*** proposed an additional division EHs and ELs into two subgroups, "a" and "b", that must have originated from two distinct parent bodies. These two parent bodies may have experienced different thermal histories: subgroups EHa and ELa may have undergone lower temperature processes than subgroups EHb and ELb (***Weyrauch et al. 2018***; ***Udry et al., 2019***). Moreover, the findings of ungrouped reduced meteorites, such as QUE 94204 (***Van Niekerk et al., 2014***), Zakłodzie (***Przylibski et al., 2005***), NWA 15915, and Ksar Ghilane 022 (***Rider-Stokes et al., 2025***), led to the hypothesis of additional source materials. Consequently, highly reduced meteorites originated from several distinct parent bodies. The sample under investigation cover some of them: these aubrites might have come from the same precursor material, since their minerochemical similarities and being all heavily brecciated; NWA 13266 seems to derive from an EHb parent body and at some point it underwent melting processes; NWA 4945 likely derives from an ELb parent body; Itqiy does not appear to have originated from EHs nor ELs parent bodies (***Patzer et al., 2001***), suggesting an additional parent body; NWA 13210 contains daubréelite, suggesting an origin from an "a" precursor, but terrestrial weathering has made it impossible to observe the other parameters on sulphides and metals.

### 3.4.2. Reflectance spectra

Aubrites and enstatite chondrites and achondrites VNIR reflectance spectra show different features related to the differences in the mineralogy and mineral chemistry. The samples' heterogeneity can be observed in the reflectance spectra: on average, aubrites spectra acquired on rock fragments tend to present different features depending on the point analysis, while for enstatite chondrites and achondrites, the spectra acquired in different areas have less variability (**Fig. 3.9**).

Enstatite chondrites Itqiy and NWA 4945, and enstatite achondrite NWA 13266 show featureless spectra with no significant variations in different portions of the analysed fragments. The higher amount of metal in these samples (7-11 % vs <0.1 % in aubrites and NWA 13210) could influence their VNIR spectra, causing the observed mild red slope (e.g., ***Cloutis et al., 1990***), which is an opposite trend to the blue slope exhibited by all other rock samples. The higher spectral variation observed in enstatite melt rock NWA 13210 is linked to the presence of terrestrial weathering affecting the whole sample, as underlined by the absorption feature at 1.9 μm, with some areas of the sample being more affected than others. In the most weathered portions band I is four times deeper and shifted to longer wavelengths (0.938 μm), due to the higher presence of oxidized iron in the alteration products, most likely goethite (***Burns, 1993; Crowley et al., 2003; Sherman et al., 1982***), also evidenced by the features at 0.501 μm and 0.697 μm.

Band I in the investigated aubrites is centred in the range 0.901-0.908 μm and is related to crystal field transitions in $Fe^{2+}$ preferentially occupying the M2 crystallographic site in pyroxene (e.g., ***Cloutis 2002***). Band II is absent in the spectra of the analysed samples, likely because the very low amount of iron, as indicated by the high En content, constrained in the M2 site, makes the crystal field absorptions at longer wavelength too weak. Moreover, the weathering products, highlighted by absorption due to H-O-H overtone around 1.9 μm, observed in Rantila, Norton County, and the NWA 14185 spectra, could make up a very weak and broad absorption. Rantila and NWA 14185 exhibit differences among spectra collected in different areas, highlighting higher mineralogical heterogeneity than Tiglit and Norton County. The Rantila fragment presents portions containing higher abundances of olivine (spectrum Rantila_1, **Fig. 3.9a and Fig. 3.10a**), that contribute to the band I pyroxene absorption causing a wider 0.9 μm band and a shifting towards longer wavelengths (0.926 μm) (***Burns, 1993***), and a weak and narrow feature at 0.503 μm attributed to a spin-forbidden $Fe^{2+}$ absorption in olivine (e.g., ***Burns 1993; Carli et al. 2018***). Therefore, in Rantila the spectral variability is caused by the mineralogical heterogeneity of the sample and it is not influenced by the incipient terrestrial weathering (1.9 μm feature) On the contrary, NWA 14185 spectral variation is determined by mineralogical heterogeneity of the sample but also by higher weathering degree in the spot were spectrum NWA 14185_3 was taken: a millimetric opaque

mineral is observed in this spot and opaque minerals are the first to be altered by terrestrial weathering. Acquiring spectra on powdered samples could reduce heterogeneity effects, at least at the scale of the fragments. We acquired the spectra on powder of Norton County, Rantila, and NWA 14185. In general, for the investigated samples, the reflectance on powders is higher than the reflectance on rocks, ca 25 % higher for all three samples, a redder slope is observed, and the absorption bands appear slightly weaker than on rocks. Band I in the Rantila powder spectrum is shaped and centred (0.904 μm) accordingly to low Fe-low Ca enstatite being the main phase, and the 0.5 μm absorption is weaker but still detected, evidencing that almost 20% of olivine modal abundance is well observed in reflectance spectra. Moreover, the higher amounts of FeO in Rantila olivine and pyroxene compared to those detected in other aubrites from this study and from literature (e.g., ***Watters & Prinz, 1979***), are reflected in the stronger band I. This suggests that the potential crystal field absorptions detection limit of mafic minerals in VNIR reflectance spectra may be constrained to a range between the compositions of other aubrites and the compositions of Rantila (***Landi et al., 2025***).

### 3.4.3. Implications for Mercury's surface exploration

Mercury's surface reflectance spectra acquired by the Mercury Atmospheric and Surface Composition Spectrometer (MASCS) evidenced the presence of different units, depending on the different geochemical terranes, with average features that include: no absorption feature around 1 μm, a red slope, and surface darker than any laboratory analogue mixture (***Izenberg et al., 2014***). Spectra acquired with the Mercury Dual Imaging System (MDIS) Camera with filters covering the range 898-996 nm, on the other hand, can present a mild absorption feature around 1 μm (***Carli et al., 2024b; Luchetti et al. 2018***): observations of the Hollow field of the Dominici crater (***Lucchetti et al. 2018; Vilas et al., 2016***) and Warhol crater (***Carli et al., 2024b***) could indicate the exposure of relatively fresh mafic minerals. Therefore, we could try to compare the featureless spectra of enstatite chondrites and achondrites to MASCS spectra and the spectra with the 1 μm mafic minerals absorption band with the MDIS spectra. The first comparison shows some discrepancies: enstatite chondrites and achondrites spectra are flat or blue and do not show the UV-downturn, concave curvature of the spectrum in the UV range (***Goudge et al., 2014***), observed particularly for hollows and pyroclastic deposits (***Barraud et al., 2020, 2021***). UV-downturn may be influenced by the presence of sulphides (***Barraud et al., 2020***), which occur in all the investigated samples, even though in different amounts, and also by space weathering, affecting Mercury's surface (***Domingue et al., 2014***),but not these samples. The second comparison is reported in **Figure 3.14**, in which aubrites' spectra are compared to two hollows spectra from ***Carli et al. (2024b)***.

Aubrite mafic absorption is located at ~0.9 μm, and the hollows absorption is around 1 μm, suggesting higher Ca-pyroxene and/or olivine amount. Moreover, hollows spectra show a ~0.6 μm feature associated with a higher concentration of sulphides (***Vilas et al., 2016***) or with a higher concentration of other transitional elements than Fe (e.g., ***Lucchetti et al., 2018***), with respect to those found in aubrites.

Therefore, even though aubrites and enstatite melts are the most promising natural analogues of Mercury's surface at our disposal (***Burbine et al., 2002***; ***Morlok et al., 2020***; ***Udry et al., 2019***; ***Wilbur et al., 2022***), some differences can be observed between their reflectance spectra and Mercury's surface ones. This may be linked to the fact that they do not represent a perfect petrological analogue. In fact, aubrites contain much less plagioclase than what is inferred for Mercury's geochemical terranes (e.g., ***Namur & Charlier, 2017***; ***Vander Kaaden et al., 2017***). Sulphides are expected to be abundant on the planet's surface, up to 10.1 % in some specific areas of hollows (***Barraud et al., 2023***), values which could be more in agreement with enstatite achondrites and melts, but in that case the absence of forsterite and Ca-pyroxene limits the petrological comparison. Aubrites and enstatite achondrites and melts present metallic Fe,Ni suggesting an incomplete core formation in their parent bodies. Nonetheless, ***Udry et al. (2019)*** propose the use of enstatite chondrite impact melts as natural examples of what we could observe with experimental petrology studies. These analogues can help to infer how elements are distributed in the phases expected to be present on Mercury's surface and how impact processes could affect the surface, considering the same highly reducing conditions. Moreover, some other reduced materials, Ca-rich pyroxene-dominated, have been recently considered as spectral analogues for the planet surface (***Rider-Stokes et al., 2025***).

It is therefore crucial to increase the knowledge of these different kinds of highly reduced meteorites. Correlating their reflectance spectra with their mineralogy and chemical composition will help in the interpretation of the upcoming data from the ESA's BepiColombo mission instruments: spectral data from the SIMBIO-SYS/VIHI imaging spectrometer (0.4-2.0 μm, ***Cremonese et al., 2020***) and the MERTIS spectrometer (***Hiesinger et al., 2020***), and compositional data from the MIXS spectrometer (***Fraser et al., 2010***).

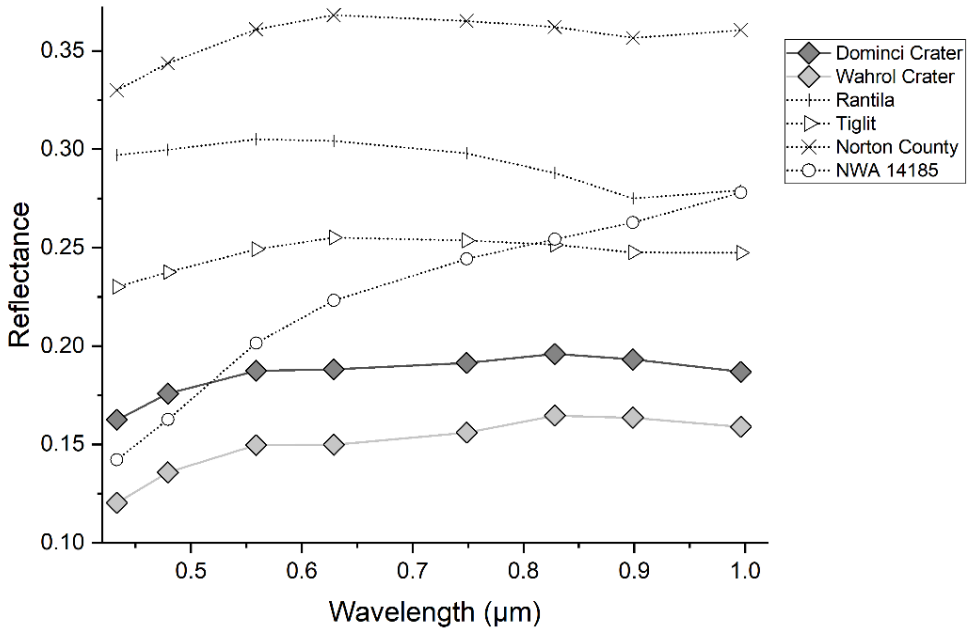


Figure 3.14. Comparison between two Hollows spectra (Dominici crater and Warhol crater) (**Carli et al. 2024**) and investigated aubrites spectra, modified after **Landi et al. (2025)**. Hollows spectra were acquired on a MDIS mosaic at 665 m per pixel, which was produced following the procedure explained in **Zambon et al. (2022)**.

### 3.5. Conclusions

In this work, we investigated the mineralogy and VNIR reflectance spectroscopy of eight enstatite-rich highly reduced meteorites belonging to different groups. We observed that aubrites show higher mineralogical heterogeneity than the other meteorites. Nevertheless, enstatite is the predominant phase in all the samples, although with different percentages. Sulphides and metals are much more abundant in enstatite chondrites and achondrites. The EL6 NWA 4945 presents diopside, which is not common in enstatite chondrites. The enstatite melt rock NWA 13210 mineralogical characterization is influenced by the high grade of terrestrial weathering, which is low for all the other samples under investigation. In addition to the melt rock NWA 13210, four other meteorites (Rantila, Tiglit, Norton County, NWA 13266) show evidence of melting processes. Silicates composition does not show significant differences among the various meteorite groups; only plagioclase has a wider compositional range in aubrite than in enstatite chondrites and achondrites. On the other hand, metal and sulphide compositions are variable. Si content (wt%) in kamacite are higher in enstatite chondrites than in aubrites and enstatite achondrites. Troilite is the main sulphide, showing variable Cr and Ti contents (wt%): on average, Cr is higher in enstatite chondrites, achondrite and melt rock, Ti is lower in enstatite chondrite and achondrite, variable in aubrites and high in enstatite melt rock. Oldhamite and Ca-rich (Fe, Mg, Ca, Mn, Cr..)S sulphides are detected in all meteorite groups. Keilite is detected in the EL NWA 4945 and enstatite achondrite NWA

13266, alabandite in anomalous EH Itqiy and aubrites, niningerite just in NWA 13266. Daubréelite is detected in aubrites and NWA 13210. These mineralogical and chemical characteristics suggest that the meteorites derive from multiple distinct enstatite chondrite-like parent bodies.

Enstatite chondrites and achondrite VNIR reflectance spectra are flat, in some cases showing a subtle red slope, maybe influenced by the high amount of metal and sulphide, and no or very weak absorption bands. Aubrites spectra exhibit 0.9 μm mafic-related absorption features, with variable intensities depending on the FeO content in pyroxene and olivine. In the portions with higher forsterite amount, a weak band around 0.5 μm is also observed. Sometimes, features at 1.9 μm related to hydrous phases from terrestrial weathering are observed; in the case of the pervasively weathered NWA 13210, they are associated to other hydrated phases, likely goethite, producing an additional absorption feature at 0.7 μm.

Highly reduced meteorites, specifically aubrites, are considered the best natural spectral analogue at our disposal for Mercury's surface. Nonetheless, the comparison between aubrite spectra and MDIS data, as well as between enstatite chondrites, achondrite and melt rock spectra and MASCS data, provides evidence attributed not only to differences in the acquisition methods and the effect of Space Weathering on Mercury's surface, but also to intrinsic mineralogical characteristics of the materials.

# 4. Ion irradiation of aubrites: visible to mid-infrared spectroscopic effects of Space Weathering simulation on Mercury analogues

This chapter is a manuscript in preparation for publication by A.I. Landi, R. Brunetto, C. Lantz, C. Carli, F. Capaccioni, and G. Pratesi.


**Abstract**

Knowledge of Mercury's surface composition is crucial to understanding the planet's origin and geological evolution. Due to the absence of a thick atmosphere, its proximity to the Sun, and weak magnetic field, Mercury's surface is strongly affected by Space Weathering (SpWe) processes, such as solar wind irradiation and micrometeoroid bombardment, which alter its physical and spectral properties. Understanding how SpWe modifies the reflectance spectra of Mercury-like materials is essential for the interpretation of spectral data retrieved from orbital missions.

In this study, we simulated the effects of solar wind irradiation through ion irradiation experiments with 20 keV $He^+$ and 30 keV $C^+$ ions on five aubrites (Rantila, Tiglit, Norton County, Peña Blanca Spring, and NWA 14185), which are highly reduced meteorites considered promising natural analogues for Mercury's surface. Both powdered pellets and rock fragments were irradiated to evaluate the influence of sample texture.

The main spectral effects for all the investigated samples are darkening and reddening in the visible to near-infrared (VNIR) range. $C^+$ irradiation produces stronger darkening. Different darkening and reddening trends are observed between pellets and rock fragments. The effects in the mid-infrared (MIR) range are the shifting of the Reststrahlen Bands (RBs) and Christiansen Features (CFs) to longer wavelengths (red shifts) and spectral contrast attenuation. The red shifts are particularly evident for the main RBs, which show a larger shift with $He^+$ irradiation. Moreover, we note that if carbon is present in the samples before irradiation, even in small amounts, the spectral modifications are stronger, especially darkening.

These results demonstrate that solar wind ions can significantly affect the spectral properties of highly reduced materials and that the chemical composition and form play a key role in the type and extent of the spectral modifications. This study provides experimental constraints that could be useful for the future interpretation of the upcoming data that will be collected by the SIMBIO-SYS/VIHI and MERTIS instruments on board BepiColombo mission, contributing to a better understanding of space weathering effects on Mercury's surface.

## 4.1. Introduction

Knowledge of Mercury's surface composition is crucial to understanding the planet's history and evolution. The latest information about Mercury's surface comes from NASA's MESSENGER (MErcury Surface, Space ENvironment, GEochemistry and Ranging) mission (***Solomon et al., 2001; Solomon et al., 2018***). The surface presents high Si and Mg/Si ratio, low Al/Si and Ca/Si and low Fe; Na, K, S and Cl are distributed on the surface with variable amounts; highly volatile species (H included) are only present in the permanently shadowed polar regions (***Evans et al., 2012, 2015; Nittler et al., 2011, 2018; Nittler & Weider, 2019; Peplowski et al., 2012a , 2012b, 2014, 2015, 2016; Weider et al., 2012 , 2014, 2015, 2016***). The high S concentration, and very low Fe concentration (1-2 wt%, of which FeO in silicates is inferred to be <1 wt% from reflectance spectroscopy studies, ***Murchie et al., 2015***), reflect the highly reduced nature of the planet (oxygen fugacity, $fO_2$, estimated 2.6-7.3 log units below the iron-wüstite buffer, ***McCubbin et al., 2012; Namur et al., 2016; Zolotov et al., 2013***). The inferred mineralogy is dominated by albitic plagioclase and FeO-free pyroxene, with minor forsterite and Mg-Ca-Fe sulphide assemblages (e.g., ***Namur & Charlier, 2017; Nittler & Weider, 2019).*** C has an estimated average concentration of 1.4 ±0.9 wt% (***Peplowski et al., 2015***), with 1–3 wt% in the lower reflectance material regions (***Peplowski et al., 2016***), and it is suggested to be in the form of graphite (***Vander Kaaden & McCubbin, 2015***)

Moreover, the planet's surface, like that of other airless bodies, is affected by Space Weathering (SpWe), which causes alteration in its physical and chemical properties (***Domingue et al., 2014; Killen et al., 2001***). SpWe is composed of different processes, such as solar wind and cosmic ions irradiation and micrometeoroid bombardment (e.g., ***Chapman, 2004; Hapke, 2001; Pieters & Noble, 2016***). These processes alter the remote sensing information from the body's surface, creating difficulties in mineralogical characterization. The main effects in the visible to near-infrared (VNIR) spectral range are a decrease in the absolute reflectance value (darkening) and an increase of the spectral slope (reddening) (***Brunetto & Strazzulla, 2005***; ***Brunetto et al., 2014; Fulvio et al., 2012; Hapke, 1973***; ***Hapke, 2001***; ***Marchi et al., 2005***; ***Penttilä et al., 2020***), although in some cases an increase in the reflectance (brightening) (e.g., ***Lantz et al., 2015, 2017; Moroz et al., 2004***) and decrease in the spectral slope (blueing) (e.g., ***Lantz et al., 2013, 2015, 2017; Nesvorný et al., 2005; Vernazza et al., 2013***) have been observed. Moreover, SpWe can cause the reduction of the bands' intensity absorption (***Fulvio et al., 2012; Hapke, 2001; Marchi et al., 2005; Penttilä et al., 2020; Strazzulla et al., 2005; Vernazza et al., 2009***). In the mid-infrared (MIR) range, shifts of the Christiansen Feature (CF), Reststrahlen Bands (RBs) and Transparency Feature (TF) positions can be observed along with the modification of band shapes and the reduction of the spectral

contrast (e.g., ***Brunetto et al., 2014; Brunetto et al., 2018; Chrbolková et al., 2021; Jäggi et al., 2021; Lantz et al., 2015; 2017; Rubino et al., 2024***). Darkening and reddening on planetary surfaces, such as the Moon and Mercury, are thought to be mostly caused by the creation of small particles of metallic iron, called "nanophase iron" ($npFe^0$) (e.g., ***Cassidy & Hapke, 1975; Domingue et al., 2014; Hapke, 2001; Vilas & Hendrix, 2015***). In asteroid SpWe, the role of the formation of nano-phase iron sulphides, amorphized layers, and implantation vesicles has also been emphasized, thanks to the laboratory analysis of returned samples from the asteroids Itokawa and Ryugu collected by JAXA's Hayabusa and Hayabusa2 missions (***Noguchi et al. 2011, 2023***). The magnetic field can shield the effects of SpWe, but in the case of Mercury, the magnetic field is weak; therefore SpWe is only slightly moderated (***Domingue et al., 2014***). Moreover, Mercury is closer to the Sun and has a greater mass than the Moon, suggesting that Mercury is affected by frequent impacts occurring at high speeds, exceeding those observed on the Moon (***Cintala, 1992***), and by stronger solar wind irradiation (***Domingue et al., 2014***).

In any case, the effects of SpWe are believed to modify significantly the spectral properties of an unprotected surface, thus biasing our understanding of the underlying original composition. Therefore, investigating the effects of SpWe on the planet's surface is crucial to interpreting its mineralogy and chemical composition.

Since no meteorites from Mercury or returned samples are available, laboratory simulations of SpWe and the study of their effects on analogue materials become crucial. Considering the mineralogy and highly reduced composition, aubrites (e.g., ***Burbine et al., 2002; Morlok et al., 2020; Wilbur et al., 2022)*** and enstatite chondrite melt rocks (***Udry et al., 2019***) have been proposed as the best natural analogues at our disposal for Mercury's surface. Taking into account the high Mg/Si ratio of the planet's surface, similarities with terrestrial high-Mg rocks have also been proposed: for instance, boninites (***Vander Kaaden & McCubbin, 2016; Vander Kaaden et al., 2017***), komatiites (***Nittler et al., 2011; Weider et al., 2015***), and norites (***McCoy et al., 2018; Stockstill-Cahill et al., 2012***) present bulk chemical compositions resembling those of different Mercury's geochemical terranes (***Vander Kaaden et al., 2017***). So far, few SpWe simulation studies have been conducted on highly reduced materials and Mercury analogues: Ar+ ion irradiation on an enstatite chondrite (***Vernazza et al., 2009***), $He^+$ ion irradiation on komatiites and boninites (***Caminiti et al., 2024***), laser irradiation on one aubrite and two enstatite chondrites (***Zhang et al., 2022***).

In this work, we performed ion irradiation with $He^+$ and $C^+$ on five aubrites (Rantila, Norton County, Peña Blanca Spring, Tiglit, and NWA 14185) working on both pellets and rock fragments, to observe possible differences in the response to the irradiation. Understanding how ion

irradiation modifies the reflectance spectra of these highly reduced materials, as reduced as Mercury's surface, will help in the interpretation of upcoming spectral data from the SIMBIO-SYS/VIHI (Spectrometer and Imaging for MPO BepiColombo Integrated Observatory SYStem/Visible and near-Infrared Hyperspectral Imaging channel, ***Cremonese et al., 2020***) and MERTIS (Mercury Radiometer and Thermal Infrared Spectrometer, ***Hiesinger et al., 2020***), instruments onboard the ESA-JAXA BepiColombo mission (***Benkhoff et al., 2021; Rothery et al., 2020***).

## 4.2. Experimental setup and analytical methods

### 4.2.1. Samples

Five aubrites were investigated in this study: four falls, Rantila (hereafter referred to as RAN), Tiglit (TIG), Norton County (NC), Peña Blanca Spring (PBS), and one find, NWA 14185 (NWA). We chose to perform ion irradiation on both powders (as pellets) and rock fragments, to investigate how the material's form influences its response to irradiation. Due to the availability, quantity, and size of the material, the ion irradiation experiments were performed on both powder and rock fragments of RAN and NWA, on powder of NC and PBS, and on a rock fragment of TIG.

In the experimental setup, the powders are investigated as pellets because the samples are held vertically (e.g., ***Brunetto et al., 2014; Caminiti et al., 2024; Lantz et al., 2015, 2017; Rubino et al., 2020***). The aubrites used to create the pellets (Rantila, NWA 14185, and Norton County) were crushed into powder and sieved to obtain a grain size ≤100 μm at the S.LAB. laboratory of the Istituto Nazionale di Astrofisica (INAF) - Istituto di Astrofisica e Planetologia Spaziali (IAPS), in Rome. Pellets of Peña Blanca Spring were also prepared, starting from powders previously arranged in the laboratory for other studies. Pellets were prepared at the Institut d'Astrophysique Spatiale (IAS, Orsay, France) using a Specac manual press. Each pellet was prepared using ~900 mg of KBr pressed under 3 tons for ~3 min as a base layer, and then ~150 mg of sample powder was added and pressed under 7 tons for ~10 min. The diameter of the pellets is 13 mm, and their thickness is 4 mm. Three pellets were prepared for each meteorite: one kept unirradiated, one to be irradiated with $He^+$, and one to be irradiated with $C^+$. They were mounted in a dedicated sample holder with 13 mm diameter holes (**Fig. 4.1**), while the rock fragments were mounted in another sample holder with 20 mm diameter holes (**Fig. 4.1**).

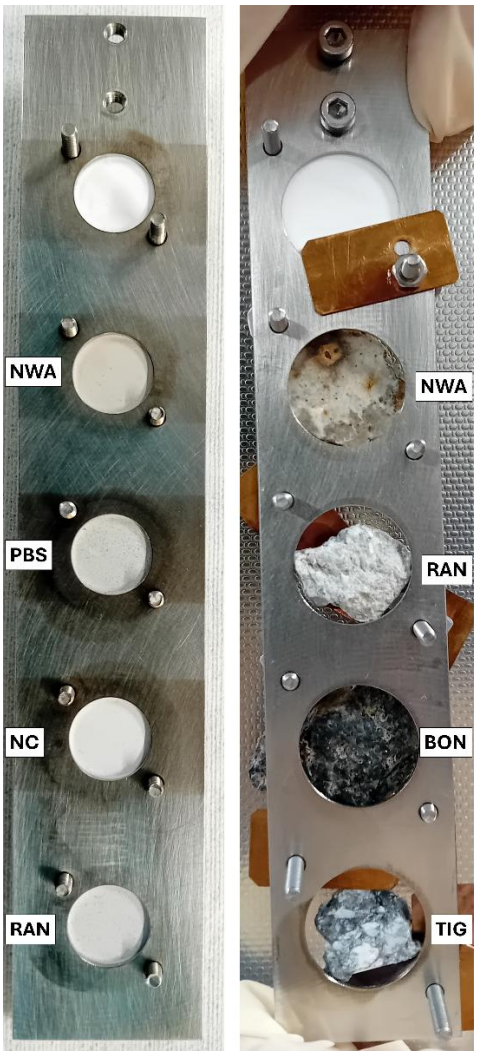


Figure 4.1. The two sample holders for pellets, on the left, and rock fragments, on the right. Pellets, from top to bottom, spectralon, NWA, PBS, NC, RAN. Rock fragments, from top to bottom, spectralon, NWA, RAN, boninite glass sample ("BON", not object of this study, to be discussed in a separate work), TIG.

### 4.2.2. Ion irradiation

To simulate the solar wind irradiation affecting Mercury's surface, we conducted two separate ion irradiation experiments using $He^+$ at 20 keV and $C^+$ at 30 keV. We chose to use $He^+$ because it represents an important component of the solar wind, helium being the second most abundant species in it (~4%) after hydrogen (~96%), and solar wind ions being the major contributors to space weathering on Mercury. To prevent implantation-induced chemical effects, we used unreactive $He^+$ ions rather than reactive $H^+$ ions (e.g. ***Brucato et al., 1997***; ***Caminiti et al., 2024***). Helium ions have an average energy of ~4 keV in the solar wind, but higher-energy ions are emitted from the Sun, from active regions and solar flares, causing significant alterations on the surfaces of airless bodies (e.g., ***Brunetto et al., 2014; Johnson, 1990***). For this reason, laboratory ion energies in the 20–40 keV range are widely used as proxies for the more energetic portion of the solar wind (e.g. ***Brunetto et al., 2014***). An exhaustive explanation of the use of $He^+$ and 20-30 keV

can be found in previous studies (e.g., ***Brunetto et al., 2014; Caminiti et al., 2024; Lantz et al., 2015, 2017, 2024; Rubino et al., 2020 and references therein***). Moreover, high energy ions are significant for SpWe simulations on Mercury's surface considering that low energy solar wind is partially shielded by the planet's intrinsic magnetic field (e.g. ***Domingue et al., 2014; Lavorenti et al., 2023***).

Nonetheless, solar wind is composed of ions of several species, and to try to simulate the effects of a heavier species, we chose $C^+$ whose irradiation effects on meteorites have been investigated only in a few studies (e.g., ***Fulvio et al., 2012***). A higher energy was used for $C^+$ implantation (30 keV instead of 20 keV) because ion penetration depth decreases as the mass increases. The $C^+$ energy was therefore increased to achieve comparable penetration depths for $He^+$ and $C^+$ ions. Carbon is particularly interesting, as the implanted ions can react with the target and form new bonds. Additionally, the implantation of carbon is explored here also as a possible contribution to the dark component on Mercury (e.g., ***Bruck Syal et al., 2015; Penttilä, 2025; Shackelford et al., 2025; Trang et al., 2015***).

The irradiation experiments were conducted using the SIDONIE electromagnetic isotope separator (***Chauvin et al., 2004***) situated at the IJCLab, Université Paris-Saclay, Orsay, France. The irradiations were conducted in the INGMAR (IrradiatioN de Glaces et Météorites Analysées par Réflectance VIS-IR, IAS & IJCLab, Université Paris-Saclay, Orsay, France) vacuum chamber (P ~ $10^{-7}$ mbar), which is connected to the SIDONIE implanter. Regarding the pellets, the whole sample surface, beside an external rim (~500 μm in width) masked by the sample holder, was irradiated at every fluence step, with additive doses, following the protocol used in previous studies (***Caminiti et al., 2024; Chrbolková et al., 2021; Lantz et al., 2017; Rubino et al., 2020, 2024***). The fluence steps were 1 x $10^{16}$, 3 x $10^{16}$, 6 x$10^{16}$ and 1 x $10^{17}$ ions/cm$^2$. We irradiated two different pellets for each sample, one with $He^+$ and one with $C^+$. For the rock fragments, we used only one fragment for each sample, irradiating two different zones of the surface, one with $He^+$ and one with $C^+$, with the same fluences used for the pellets. For the smallest sample (TIG), this procedure could not be applied because the surface was not big enough to separate the two irradiations (irradiation beam being 18 mm in diameter), therefore, we performed $C^+$ implantation on top of $He^+$ implantation.

### 4.2.3. Reflectance spectra measurements

VNIR spectra were acquired in situ through the INGMAR setup. Measurements were taken on the fresh samples and after each irradiation step, under vacuum (P ~ $10^{-7}$ mbar) and at room temperature. VIS bidirectional reflectance spectra were acquired in the range 0.4-1.1 μm using a halogen

visible source and a *Maya2000Pro (Ocean Optics)* spectrometer, with a 0.5 nm spectral resolution and 450 scans. NIR bidirectional reflectance spectra were acquired in the range 0.9-5.0 μm using a Fourier Transform spectrometer (*Tensor37 Bruker*) with an 8 $cm^{-1}$ spectral resolution and 1024 scans. The acquisition angles were as follows: illumination angle (*i*)=15° and emission angle (*e*)=15° for VIS, and *i*=20°, *e*=15° for NIR. The illumination spot sizes were 12 mm in diameter for the VIS and 20 mm in diameter for the NIR, with a collecting spot size of 8 mm. VIS and NIR measurements were performed on the same spot for each sample. The calibration of the samples' absolute reflectance was made using a 99% Spectralon standard (Labsphere) and an additional Infragold standard for the calibration of the NIR spectra. VNIR final spectra were obtained merging VIS and NIR spectral ranges, overlapping the region with common wavelengths.

MIR spectra were taken ex situ on fresh samples and on the samples after the final irradiation dose at SMIS (Spectroscopy and Microscopy in the Infrared using Synchrotron) beamline of the Synchrotron SOLEIL, France. Reflectance spectra on pellets were acquired in the range 2.5-12.5 μm using an Agilent Cary 670/620 micro-spectrometer equipped with an MCT detector. The measurements were taken at ambient conditions with a 15x objective, 250 nm measurement spot, 4 $cm^{-1}$ spectral resolution, 256 scans. A gold sample was used as standard. Visible images of the measured spots were acquired using the imaging microscope. Reflectance hyperspectral maps on rock fragments were acquired in the range 2.5-12.5 μm with the same *Agilent Cary 670/620* micro-spectrometer but using a 128 x 128 pixels FPA (Focal Plane Array). The measurements were taken at ambient conditions, with a 15x objective with a numerical aperture of 0.62, a reduced 64 x 64 pixels FPA size, 4 $cm^{-1}$ spectral resolution, 256 scans. A gold sample was used as standard. We obtained visible images, using the imaging microscope, and MIR images of different portions of the rock fragments. Additional information on the instrument protocol can be found in ***Brunetto et al. (2018, 2020)***.

### 4.3. Results

The analysed samples are mainly composed of enstatite, with minor forsterite, diopside, plagioclase, and Fe-Mn-Mg-Ca-Cr sulphides, and accessory amounts of Fe,Ni metal. Silicates are characterized by very low FeO contents (<0.3 wt%).[1]

[1] For a detailed characterization of the mineral assemblages and mineral chemistry of the investigated samples, the reader is referred to Chapters 2 and 3.

### 4.3.1. VNIR spectra

VNIR spectra are characterized by a blue slope and no or weak absorption features around 0.9 μm related to mafic minerals (e.g., ***Burns, 1993; Cloutis & Gaffey, 1991; Klima et al., 2008***). Minor absorptions at ~0.5 μm are observed in the samples presenting more abundant olivine (e.g., ***Carli et al., 2018; Landi et al., 2025***). Weak features can be present in the 1.9-2.1 μm region, related to incipient terrestrial aqueous alteration of the samples (e.g., ***Burbine et al., 2002; Gaffey et al., 1993***). PBS spectra show features at 1.7 μm and 2.3 μm, which are not detected in the other samples. Moreover, this sample is the only one showing a strong absorption at 3.4 μm (**Fig. S4.1**). These three features are organics related, most likely deriving from contamination (maybe from acetone) during the sample preparation.

The effects of progressive ion implantation on the VNIR spectra are shown in **Figure 4.2**. General darkening and reddening are observed in all samples, whether in pellet or rock fragment form. $C^+$ implantation appears more effective than $He^+$ in generating albedo changes. The infrared (IR) range is less affected than the visible (VIS) range for both ions. However, C irradiation at the highest fluence ($1x10^{17}$ ions/cm$^2$) causes an albedo decrease in the whole spectral range for pellets, which is not observed for rock fragments. On the other hand, for rocks, the darkening is much stronger with the first irradiation dose ($1x10^{16}$ ions/cm$^2$), and this is observed with He implantation as well. The highest He fluence causes a bump in the VIS range (~0.6-0.8 μm), especially for pellets. The absorption bands at 0.9 μm are not strongly affected by He and C implantation, only causing a slight attenuation. These effects are observed for RAN, NWA, NC, and TIG samples. However, for TIG spectra after C irradiation, the reddening effect is visible for all the fluences, while darkening only begins after $6x10^{16}$ ions/cm$^2$. It should be noted that in this case, the absolute reflectance before C implantation is lower than before He implantation: this is because C irradiation was performed on the same surface previously irradiated with He, and therefore already darkened. For PBS, ion irradiation produces the same effects as for the other samples, though with some differences. The darkening, although still stronger in the VIS range, is visible in the whole spectral range and progressively intensifies with increasing fluence, particularly with C irradiation.

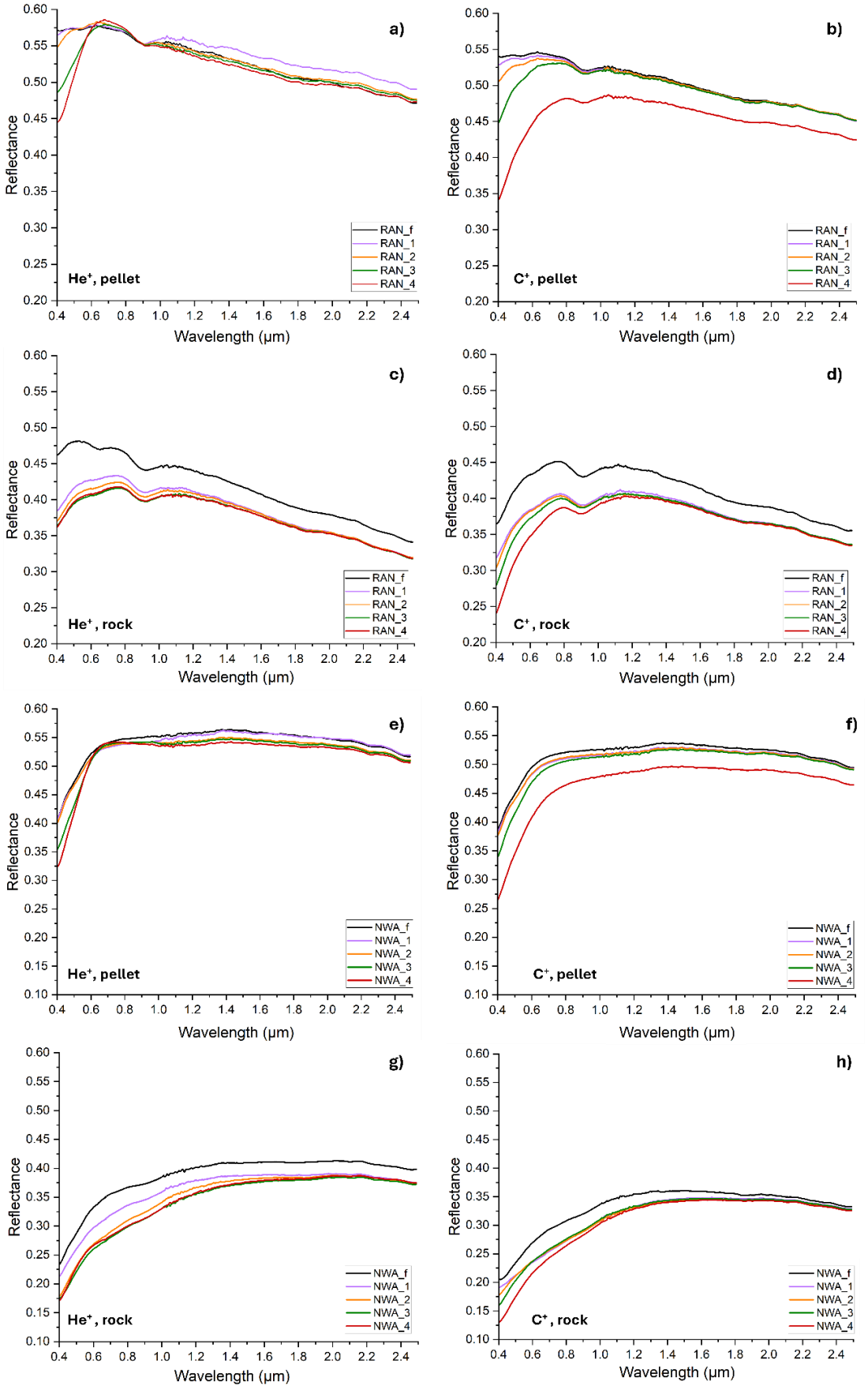


Figure 4.27. VNIR spectra of the investigated aubrites before and after He and C implantation. Black before irradiation, purple after $1x10^{16}$ ions/cm$^2$, yellow after $3x10^{16}$ ions/cm$^2$, green after $6x10^{16}$ ions/cm$^2$, red after $1x10^{17}$ ions/cm$^2$.

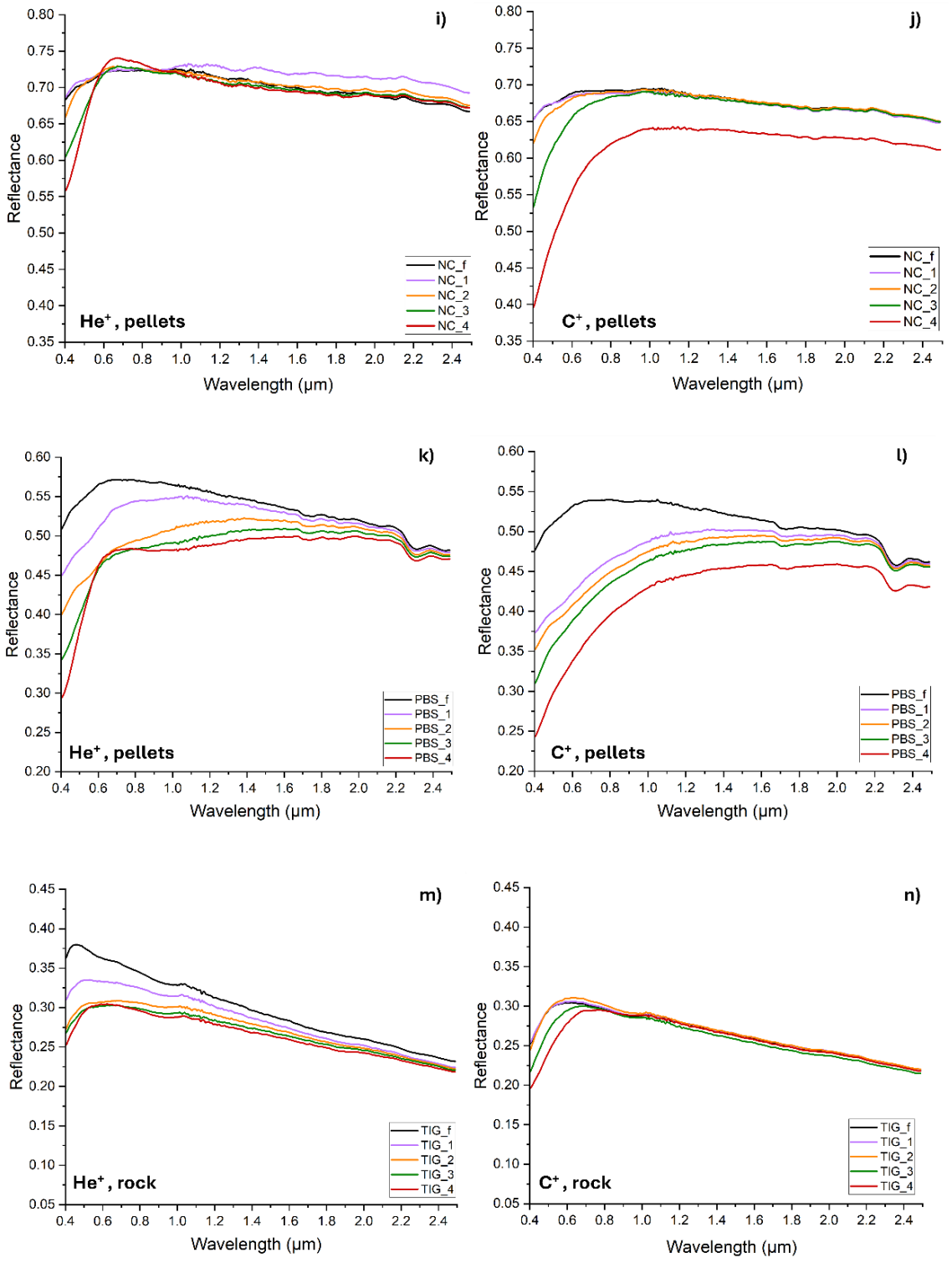


Figure 4.2. continue.

The darkening trend as a function of irradiation fluence shows a non-linear behaviour (**Fig. 4.3**). For pellets, the final darkening is greater after C irradiation than after He irradiation, between 23-28% and between 7-11%, respectively (PBS shows greater values, around 42% for C and 30% for He). For rock fragments final values are up to 25% for C and 22% for He. Darkening induced by

He implantation occurs until $6\times10^{16}$ ions/cm², then, after $1\times10^{17}$ ions/cm², an increase in albedo is observed, although it remains lower than the initial value. This increase is not observed after C implantation. Therefore, darkening trends are different between rocks and pellets, yet they are similar within the pellets and within the rock fragments, except for PBS. PBS shows not only higher final darkening, but also distinct trends compared to the other samples. The reflectance decreases more rapidly already at the first fluence. He induced darkening is quite linear, while C irradiation produces a steep albedo decrease after the first irradiation dose.

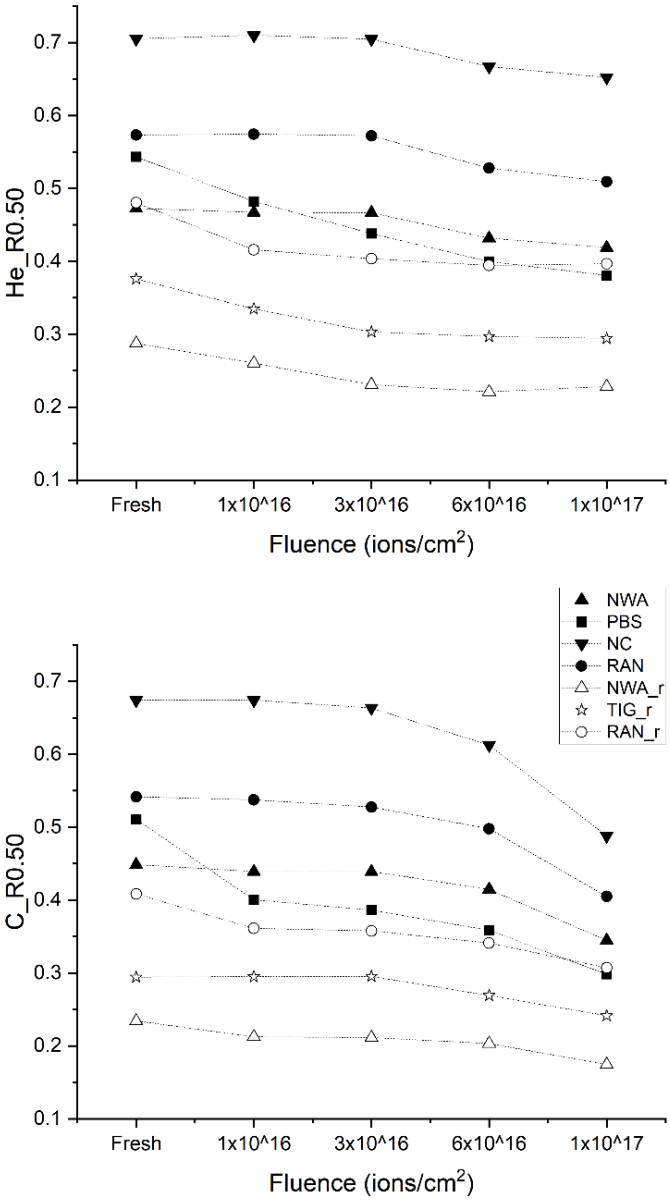


Figure 4.3. Darkening effect as a function of the fluence. The darkening is expressed as the absolute reflectance value at 0.5 µm. The top panel shows He irradiation, the bottom panel shows C irradiation. Filled symbols indicate pellets, open symbols indicate rock fragments.

The reddening trend as a function of irradiation fluence (**Fig. 4.4**) is also not linear. It shows a higher variability than darkening: distinct trends are observed not only between pellets and rock fragments but also among pellets and rocks of different samples. For pellets, PBS is the only sample showing a steep increase in the spectral slope after the first irradiation dose, while RAN spectra show a very weak reddening, NWA and NC display an initial blueing. After the irradiation with $6x10^{16}$ ions/cm$^2$, we observe a steep increase in the spectral slope for all four pellets. These effects are similar for both He and C irradiation. The trend is different for rock fragments. For RAN and TIG, He irradiation produces a strong reddening after the first dose, but as the fluence increases, the reddening becomes less pronounced. In contrast, blueing is observed for NWA, with the final slope being lower than the initial one. C irradiation produces reddening for all the samples. For RAN and TIG, the slope remains almost unaltered up to $6x10^{16}$ ions/cm$^2$, after which it increases steeply. Reddening is weaker for NWA, and an initial blueing is observed. Overall, the reddening effect is much stronger on pellets than on rocks, and the final slope increase is similar between He and C irradiation. The stronger reddening observed in pellets spectra is consistent with the higher efficiency of ion irradiation effects on fine-grained materials. Pellets represent a more realistic analogue of Mercury's surface regolith, while rocks may be considered closer to less weathered, and more coherent material.

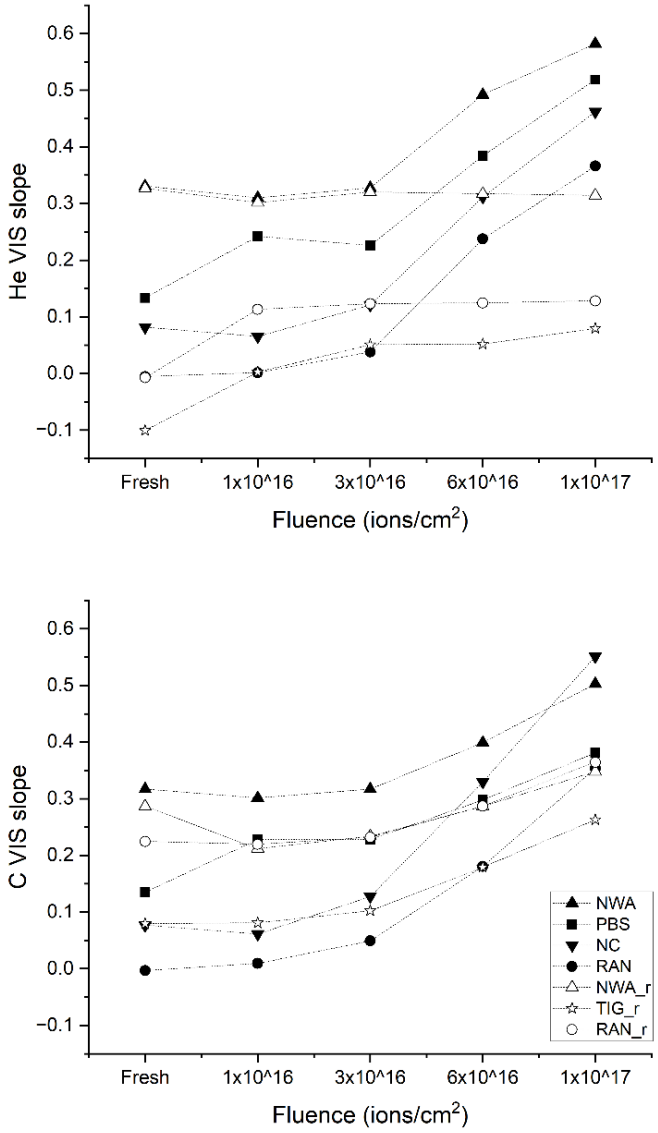


Figure 4.4. Reddening effect as a function of the fluence. The reddening is expressed as the slope in the VIS range (0.45-0.75 µm). The top panel shows He irradiation, the bottom panel shows C irradiation. Filled symbols indicate pellets, open symbols indicate rock fragments.

### 4.3.2. MIR spectra

In this section, we focus on the 7-14 µm spectral range, where the CFs and RBs are located, which will be investigated by MERTIS (***Hiesinger et al., 2020***). The MIR spectra of the four powdered samples show CFs and RBs consistent with enstatite being the predominant phase (e.g., ***Markus et al., 2018; Morlok et al., 2020***) (**Fig. 4.5**). The irradiation effects on MIR spectra are quite similar among the different samples (**Fig. 4.5**). After irradiation, the spectral contrast is reduced, the band shapes have changed, and the CFs and RBs are slightly shifted towards longer wavelengths (red shift). The shifts are in the order of hundreds of nanometres, with the biggest shifts (~0.30 µm) happening for the most intense RB located at ~ 10.5 µm, when the sample is irradiated with He (**Table 4.1**). This band appears to be the most sensitive to ion implantation, also displaying the

highest spectral contrast reduction and band shape alteration. The CFs shifts are not the same for all the samples. They remain essentially unaltered in NC. For PBS, they vary slightly under C irradiation and a bit more under He irradiation. In contrast, for NWA and RAN, the CFs shift more with C than with He irradiation, and for RAN, C-implantation-induced shift is larger than the main RB one.

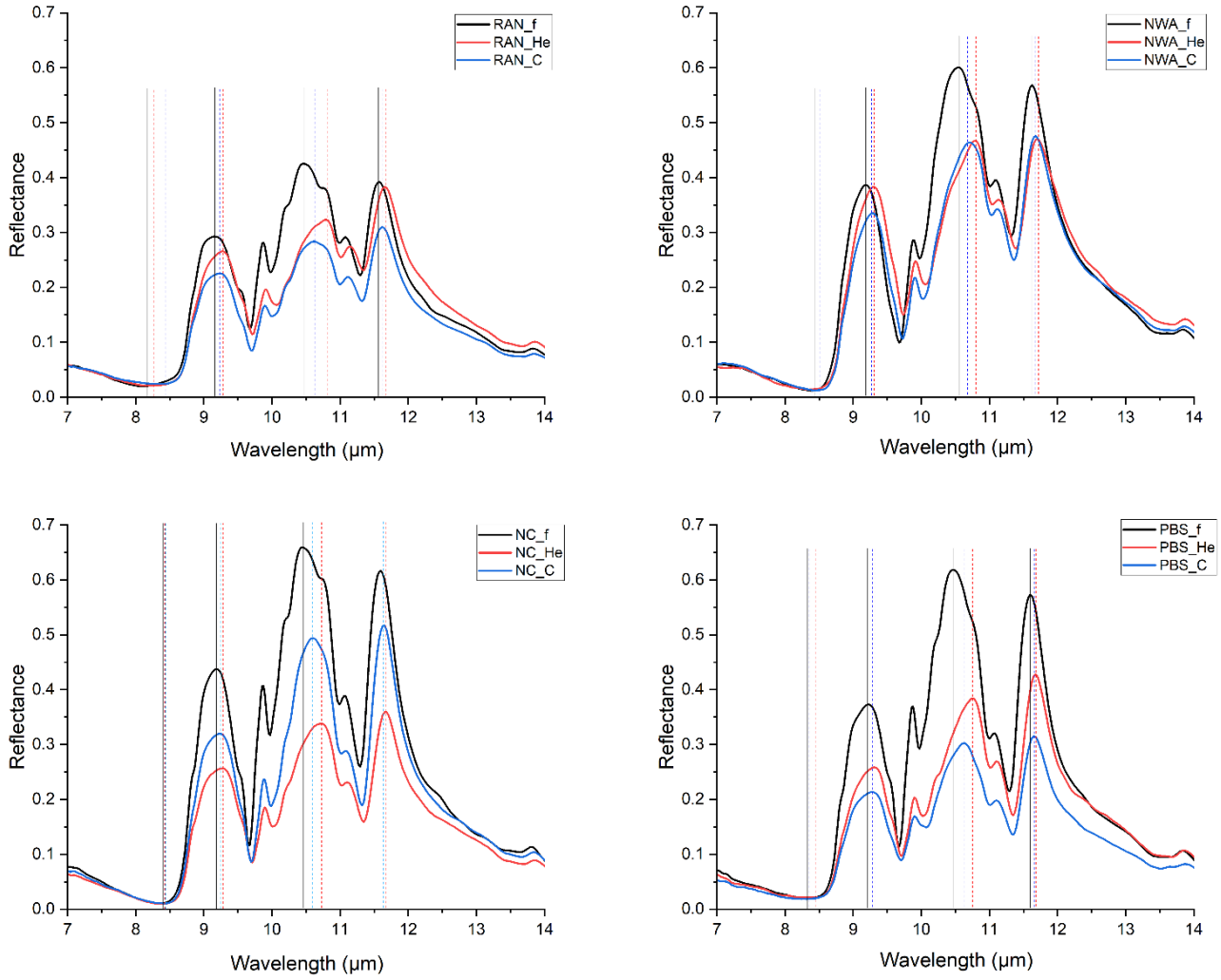


Figure 4.58. MIR spectra of the investigated samples before (black) and after He (red) and C (blue) irradiation. The dashed vertical lines are set to help visualize the band red shifts.

| | | CF (μm) | RB1 (μm) | RB2 (μm) | RB3 (μm) |
|---|---|---|---|---|---|
| RAN | Fresh | 8.11 | 9.15 | 10.47 | 11.57 |
| | He+ | 8.23 | 9.28 | 10.80 | 11.67 |
| | **shift** | **0.12** | **0.13** | **0.33** | **0.10** |
| | C+ | 8.41 | 9.23 | 10.62 | 11.62 |
| | **shift** | **0.30** | **0.08** | **0.15** | **0.05** |
| NWA | Fresh | 8.41 | 9.18 | 10.54 | 11.63 |
| | He+ | 8.46 | 9.31 | 10.80 | 11.71 |
| | **shift** | **0.05** | **0.13** | **0.26** | **0.08** |
| | C+ | 8.47 | 9.26 | 10.68 | 11.68 |
| | **shift** | **0.06** | **0.08** | **0.14** | **0.05** |
| NC | Fresh | 8.34 | 9.18 | 10.46 | 11.59 |
| | He+ | 8.38 | 9.29 | 10.73 | 11.67 |
| | **shift** | **0.04** | **0.11** | **0.27** | **0.08** |
| | C+ | 8.41 | 9.25 | 10.59 | 11.64 |
| | **shift** | **0.07** | **0.07** | **0.13** | **0.05** |
| PBS | Fresh | 8.30 | 9.21 | 10.47 | 11.60 |
| | He+ | 8.44 | 9.32 | 10.75 | 11.69 |
| | **shift** | **0.12** | **0.11** | **0.28** | **0.09** |
| | C+ | 8.30 | 9.28 | 10.62 | 11.66 |
| | **shift** | **0.00** | **0.07** | **0.15** | **0.06** |

Table 4.1. Red shifts (μm) of the Christiansen Feature (CF) and Reststrahlen Bands (RBs) after He and C irradiation.

## 4.4. Discussion

The major spectral effects induced by He and C irradiation on these aubrites are darkening and reddening in the VNIR range and red shifts of band positions, spectral contrast attenuation, and band shape alterations in the MIR.

### 4.4.1. Darkening and reddening

The observed darkening in the VNIR region is higher than the one experienced by another enstatite-rich reduced meteorite (Eagle, EL6) irradiated as a pellet, with $Ar^+$ at 200 keV up to $10^{17}$ ions/cm$^2$ in ***Vernazza et al. (2009)***. The authors observed a very weak reddening and an albedo decrease lower than 3%, versus the 5-16% we observed after He irradiation and the 11-22% after C irradiation. We observe that, for aubrites, C has a stronger darkening effect than He, suggesting that the spectral changes depend on the type of implanted ion. On the other hand, the low degree of darkening and reddening observed for Eagle enstatite chondrite is unlikely related to the use of $Ar^+$ as space weathering agent: experiments on silicates, ordinary chondrites, and HED achondrites irradiated with Ar evidenced strong darkening and reddening (e.g., ***Brunetto & Strazzulla, 2005;***

***Fulvio et al., 2012; Strazzulla et al., 2005***). Moreover, heavier ions should produce stronger darkening and reddening than lighter ions, at comparable fluences (***Brunetto & Strazzulla, 2005***). Therefore, the sample composition and the darkening/reddening causes must be taken into account. One of the proposed causes for darkening and reddening airless bodies surfaces is the formation of $npFe^0$ (***Cassidy & Hapke, 1975; Hapke, 1979; Hapke, 2001; Pieters & Noble, 2016***). Silicates in enstatite chondrites are essentially FeO-free, and the iron necessary for the formation of $npFe^0$ may be provided by sputtering processes just on the metallic Fe,Ni phase and Fe sulphides (***Vernazza et al., 2009***). In the case of aubrites, metallic Fe,Ni phases are present only in trace amounts, sulphides in minor amounts, and the FeO content in silicates is very low (up to 0.3 wt%). Even though additional minor amounts of FeO might be present in the samples due to terrestrial alteration, the formation of $npFe^0$ alone is probably not the first cause of darkening and reddening in these meteorites, considering the greater effects compared to the Eagle enstatite chondrite. This is confirmed by laser irradiation effects on Norton County aubrite studied by ***Zhang et al. (2022)***: they found that the aubrite irradiated surface shows an amorphous layer but no presence of metallic iron particles, observed for the other investigated meteorites, including two enstatite chondrites. Moreover, it was suggested that $npFe^0$ forming iron sputtering becomes very significant for ion irradiation fluences above $10^{18}$ ions/cm² and that at lower fluences the primary cause of darkening and reddening might be the amorphization of the upper layers of the irradiated surface (***Brunetto & Strazzulla, 2005***).

The mineralogy, chemical composition, and surface texture play a major role in the spectral changes caused by space weathering (e.g., ***Caminiti et al., 2024; Chrbolková et al., 2021; Fulvio et al., 2012; Lantz et al., 2017***). However, in this work, all the investigated samples are aubrites with similar mineralogy and composition. We observed that ion irradiation-induced darkening depends on the used ions: $C^+$ ions implantation produces stronger darkening than $He^+$ ions. As already suggested by previous studies, C greater efficiency might be caused by the implanted ions forming nanoclusters that darken the surface (***Fulvio et al., 2012***). The effect is slightly stronger for pellets than for rock fragments, but no major differences were observed. On the contrary, the reddening effect is much more dependent on the sample state (pellets or rock fragments) than on the type of ion used: the effects induced by He and C are similar, while they are much stronger for pellets than for rock fragments. This could be related to the different surface roughness and scattering properties of the two surface forms.

### 4.4.2. MIR spectral effects

The observed spectral contrast reduction and CFs and RBs red shifts caused by ion irradiation have already been observed in previous studies. The spectral contrast reduction is linked to the sample partial amorphization (***Brucato et al., 2004***). The red shifts are of the same order of magnitude as the shifts observed by ***Brunetto et al. (2014)*** in a carbonaceous chondrite (Allende) and by ***Caminiti et al. (2024)*** in terrestrial komatiites and boninites $He^+$ irradiated. The shifts are similar for all the samples, and the largest shift is registered for the main RB (~ 10.5 μm), which is consistent with previous studies (***Brunetto et al., 2014; Caminiti et al., 2024; Lantz et al., 2017***). He irradiation induces a shift twice as large as the one produced by C. The CFs should undergo the same shifts as the RBs (***Brunetto et al., 2020***); in our samples, we observed CFs shifting a bit differently among the different samples. ***Caminiti et al. (2024)*** suggest that the CFs behaviour may be influenced by amorphization.

### 4.4.3. Carbon presence in the fresh sample

Ion irradiation effects in the VNIR spectra are similar for pellets of distinct samples, except PBS, which exhibits more pronounced darkening, affecting the whole spectral range, and faster reddening, already evident after the first irradiation fluence for both $C^+$ and $He^+$ implantation (**Fig. S4.2**). The mineralogical and compositional differences among PBS and the other samples cannot explain the distinct spectral response to irradiation, since the variability between PBS and the other aubrites is comparable to that among the other aubrites themselves. The only major difference is the detection of organics-related features (1.7 μm, 2.3 μm, 3.4 μm, **Fig. 4.1k,l** and **Fig. S4.1**) in PBS spectra. These observations suggest that the main factor responsible for the distinct spectral effects is the presence of C-bearing molecules and organics in the initial sample. ***Lantz et al. (2017)*** proposed that in carbonaceous chondrites, the darkening effect is higher in the meteorites containing higher C (wt%). C, in graphite form, mixed with silicates leads to a reduction in the albedo, and this effect is particularly pronounced for silicates with very low iron content (***Bruschini et al., 2022***) and in the case of internal mixing (***Penttilä, 2025***). Space weathering simulations on FeO-free enstatite mixed with carbon black lead to more pronounced spectral changes after laser irradiation compared to pure enstatite (***Shackelford et al., 2025***). However, in this case, the larger changes are primarily observed in the spectral slope rather than in the darkening of the material. ***Bruck Syal et al. (2015)*** performed hypervelocity impact experiments to simulate micrometeorite bombardments on Mercury's surface and noted that in the silicate sample mixed with organics, the impact created much darker agglutinates than in the organics-free sample, with the formation of opaque carbon. The creation of these dark carbon agglutinates could explain the more effective

darkening in PBS compared to the other samples. Nevertheless, further investigation is needed to evaluate the influence of preexisting carbon in the samples as a potentially more effective darkening agent under ion irradiation.

It should also be noted that the features at 1.7 μm and 2.3 μm do not present spectral attenuation, but the spectra in that region present progressive darkening with increasing fluences, while no modifications are observed for the organics band at 3.4 μm (**Fig. S4.1**). This is probably because at this wavelength the measured reflectance originates from deeper layers not affected by ion irradiation (***Lantz et al., 2015***), confirming that the 3.4 μm in remote sensing data of planetary surfaces may be one of the least affected by space weathering.

### 4.4.4. Implications for Mercury

In this work, we found that highly reduced materials containing very little FeO, such as aubrites, experience significant darkening and reddening after ion irradiation. The primary cause for these spectral variations might be the amorphization of the upper layers of the irradiated sample. Moreover, ion irradiation seems to induce greater effects if carbon is present in the irradiated object. These results are relevant for the study of Mercury's surface spectra, as carbon is inferred to be present on the planet's surface (1.4 ±0.9 wt%, ***Peplowski et al., 2015***). The carbon can be endogenic (***Vander Kaaden & McCubbin, 2015***) or exogenic from solar wind irradiation and impactors (***Bruck Syal et al., 2015***). The inferred iron contents on the planet's surface are low (up to 4 wt%, ***Nittler et al., 2011***; of which FeO on silicates is estimated <1 wt%, ***Murchie et al., 2015***). However, it was suggested that the efficiency and rate of space weathering processes may result in the formation of $npFe^0$ in amounts even greater than those observed on the Moon, in different abundances depending on the original quantity of FeO in the diverse geochemical units of the surface (***Domingue et al., 2014***). ***Lucey and Riner (2011)*** stated that most of the iron present on the surface has been converted into $npFe^0$ of various sizes, leading to different spectral effects. Smaller $npFe^0$ (<10 nm) leads to darkening and reddening, larger $npFe^0$ (>40 nm) produces darkening alone (***Noble et al., 2007***). Nonetheless, modeling suggests that, beside $npFe^0$, other darkening agents must be involved in the spectral changes induced by space weathering, such as amorphous carbon (***Bruck Syal et al., 2015; Trang et al., 2015***) and opaque compounds containing S (***Domingue et al., 2014***), considering the high amount of Sulphur estimated on the surface (4 wt%, ***Nittler et al., 2011***).

Previous studies suggested that SpWe could produce different spectral changes across the distinct Mercury's geochemical terranes (***Caminiti et al., 2024***). It has been observed, for example, that forsterite is more sensitive to darkening and reddening than pyroxene (e.g., ***Chrbolková et al.,***

***2021***) and that samples containing less iron are more sensitive to darkening and reddening (***Caminiti et al., 2024***). In this work, we propose that pre-existing carbon in the sample prior to irradiation may amplify spectral darkening following ion irradiation.

The main RB shifts observed in the MIR range are intense enough to exceed MERTIS spectral resolution (90 nm, ***Hiesinger et al., 2020***), therefore they could be detected by the instrument, as already suggested by ***Caminiti et al. (2024)*** in their ion irradiation study on terrestrial analogues. Since we observe similar band shifts for highly reduced extraterrestrial analogues, these effects must be taken into account when retrieving surface composition from MERTIS spectra, as they can bias the mineral identification.

### 4.5. Conclusions

The spectral changes induced by $He^+$ and $C^+$ ion irradiation on aubrites, simulating solar wind irradiation, are the following:

- Darkening and reddening in the VNIR spectral range. C is more effective in producing darkening. Reddening after the last irradiation fluence, on the other hand, is similar for both ions, while it is quite different between pellets and rock fragments. Having these samples similar mineralogy and chemical compositions, the differences in the spectral modifications induced by the two ions are due to the different nature of the atoms themselves. Moreover, we observed that the target material form plays a role in the spectral modifications induced by ion irradiation.
- Darkening effect is greater when carbon is present in the target sample, even in small amounts.
- Red shifts of RBs and CFs, especially for the main RB, in the MIR spectral range. The biggest shift is observed for the main RB, being twice as large with He irradiation as with C irradiation, and it is similar for all the investigated samples.

Since aubrites are considered one of the most promising analogues of the Mercurian surface, these findings provide further insights into how solar wind irradiation may influence the planet's reflectance spectra. However, Mercury's surface is influenced by multiple and complex SpWe, and the comprehensive investigation carried out by the BepiColombo mission will provide new valuable data on how these processes affect the planet's surface.

# 5. From Earth to Mercury: Compositional, Reflectance Spectroscopy, and Emissivity Studies on Boninites as Surface Natural Analogues

This chapter is a published paper in Journal of Geophysical Research: Planets by A.I. Landi, C. Carli, A. Maturilli, G. Alemanno, O. Barraud, F. Capaccioni, and G. Pratesi.

Authors contribution
Writing – original draft: A.I.L.; Methodology: A.I.L., C.C., A.M., G.A.; Investigation: A.I.L., C.C.; Formal analysis: A.I.L., C.C.; Conceptualization: A.I.L., C.C., O.B., F.C., G.P.; Writing – review & editing: C.C., G.A., O.B., G.P.; Supervision: C.C., A.M., G.A., G.P.; Funding acquisition: F.C.; Validation: O.B.; Resources: G.P.; Project administration: G.P.

**Abstract**

Boninites are high-magnesium volcanic rocks proposed as terrestrial analogues for Mercury's surface, based on elemental data from NASA's MErcury Surface, Space ENvironment, GEochemistry, and Ranging (MESSENGER) mission. In this study, we investigate boninite samples from the Troodos Massif (Cyprus) using a multi-methodological approach to characterize their mineralogical, chemical, and spectroscopic properties, including reflectance and emissivity spectra. Geochemical analyses confirm that the bulk composition of the samples closely matches Mercury's geochemical terrains in terms of $SiO_2$, MgO, and $Al_2O_3$ content, though FeO concentrations are higher (~8 wt% vs 1–2 wt%). Samples from different localities show some mineralogical differences but generally contain less orthopyroxene and albitic plagioclase than expected on Mercury, along with hydrated minerals from aqueous alteration, which are not expected on the planet's surface. Reflectance spectra in the ultraviolet (UV), visible (VIS), and near-infrared (NIR) range show major absorption features around 1 µm, associated with mafic minerals, and minor bands at ~1.4 µm, ~1.9 µm, and 2.2–2.3 µm, linked to hydrated phases, with spectral variations reflecting mineralogical differences. In the mid-infrared (MIR) range and emissivity spectra, we observe Christiansen Features (CF) and Reststrahlen Bands (RB) at different positions, mainly influenced by plagioclase content, and shifts in emissivity minima with increasing temperature. Spectral differences between the boninites and Mercury mainly result from the intrinsic mineralogy of the samples. Nonetheless, Troodos boninites represent the best Mercury analogue currently available on Earth, and understanding their spectral behaviour in relation to their mineralogy could support future investigations with ESA's BepiColombo mission.

## 5.1. Introduction

Boninites are porphyritic rocks presenting a distinctive chemical composition characterized by SiO2> 52%, MgO> 8% and TiO2< 0.5% (***Le Bas, 2000***). Their mineralogical assemblage mainly consists of olivine, orthopyroxene, and clinopyroxene phenocrysts embedded in a glassy or finely crystalline groundmass (***Crawford et al., 1989***). Plagioclase is absent in boninites sensu strictu (***Taylor et al., 1994***), but it may occur as phenocrysts in certain boninitic lavas (***Taylor et al., 1994***) or as a component of the groundmass in more evolved and slowly cooled boninites (***Crawford et al., 1989***). These rocks originate in forearc tectonic settings, where they form through hydrous partial melting of the mantle within a supra-subduction zone, at shallow depths and under low-pressure conditions (***Arndt, 2003; Cameron et al., 1983; Crawford et al., 1989***).

Boninites (***Vander Kaaden & McCubbin, 2016; Vander Kaaden et al., 2017***), along with komatiites (***Nittler et al., 2011; Weider et al., 2015***) and norites (***McCoy et al., 2018; Stockstill-Cahill et al., 2012***) have been proposed as terrestrial analogues for different regions of Mercury's surface, known as geochemical terranes (***Weider et al., 2015***), on the basis of the geochemical data from NASA's MESSENGER (MErcury Surface, Space ENvironment, GEochemistry and Ranging) mission (***Solomon et al., 2001***). The chemical analysis of the surface from the X-Ray Spectrometer (XRS) and Gamma-Ray and Neutron Spectrometer (GRNS) evidenced an overall elemental distribution characterized by high Si and Mg/Si ratio, low Al/Si and Ca/Si, low Fe, and variable but abundant and widespread Na, K, S and Cl; highly volatile species (H included) are present but confined to the permanently shadowed polar regions (***Evans et al., 2012, 2015; Nittler et al., 2011, 2018; Nittler & Weider, 2019; Peplowski et al., 2012a , 2012b, 2014, 2015, 2016; Weider et al., 2012 , 2014, 2015, 2016***). In particular, the high Mg/Si ratio leads to the suggestion of similarity with terrestrial komatiites, while the higher $SiO_2$ of some regions suggests more accurate similarity with terrestrial boninites: the petrologic classification from ***Vander Kaaden et al. (2017)*** suggests that the nine geochemical regions can be assigned as komatiites or boninites. Despite some differences, the comparison between these terrestrial rocks and Mercury's surface can provide a better understanding of planetary crusts formed under different conditions than Earth's crust conditions. Specifically, two significant differences must be taken into account: Mercury's surface presents a notably high S concentration, ~4 wt%, which is much higher than the <0.1 wt% in Earth's crust, and it exhibits a very low Fe concentration, 1-2 wt%, compared to the terrestrial 4-8 wt%. Of this Fe on Mercury's surface, FeO is inferred to be <1 wt% from reflectance spectroscopy studies (***Murchie et al., 2015***). These S and Fe concentrations reflect the highly reduced nature of the planet with an oxygen fugacity (fO2) estimated to be in the range 2.6-7.3 log units below the iron-wüstite buffer (***McCubbin et al., 2012; Namur et al., 2016; Zolotov et al., 2013***).

Also, the forming processes of terrestrial and Mercurian boninites are different: on Earth boninites form through arc magmatism and in hydrous conditions (***Cameron et al., 1983***), while it has been suggested that on Mercury they form through partial melting of a shallow portion of Mercurian mantle composed of a mineral assemblage (forsterite, orthopyroxene, and albitic plagioclase) that did not experience hydrous and oxidizing conditions (***Vander Kaaden & McCubbin, 2016***).

The inferred mineralogy of Mercury's surface is mostly composed of enstatite, forsterite, albitic plagioclase, and Mg-C-Fe sulphide assemblages (e.g., ***Namur & Charlier, 2017; Nittler & Weider, 2019***). Also, graphite is present on the planet's surface: C has an estimated average concentration of 1.4 ±0.9 wt% (***Peplowski et al., 2015,*** 1–3 wt% in the lower reflectance material regions (***Peplowski et al., 2016***). ***Vander Kaaden and McCubbin (2015)*** suggested that C must be in the form of graphite: C escaped from core capture may have formed a primary graphite floatation crust in the cooling of the magma ocean. Boninites, when unaltered, are mainly composed of clino- and orthopyroxene, olivine, glass, and plagioclase. This suggests a good mineralogical correlation with Mercury's surface, yet the spectral comparison is complicated by two factors: the higher FeO content in terrestrial silicates (up to 12 wt% in olivine, up to 15 wt% in orthopyroxene, up to 11 wt% in clinopyroxene, e.g., ***Cameron, 1985, Taylor et al., 1994***) and the alteration process, which can extensively change the mineralogy of terrestrial boninites. In fact, boninites are pervasively affected by hydrothermal alteration resulting in the formation of secondary minerals (serpentine, chlorite, clay minerals, calcite, zeolite) replacing olivine and pyroxene. These two factors lead to differences in the reflectance spectra features of terrestrial boninites and Mercury's surface. Moreover, the common and pervasive alteration of boninites, their spectral similarity with other mafic and ultramafic rocks and their rarity on Earth make it difficult to detect the spectral properties of these rocks from terrestrial remote sensing. Thus, studying selected boninite samples through laboratory measurements and a multimethodological approach is essential for an insightful comparison with Mercury's surface.

With the ongoing ESA/JAXA BepiColombo mission (***Benkhoff et al., 2021***), new compositional and mineralogical data of Mercury's surface will be retrieved, and the study of both natural and synthetic analogue materials remains crucial. Recent studies have investigated various analogues using different analytical techniques, including: reflectance spectroscopy in the visible to near-infrared (VNIR) range (e.g.,, ***Burbine et al., 2002; Cantillo et al., 2024; Cloutis & Gaffey, 1993; Cloutis et al., 2016; Dibb et al., 2022; Landi et al., 2025***) and in the mid-infrared (MIR) range on aubrites (***Markus et al., 2018; Morlok et al., 2020***) as well as on synthetic glass and mixtures (***Bruschini et al., 2022; Morlok et al., 2017, 2021, 2023; Weber et al., 2023***). Additionally, visible-VNIR-MIR reflectance spectroscopy has been applied to synthetic mixtures (***Carli et al.,***

***2025***), while VNIR-MIR reflectance spectroscopy and emissivity studies have focused on terrestrial komatiites (***Carli et al., 2013; Maturilli et al., 2014***) and VNIR reflectance spectroscopy on terrestrial boninites ***(Mari et al., 2023***). The emissivity of both natural (***Ferrari et al., 2014; Helbert et al., 2013***) and synthetic materials of varying compositions (***Bott et al., 2023; Carli et al., 2024a; Ferrari et al., 2020***) has also been investigated. Furthermore, space-weathering simulations have been conducted on terrestrial komatiites and boninites (***Caminiti et al., 2024***). In preparation for the interpretation of BepiColombo's incoming data, a blind sample simulating Mercury's regolith has also been developed for analysis using multiple analytical techniques (***Barraud et al., 2025***).

In this study, we characterize the mineralogy and chemical composition of terrestrial boninite samples and investigate their spectral properties using visible (VIS)-VNIR-MIR reflectance and thermal-infrared (TIR) emissivity studies, simulating Mercury's surface conditions. The correlation between the spectral properties and the mineralogy and chemical composition of these terrestrial analogues gives a contribution to the existing database of Mercury analogues in preparation for the interpretation of the data expected from SIMBIO-SYS/VIHI (Spectrometer and Imaging for MPO BepiColombo Integrated Observatory SYStem/Visible and near-Infrared Hyperspectral Imaging channel) and MERTIS (Mercury Radiometer and Thermal Infrared Spectrometer) instruments onboard the ESA's BepiColombo mission (***Cremonese et al., 2020; Hiesinger et al., 2020***).

## 5.2. Samples and analytical methods

### 5.2.1. Geological setting and samples

The samples were collected from three localities of the Troodos Massif, Cyprus. The Troodos Massif is a product of supra-subduction zone (SSZ) magmatism (e.g., ***Osozawa et al., 2012; Pearce et al., 1984; Pearce & Robinson, 2010***). It extends for ca 3000 km2 in the central part of the island. It is one of the best-preserved ophiolites and presents the typical ophiolite sequence, superimposed by layered gabbros, a sheeted dike complex, and an extrusive volcanic series covered by Cretaceous sedimentary rocks (e.g., ***Gass, 1968; Moores & Vine, 1971***). The extrusive volcanic series has been divided into two main series: the upper pillow lavas (UPL) and the lower pillow lavas (LPL) (e.g., ***Pearce & Robinson, 2010***). The UPL corresponds to boninitic lavas (e.g., ***Cameron et al., 1979***) erupted after the LPL tholeiitic lavas (e.g., ***Osozawa et al., 2012***). The boninitic lavas are present in proximity of the E-W trending Arakapas transform fault zone (AFZ)

(e.g., ***Osozawa et al., 2012; Pearce & Robinson, 2010***), and near the Parekklisia village (***Woelki et al., 2018***).

The samples were collected in three different spots located next to Arakapas (Lat. 34°50.6560N, Long. 33°07.1870E), Parekklisia (Lat. 34°45.5270N, Long. 33°09.6300E), and Athrakos (Lat. 34°50.5970N, Long. 33°04.0010E). According to the geologic map of the southern Troodos transform fault zone (***Geological Survey Department, Nicosia, Cyprus***), the collection spots near Arakapas and Parekklisia correspond to vitrophyric pillow lavas, while the spot near Athrakos corresponds to a sheeted dike complex. The accuracy in the sampling spots choice was essential because distinguishing tholeiitic lavas (LPL) from boninitic lavas (UPL) is not straightforward in the field (e.g., ***Osozawa et al., 2012***). Almost all the rocks from the different localities show signs of weathering; therefore, fragments from the least altered portions of the rocks were selected for this work. The selected samples show different characteristics (**Figure S5.1**): samples from Parekklisia (referred to as PARn in this work) exhibit glass portions, which are not observed in the samples from Arakapas (referred to as ARAn) or in those from Athrakos (referred to as ATHn). The latter are much more fragile and richer in vesicles than the others. The glassy portions of Parekklisia samples were investigated by means of microprobe analysis to determine the chemical composition of the glass. No other analyses were performed on these portions, which will be the subject of future studies[2].

### 5.2.2. XRF

X-ray Fluorescence (XRF) analyses were performed at the "Centro di Servizi di Cristallografia Strutturale (CRIST)" of the University of Firenze, with a *Rigaku ZSX Primus II* WDS spectrometer. Two PAR and ARA samples and one ATH sample were powdered for the analyses. The unsorted powders were left in the oven at 100°C for one hour. Mixtures of sample powder and lithium tetraborate ($Li_2B_4O_7$) powder in a proportion of 1 part to 10 were used to prepare glass beads. Glass beads 30 mm in diameter were produced using an *xrFuse1* instrument with a maximum

[2] See Appendix B.

temperature of 1000°C. Operating conditions were an accelerating voltage of 50 kV and beam current of 60 mA.

### 5.2.3. SEM and EPMA

Fragments of one representative sample for each locality were chosen and embedded in epoxy resin to perform scanning electron microscope (SEM) and electron probe microanalysis (EPMA). SEM analyses were performed at the "Centro di Servizi di Microscopia Elettronica e Microanalisi (MEMA)" of the Università degli Studi di Firenze using a *ZEISS EVO-MA15* equipped with an Oxford *ULTIM MAX* 40 $mm^2$ EDS (Energy Dispersive Spectroscopy) detector and Oxford Symmetry EBSD (Electron Backscattered Diffraction) detector. An accelerating voltage of 15 kV was used to collect point analyses; pure Co standard was used for the calibration of the semiquantitative chemical data. Quantitative analyses of the detected mineral phases were performed at "Filippo Olmi" laboratory, Dipartimento di Scienze della Terra of the Università degli Studi di Firenze, using a *JEOL JXA-8230* Electron Microprobe equipped with five wavelength-dispersive spectrometers (WDS). The operating conditions (accelerating voltage, beam current, beam size, correction) and the used certified standards (Astimex, Smithsonian, MAC) are summarized in **Table S5.1**. Modal abundances of the detected phases were obtained with XMapTools 4.1 (***Lanari et al., 2014***) starting from EPMA-WDS maps of Mg, Fe, Ca, Na, Al, Si, Ti. Operating conditions for WDS maps acquisition were 15 kV accelerating voltage, 50 nA beam current, 20 s dwell time, beam size <3 μm.

### 5.2.4. Reflectance spectroscopy

The samples analysed with XRF were studied by means of reflectance spectroscopy and emissivity. For spectroscopy studies, the samples were accurately sieved at the S.LAB. laboratory of the Istituto Nazionale di Astrofisica (INAF)- Istituto di Astrofisica e Planetologia Spaziali (IAPS), Rome. For one of the PAR samples, four grain sizes were analysed: 250-150 μm, 150-63 μm, 63-36 μm and <36 μm, for all the others, only the finest grain size was considered. The decision to study grain-size-dependent spectral variations on one of the PAR samples was based on the fact that PAR samples are the least affected by alteration. Reflectance spectra were acquired in the ultraviolet (UV)-VNIR range (0.35-2.50 μm) with a *Fieldspec Pro*® spectrophotometer mounted on the goniometer at the S.LAB. laboratory. The illumination (*i*) and collection (*e*) angles were 30° and 0°, respectively.

Reflectance in the VIS range (0.45-1.05 μm), NIR range (0.6-2.6 μm), and MIR range (1.25-25 μm) were taken with a Bruker *Vertex 80V FTIR* spectrometer at the Planetary Spectroscopy

Laboratory (PSL) of German Aerospace Center (DLR), Berlin. All the measurements were taken in low vacuum (0.7 mbar). The angles were *i*=30°, *e*=0° and *i*=30°, *e*=60°. Reflectance spectra were taken on the fresh samples and on the heated samples after the emissivity measurements. The VNIR spectra (from 0.45 μm) obtained with the two setups are highly consistent; however, we chose to present in this study the spectra acquired with the Bruker *Vertex 80V FTIR* spectrometer due to its superior resolution and smaller spot size. The continuum line was created by connecting the reflectance maxima in the spectrum with straight-line segments as a function of wavelengths (***Clark & Roush, 1984***). After removing the continuum, the band center is defined as the point where the reflectance reaches its minimum within the band. The band depth is calculated as 1-(R/C), R being the original reflectance and C the continuum reflectance.

### 5.2.5. Emissivity

Emissivity measurements were taken at PSL. Powdered samples were put in the emissivity chamber in stainless steel cups, covering the cup surface with ~3 mm thickness, and heated with an induction system. Temperature sensors were placed in contact with the cup and with the sample to monitor the sample temperature during the whole experiment. In addition, samples can be visually monitored with a webcam placed in the emissivity chamber (***Helbert & Maturilli, 2009***; ***Helbert et al., 2013, Maturilli et al., 2017***). The chamber is attached to a *Bruker Vertex 80V FTIR* spectrometer with a MCT HgCdTe detector (cooled with liquid nitrogen) and KBr beamsplitter. Both chamber and spectrometer can be evacuated (down to 0.7 mbar). Emissivity spectra were acquired between 1.25 μm and 25 μm with a spectral resolution of 4 cm-1 at four temperatures, 150°C, 250°C, 350°C, and 450°C. A black body sample (graphite) has been measured in the same operating conditions, at several temperature steps, covering the whole temperature range of the sample measurements, and used for the data calibration. The absolute emissivity of the sample is obtained with the formula $E=I(T)/BB(T)*E_{BB}$, I(T) being the sample's radiance at a certain temperature (T), BB(T) the black body radiance at a certain temperature (T) and $E_{BB}$ the black body emissivity spectrum (***Ferrari et al., 2014***).

## 5.3. Results

### 5.3.1. Bulk composition

The whole-rock geochemistry of the samples is reported in **Table 5.1**. All the samples can be defined as boninite sensu strictu, having $SiO_2$>52 wt%, MgO>8 wt% and $TiO_2$<0.5 wt% (***Le Bas, 2000***). PAR samples are enriched in CaO (12 wt%) compared to ARA and ATH samples (5 and 9

wt%, respectively). The glass portion has slightly lower MgO content (9 wt%) than the rock (12 wt%). ARA samples are enriched in $Na_2O$ (5 wt%) compared to the others (<1 wt%). ATH samples are the ones with the highest MgO content (18 wt%) and the lowest $Al_2O_3$ content (9 wt%). FeO contents are similar (7-8 wt%) in all the samples.

| | $SiO_2$ | $TiO_2$ | $Al_2O_3$ | FeO | MnO | MgO | CaO | $Na_2O$ | $K_2O$ | V | Cr | Ni | Cu | Zn | Total |
|---|---|---|---|---|---|---|---|---|---|---|---|---|---|---|---|
| **G (PAR)** | 52.42 (0.23) | 0.32 (0.01) | 13.91 (0.13) | 7.37 (0.11) | 0.15 (0.04) | 8.93 (0.12) | 12.49 (0.10) | 0.79 (0.05) | 0.10 (0.01) | 0.04 (0.01) | 0.07 (0.02) | b.d. | b.d. | b.d. | 96.75 (0.20) |
| **PAR2** | 54.11 (1.08) | 0.32 (0.01) | 13.53 (0.68) | 8.18 (0.08) | 0.15 | 11.90 (0.60) | 12.09 (0.12) | 0.51 (0.03) | 0.23 | 0.02 | 0.08 | 0.03 | 0.01 | b.d. | 100.06 |
| **PAR1** | 52.71 (1.05) | 0.30 (0.01) | 13.02 (0.65) | 7.89 (0.08) | 0.15 | 11.12 (0.56) | 11.53 (0.12) | 0.50 (0.03) | 0.14 | 0.02 | 0.08 | 0.03 | 0.01 | b.d. | 98.48 |
| **ARA1** | 54.39 (1.09) | 0.34 (0.01) | 14.69 (0.73) | 7.53 (0.08) | 0.08 | 9.06 (0.45) | 5.83 (0.06) | 5.01 (0.25) | 0.10 | 0.03 | 0.01 | 0.01 | 0.01 | 0.01 | 97.96 |
| **ARAD** | 55.33 (1.11) | 0.36 (0.01) | 15.53 (0.78) | 8.43 (0.08) | 0.12 | 7.25 (0.36) | 4.85 (0.05) | 5.39 (0.27) | 0.10 | 0.03 | 0.01 | 0.01 | 0.01 | 0.01 | 98.43 |
| **ATH1** | 52.43 (1.03) | 0.18 (0.01) | 8.94 (0.45) | 7.46 (0.07) | 0.15 | 17.85 (0.89) | 9.73 (0.10) | 0.48 (0.02) | 0.04 | 0.02 | 0.16 | 0.04 | b.d. | b.d. | 97.17 |

Table 5.1. Whole-rock geochemistry (wt%) of the investigated samples. Acquired with XRF, expect for the glass (G) of PAR samples, measured with EPMA. Standard deviation in brackets. b.d.= below detection limit.

### 5.3.2. Texture and mineralogy

PAR samples show black glass covering the rock (**Figure S5.1**). The glass composition is: $SiO_2$ 52 wt%; $TiO_2$ 0.3 wt%; $Al_2O_3$ 14 wt%; FeO 7 wt%; MgO 9 wt%; CaO 12 wt%; $Na_2O$ 0.8 wt%; $K_2O$ 0.1 wt%; MnO 0.1 wt%. The rock has a vitrophyric texture with olivine and clinopyroxene phenocrysts in glassy groundmass (**Figure 5.1**). The groundmass represents 55% of the samples, the phenocrysts the 45%: clinopyroxene is the most abundant phase (29%), followed by olivine (13%) and then calcite (3%), which is a product of weathering. The groundmass average composition is: $SiO_2$ 57 wt%; $TiO_2$ 0.3 wt%; $Al_2O_3$ 19 wt%; FeO 5 wt%; MgO 2 wt%; CaO 9 wt%; $Na_2O$ 1 wt%; $K_2O$ 0.2 wt%; MnO 0.1 wt%. Olivine phenocrysts (average composition $Fo_{89}$), up to 300 μm, often show zoning with an increase of FeO content (10 wt% to 18 wt%) from cores to rims, and some of them have an augitic rim ($En_{28}Wo_{51}Fs_{21}$). Clinopyroxene phenocrysts have elongated, up to 600 μm in length, and often skeletal shapes (average composition $En_{48}Wo_{38}Fs_{14}$), or they are present as not elongated, smaller (max 50 μm) grains (average composition $En_{64}Wo_{24}Fs_{12}$). In both cases, crystals show zoning with an increase of CaO (6 wt% to 19 wt%) from core to rim. Abundant clinopyroxene acicular microcrystals (average composition $En_{34}Wo_{42}Fs_{24}$) are present in the glass. Plagioclase crystals are not detected. Opaque minerals are present as accessory phases and are represented mostly by chromite, commonly as inclusions in olivine, and pyrite, as inclusions in clinopyroxene microcrystals (**Figure 5.1c**). Only minor weathering is visible, mostly represented by sporadic calcite grains (up to 500 μm).

ARA samples are composed of an albitic ($Ab_{98}An_2$) groundmass (50%) with clinopyroxene grains (average composition $En_{47}Wo_{40}Fs_{13}$) up to 300 μm (22%), clinochlore grains up to 500 μm (25%),

and prehnite grains up to 100 μm (3%) (**Figure 5.1**). Minor micrometric titanite grains are present. Opaque minerals are mostly represented by Fe-Ti oxides, with minor pyrite. Olivine is not detected. The weathering in these samples is more advanced, as indicated by clinochlore replacing primary mineral grains and occupying interstitial spaces.

ATH samples are holocrystalline and composed of euhedral clinopyroxene (average composition $En_{49}Wo_{41}Fs_{10}$) and orthopyroxene (average composition $En_{82}Wo_{4}Fs_{14}$) crystals up to 300 μm surrounded by plagioclases presenting a wide range of compositions (from $Ab_{96}An_{4}$ to $Ab_{6}An_{94}$) (Figure 1). Occasional micrometric titanite grains were observed. Opaque minerals are Fe-Ti oxides and chromite. Olivine is not detected. In these samples, the weathering is more intense, and it is not uniform throughout the sample: some areas are fully altered and consist entirely of clay minerals, while others show only minor amounts of clay minerals in the interstitial spaces. The less

altered portions are composed mostly of anorthite (35%), followed by clinopyroxene (27%), orthopyroxene (26%), clay minerals (7%), and albite (4%).

The chemical composition of all the detected minerals and their percentage in the different samples are summarized in **Table 5.2**.

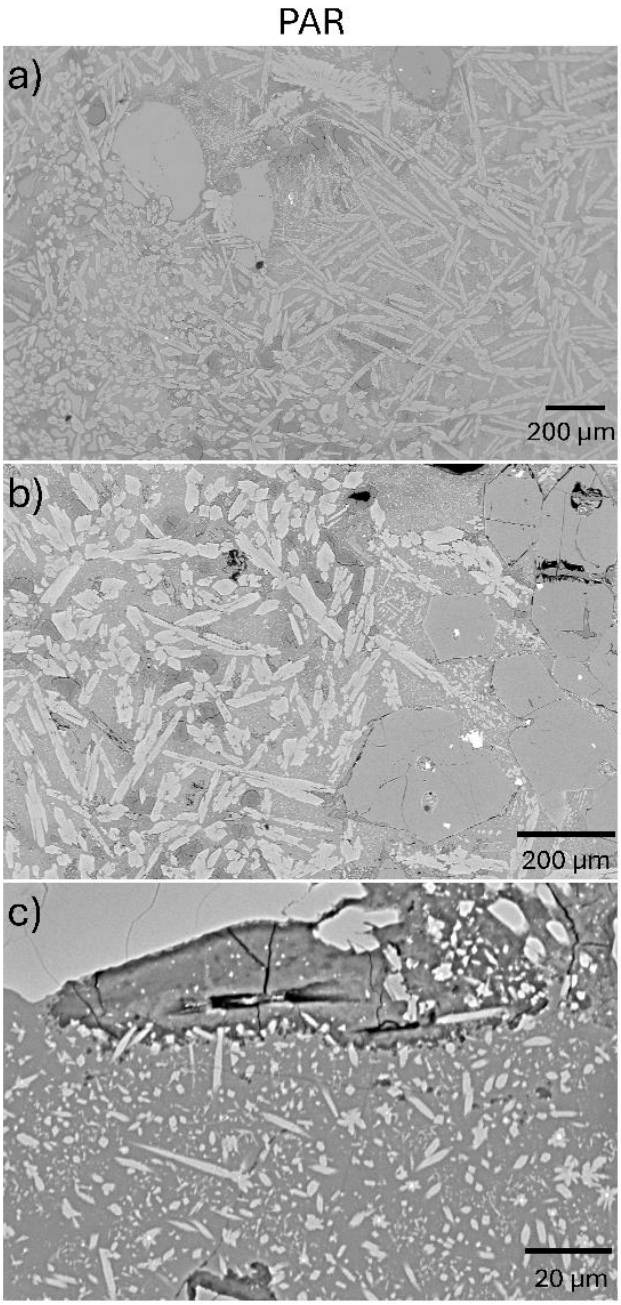


Figure 5.1. a) Vitrophyric texture of PAR samples. Clinopyroxenes in different shapes can be observed: elongated, skeletal, rounded, needle shaped. The big grains in the upper left are examples of calcite grains. b) higher magnification on PAR mineralogy: in addition to the other phases, euhedral olivine crystals can be observed. c) higher magnification on clinopyroxene microcrystals in PAR samples often showing pyrite inclusions. d) ARA samples textures: albitic groundmass with clinopyroxenes, clinochlore and prehnite grains. e) higher magnification on ARA samples texture. f) association of prehnite (lower left), clinochlore (middle), and clinopyroxene (upper right) in ARA samples. g) ATH sample showing intense weathering (right side). h) higher magnification on a less weathered portion of ATH sample showing plagioclases (mostly anorthite) and clino- and orthopyroxenes. i) higher magnification on clay minerals replacing the original mineralogy in ATH samples. BSE images acquired with a JEOL JXA-8230 Electron Microprobe (a, d) and a ZEISS EVO-MA15 scanning electron microscope (b, c, e, f, g, h, i).

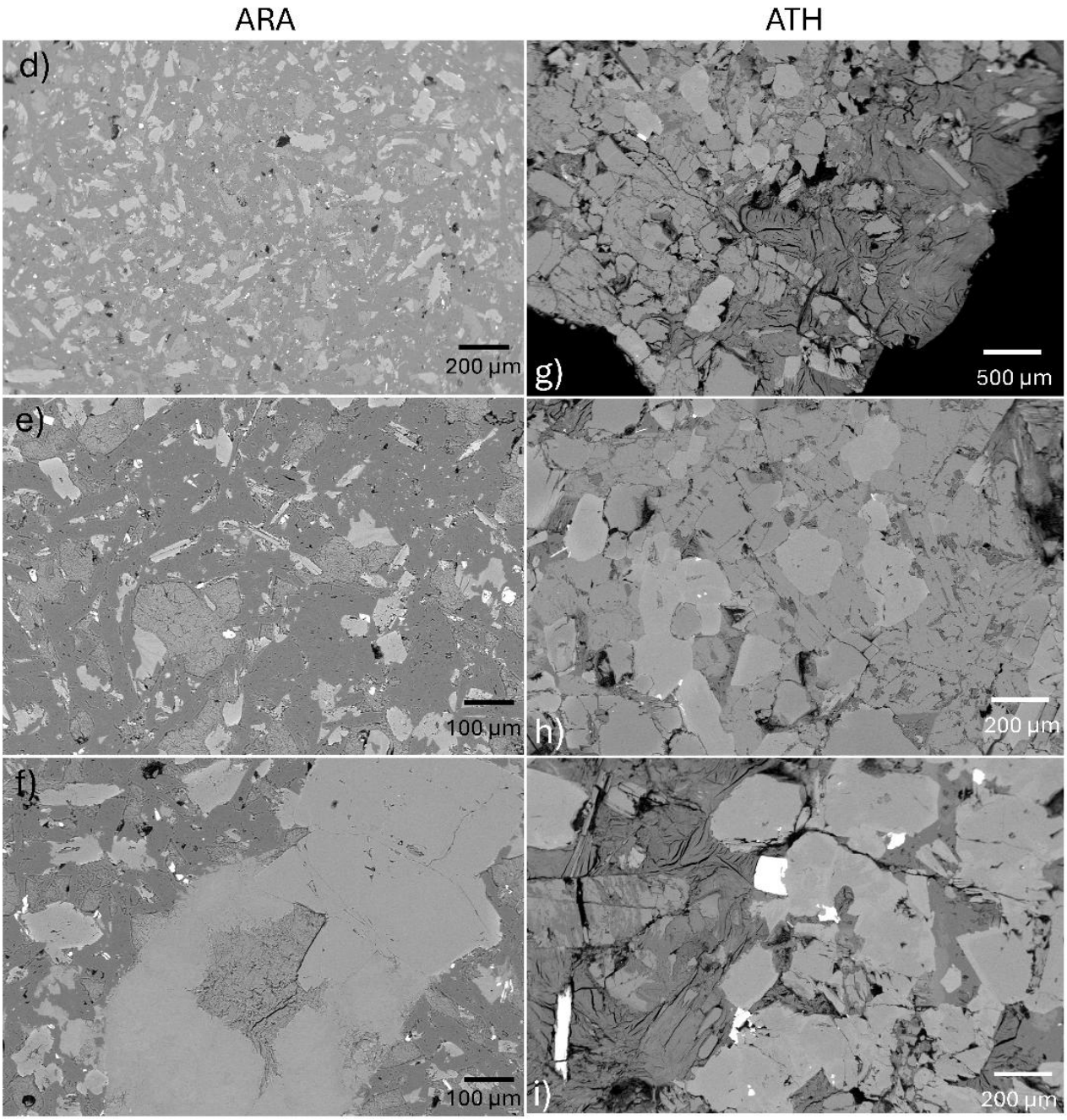


Figure 5.1. continue.

| | phase | % | n. | $SiO_2$ | $TiO_2$ | $Al_2O_3$ | $Cr_2O_3$ | FeO | $Fe_2O_3$ | MnO | NiO | MgO | CaO | $Na_2O$ | $K_2O$ | $SO_3$ | $V_2O_3$ | ZnO | Total | |
|---|---|---|---|---|---|---|---|---|---|---|---|---|---|---|---|---|---|---|---|---|
| PAR | olivine | 13 | 33 | 40.41 (0.24) | 0.03 (0.01) | 0.03 (0.02) | 0.07 (0.04) | 10.26 (0.61) | / | 0.15 (0.02) | 0.30 (0.04) | 48.54 (0.52) | 0.23 (0.02) | n.a. | n.a. | n.a. | n.a. | n.a. | 100.01 (0.45) | Fo89 |
| | clinopyroxene (elongated) | 18 | 30 | 48.56 (1.78) | 0.39 (0.10) | 8.73 (2.10) | 0.13 (0.06) | 8.16 (1.66) | / | 0.19 (0.03) | b.d. | 15.55 (3.03) | 17.35 (2.77) | 0.09 (0.04) | b.d. | n.a. | n.a. | n.a. | 99.15 (0.48) | En48Wo38Fs14 |
| | clinopyroxene (needle) | 1 | 3 | 46.09 (2.11) | 0.51 (0.01) | 12.48 (2.47) | 0.08 (0.05) | 12.27 (3.67) | / | 0.24 (0.08) | b.d. | 10.06 (2.24) | 17.19 (1.70) | 0.17 (0.10) | b.d. | n.a. | n.a. | n.a. | 99.11 (0.42) | En34Wo42Fs24 |
| | clinopyroxene | 10 | 15 | 52.72 (1.42) | 0.21 (0.09) | 4.01 (1.45) | 0.44 (0.22) | 7.00 (0.67) | / | 0.18 (0.03) | b.d. | 22.51 (3.51) | 11.91 (4.29) | 0.06 (0.03) | b.d. | n.a. | n.a. | n.a. | 99.04 (0.52) | En64Wo24Fs12 |
| | orthopyroxene | <1 | 1 | 56.12 | 0.08 | 1.04 | 0.26 | 8.68 | / | 0.25 | 0.07 | 31.05 | 2.51 | b.d. | b.d. | n.a. | n.a. | n.a. | 100.06 | En82Wo5Fs13 |
| | clinopyroxene (augite)° | <1 | 1 | 43.90 | 0.46 | 12.45 | 0.14 | 11.86 | / | 0.18 | b.d. | 8.79 | 22.22 | b.d. | b.d. | n.a. | n.a. | n.a. | 100.00 | En29Wo50Fs21 |
| | glass matrix | 55 | 15 | 56.58 (1.80) | 0.27 (0.06) | 18.96 (0.93) | b.d. | 5.12 (1.30) | / | 0.08 (0.03) | b.d. | 1.68 (0.93) | 8.84 (0.69) | 1.42 (0.14) | 0.16 (0.02) | 0.09 (0.03) | b.d. | b.d. | 93.28 | / |
| | chromite | <1 | 1 | 0.06 (0.01) | 0.20 (0.02) | 12.85 (0.29) | 53.13 (0.52) | 18.07 (0.18) | / | b.d. | 0.12 (0.04) | 13.05 (0.28) | 0.07 (0.01) | n.a. | n.a. | n.a. | 0.20 | 0.06 (0.02) | 98.13 (0.55) | / |
| | calcite | 3 | 7 | b.d. | b.d. | b.d. | b.d. | 0.30 (0.18) | / | 0.20 (0.11) | n.a. | 1.53 (0.51) | 52.01 (0.75) | b.d. | b.d. | n.a. | n.a. | n.a. | 54.12 (0.57) | / |
| ARA | clinopyroxene | 22 | 21 | 51.49 (0.85) | 0.25 (0.08) | 3.15 (0.56) | 0.07 (0.05) | 7.87 (2.17) | / | 0.19 (0.02) | b.d. | 16.53 (1.56) | 19.20 (0.97) | 0.08 (0.03) | b.d. | n.a. | n.a. | n.a. | 98.83 (0.33) | En47Wo40Fs13 |
| | albite | 50 | 15 | 67.71 (0.46) | 0.03 (0.02) | 20.07 (0.19) | n.a. | 0.23 (0.07) | / | b.d. | n.a. | b.d. | 0.49 (0.38) | 11.78 (0.29) | 0.05 (0.02) | n.a. | n.a. | n.a. | 100.46 (0.37) | Ab98An2 |
| | clinochlore | 25 | 9 | 31.54 (0.97) | b.d. | 15.37 (0.59) | b.d. | / | 19.97 (0.45) | 0.07 (0.03) | n.a. | 20.79 (0.75) | 0.48 (0.06) | b.d. | b.d. | n.a. | n.a. | n.a. | 88.36 (0.67) | / |
| | prehnite | 3 | 10 | 42.46 (0.41) | 0.12 (0.04) | 19.94 (1.31) | b.d. | / | 6.39 (0.56) | b.d. | b.d. | b.d. | 25.67 (0.31) | 0.07 (0.03) | b.d. | n.a. | n.a. | n.a. | 94.73 (0.46) | / |
| | Fe-Ti oxide | <1 | 5 | 0.18 (0.06) | 8.00 (1.82) | 2.73 (0.29) | b.d. | 78.53 (3.46) | / | 0.31 (0.12) | b.d. | 0.59 (0.34) | 0.05 (0.03) | n.a. | n.a. | n.a. | 1.70 (1.00) | 0.06 (0.02) | 92.17 (0.05) | / |
| ATH* | clinopyroxene | 27 | 20 | 52.77 (0.93) | 0.21 (0.16) | 1.91 (0.17) | 0.44 (0.22) | 6.22 (2.31) | / | 0.17 (0.04) | b.d. | 17.20 (1.56) | 20.19 (0.37) | 0.10 (0.05) | b.d. | n.a. | n.a. | n.a. | 99.21 (0.43) | En49Wo41Fs10 |
| | orthopyroxene | 26 | 17 | 55.80 (0.79) | 0.06 (0.02) | 1.13 (0.29) | 0.26 (0.11) | 9.51 (2.19) | / | 0.21 (0.02) | b.d. | 30.44 (1.78) | 1.88 (0.12) | b.d. | b.d. | n.a. | n.a. | n.a. | 99.30 (0.61) | En82Wo4Fs14 |
| | albite | 4 | 11 | 67.76 (1.44) | 0.03 (0.02) | 20.04 (0.97) | n.a. | 0.34 (0.22) | / | b.d. | n.a. | b.d. | 0.82 (0.71) | 11.32 (0.58) | 0.09 (0.05) | n.a. | n.a. | n.a. | 100.50 (0.53) | Ab96An4 |
| | anorthite | 35 | 18 | 44.43 (0.55) | b.d. | 35.57 (0.57) | n.a. | 0.54 (0.10) | / | b.d. | n.a. | 0.10 (0.04) | 20.14 (0.49) | 0.65 (0.24) | b.d. | n.a. | n.a. | n.a. | 101.57 (0.31) | Ab6An94 |
| | titanite | <1 | 1 | 30.99 | 25.40 | 4.09 | 0.04 | / | 5.62 | 0.04 | 0.00 | 0.65 | 26.72 | 0.00 | 0.01 | n.a. | n.a. | n.a. | 93.56 | / |
| | chromite | <1 | 1 | 0.03 | 0.17 | 9.45 | 53.94 | 23.59 | / | 0.04 | 0.11 | 8.93 | 0.07 | n.a. | n.a. | n.a. | 0.20 | 0.11 | 96.63 | / |
| | Fe-Ti oxide | <1 | 1 | 0.01 | 42.78 | 0.02 | 0.07 | 49.76 | / | 0.45 | 0.00 | 2.20 | 0.02 | n.a. | n.a. | n.a. | 0.59 | 0.01 | 95.91 | / |
| | clay minerals | 7 | 14 | 44.43 (0.83) | b.d. | 7.99 (0.66) | b.d. | / | 10.19 (0.45) | 0.10 (0.04) | n.a. | 21.07 (1.18) | 2.14 (0.28) | 0.20 (0.13) | b.d. | n.a. | n.a. | n.a. | 86.37 (2.08) | / |

Table 5.2. Chemical composition of the detected phases. % phase percentage in the analyzed fragments; n. number of point analysis; n.a. not analyzed; b.d. below detection limit; *phase percentage on the least weathered portion of the sample, PAR and ARA samples are homogeneous, thus the percentage here reported are representative for the whole fragments; °rim on olivine crystals. Standard deviation in brackets.

### 5.3.3. Reflectance spectra

Reflectance spectra of the investigated samples in UV-VIS-NIR ranges are reported in **Figure 5.2 and Figure 5.3**.

All the spectra show a red slope in the UV region (0.35-0.45 μm) and in the VIS region (0.45-0.75 μm) (**Table 5.3**), even though in the VIS region it is interrupted by minor absorption features around 0.7 μm. All samples exhibit a main absorption feature at ~1 μm associated with mafic mineralogy, related to the presence of $Fe^{2+}$ charge transfer (***Burns, 1993***). As it is observed in sample PAR2, the spectra flatten and the red slope, the reflectance intensity, and the absorption bands intensity decrease with the increase of the grain size. Aqueous alteration is responsible for the bands observed at ~1.4 μm, ~1.9 μm, and in the 2.2-2.3 μm range, which are associated with the presence of hydrated minerals. The spectral properties of the absorption bands, specifically band center, band depth and band area (**Table 5.3**), vary between the different samples, reflecting

the different mineralogy. Specifically, PAR samples do not show significant absorption in the VIS, while ARA and ATH samples show similar features at 0.7 µm. This band can be attributed to $Fe^{2+}$-$Fe^{3+}$ charge transfer in pyroxene (***Burns, 1993***) or in some hydrated minerals (e.g., mineral of chlorite group, serpentine group, phyllosilicates) (e.g., ***Cloutis et al., 2011***). The second explanation is more consistent with the observed mineralogy of the samples (**Table 5.2**). Main absorptions in the NIR are centered at 1.01 µm in PAR samples and at 1.02 µm in ARA samples and in ATH samples as well, where it appears broader. The differences in these absorption features reflect the presence of olivine in PAR samples and not in ARA and ATH samples, as well as the difference in ortho- and clinopyroxene ratios (**Table 5.2**). The hydrated minerals related features at 1.4 µm and 1.9 µm are much stronger in ATH samples than in all the others; in fact, this sample presents the highest aqueous alteration grade. The reflectance spectra acquired on the heated samples (above 450°C) show some common traits for all the samples, including: a mild feature at ~0.5 µm (**Table 5.3**), attributable to spin-forbidden electronic transitions of $Fe^{3+}$ (***Burns, 1993***), a reddening of the VIS slope (**Table 5.3**), the disappearance of the 0.7 µm, 1.4 µm and 1.9 µm features.

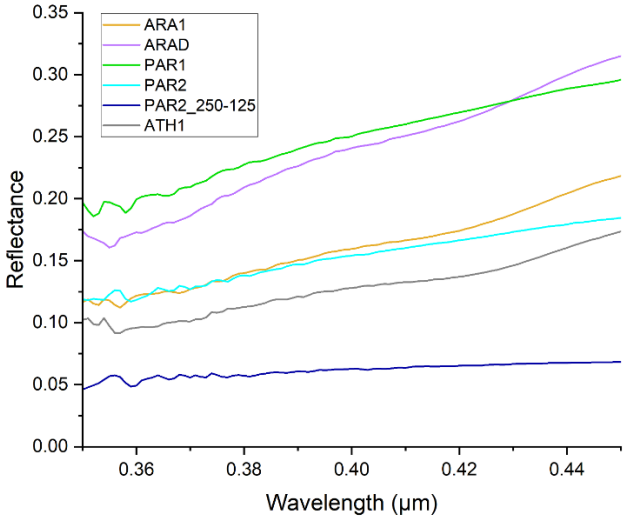


Figure 5.2. Bidirectional reflectance spectra of the investigated samples in the UV range at incidence angle of 30°and emission angle of 0°.

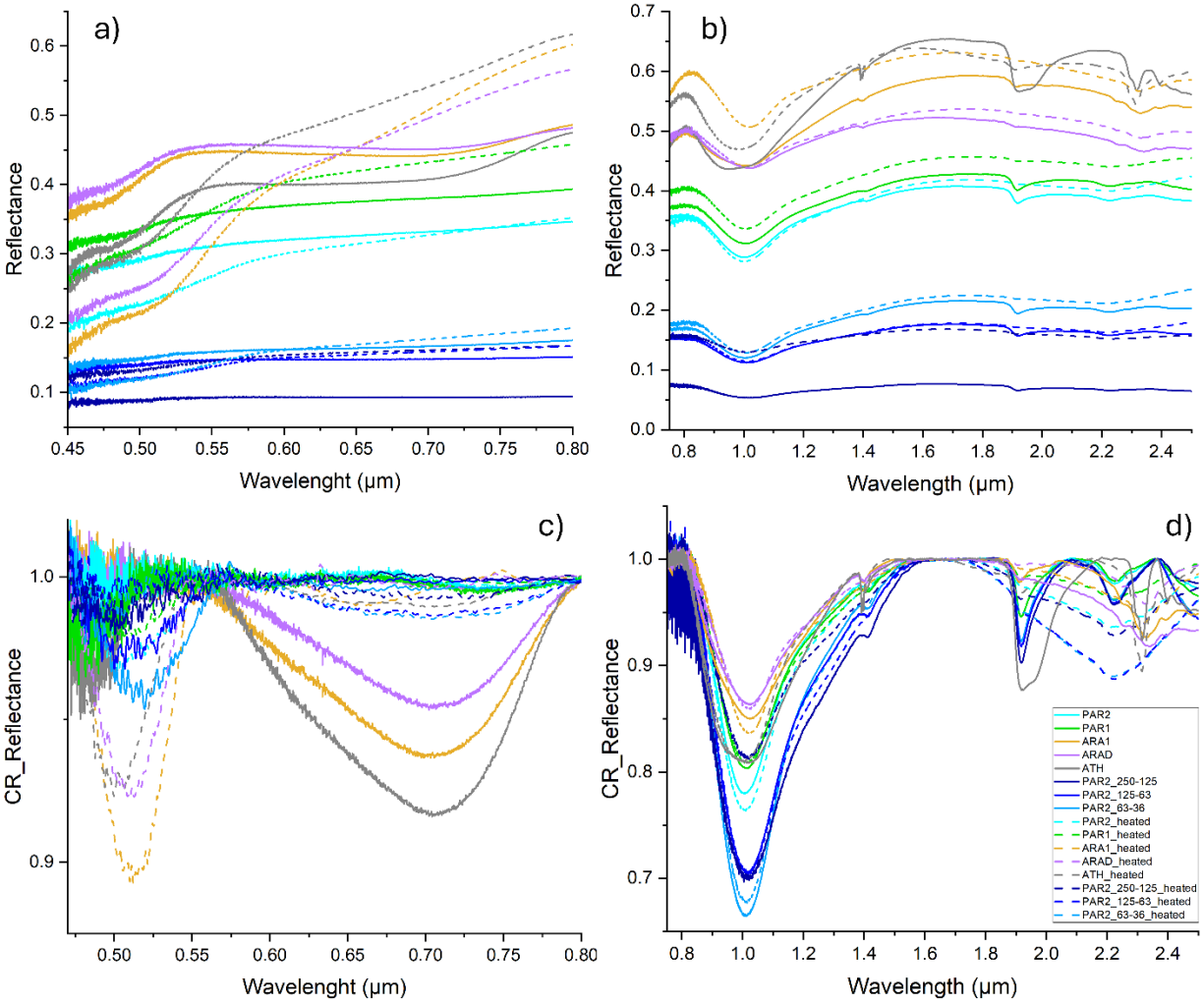


Figure 5.3. a) Bidirectional reflectance spectra of the investigated samples at incidence angle and emission angle of 30° and 0°, respectively: a) VIS range, b) NIR range. Continuum removed spectra, obtained subtracting a multiple segments baseline: c) VIS range, d) NIR range.

| Sample | UV slope | VIS slope | Center 1 | Depth 1 | Area 1 | Center 2 | Depth 2 | Area 2 |
|---|---|---|---|---|---|---|---|---|
| **PAR2** | 0.94 | 0.22 | 0.755 | 0.01 | 0.33 | 1.00 | 0.22 | 61.04 |
| **PAR2_63-36** | / | 0.04 | 0.697 | 0.02 | 1.92 | 1.01 | 0.34 | 103.62 |
| **PAR2_125-63** | / | 0.02 | 0.702 | 0.02 | 2.34 | 1.02 | 0.30 | 94.11 |
| **PAR2_250-125** | / | 0.02 | 0.697 | 0.02 | 0.96 | 1.00 | 0.30 | 102.27 |
| **PAR1** | 0.99 | 0.24 | 0.747 | 0.01 | 0.40 | 1.01 | 0.20 | 58.79 |
| **ARA1** | 1.02 | 0.37 | 0.705 | 0.06 | 8.86 | 1.02 | 0.15 | 49.77 |
| **ARAD** | 1.41 | 0.29 | 0.702 | 0.05 | 6.42 | 1.03 | 0.14 | 44.35 |
| **ATH1** | 1.01 | 0.52 | 0.704 | 0.08 | 11.71 | 1.02 | 0.19 | 64.77 |
| **PAR2_h** | / | 0.49 | 0.503 | 0.03 | 1.42 | 1.01 | 0.24 | 67.52 |
| **PAR2_63-36_h** | / | 0.24 | 0.504 | 0.06 | 1.06 | 1.01 | 0.32 | 95.82 |
| **PAR2_125-63_h** | / | 0.16 | 0.507 | 0.05 | 0.85 | 1.02 | 0.30 | 101.10 |
| **PAR2_250-125_h** | / | 0.13 | / | / | / | 1.02 | 0.19 | 62.34 |
| **PAR1_h** | / | 0.59 | 0.502 | 0.02 | 0.90 | 1.01 | 0.19 | 60.41 |
| **ARA1_h** | / | 1.33 | 0.512 | 0.11 | 4.67 | 1.03 | 0.16 | 48.13 |
| **ARAD_h** | / | 1.12 | 0.510 | 0.08 | 3.51 | 1.02 | 0.14 | 44.75 |
| **ATH1_h** | / | 1.12 | 0.500 | 0.08 | 3.38 | 1.00 | 0.19 | 56.04 |

Table 5.3. Spectral slopes in the UV and VIS ranges and absorption bands parameters in the VIS-NIR region. h= heated. Centers in µm.

| | Center 3 | Depth 3 | Area 3 | Center 4 | Depth 4 | Area 4 | Center 5 | Depth 5 | Area 5 |
|---|---|---|---|---|---|---|---|---|---|
| **PAR2** | / | / | / | 1.92 | 0.05 | 2.25 | 2.23 | 0.02 | 2.32 |
| **PAR2_63-36** | / | / | / | 1.92 | 0.08 | 3.95 | 2.23 | 0.04 | 4.04 |
| **PAR2_125-63** | / | / | / | 1.92 | 0.08 | 4.09 | 2.22 | 0.04 | 4.74 |
| **PAR2_250-125** | / | / | / | 1.92 | 0.10 | 4.12 | 2.23 | 0.04 | 4.36 |
| **PAR1** | / | / | / | 1.92 | 0.05 | 2.04 | 2.23 | 0.02 | 2.01 |
| **ARA1** | / | / | / | 1.91 | 0.02 | 0.26 | 2.23 | 0.07 | 2.80 |
| **ARAD** | / | / | / | 1.91 | 0.01 | 0.20 | 2.34 | 0.08 | 1.52 |
| **ATH** | 1.39 | 0.05 | 0.94 | 1.92 | 0.12 | 16.81 | 2.32 | 0.08 | 3.13 |
| **PAR2_h** | / | / | / | / | / | / | 2.21 | 0.06 | 26.57 |
| **PAR2_63-36_h** | / | / | / | / | / | / | 2.22 | 0.11 | 51.75 |
| **PAR2_125-63_h** | / | / | / | / | / | / | 2.23 | 0.11 | 50.98 |
| **PAR2_250-125_h** | / | / | / | / | / | / | 2.22 | 0.07 | 30.59 |
| **PAR1_h** | / | / | / | / | / | / | 2.22 | 0.04 | 13.17 |
| **ARA1_h** | / | / | / | / | / | / | 2.33 | 0.06 | 17.34 |
| **ARAD_h** | / | / | / | / | / | / | 2.33 | 0.04 | 18.02 |
| **ATH_h** | 1.40 | 0.04 | 0.74 | 1.91 | 0.03 | 5.71 | 2.32 | 0.10 | 10.04 |

Table 5.3. continue.

For the MIR reflectance spectra, we focus on the range 7-14 µm. The spectra (**Figure 5.4**) evidence Christiansen feature (CF) around 8-8.5 µm and Reststrahlen bands (RBs) between 8.3 and 12 µm. Considering the position (**Table 5.4**) and shapes of these bands we can clearly observe that the spectra are divided into three groups following their mineralogy. CF are centred at 8.4 µm in PAR samples, 7.9 µm in ARA samples and 8.3 µm in ATH samples: CFs are located at lower

wavelengths for higher plagioclase content (%) (**Figure 5.5a**) and for higher $SiO_2$ content (%) (**Figure 5.5c**). RBs are centred at 9.5 and 11.1 µm in PAR samples; at 8.3, 9.8 and 11.7 µm in ARA samples; at 9.2, 9.7, 11.9 µm in ATH samples. Also, in PAR samples RBs appear broader, and the separation is less marked than in ARA and ATH samples (**Figure 5.4**). This is attributed to the presence (55%) of volcanic glass that can reduce the spectral contrast of absorption bands (e.g., ***Caminiti et al., 2024***). Furthermore, the spectral contrast reduces the bands broaden with the increase of the grain size (**Figure 5.4**). In this spectral range, the main effect that we can observe on the spectra of heated samples is a decrease in the spectral contrast between the CFs and the RBs (**Figure 5.4**). The CFs positions do not change much for ATH and PAR finer samples, while they appear shifted for ARA samples and PAR coarser samples.

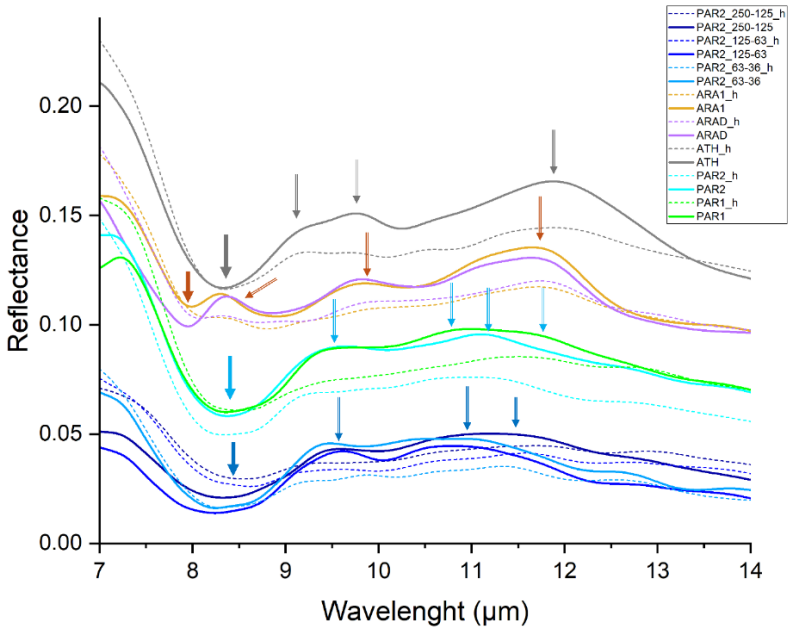


Figure 5.4. Hemispherical reflectance spectra of the investigated samples in the 7-14 µm MIR range. ARA1, ARAD and ATH spectra were vertically shifted for figure clarity (+0.6, + 0.6 and +0.9, respectively). CFs and RBs pointed by arrows.

| | CF | RB1 | RB2 | RB3 |
|---|---|---|---|---|
| **PAR2** | 8.38 | 9.47 | 11.11 | / |
| **PAR2_63-36** | 8.25 | 9.43 | 10.99 | / |
| **PAR2_125-63** | 8.28 | 9.60 | 10.90 | / |
| **PAR2_250-125** | 8.32 | 9.49 | 11.23 | / |
| **PAR1** | 8.36 | 9.47 | 10.70 | 11.70 |
| **ARA1** | 7.98 | 8.30 | 9.85 | 11.75 |
| **ARAD** | 7.95 | 8.37 | 9.82 | 11.74 |
| **ATH** | 8.32 | 9.16 | 9.76 | 11.89 |

Table 5.4. Position (µm) of the Christiansen features (CF) and the Reststrahlen bands (RB) in the MIR spectra of the investigated samples.

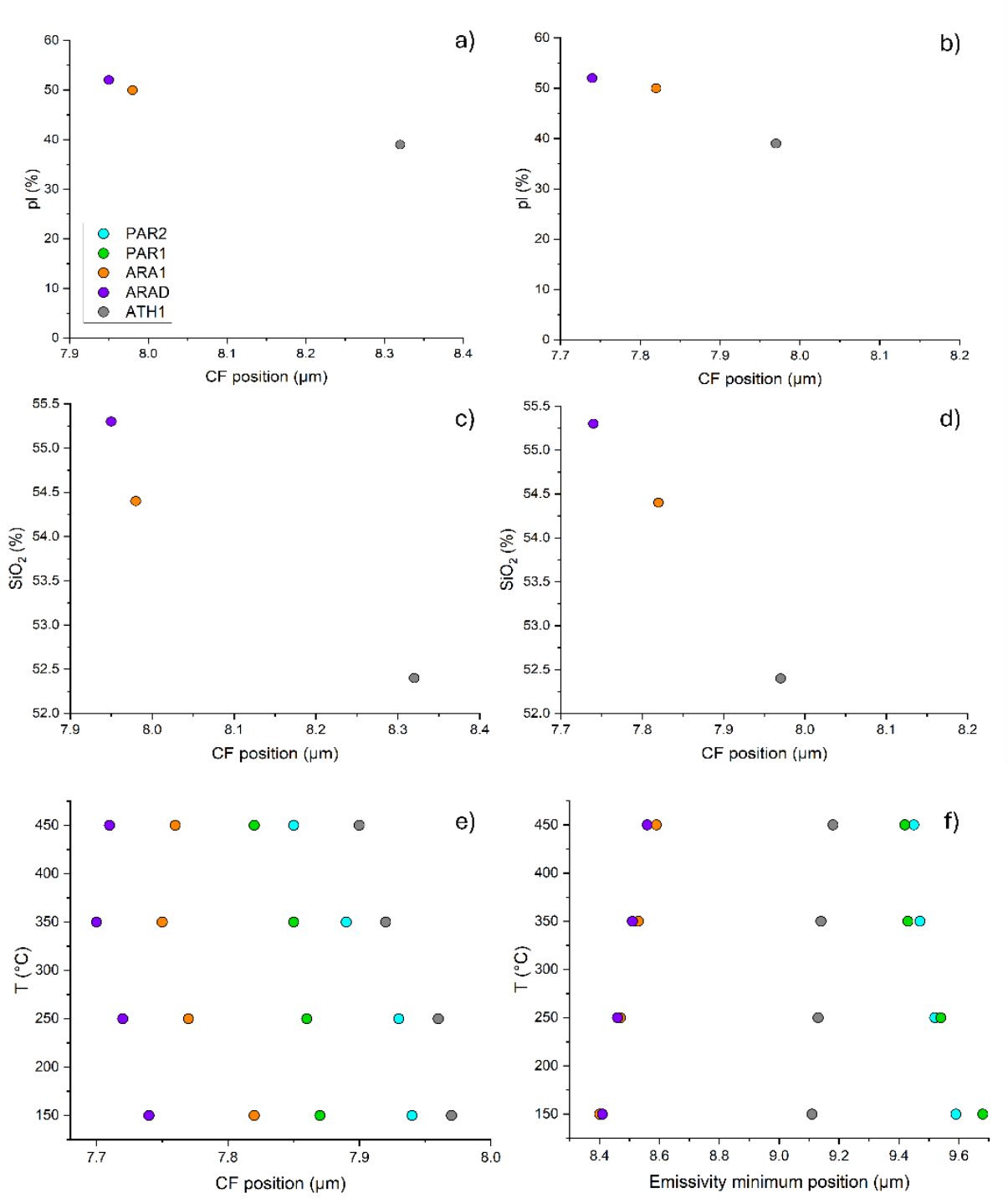


Figure 5.5. a) MIR CF positions as a function of plagioclase content; b) emissivity CF positions at the lowest T (150°C) as a function of plagioclase content; c) MIR CF positions as a function of SiO2 bulk content; d) emissivity CF positions at the lowest T (150°C) as a function of SiO2 bulk content. e) comparison between emissivity CF positions collected at 150°C, 250°C, 350°C, 450°C; f) comparison between emissivity minimum positions collected at 150°C, 250°C, 350°C, 450°C.

### 5.3.4. Emissivity

Emissivity spectra of the investigated samples are shown in **Figure 5.6**. The CF at the lowest temperature (150°C) are located around 7.9 µm, 7.8 µm and 8.0 µm for PAR, ARA and ATH samples, respectively. The relationship between plagioclase content (%) and CFs positions already

observed in the MIR reflectance spectra is maintained (**Figure 5.5b**), as well as the one between $SiO_2$ content and CFs positions (**Figure 5.5d**). Increasing the temperature from 150°C to 450°C, three main changes occur for all the samples (<36 μ): the shifting of the CFs positions, the shifting of the emissivity minima, and the increase of the spectral contrast between CFs and RBs (**Table 5.5**). Some differences can be observed in the shifting of the CFs (**Figure 5.5e**) and of the emissivity minima (**Figure 5.5f**) between the samples. For PAR and ATH samples, the CFs shift towards shorter wavelengths with increasing temperature, for ARA samples the shift is towards shorter wavelengths until 350°C, and at 450°C we can observe a shift to higher wavelengths. The emissivity minima show a shifting towards shorter wavelengths (from 9.6 μm to 9.4 μm) for PAR samples and a shifting towards longer wavelengths for ARA (from 8.4 μm to 8.6 μm) and ATH samples (from 9.1 μm to 9.2 μm).

Bigger grain sizes (for sample PAR2) exhibit different features. First of all, the spectral contrast between CFs and RBs reduces with the increase of the grain size, although it still intensifies with the temperature rising for every grain size (**Figure 5.6**). The shifting of the emissivity minima does not follow a linear trend in any of the three samples (PAR2_63-36, PAR2_125-63, PAR2_250-125), and the position of the emissivity minima at 450°C is located around 11.0 μm and not around 9.4 μm as for the other measurements (at 150°C, 250°C, 350°C) (**Table 5.5**). For the sample with the coarsest grain size range (PAR2_250-125), the emissivity minima are located around 11.2 μm for all the measurements.

| | **CF** | | | | **Emissivity minimum** | | | |
|---|---|---|---|---|---|---|---|---|
| | **150°C** | **250°C** | **350°C** | **450°C** | **150°C** | **250°C** | **350°C** | **450°C** |
| **PAR2** | 7.94 | 7.93 | 7.89 | 7.85 | 9.59 | 9.52 | 9.47 | 9.45 |
| **PAR2_63-36** | 7.82 | 7.81 | 7.81 | 7.76 | 9.45 | 9.41 | 9.42 | 10.77 |
| **PAR2_125-63** | 7.88 | 7.80 | 7.80 | 7.99 | 9.44 | 9.44 | 9.45 | 11.04 |
| **PAR2_250-125** | 7.29 | 7.62 | 7.69 | 7.80 | 11.28 | 11.29 | 11.16 | 11.24 |
| **PAR1** | 7.87 | 7.86 | 7.85 | 7.82 | 9.68 | 9.54 | 9.43 | 9.42 |
| **ARA1** | 7.82 | 7.77 | 7.75 | 7.76 | 8.40 | 8.47 | 8.53 | 8.59 |
| **ARAD** | 7.74 | 7.72 | 7.70 | 7.71 | 8.41 | 8.46 | 8.51 | 8.56 |
| **ATH** | 7.97 | 7.96 | 7.92 | 7.90 | 9.11 | 9.13 | 9.14 | 9.18 |

Table 5.5. Position (μm) of the Christiansen features (CF) and the emissivity minimum of emissivity spectra collected at 150°C, 250°C, 350°C and 450°C.

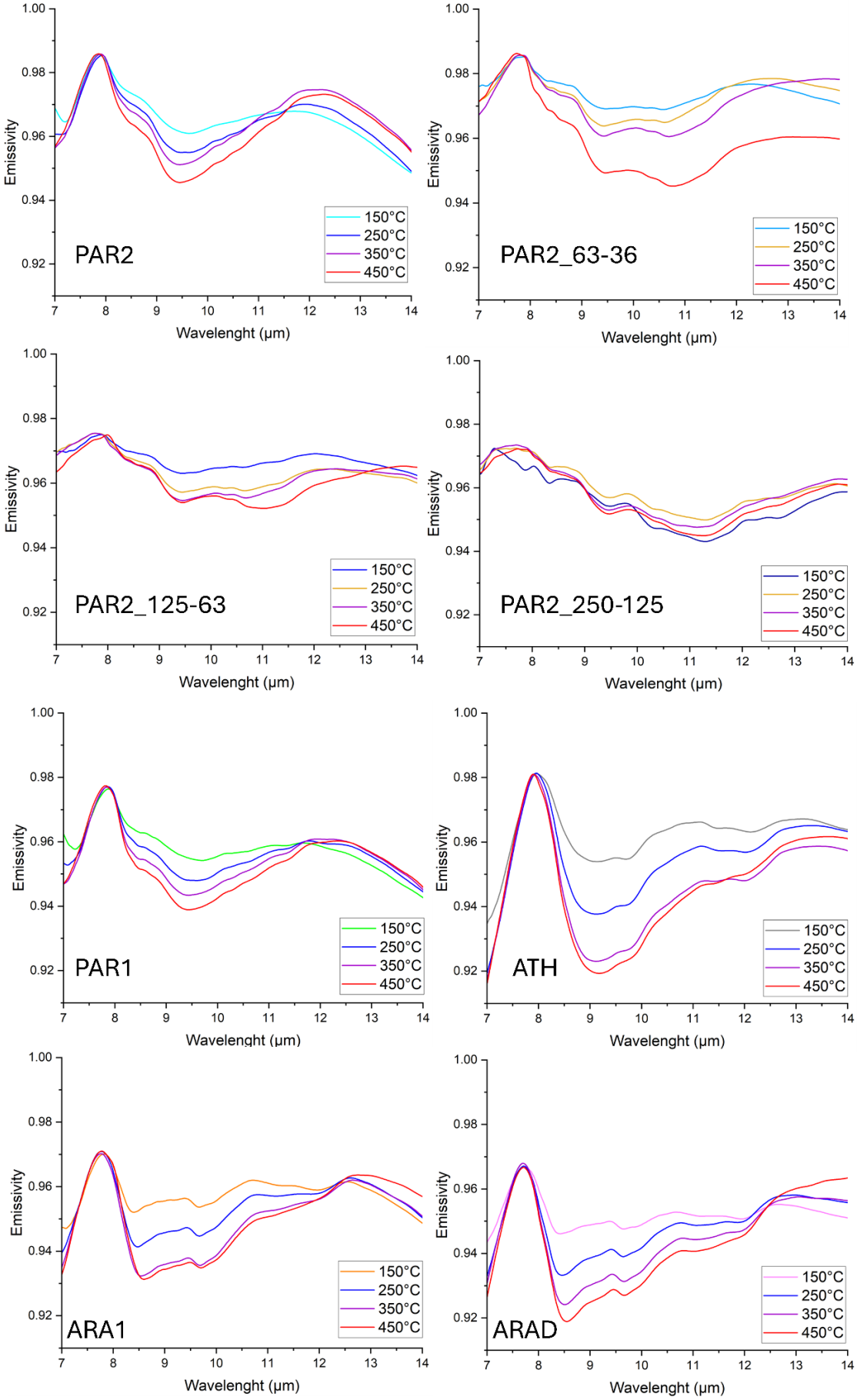


Figure 5.6. Emissivity spectra of the investigated samples.

## 5.4. Discussion

### 5.4.1. Whole-rock chemistry and mineralogy: Comparison to Mercury's surface

The chemical composition of the boninites under investigation closely correlates with the composition of Mercury's geochemical terranes (***Vander Kaaden et al., 2017***) in terms of major elements contents (wt%), as it can be observed in **Figure 5.7**. $SiO_2$ values of the investigated samples (**Table 5.1**) lie within the large $SiO_2$ range proposed for Mercury's terranes. $Al_2O_3$ values of the samples (**Table 5.1**) fall in the range of Mercury's terranes as well: ARA samples are analogous to the intermediate terrane (IT); PAR samples to the intermediate terrane (IT) and the northern volcanic plains, both high and low Mg (NP-HMg and NP-LMg); ATH sample to high-Mg region (HMR), high-Mg region with the highest Ca and S (HMR-CaS), and Rachmaninoff Basin (RB). MgO contents of the investigated samples (**Table 5.1**) are, on average, slightly lower than on Mercury's surface but still in agreement: PAR whole rock samples have MgO contents comparable with those of the northern volcanic plains with low Mg (NP-LMg) and the Caloris basin (CB); MgO values in PAR glass and ARA whole rock samples are at the lower boundary of the NP-LMg; the ATH sample show MgO contents comparable with the intermediate terrane (IT), the high-Al region (HAI) and the northern volcanic plains with high Mg (NP-HMg). CaO contents (**Table 5.1**) are on average higher for PAR and ATH samples; CaO values in ARA samples, on the contrary, closely resemble those of five of Mercury's terranes (NP-HMg, HAI, IT, CB and NP-LMg). FeO contents (**Table 5.1**) are higher in the investigated samples than on Mercury's surface: 7.4-8.4 wt% VS 1.0-2.2 wt% (***Vander Kaaden et al., 2017***). Also, it is to point out that $Na_2O$ is a minor element in PAR and ATH samples (0.5-0.8 wt%) while it is a major element in ARA samples, with much more similar values (4.8-5.8 wt%) to those proposed for Mercury's terranes (3.5-6.5 wt%, ***Vander Kaaden et al., 2017***). This is related to the important presence (50 %) of albitic plagioclase in ARA samples, which is much less abundant (4 %) in ATH samples and is not present in PAR samples.

It is worth noting that the discrepancies we can observe for CaO and FeO contents between the investigated samples and Mercury's surface may be influenced by the alteration of the boninites. For example, PAR samples contain calcite as weathering products, which could be an explanation for the high bulk calcium values. ARA samples present clinochlore and prehnite replacing the primary mafic mineralogy, which could justify magnesium depletion and iron enrichment. ATH samples are rich in clay minerals' alteration, which again may have caused magnesium depletion and iron enrichment. Regardless, FeO concentrations in these terrestrial samples are higher than expected on Mercury's surface. To date, besides Troodos boninites, other reasonably not altered terrestrial boninites having the lowest iron contents seem to be those from New Caledonia (5.96 wt% FeO and 1.47 wt% $Fe_2O_3$, ***Ohnenstetter & Brown, 1992***), from New Zealand (6.06 wt% FeO

and 1.57 wt% $Fe_2O_3$, ***Cameron et al., 1983***) and from Mariana forearc (5.8 wt% FeO and 1.1 wt% $Fe_2O_3$, ***Johnson & Fryer, 1990***), although still higher than Mercury's terranes values. In fact, the total amount of Fe estimated on Mercury's surface is 1-2 wt% (e.g., ***Nittler & Weider***, 2019 and references therein), of which FeO is inferred to be <1 wt% from reflectance spectroscopy studies (***Murchie et al., 2015***).

In the investigated samples, the most abundant mafic mineral is represented by clinopyroxene, and not orthopyroxene, as expected on Mercury's surface. Also, Mg-Ca-Fe sulphide assemblages are not present, and the fayalite and ferrosilite component in olivine and orthopyroxene, respectively, are much more abundant. Bearing in mind these major differences, among the investigated samples, the ones with a mineral assemblage that could resemble the most Mercury's surface mineralogy are ARA samples, assuming that the original mineralogy presented olivine, here replaced by hydrated minerals (clinochlore and prehnite) due to hydrothermal alteration (***Gillis & Robinson, 1990***). ATH samples could be a better fit in terms of orthopyroxene presence, and consequently MgO values more fitting to Mercury's terranes average composition, but the plagioclase is mostly anorthite, and the weathering grade is very high, and no hypothesis of the presence of a primary mineralogy presenting olivine can be made. PAR samples are much less weathered and present olivine, possibly providing a better comparison between terrestrial fresh boninites and Mercury's surface VNIR spectral features, with less contribution of hydrated minerals, but albitic plagioclase is absent.

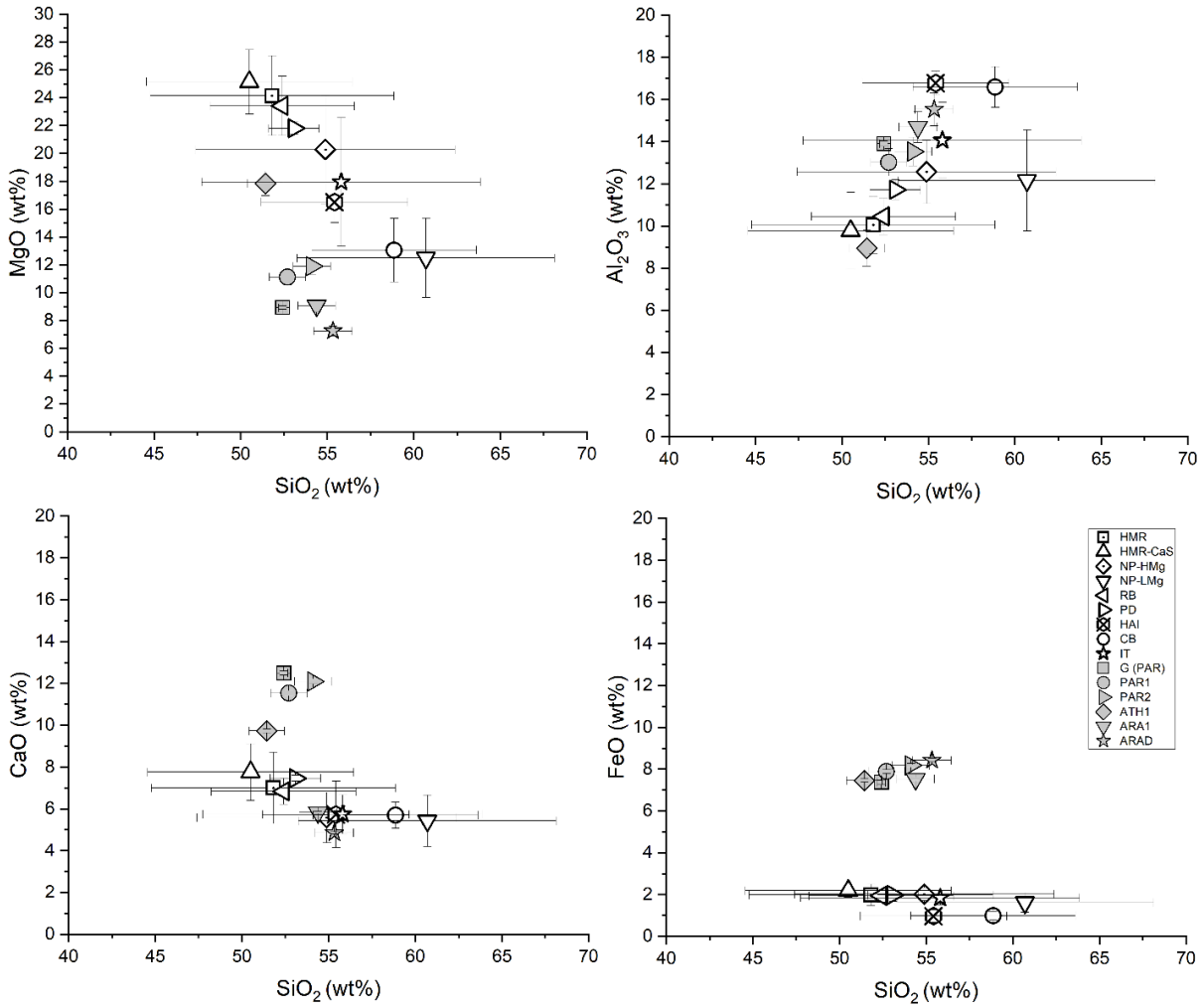


Figure 5.7. Average chemical compositions of the boninite samples compared with average composition of Mercury's geochemical terranes (**Vander Kaaden et al., 2017**). HMR= high-Mg region; HMR-CaS= high-Mg region with highest Ca and S; NP-HMg= northern volcanic plains with high Mg; NP-LMg= northern volcanic plains with low Mg; RB= Rachmaninoff Basin (RB); PD= pyroclastic deposits; HAI= high-Al region; CB= Caloris Basin; IT= intermediate terrane.

### 5.4.2. Spectral features

The differences in the mineralogy of the boninite samples from the three different localities are observed in their different reflectance spectra features in the VIS-MIR region, as illustrated in the results section. The main difference in the MIR reflectance spectra is related to the CFs and RBs positions, which tend to be located at shorter wavelengths with the increase in plagioclase content. Further observations can be made regarding the differences between fresh and heated (above 450°C) samples' spectra in the VIS-VNIR spectral range. In the VIS range, the increase in the reflectance maxima for the heated spectra is not the same for all the samples with the same finest granulometry: it is higher for ARA and ATH samples, intermediate for PAR1, and absent for PAR2, where the reflectance maximum for the fresh and the heated spectra remains the same.

Additionally, the increase is very low for the intermediate grain sizes of the PAR2 sample (PAR2_63-36 and PAR2_125-63 μm) but becomes more pronounced again for the coarsest granulometric range (PAR2_250-125 μm). Similarly, the increase of the visible slope (reddening) is higher for ARA and ATH samples, intermediate for PAR samples, and lower for the three PAR2 coarser granulometries. The mild feature at ~0.5 μm, which appears in the heated spectra, is more evident in ARA and ATH samples, probably due to an increase of $Fe^{3+}$ caused by the heating process. Therefore, it is possible to observe that ARA and ATH samples exhibit similar spectral changes due to heating processes. On average, greater changes in the spectral properties between fresh and heated samples appear for finer grain sizes, as already observed for komatiite samples by ***Maturilli et al. (2014)***. A difference observed between komatiites in the previous study (***Maturilli et al., 2014***) and the boninite samples here investigated is that heated komatiites exhibited a general darkening and reddening of VIS-VNIR spectra, while the investigated boninite samples show reddening but no darkening, and on the contrary, they exhibit a higher reflectance. The reddening of the visible spectral slope could be associated with the oxidation of the samples caused by the heating process under low vacuum environment (e.g., ***Bott et al., 2023; Potin et al., 2019***). In the VNIR range, the main difference between fresh and heated samples' spectra is the reduction of absorption features related to hydrous minerals (at ~1.4 μm, ~1.9 μm and in the 2.2-2.3 μm range). This occurs similarly in all the samples, except for ATH sample, where these features remain visible in heated spectra. Spectral changes after the heating process are stronger in the VIS than in the NIR and MIR regions. In the MIR spectral range, the changes between fresh and heated spectra consist mainly of a decrease in the spectral contrast between the CFs and the RBs and are more evident for ARA samples, showing also a shift of the CFs position to longer wavelengths than for PAR and ATH samples. Furthermore, the spectra of samples with smaller particle size appear to be more affected by the heating process, with a greater spectral contrast decrease, than those with coarser particles' size, as already observed for some komatiites samples by ***Maturilli et al. (2014)***.

Emissivity spectra depend on the mineralogy of the samples, on the granulometry and on the temperature, as illustrated in the results section. The mineralogy affects the band positions and shapes, and there is a tendency for absorption bands to be centred at longer wavelengths for samples with lower plagioclase content, reflecting the higher contribution of less polymerized minerals, such as olivine and pyroxene (e.g., ***Cooper et al., 2002; Ferrari et al. 2020; Morlok et al. 2023***). With increasing temperature, there is an opposite trend in the shifting of emissivity minima: towards shorter wavelengths for mafic-richer samples (PAR) and longer wavelengths for felsic-richer samples (ATH and ARA). The trend seen in this work for mafic-richer samples was also observed for

the emissivity spectra of some komatiite samples investigated by ***Carli et al. (2013)***, showing emissivity minima shifting towards shorter wavelengths with increasing temperature. Komatiites are ultramafic rocks (e.g., ***Arndt, 2003***), therefore it appears to be a correlation between the mafic component of these rocks and the shifting of the emissivity minima with increasing temperature. Although an opposite shifting in the emissivity minima of the mafic-richer and the felsic-richer boninite samples under investigation, the minima absorption positions are still quite different. So, given the importance of considering spectra acquired at temperatures matching those on Mercury's surface to have a consistent comparison (***Helbert & Maturilli, 2009***), we can hypothesize that even regardless of the exact Mercury's surface temperature, the emissivity spectra of mafic-richer terranes and felsic-richer terranes in the 7-14 μm range should be clearly distinguishable with the MERTIS instrument, as already suggested by other authors (e.g., ***Ferrari et al., 2020***).

### 5.4.3. Spectral features-comparison with Mercury's surface

The main analogy between Mercury's surface and the investigated terrestrial samples is represented by the bulk chemical composition. However, it should be noted that, in terms of spectral features, the boninite samples exhibit clear absorption bands related to FeO, H–O–H, and O–H, which are not visible in Mercury's spectra (e.g., ***Barraud et al., 2020***). Taking this into account, we tried to compare the UV and VIS spectral slope values of these samples to those of various regions of Mercury's surface, considering only the samples with the finest granulometry range. The Mercury's surface areas considered in this study were selected to represent different UV and VIS slope values: low-reflectance material (LRM) (e.g., ***Barraud et al., 2020, Thomas et al., 2016***), hollows (e.g., ***Barraud et al., 2020, 2023; Blewett et al., 2018***); faculae and other pyroclastic and volcanic originated deposits (e.g., ***Barraud et al., 2021; Blewett et al., 2011; Head et al., 2008; Kerber et al., 2009, 2011; Galiano et al., 2022; Goudge et al., 2014; Thomas et al., 2014***). LRM represents the darkest (low reflectance values) areas of the surface. Hollows are among the brightest features on the surface (***Barraud et al., 2020***) and have a wide range of VIS spectral slope. Faculae are the brightest and reddest features on the surface, brighter and redder than the Average Mercury Terrain (AMT) (e.g., ***Head et al., 2008; Goudge et al., 2014***) or, at least, of their local surroundings (***Barraud et al., 2021***).

In **Figure 5.8** it is possible to observe that the UV slope values for the investigated boninite samples are, on average, lower than the UV slope values calculated for different regions of Mercury's surface, with the only exception of one ARA sample. VIS slope values are lower as well, even in respect to the hollows. In general, the bluer spectral slope could be attributed to three factors. Firstly, the absorption bands present in the investigated samples affect the slope. Subsequently,

the differences in the acquisition geometry: our data were collected using a standard bidirectional geometry with an incidence angle ($i$) of 30° and an emission angle ($e$) of 0°, resulting in a phase angle ($\alpha$) of 30°; the Mercury data used for the comparison, acquired by the MESSENGER Mercury Atmospheric and Surface Composition Spectrometer (MASCS), were normalized to a geometry of $i$ = 30°, $e$ = 45°, and $\alpha$ = 90° (***Izenberg et al., 2014***). Finally, Mercury's surface is affected by space weathering, which increases the VIS spectral slope (spectral reddening) and suppresses the absorption features in the VIS-NIR spectral range, due to the presence of iron nanoparticles (npFe$^0$) (e.g., ***Domingue et al., 2014; Galiano et al., 2023; Vilas & Hendrix, 2015***). While the absorption features related to the first factor cannot be avoided, we investigated the potential effects of the second and third factors. To improve our comparison with MASCS data, we tried to acquire VIS and VNIR spectra with $\alpha$=90° and we observed that the VIS slopes remain substantially unchanged (**Figure 5.8**). The space weathering influence on the VIS slope was recently investigated by ***Caminiti et al. (2024)*** in a study about the simulation of space weathering by ion irradiation ($He^+$ at 20 keV) on some terrestrial samples, including one boninite. The authors found no identifiable trend between the irradiation dose and the spectral reddening: the spectra redden by approximately 0.1% up to a fluence of ~ 1.0 x $10^{17}$ ions/cm$^2$, but at higher fluences the VIS slope values return close to the initial value of the fresh sample. Therefore, the spectral differences between boninites and Mercury's surface can be attributed mainly to the differences in their mineralogical and chemical characteristics.

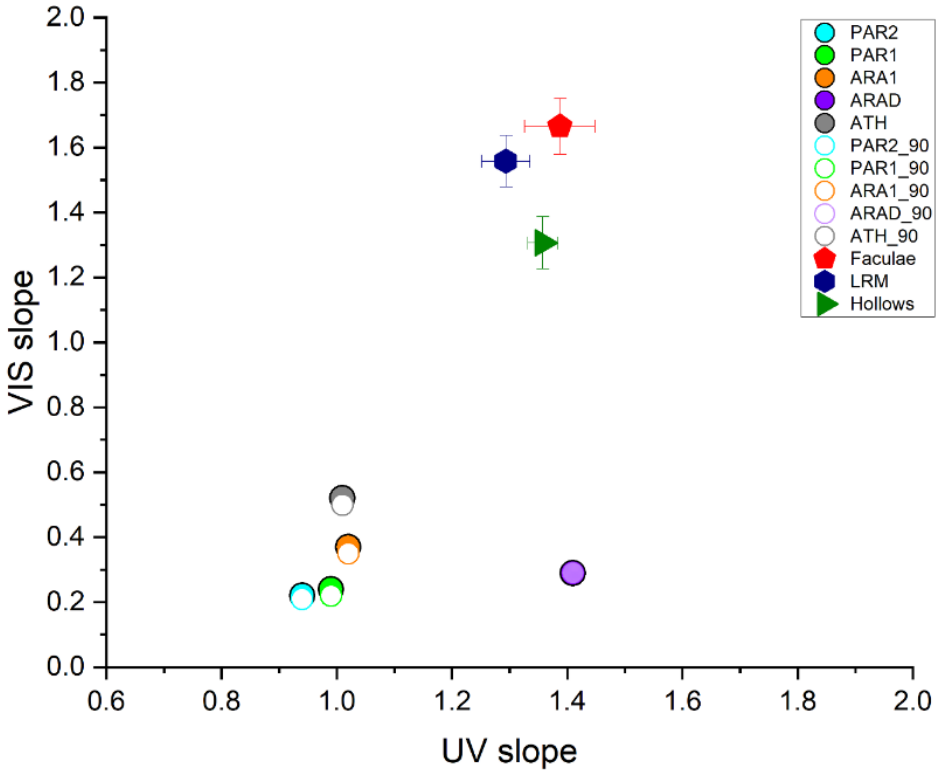


Figure 5.8. Comparison between UV and VIS spectral slopes of boninite samples and Mercury's surface. Faculae from **Barraud et al. (2021)**, LRM from **Barraud et al. (2020)** and Hollows from **Barraud et al. (2020, 2023)**.

### 5.5. Conclusions

The boninite samples analysed in this study, collected from different localities of the Troodos Massif (Cyprus), show variations in mineral assemblages and whole-rock chemical compositions. Overall, their whole-rock geochemistry closely correlates with the estimated composition of Mercury's geochemical terranes in terms of major elements contents (wt%). The only substantial difference is represented by FeO concentration, which is higher in these terrestrial samples. In addition to this relevant geochemical distinction, the main mineralogical differences with Mercury's surface are the presence of hydrated minerals from aqueous alteration, which are not expected on the planet, and the absence of Fe, Ca, Mn, Mg sulphides, indicative of the highly reduced conditions under which Mercury's surface materials formed. Also, in PAR and ARA boninite samples, clinopyroxene is the dominant mafic mineral, whereas clino- and orthopyroxene are present in roughly equal amounts in ATH boninites, while orthopyroxene is expected to be more abundant on Mercury's surface.

Among the investigated samples, ARA samples exhibit a mineral assemblage that could more closely resemble Mercury's surface mineralogy, assuming the original mineralogy presented olivine, here replaced by hydrated minerals (clinochlore and prehnite) due to hydrothermal alteration.

PAR samples may provide a better comparison, as they are less altered and present olivine, but no albitic plagioclase is present. ATH samples are highly affected by aqueous alteration, limiting their comparability to Mercury's surface.

The mineralogical and chemical differences observed among the samples are reflected in their reflectance and emissivity spectra. Overall, the spectra show a red slope in the UV region and a subtle red slope in the VIS region, in some cases interrupted by minor absorption features around 0.7 μm. The main absorption feature is in the VNIR range, at ~1 μm, associated with mafic mineralogy. Features at ~1.4 μm, ~1.9 μm, and within the 2.2–2.3 μm range result from aqueous alteration. In the MIR range, the CFs are located around 8-8.5 μm and the RBs between 8.3 and 12 μm. CFs are located at lower wavelengths for the samples with higher plagioclase content. The increase of the grain size leads to spectral flattening and to a red slope, reflectance intensity, and absorption bands intensity decreasing.

Heating the samples at Mercury's surface temperatures (up to 450°C) causes some effects on the reflectance spectra: a mild feature appearing at ~0.5 μm; the reddening of the VIS slope; the disappearance of the 0.7 μm, 1.4 μm and 1.9 μm features; the decrease in the spectral contrast between CFs and RBs and the shift in the RBs positions. The emissivity spectra show three changes occurring for all the samples (<36 μ) as the temperature increases from 150°C to 450°C: CFs positions shift, emissivity minima shift, and the spectral contrast between CFs and RBs increases. These shifting vary among the samples with different mineralogy. In particular, we can observe an opposite trend for the emissivity minima shifting between mafic-richer and felsic-richer samples. Still, the minima positions remain distinct, suggesting that mafic-richer and felsic-richer terranes should be easily identifiable with the MERTIS instrument.

Comparing some spectral parameters of the investigated samples with Mercury's surface spectra, we observe that boninites generally have UV and VIS slope values lower than those calculated for different regions of the planet's surface. After investigating the possible influence of the acquisition geometry and the space weathering affecting Mercury's surface, we conclude that the spectral differences between boninites and the planet's surface can be mainly attributed to their different mineralogical and chemical characteristics. In the future, we aim to analyse more boninite samples, with similar alteration degree and FeO content, from other localities to further strengthen the findings of this study.

The findings of this study may have significant implications for the future investigation of Mercury's surface with the ESA's BepiColombo mission, particularly for the interpretation of the data expected to arrive from the SIMBIO-SYS/VIHI imaging spectrometer and the MERTIS instrument.

# 6. Conclusions

This thesis focused on the mineralogical, chemical, and spectroscopic study of Mercury's surface natural analogues, to contribute to the understanding of the planet's formation and evolution. The investigated analogues are highly reduced meteorites of different groups (aubrites, enstatite chondrites, achondrites, and melt rocks) and terrestrial boninites from Troodos massif, Cyprus. I focused on three main topics, investigating different aspects that can contribute to increasing our knowledge of the planet's surface: the mineralogical and spectroscopic characterization of highly reduced meteorites (Chapters 2 and 3); laboratory simulation of space weathering on highly reduced materials (aubrites) (Chapter 4); and chemical, mineralogical and spectroscopic, including emissivity, studies on boninites (Chapter 5).

The study of highly reduced meteorites from different groups highlights their mineralogical differences. All the investigated samples are dominated by almost FeO-free enstatite, the presence and abundance of the other mineralogical phases vary among the different samples. Aubrites show a greater heterogeneity than enstatite chondrites and achondrites. Mineral chemistry also differs among meteorites from different groups, suggesting that they originated from multiple reduced parent bodies. The heterogeneity of aubrites is well represented by the Rantila meteorite, for which several fragments very diverse from one another were characterized. Although none of these meteorites represents a perfect petrological analogue of Mercury's surface, they are the best natural analogues currently available. In particular, aubrites represent the best spectral analogue, and improving our understanding of the relationship between spectral properties and minero-chemistry of these reduced materials can provide valuable information for the future interpretation of Bepi-Colombo data from SIMBIO-SYS and MIXS instruments.

For a consistent comparison between aubrites and Mercury's surface spectra, the effect of SpWe on the planet's surface must be taken into account. Therefore, ion irradiation experiments were conducted on aubrites to simulate the effects of solar wind irradiation on the spectra of highly reduced materials. The observed spectral changes include darkening and reddening in the VNIR range, as well as red shifts of the CFs and RBs positions, and a reduction of spectral contrast in the MIR range. The extent of these changes depends on the composition of the target materials, on their surface form (with differences observed between pellets and rock fragments), and on the type of ion used. The low amount of iron present in aubrite limits the formation of $npFe^0$, suggesting

that the spectral changes induced by ion irradiation result from different mechanisms. Based on our observations, the presence of carbon in the target material might cause enhanced spectral changes, especially darkening, which is particularly interesting for Mercury, where carbon is present on the surface. We can assume that the different Mercury's geochemical terranes might react differently to SpWe, depending on their composition.

Additional spectral information that can be useful for understanding Mercury's surface was obtained from the investigation of boninites. These terrestrial samples show mineral assemblages that do not exactly match the inferred mineralogy of Mercury's surface (e.g., the presence of hydrated phases from aqueous alteration and the absence of metals and Mg, Ca, Mn sulphides). On the other hand, bulk composition analyses confirmed a good match in major element contents (wt%) with the estimated composition of Mercury's geochemical terranes, although FeO is substantially higher in the terrestrial rocks. The samples were heated to Mercury's surface temperatures. In the VNIR range, heating caused spectral changes mainly related to the loss of hydrated phases, while in the MIR range, we observed a decrease in the spectral contrast and a shift in the RBs positions. This is particularly relevant for the future interpretation of MERTIS data. Moreover, the emissivity spectra show that the CFs and emissivity minima shift with increasing temperature. In particular, the emissivity minima shift in opposite directions for mafic-richer and felsic-richer samples. However, the minima positions remain distinct, suggesting that MERTIS will easily identify mafic-richer and felsic-richer terranes.

Overall, the results presented in this thesis can help in the interpretation of Mercury's surface data. By relating the mineralogy and chemical composition to spectral behaviour, and considering the effects of SpWe, this work provides information that could be useful for the BepiColombo mission. Specifically, it can help in the understanding and linking of the data from SIMBIO-SYS, MERTIS, and MIXS instruments. Linking the information coming from these three instruments, along with the others onboard the mission, will give us insights into Mercury's formation and evolution.

## Acknowledgements

The research work presented in this thesis has been conducted during and with the support of the Italian national inter-university PhD programme in Space Science and Technology, University of Trento - University of Florence.

The research activities were supported by the Italian Space Agency (ASI) under ASI-INAF agreement 2017-47-H.0 (Bepicolombo SIMBIO-SYS).

The collection of samples used in this study was financed by by the Space It Up project funded by the Italian Space Agency, ASI, and the Ministry of University and Research, MUR, under contract n. 2024-5-E.0 – CUP n. I53D24000060005.

The experiments on INGMAR-SIDONIE were supported by the French CNES (BepiColombo mission). I am grateful to Dr. M. Vincendon for supporting the experimental campaign.

I wish to thank Dr. Andreas Morlok for kindly providing the thin sections of the Norton County meteorite and the powders of the the Peña Blanca Spring meteorite.

I would like to acknowledge the valuable technical support of Dr. L. Chiarantini and Dr. T. Catelani for SEM analyses; Dr. E. Braschi, Dr. A. Orlando, and Dr. D. Borrini for EPMA analyses; Dr. A. Orlando and D. Borrini for experimental petrology activities; Dr. L. Chelazzi and S. Ciattini for XRF and XRD analyses; O. Mivumbi, K. Guernon, and P. Benoit-Lamaitrie for the SIDONIE and INGMAR setup; and F. Borondics for MIR measurements.

I sincerely thank Dr. G. Alemanno, Dr. C. Lantz, Dr. A. Maturilli, and Dr. R. Brunetto, my tutors abroad, for their guidance, their warm welcome, and everything they taught me during my research periods abroad.

I am especially grateful to Prof. G. Pratesi and Dr. C. Carli for their guidance, their encouragement, and for sharing their knowledge and research ideas with me.

# References


Arndt, N. (2003). Komatiites, kimberlites, and boninites. Journal of Geophysical Research: Solid Earth, 108. https://doi.org/10.1029/2002JB002157.

Barrat, J. A., Greenwood, R.C., Keil, K., Rouget, M.L., Boesenberg, J.S., Zanda, B., & Franchi, I. A. (2016). The origin of aubrites: Evidence from lithophile trace element abundances and oxygen isotope compositions. Geochimica et Cosmochimica Acta, 192, 29–48. https://doi.org/10.1016/j.gca.2016.07.025.

Barraud, O., Besse, S. & Doressoundiram, A. (2023). Low sulfide concentration in Mercury's smooth plains inhibits hollows. Science Advances, 9, eadd6452. DOI:10.1126/sciadv.add6452.

Barraud, O., Besse, S., Doressoundiram, A., Cornet, T., & Muñoz C. (2021). Spectral investigation of Mercury's pits' surroundings: Constraints on the planet's explosive activity. Icarus, 370, 114652. https://doi.org/10.1016/j.icarus.2021.114652.

Barraud, O., Doressoundiram, A., Besse, S., & Sunshine J.M. (2020). Near-Ultraviolet to Near-Infrared Spectral Properties of Hollows on Mercury: Implications for Origin and Formation Process. Journal of Geophysical Research: Planets, 125. https://doi.org/10.1029/2020JE006497.

Barraud, O., et al. (2025). Mercury-Y lab: a scientific rehearsal for future BepiColombo observations. 56th LPSC (2025), n.1962.

Benkhoff, J., Murakami, G., Baumjohann,W., Besse, S., Bunce, E., Casale, M., et al. (2021). BepiColombo - Mission Overview and Science Goals. Space Science Reviews, 217:90. https://doi.org/10.1007/s11214-021-00861-4.

Berthet, S., Malavergne, V., & Righter, K. (2009). Melting of the Indarch meteorite (EH4 chondrite) at 1 GPa and variable oxygen fugacity: Implications for early planetary differentiation processes. Geochimica et Cosmochimica Acta, 73, 6402–6420. https://doi.org/10.1016/j.gca.2009.07.030.

Blewett, D.T., Chabot, N.L., Denevi, B.W., Ernst, C.M., Head, J.W., Izenberg, N.R., et al. (2011). Hollows on Mercury: MESSENGER evidence for geologically recent volatile-related activity. Science 333 (Issue 6051), 1856–1859. https://doi. org/10.1126/science.1211681.

Blewett, D.T., Ernst, C.M., Murchie, S.L., & Vilas, F. (2018). Mercury's Hollows. In: Solomon SC, Nittler LR, Anderson BJ, eds. Mercury: The View after MESSENGER. Cambridge Planetary Science. Cambridge University Press; 2018:324-345.

Blewett, D. T., Robinson, M. S., Denevi, B. W., Gillis-Davis, J. J., Head, J. W., Solomon, S. C., et al. (2009). Multispectral images of Mercury from the first MESSENGER flyby: Analysis of global and regional color trends. Earth and Planetary Science Letters, 285(3-4), 272-282. https://doi.org/10.1016/j.epsl.2009.02.021.

Blewett, D. T., Vaughan, W. M., Xiao, Z., Chabot, N. L., Denevi, B. W., Ernst, C. M., et al. (2013). Mercury's hollows: Constraints on formation and composition from analysis of geological setting and spectral reflectance. Journal of Geophysical Research: Planets, 118(5), 1013-1032. https://doi.org/10.1029/2012JE004174.

Bott, N., Brunetto, R., Doressoundiram, A., Carli, C., Capaccioni, F., Langevin, Y., et al., (2023). Effects of Temperature on Visible and Infrared Spectra of Mercury Minerals Analogues. Minerals, 13, 250. https://doi.org/10.3390/min13020250.

Brucato, J.R., Palumbo, M.E., & Strazzulla, G. (1997). Carbonic acid by ion implantation in water/carbon dioxide ice mixtures. Icarus 125 (1), 135–144. https://doi.org/10.1006/icar.1996.5561.

Brucato, J.R., Strazzulla, G., Baratta, G., & Colangeli, L. (2004). Forsterite amorphisation by ion irradiation: Monitoring by infrared spectroscopy. Astronomy & Astrophysics, 413(2), 395-401. https://doi.org/10.1051/0004-6361:20031574.

Bruck Syal, M., Schultz, P.H., & Riner, M.A. (2015). Darkening of Mercury's surface by cometary carbon. Nature Geoscience, 8(5), 352–356, doi:10.1038/ngeo2397.

Brunetto, R., & Strazzulla, G. (2005). Elastic collisions in ion irradiation experiments: a mechanism for space weathering of silicates. Icarus, 179 (1), 265–273. https://doi.org/10.1016/j.icarus.2005.07.001.

Brunetto, R., Lantz, C., Dionnet, Z., Borondics, F., Aléon-Toppani, A., Baklouti, et al. (2018). Hyperspectral FTIR imaging of irradiated carbonaceous meteorites. Planetary and Space Science, 158, 38-45. https://doi.org/10.1016/j.pss.2018.05.008.

Brunetto, R., Lantz, C., Ledu, D., Baklouti, D., Barucci, M.A., Beck, P., et al. (2014). Ion irradiation of Allende meteorite probed by visible, IR, and Raman spectroscopies. Icarus, 237, 278–292. https://doi.org/10.1016/j.icarus.2014.04.047.

Brunetto, R., Lantz, C., Nakamura, T., Baklouti, D., Le Pivert-Jolivet, T., Kobayashi, S., & Borondics, F. (2020). Characterizing irradiated surfaces using IR spectroscopy. Icarus, 45, 113722. https://doi.org/10.1016/j.icarus.2020.113722.

Bruschini, E., Carli, C., Buellet, A.-C., Vincendon, M., Capaccioni, F., Ferrari, M., et al. (2022). VNIR reflectance spectra of silicate-graphite mixtures: The effect of graphite content and particle size. Icarus, 378, 114950. https://doi.org/10.1016/j.icarus.2022.114950.

Burbine, T. H., McCoy, T. J., & Dickinson, T. L. (2000). Origin of plagioclase-enriched, igneous, enstatite achondrites. Meteoritics & Planetary Science, 35 (Supplement), A36.

Burbine, T.H., McCoy, T.J., Nittler, L., Benedix, G.K., Cloutis, E.A., & Dickinson, T.L. (2002). Spectra of extremely reduced assemblages: Implications for Mercury. Meteoritics & Planetary Science, 37,1233-1244. https://doi.org/10.1111/j.1945-5100.2002.tb00892.x.

Burns, R.G. (1993). Mineralogical Applications of Crystal Field Theory. 2nd Edition, Cambridge University Press, Cambridge.

Cameron, W.E. (1985). Petrology and origin of primitive lavas from the Troodos ophiolite, Cyprus. Contributions to Mineralogy and Petrology, 89, 239–255. https://doi.org/10.1007/BF00379457.

Cameron, W.E., McCulloch, M.T., & Walker, D.A. (1983). Boninite petrogenesis: chemical and Nd-Sr isotopic constraints. Earth and Planetary Science Letters, 65, 75-89. https://doi.org/10.1016/0012-821X(83)90191-7.

Cameron, W.E., Nisbet, E.G., & Dietrich, V.J. (1979). Boninites, komatiites and ophiolitic basalts. Nature, 280, 550–553. https://doi.org/10.1038/280550a0.

Caminiti, E., Lantz, C., Besse, S., Brunetto, R., Carli, C., Serrano, L., et al. (2024). Effects of ion irradiation on Mercury terrestrial analogues in the visible to mid-infrared. Icarus, 420, 116191. https://doi.org/10.1016/j.icarus.2024.116191.

Cantillo, D.C., Ridenhour, K.I., Battle, A., Joyce, T., Nunez Breceda, J., Pearson, N., & Reddy, V. (2024). Laboratory Spectral Characterization of Ribbeck Aubrite: Meteorite Sample of Earth-impacting Near-Earth Asteroid 2024 BX1. The Planetary Science Journal, 5(138). 10.3847/PSJ/ad4885.

Carli, C., Ferrari, S., Maturilli, A., Serventi, G., Sgavetti, M., Secchiari, A., Montanini, A., & Helbert, J. (2024a). Laboratory Emissivity Spectra of Sulphide-Bearing Samples, New Constraints for the Surface of Mercury: Oldhamite in Mafic Aggregates. Minerals, 14, 62. https://doi.org/10.3390/min14010062.

Carli, C., Maturilli, A., Galiano, A., Penttilä, A., Landi A.I., et al. (2025). Laboratory spectral measurements of mineral mixtures simulating pyroclastic material on Mercury. 56th LPSC (2025), n.1202.

Carli, C., Pratesi, G., Moggi-Cecchi, V., Zambon, F., Capaccioni, F., & Santoro, S. (2018). Northwest Africa 6232: Visible–near infrared reflectance spectra variability of an olivine diogenite. Meteoritics & Planetary Science, 53(10), 2228–2242. https://doi.org/10.1111/maps.13056.

Carli, C., Serrano, L.M., Maturilli, A., Massironi, M., Capaccioni, F., & Helbert, J. (2013). VNIR and TIR spectra of terrestrial komatiites possibly analogues of some hermean terrain compositions. In Proceedings of the 44th Lunar and Planetary Science Conference, The Woodlands, TX, USA, 18–22 March 2013. Abstract 1923.

Carli, C. & Sgavetti, M. (2011). Spectral characteristics of rocks: Effects of composition and texture and implications for the interpretation of planet surface compositions. Icarus, 211, 1034-1048. https://doi.org/10.1016/j.icarus.2010.11.008.

Carli, C., Zambon F., Giacomini, L., De Toffoli, B., Galiano, A., Massironi, M., Galluzzi, V., Capaccioni, F., & Palumbo, P., (2024b). Hollows-like materials, what are their spectral properties telling us? EPSC Abstracts, Vol. 17, EPSC2024-576, 2024. https://doi.org/10.5194/epsc2024-576.

Cartier, C., Hammouda, T., Doucelance, R., Boyet, M., Devidal, J., & Moine, B. (2014). Experimental study of trace element partitioning between enstatite and melt in enstatite chondrites at low oxygen fugacities and 5 GPa. Geochimica et Cosmochimica Acta, 130, 167-187. https://doi.org/10.1016/j.gca.2014.01.002.

Cartier, C., & Wood, B.J. (2019). The Role of Reducing Conditions in Building Mercury. Elements, 15, 39-45. https://doi.org/10.2138/gselements.15.1.39.

Casanova, I., Keil, K., & Newsom, H.E. (1993). Composition of metal in aubrites: constraints on core formation. Geochimica et Cosmochimica Acta, 57, 675–682.

Cassidy, W., & Hapke, B., (1975). Effects of darkening processes on surfaces of airless bodies. Icarus 25, 371–383. https://doi.org/10.1016/0019-1035(75)90002-0.

Cavanaugh, J. F., Smith, J. C., Sun, X., Bartels, A. E., Ramos-Izquierdo, L., Krebs, D. J., et al. (2007). The Mercury Laser Altimeter instrument for the MESSENGER mission. Space Science Reviews, 131, 451-479. https://doi.org/10.1007/s11214-007-9273-4.

Chapman, C. R. (2004). Space Weathering of Asteroid Surfaces. Annual Review of Earth and Planetary Sciences, 32, 539. https://doi.org/10.1146/annurev.earth.32.101802.120453.

Charlier, B., Grove, T. L., & Zuber, M. T. (2013). Phase equilibria of ultramafic compositions on Mercury and the origin of the compositional dichotomy. Earth and Planetary Science Letters, 363, 50-60. https://doi.org/10.1016/j.epsl.2012.12.021.

Chauvin, N., Dayras, F., Le Du, D., & Meunier, R., (2004). SIDONIE: an electromagnetic isotope separator for preparation of high purity thin targets. Nuclear Instruments and Methods in Physics Research, Sect. A 521 (1), 149–155. https://doi.org/10.1016/j.nima.2003.11.417.

Chassefière, E., Maria, J. L., Goutail, J. P., Quémerais, E., Leblanc, F., Okano, S., et al. (2010). PHEBUS: A double ultraviolet spectrometer to observe Mercury's exosphere. Planetary and Space Science, 58(1-2), 201-223. https://doi.org/10.1016/j.pss.2008.05.018.

Chrbolková, K., Brunetto, R., Ďurech, J., Kohout, T., Mizohata, K., Malý, P., et al. (2021). Comparison of space weathering spectral changes induced by solar wind and micrometeoroid impacts using ion-and femtosecond-laser-irradiated olivine and pyroxene. Astronomy & Astrophysics, 654, A143. https://doi.org/10.1051/0004-6361/202140372.

Cintala, M.J., (1992). Impact-induced thermal effects in the lunar and Mercurian regoliths. Journal of Geophysical Research, 97, 947. https://doi.org/10.1029/91JE02207.

Clark, R.N., (1999). Spectroscopy of rocks and minerals and principles of spectroscopy. In: Rencz, A.N. (Ed.), Remote Sensing for the Earth Sciences: Manual of Remote Sensing, third ed. John Wiley and Sons, Inc, pp. 3–52.

Clark, B.E., Bus, S.J., Rivkin, A.S., McConnochie, T., Sanders, J., Shah, S., Hiroi, T., & Shepard, M. (2004). E-type asteroid spectroscopy and compositional modeling, Journal of Geophysical Research, 109, E02001, doi:10.1029/2003JE002200.

Clark, R.N., & Roush, T.L. (1984). Reflectance spectroscopy: Quantitative analysis techniques for remote sensing applications. Journal of Geophysical Research: Solid Earth, 89, 6329-6340. https://doi.org/10.1029/JB089iB07p06329.

Cloutis, E. A., (2002). Pyroxene reflectance spectra: Minor absorption bands and effects of elemental substitutions. Journal of Geophysical Research, 107(E6), 5039. https://doi.org/10.1029/2001JE001590.

Cloutis, E.A., Craig, M.A., Kruzelecky, R.V., Jamroz, W.R., Scott, A., Hawthorne, F.C., & Mertzman S.A., (2008). Spectral reflectance properties of mineral exposed to simulated Mars surface conditions. Icarus, 195, 140-168. https://doi.org/10.1016/j.icarus.2007.10.028.

Cloutis, E.A., & Gaffey M.J. (1991). Pyroxene spectroscopy revisited: Spectral-compositional correlations and relationship to geothermometry. Journal of Geophysical Research : Planets, 96, 22809–22826. https://doi.org/10.1029/91JE02512.

Cloutis, E.A., & Gaffey M.J. (1993). Accessory phases in aubrites: spectral properties and implications for asteroid 44 Nysa. Earth, Moon and Planets, 63, 227–243. https://doi.org/10.1007/BF00572470.

Cloutis, E.A., Gaffey M.J., & Applin, D.M. (2016). Spectral reflectance properties of aubrites. 47th Lunar and Planetary Conference (2016).

Cloutis, E.A., Gaffey, M.J., Jackowski, T.L., & Reed K.L. (1986). Calibrations of Phase Abundance, Composition, and Particle Size Distribution for Olivine-Orthopyroxene Mixtures From Reflectance Spectra. Journal of Geophysical Research, 91, B11, 11,641-11,653.

Cloutis, E.A., Gaffey, M.J., Smith, D.G.W., & Lambert, R.S.J. (1990). Reflectance spectra of "featureless" materials and the surface mineralogies of M- and E-class asteroids. Journal of Geophysical Research: Solid Earth, 95, 281-293. https://doi.org/10.1029/JB095iB01p00281.

Cloutis, E.A., Hudon, P., Hiroi, T., Gaffey, M.J., & Mann, P. (2011). Spectral reflectance properties of carbonaceous chondrites: 2. CM chondrites. Icarus, 216, 309-346. https://doi.org/10.1016/j.icarus.2011.09.009.

Cloutis, E.A., Izawa, M.R.M., Pompilio, L., Reddy, V., Hiesinger, H., Nathues, A., Mann, P., Le Corre, L., Palomba, E., & Bell III, J.F. (2013). Spectral reflectance properties of HED meteorites + CM2 carbonaceous chondrites: Comparison to HED grain size and compositional variations and implications for the nature of low-albedo features on Asteroid 4 Vesta. Icarus, 223, 850-877. https://doi.org/10.1016/j.icarus.2013.02.003.

Cloutis, E.A., Reddy, V., & Blewett, D.T. (2018). The ungrouped achondrite Northwest Africa (NWA) 7325: Spectral reflectance properties and implications for parent body identification. Icarus, 311, 384-393. https://doi.org/10.1016/j.icarus.2018.04.027.

Cooper, B.L., Salisbury, J.W., Killen, R.M., & Potter, A.E. (2002). Midinfrared spectral features of rocks and their powders. Journal of Geophysical Research: Planets, 107, E4, 5017. https://doi.org/10.1029/2000JE001462.

Crawford, A.J., Falloon, T.J. & Green, D.H. (1989). Classification, petrogenesis and tectonic setting of boninites. In Crawford, A.J. (ed.), Boninites: And related Rocks. London, Unwin Hyman Ltd., p. 1–49.

Cremonese, G., Capaccioni, F., Capria, M.T., Doressoundiram, A., Palumbo, P., Vincendon, M., et al. (2020). SIMBIO-SYS: Scientific Cameras and Spectrometer for the BepiColombo Mission. Space Science Reviews, 216(75). https://doi.org/10.1007/s11214-020-00704-8.

Crowley, J.K., Williams, D.E., Hammarstrom, J.M., Piatak, N., Ming Chou, I., & Mars, J.C. (2003). Spectral reflectance properties (0.4-2.5 µm) of secondary Fe-oxide, Fe-hydroxide, and Fe-sulphate-hydrate minerals associated with sulphide-bearing mine wastes. Exploration, Environment, Analysis, 3, 219-228. https://doi.org/10.1144/1467-7873/03-001.

Denevi, B. W., Ernst, C. M., Meyer, H. M., Robinson, M. S., Murchie, S. L., Whitten, J. L., et al. (2013). The distribution and origin of smooth plains on Mercury. Journal of Geophysical Research: Planets, 118(5), 891-907. https://doi.org/10.1002/jgre.20075.

Derham, C. J., Geake, J. E., & Walker, G. (1964). Luminescence of enstatite achondrite meteorites. Nature, 203, 134-136. https://doi.org/10.1038/203134b0.

Dibb, S.D., Bell, J.F., & Garvie, L.A.J. (2022). Spectral reflectance variations of aubrites, metal-rich meteorites, and sulfides: Implications for exploration of (16) Psyche and other "spectrally featureless" asteroids. Meteoritics & Planetary Science, 57(8), 1570–1588. https://doi.org/10.1029/2022EA002694.

Domingue, D.L., Chapman, C.R., Killen, R.M., Zurbuchen, T.H., Gilbert, J.A., Sarantos, M., et al. (2014). Mercury's weather-beaten surface: understanding mercury in the context of lunar and Asteroidal space weathering studies. Space Science Reviews, 181, 121–214. https://doi.org/10.1007/s11214-014-0039-5.

Domingue, D.L., Hash, C.D., Denevi, B.W., & Murchie, S.L. (2017). Extending MESSENGER's Mercury dual imager's eight-color photometric standardization to cover all eleven filters. Icarus, 297, 83-89. https://doi.org/10.1016/j.icarus.2017.06.023.

Dunn, T.L., McCoy, T.J., Sunshine, J.M., & McSween Jr., H.Y. (2010). A coordinated spectral, mineralogical, and compositional study of ordinary chondrites. Icarus, 208, 789-797. https://doi.org/10.1016/j.icarus.2010.02.016.

Dunne, J. A., & Burgess, E. (1978). The voyage of Mariner 10: mission to Venus and Mercury (Vol. 424). Scientific and Technical Information Division, National Aeronautics and Space Administration.

Edgett, K.S., et al. (2012). Curiosity's Mars Hand Lens Imager (MAHLI) Investigation. Space Science Reviews, 170, 259-317. https://doi.org/10.1007/s11214-012-9910-4.

Evans, L.G., Peplowski, P.N., McCubbin, F.M., McCoy, T.J., Nittler, L.R., Zolotov, M.Y., et al. (2015). Chlorine on the surface of Mercury: MESSENGER gamma-ray measurements and implications for the planet's formation and evolution. Icarus, 257, 417–427. https://doi.org/10.1016/j.icarus.2015.04.039.

Evans, L.G., Peplowski, P.N., Rhodes, E.A., Lawrence, D.J., McCoy, T.J., Nittler, L.R., et al. (2012). Major-element abundances on the surface of Mercury: results from the MESSENGER gamma-ray spectrometer. Journal of Geophyical Research: Planets, 117, E00L07. https://doi.org/10.1029/2012JE004178.

Fang, Z., Hao, Z., Zhang, L., Wu, H., Wu, Hu., Pan, G., & Zhang, J. (2022). $Cr^{3+}$ doped broadband near infrared dipside phopshor for NIR pc-LED. Materials Research Bulletin, 149, 111725. https://doi.org/10.1016/j.materresbull.2021.111725.

Ferrari, S., Maturilli, A., Carli, C., D'Amore, M., Helbert, J., Nestola, F., & Hiesinger, H. (2020). Thermal infrared emissivity of felsic-rich to mafic-rich analogues of hot planetary regoliths. Earth and Planetary Science Letters, 534, 116089. https://doi.org/10.1016/j.epsl.2020.116089.

Ferrari, S., Nestola, F., Massironi, M., Maturilli, A., Helbert, J., Alvaro, M., Domeneghetti, M.C., & Zorzi F. (2014). In-situ high-temperature emissivity spectra and thermal expansion of C2/c pyroxenes: Implications for the surface of Mercury. American Mineralogist, 99, 786–792. https://doi.org/10.2138/am.2014.4698.

Finch, A.A., Dumańska-Słowik, M., González-Acebrón, L., & Schertl, H-P. (2024). Luminescence Applications in Petrology. Elements, 20, 305-311. https://doi.org/10.2138/gselements.20.5.305.

Floss, C., Fogel, R. A., Lin, Y., & Kimura, M. (2003). Diopside-bearing EL6 EET 90102: Insights from rare earth element distributions. Geochimica et Cosmochimica Acta, 67(3), 543–555. https://doi.org/10.1016/S0016-7037(02)01117-1.

Fogel, R.A. (1997). On the significance of diopside and oldhamite in enstatite chondrites and aubrites. Meteoritics & Planetary Science, 32, 577-591. https://doi.org/10.1111/j.1945-5100.1997.tb01302.x.

Fogel, R.A. (2005). Aubrite basalt vitrophyres: The missing basaltic component and high-sulfur silicate melts. Geochimica et Cosmochimica Acta, 69(6), 1633–1648. https://doi.org/10.1016/j.gca.2003.11.032.

Fraser, G.W., Carpenter, J.D., Rothery, D.A., Pearson, J.F., Martindale, A., Huovelin, J., et al., 2010. The Mercury Imaging X-ray Spectrometer (MIXS) on BepiColombo, Planetary and Space Science, 58, 79–95. https://doi.org/10.1016/j.pss.2009.05.004.

Fulvio, D., Brunetto, R., Vernazza, P., & Strazzulla, G., (2012). Space weathering of Vesta and V-type asteroids: New irradiation experiments on HED meteorites. Astronomy & Astrophyics, 537, 1–5, L11. https://doi.org/10.1051/0004-6361/201118486.

Gaffey, M.J., Burbine, T.H. & Binzel, R.P. (1993). Asteroid spectroscopy: Progress and perspectives. Meteoritics, 28, 161-187. https://doi.org/10.1111/j.1945-5100.1993.tb00755.x.

Gaft, M., Megaw, P.K.M., Lambeck, L., & Cantor, S. (2024). Luminescence Applications in Ore Geology, Mining, and Industry. Elements, 20, 318-323. https://doi.org/10.2138/gselements.20.5.318.

Gaft, M., Reisfeld, R., & Panczer, G. (2015). Modern Luminescence Spectroscopy of Minerals and Materials. Springer.

Galiano, A., Capaccioni, F., Filacchione, G., & Carli, C. (2022). Spectral identification of pyroclastic deposits on Mercury with MASCS/MESSENGER data. Icarus, 388, 115233. https://doi.org/10.1016/j.icarus.2022.115233.

Galiano, A., Capaccioni, F., Filacchione, G., & Carli, C. (2023). Principal Component Analysis applied on MASCS/MESSENGER data for the spectral investigation of Mercury's surface. Icarus, 401, 115609. https://doi.org/10.1016/j.icarus.2023.115609.

Gass, I.G., (1968). Is the Troodos Massif of Cyprus a Fragment of Mesozoic Ocean Floor? Nature, 220, 39–42. https://doi.org/10.1038/220039a0.

Gattacceca, J., McCubbin, F. M., Grossman, J. N., Schrader, D. L., Chabot, N. L., D'Orazio, M., et al. (2022). The Meteoritical Bulletin, No. 110. Meteoritics & Planetary Science, 57(11), 2102–2105. https://doi.org/10.1111/maps.13918.

Gattacceca, J., McCubbin, F. M., Grossman, J. N., Schrader, D. L., Chabot, N. L., D'Orazio, M., et al. (2023). The Meteoritical Bulletin, No. 111. Meteoritics & Planetary Science, 58(6), 901–904. https://doi.org/10.1111/maps.13995.

Gattacceca, J., McCubbin, F. M., Grossman, J. N., Schrader, D. L., Chabot, N. L., D'Orazio, M., et al. (2024). The Meteoritical Bulletin, No. 112. Meteoritics & Planetary Science, 59(7), 1820–1823. https://doi.org/10.1111/maps.14181.

Gattacceca, J., McCubbin, F. M., Grossman, J., Bouvier, A., Bullock, E., Chennaoui Aoudjehane, H., et al. (2021). The Meteoritical Bulletin, No. 109. Meteoritics & Planetary Science, 56(8), 1626–1630. https://doi.org/10.1111/maps.13714.

Geake, J.E., & Walker, G. (1966). The luminescence spectra of meteorites. Geochimica et Cosmochimica Acta, 30, 929-937. https://doi.org/10.1016/0016-7037(66)90028-7.

Geological Survey Department, Nicosia, Cyprus (1991). Geological Map of The Southern Troodos Transform Fault Zone. Scale 1:35,000 reprinted in 2017, sheet 2.

Gillis, K.M., & Robinson, P.T. (1990). Patterns and Processes of Alteration in the Lavas and Dykes of the Troodos Ophiolite, Cyprus. Journal of Geophysical Research: Solid Earth, 95, 21,523-21,548. https://doi.org/10.1029/JB095iB13p21523.

Goldsten, J. O., Rhodes, E. A., Boynton, W. V., Feldman, W. C., Lawrence, D. J., Trombka, J. I., et al. (2007). The MESSENGER gamma-ray and neutron spectrometer. Space Science Reviews, 339-391. https://doi.org/10.1007/s11214-007-9262-7.

Götze, J., MacRae, C.M., & Nasdala, L. (2024). Luminescence Images: What is That You See? Elements, 20, 299-304. https://doi.org/10.2138/gselements.20.5.299.

Goudge, T.A., Head, J.W., Kerber, L., Blewett, D.T., Denevi, B.W., Domingue, D.L., et al. (2014). Global inventory and characterization of pyroclastic deposits on mercury: new insights into pyroclastic activity from MESSENGER orbital data. Journal of Geophysical Research: Planets 119 (Issue3), 635–658. https://doi.org/10.1002/2013JE004480.

Green, G., & Walker, G. (1985). Luminescence excitation spectra of Mn2+ in synthetic forsterite. Physics and Chemistry of Minerals, 12, 271–278. https://doi.org/10.1007/BF00310339.

Grossman, J. N., & Zipfel, J. (2001). The Meteoritical Bulletin, No. 85, 2001 September. Meteoritics & Planetary Science, 36(S9), A293–A322. https://doi.org/10.1111/j.1945-5100.2001.tb01542.x.

Hapke, B. (1973). Darkening of silicate rocks by solar wind sputtering. Moon, 7, 342-355. https://doi.org/10.1007/BF00564639.

Hapke, B. (2001). Space weathering from mercury to the asteroid belt. Journal of Geophysical Research: Planets, 106 (E5), 10039–10073. https://doi.org/10.1029/2000JE001338.

Harloff, J., & Arnold, G. (2001). Near-infrared reflectance spectroscopy of bulk analog materials for planetary crust. Planetary and Space Science, 49, 191-211. https://doi.org/10.1016/S0032-0633(00)00132-X.

Hawkins, S. E., Boldt, J. D., Darlington, E. H., Espiritu, R., Gold, R. E., Gotwols, B., et al. (2007). The Mercury dual imaging system on the MESSENGER spacecraft. Space Science Reviews, 131, 247-338. https://doi.org/10.1007/s11214-007-9266-3.

Head, J.W., Murchie, S.L., Prockter, L.M., Robinson, M.S., Solomon, S.C., Strom, R.G., et al. (2008). Volcanism on mercury: evidence from the first MESSENGER flyby. Science, 321 (Issue 5885), 69–72. 10.1126/science.1159256.

Helbert, J., & Maturilli, A. (2009). The emissivity of a fine-grained labradorite sample at typical Mercury dayside temperatures. Earth and Planetary Science Letters, 285, 347–35. https://doi.org/10.1016/j.epsl.2009.02.031.

Helbert, J., Nestola, F., Ferrari, S., Maturilli, A., Massironi, M., Redhammer, G.J., et al. (2013). Olivine thermal emissivity under extreme temperature ranges: Implication for Mercury surface. Earth and Planetary Science Letters, 371–372, 252–257. https://doi.org/10.1016/j.epsl.2013.03.038.

Hiesinger, H., Helbert, J., Alemanno, G., Bauch, K.E., D'Amore, M., Maturilli, A., et al. (2020). Studying the Composition and Mineralogy of the Hermean Surface with the Mercury Radiometer and Thermal Infrared Spectrometer (MERTIS) for the BepiColombo Mission: An Update. Space Science Reviews, 216(110). https://doi.org/10.1007/s11214-020-00732-4.

Izawa, M.R.M., Applin, D.M., Mann, P., Craig, M.A., Cloutis, E.A., Helbert, J., & Maturilli, A. (2013). Reflectance spectroscopy (200–2500 nm) of highly-reduced phases under oxygen- and water-free conditions. Icarus, 226(2), 1612-1617. https://doi.org/10.1016/j.icarus.2013.08.014.

Izenberg, N.R., Klima, R.L., Murchie, S.L., Blewett, B.T., Holsclaw, G.M., McClintock, W.E., et al. (2014). The low-iron, reduced surface of mercury as seen in spectral reflectance by MESSENGER. Icarus 228, 364–374. https://doi.org/10.1016/j.icarus.2013.10.023.

Jäggi, N., Galli, A., Wurz, P., Biber, H., Szabo, P.S., Brötzner, J., et al. (2021). Creation of lunar and Hermean analogue mineral powder samples for solar wind irradiation experiments and mid-infrared spectra analysis. Icarus, 365, 114492. https://doi.org/10.1016/j.icarus.2021.114492.

Johnson, L.E., & Fryer, P. (1990). The first evidence for MORB-like lavas from the outer Mariana forearc: geochemistry, petrography and tectonic implications. Earth and Planetary Science Letters, 100, 304- 316. https://doi.org/10.1016/0012-821X(90)90193-2.

Johnson, R.E., 1990. Energetic charged–particle interactions with atmospheres and surfaces. In: Lanzerotti, L.J., Hill, M., Stoffler Munster, D. (Eds.), Physics and Chemistry in Space Planetology, vol. 19. Springer, Berlin, 232pp.

Kallemeyn, G.W., & Wasson, J.T. (1986). Compositions of enstatite (EH3, EH4,5 and EL6) chondrites: Implications regarding their formation. Geochimica et Cosmochimica Acta, 50(10), 2153-2164. https://doi.org/10.1016/0016-7037(86)90070-0.

Keil K. (1968). Mineralogical and chemical relationships among enstatite chondrites. Journal of Geophysical Research, 73, 6945–6976. https://doi.org/10.1029/JB073i022p06945.

Keil, K. (1989). Enstatite meteorites and their parent bodies. Meteoritics, 24, 195-208. https://doi.org/10.1111/j.1945-5100.1989.tb00694.x.

Keil, K. (2007). Occurrence and origin of keilite, $(Fe_{>0.5},Mg_{<0.5})S$, in enstatite chondrite impact-melt rocks and impact-melt breccias. Chemie der Erde, 67, 37–54. https://doi.org/10.1016/j.chemer.2006.05.002.

Keil, K. (2010). Enstatite achondrite meteorites (aubrites) and the history of their asteroidal parent bodies. Chemie der Erde, 70, 295-317. https://doi.org/10.1016/j.chemer.2010.02.002.

Keil, K., & Bischoff, A. (2008). Northwest Africa 2526: A partial melt residue of enstatite chondrite parentage. Meteoritics & Planetary Science 43(7), 1233–1240. https://doi.org/10.1111/j.1945-5100.2008.tb01125.x.

Keller, L.P., & McKay, D.S. (1993). Discovery of vapor deposits in the lunar regolith. Science, 261(5126), 1305-1307. 10.1126/science.261.5126.1305.

Kerber, L., Head, J.W., Blewett, D.T., Solomon, S.C., Wilson, L. Murchie, S.L., et al. (2011). The global distribution of pyroclastic deposits on mercury: the view from MESSENGER flybys 1-3. Planetary and Space Science, 59 (Issue 15), 1895–1909. https://doi.org/10.1016/j.pss.2011.03.020.

Kerber, L., Head, J.W., Solomon, S.C., Murchie, S.L., Blewett, D.T., & Wilson, L. (2009). Explosive volcanic eruptions on Mercury: eruption conditions, magma volatile content, and implications for interior volatile abundances. Earth and Planetary Science Letters, 285 (issue 3-4), 263–271. https://doi.org/10.1016/j.epsl.2009.04.037.

Kerr, A.C., & Arndt, N.T. (2001). A Note on the IUGS Reclassification of the High-Mg and Picritic Volcanic Rocks. Journal of Petrology, 42(11), 2169-2171. https://doi.org/10.1093/petrology/42.11.2169.

Killen, R., Potter, A.E., Reiff, P., Sarantos, M., Jackson, B.V., Hick, P., & Giles, B. (2001). Evidence for space weather at Mercury. Journal of Geophysical Research: Planets, 106, 20509-20525. https://doi.org/10.1029/2000JE001401.

Kimura, M., Lin, Y.-T., Ikeda, Y., El Goresy, A., Yanai, K., & Kojima, H. (1993). Petrology and mineralogy of Antarctic aubrites, Y-793592 and ALH-78113, in comparison with non-Antarctic aubrites and E-chondrites. Antarctic Meteorites XVII. Papers presented to the 17th Symposium on Antarctic Meteorites, NIPR, Tokyo, August 19–21.

Klima, R.L., Dyar, M.D., & Pieters, C.M. (2011). Near-infrared spectra of clinopyroxenes: Effects of calcium content and crystal structure. Meteoritics & Planetary Science, 46(3), 379-395. https://doi.org/10.1111/j.1945-5100.2010.01158.x

Klima, R.L., Pieters, C.M., & Dyar, M.D. (2007). Spectroscopy of synthetic Mg-Fe pyroxenes I: Spin-allowed and spin-forbidden crystal field bands in the visible and near-infrared. Meteoritics & Planetary Science, 42(2), 235-253. https://doi.org/10.1111/j.1945-5100.2007.tb00230.x.

Klima, R.L., Pieters, C.M., & Dyar, M.D. (2008). Characterization of the 1.2 μm M1 pyroxene band: Extracting cooling history from near-IR spectra of pyroxenes and pyroxene-dominated rocks. Meteoritics & Planetary Science, 43(10), 1591–1604. https://doi.org/10.1111/j.1945-5100.2008.tb00631.x.

Lafuente, B., Downs, R.T., Yang, H., & Stone, N. (2016). “1. The power of databases: The RRUFF project". Highlights in Mineralogical Crystallography, edited by Thomas Armbruster and Rosa Micaela Danisi, Berlin, München, Boston: De Gruyter (O), 2016, pp. 1-30. https://doi.org/10.1515/9783110417104-003.

Lanari, P., Vidal, O., De Andrade, V., Dubacq, B., Lewin, E., Grosch, E.G., & Schwartz, S. (2014). XMapTools: A MATLAB©-based program for electron microprobe X-ray image processing and geothermobarometry. Computers and Geosciences, 62, 227–240. https://doi.org/10.1016/j.cageo.2013.08.010.

Landi, A.I., Gaft, M., Carli, C., Capaccioni, F., & Pratesi, G. (2025). Insights into the mineralogy of the Rantila aubrite: A luminescence and VNIR reflectance spectroscopy study. Icarus, 441, 116725. https://doi.org/10.1016/j.icarus.2025.116725.

Lantz, C., Brunetto, R., Barucci, M.A., Dartois, E., Duprat, J., Engrand, C., et al. (2015). Ion irradiation of the Murchison meteorite: visible to mid-infrared spectroscopic results. Astronomy & Astrophysics, 577, A41. https://doi.org/10.1051/0004-6361/201425398.

Lantz, C., Brunetto, R., Barucci, M.A., Fornasier, S., Baklouti, D., Bourçois, J., & Godard, M. (2017). Ion irradiation of carbonaceous chondrites: a new view of space weathering on primitive asteroids. Icarus, 285, 43–57. https://doi.org/10.1016/j.icarus.2016.12.019.

Lantz, C., Clark, B. E., Barucci, M. A., & Lauretta, D. S. (2013). Evidence for the effects of space weathering spectral signatures on low albedo asteroids. Astronomy & Astrophysics, 554, A138. https://doi.org/10.1051/0004-6361/201321593.

Lantz, C., Nakamura, T., Baklouti, D., Brunetto, R., Henault, E., Kobayashi, S., Mivumbi, O., Djouadi, Z., Quirico, E., Zolensky, M., & Hiroi, T. (2024). Mid-InfraRed measurements of ion irradiated carbonaceous meteorites: How to better detect the space weathering effects? The Planetary Science Journal, 5(9). 10.3847/PSJ/ad5d6f.

LaPaz, L. (1948). The Norton County, Kansas, Meteorite. Science, 107(2786), 543. https://doi.org/10.1126/science.107.2786.543.b.

Laurent, B., Cousins, C.R., Gunn, B., Huntly, C., Cross, R., & Allender, E. (2019). UV luminescence characterisation of organics in Mars-analogue substrates. Icarus, 321, 929-937. https://doi.org/10.1016/j.icarus.2018.12.031.

Lavorenti, F., Jensen, E.A., Aizawa, S., Califano, F., D'Amore, M., Domingue, D., et al. (2023). Maps of solar wind plasma precipitation onto Mercury's surface: a geographical perspective. The Planetary Science Journal, 4(9). 10.3847/PSJ/acef15.

Lawrence, D. J., Feldman, W. C., Goldsten, J. O., Maurice, S., Peplowski, P. N., Anderson, B. J., et al. (2013). Evidence for water ice near Mercury's north pole from MESSENGER Neutron Spectrometer measurements. Science, 339(6117), 292-296. 10.1126/science.1229953.

Le Bas, M.J. (2000). IUGS Reclassification of the High-Mg and Picritic Volcanic Rocks. Journal of Petrology, 41(10), 1467-1470. https://doi.org/10.1093/petrology/41.10.1467.

Lin, Y., & Kimura, M. (1998). Petrographic and mineralogical study of new EH melt rocks and a new enstatite chondrite grouplet. Meteoritics & Planetary Science, 33(5), 501–511. https://doi.org/10.1111/j.1945-5100.1998.tb01654.x.

Leili, M.H., Chennaoui Aoudjehane, H., Devouard, B., Rochette, P., Gattacceca, J., Folco, L., Gemelli, M. & Baziotis, I. (2024). Strewn field, mineralogy, and petrology of Al Haggounia 001: A unique enstatite chondrite. Meteoritics & Planetary Science, 59(2), 301–320. https://doi.org/10.1111/maps.14119.

Lorenz, C.A., Ivanova, M.A., Brandstaetter, F., Kononkova, N.N., & Zinovieva, N.G. (2020). Aubrite Pesyanoe: Clues to composition and evolution of the enstatite achondrite parent body. Meteoritics & Planetary Science, 55, 2670–2702. https://doi.org/10.1111/maps.13612.

Love, S.G., & Keil, K. (1995). Recognizing mercurian meteorites. Meteoritics 30, 269–278.

Lucchetti, A., Pajola, M., Galluzzi, V., Giacomini, L., Carli, C., Cremonese, G., et al. (2018). Mercury Hollows as Remnants of Original Bedrock Materials and Devolatilization Processes: A Spectral Clustering and Geomorphological Analysis. Journal of Geophysical Research: Planets, 123, 2365–2379. https://doi.org/10.1029/2018JE005722.

Lucey, P.G., & Riner, M.A. (2011). The optical effects of small iron particles that darken but do not redden: evidence of intense space weathering on mercury. Icarus, 212 (2), 451–462. https://doi.org/10.1016/j.icarus.2011.01.022.

Lymer, E.A., Daly, M.G., Tait, K.T., Di Cecco, V.E., & Lalla, E.A. (2020). UV laser-induced fluorescence spectroscopy as a non-destructive technique for mineral and organic detection in carbonaceous chondrites. Meteoritics & Planetary Science, 55 (10), 2287–2300. https://doi.org/10.1111/maps.13580.

Marchi, S., Brunetto, R., Magrin, S., Lazzarin, M., & Gandolfi, D. (2005). Space weathering of near-Earth and main belt silicate-rich asteroids: observations and ion irradiation experiments. Astronomy & Astrophysics, 443, 769- 775. https://doi.org/10.1051/0004-6361:20053525.

Mari, N., Eggers, G.L., Filiberto, J., Carli, C., Pratesi, G., Alvaro, M., et al. (2023). Boninites as Mercury lava analogues: Geochemical and spectral measurements from pillow lavas on Cyprus island. Planetary and Space Science, 236, 105764. https://doi.org/10.1016/j.pss.2023.105764.

Markus, K., Arnold, G., Moroz, L., Henckel, D., & Hiesinger, H. (2024). Laboratory reflectance spectra of enstatite and oldhamite mixtures for comparison with Earth-based reflectance spectra of asteroid 2867 Šteins and Mercury. Planetary and Space Science, 244, 105887. https://doi.org/10.1016/j.pss.2024.105887.

Markus, K., Moroz, L., Arnold, G., Henckel, D., Hiesinger, H., Rohrbach, A., & Klemme, S. (2018). Reflectance spectra of synthetic Fe-free ortho- and clinoenstatites in the UV/VIS/IR and implications for remote sensing detection of Fe-free pyroxenes on planetary surfaces. Planetary and Space Science, 159, 43-55. https://doi.org/10.1016/j.pss.2018.04.006.

Maturilli, A., Helbert, J., St. John, J.M., Head, J.W., Vaughan, W.M., D'Amore, M., Gottschalk, M., & Ferrari, S. (2014). Komatiites as Mercury surface analogues: spectral measurements at PEL. Earth and Planetary Science Letters, 398, 58–65. https://doi.org/10.1016/j.epsl.2014.04.035.

Maturilli, A., Helbert, J., Varatharajan, I., & D'Amore, M. (2017). Emissivity Spectra of Mercury Analogues under Mercury Pressure and Temperature Conditions. EPSC Abstracts, Vol. 11, EPSC2017-610, 2017, European Planetary Science Congress 2017.

Maurice, S., Wiens, R.C., & Bernardi, P. et al. (2021). The SuperCam Instrument Suite on the Mars 2020 Rover: Science Objectives and Mast-Unit Description. Space Science Reviews, 217(47). https://doi.org/10.1007/s11214-021-00807-w.

McClintock, W. E., & Lankton, M. R. (2007). The Mercury atmospheric and surface composition spectrometer for the MESSENGER mission. Space Science Reviews, 131, 481-521. https://doi.org/10.1007/s11214-007-9264-5.

McClintock, W. E., Izenberg, N. R., Holsclaw, G. M., Blewett, D. T., Domingue, D. L., Head III, J. W., et al. (2008). Spectroscopic observations of Mercury's surface reflectance during MESSENGER's first Mercury flyby. Science, 321(5885), 62-65. 10.1126/science.1159933.

McCoy, T. J. & Bullock, E.S. (2017). Differentiation under highly-reducing conditions: New insights from enstatite meteorites and Mercury. In L. T. Elkins-Tanton & B. P. Weiss (Eds.), Planetesimals: Early differentiation and consequences for planets. Cambridge University Press. 71-91.

McCoy, T.J., Dickinson, T.L., & Lofgren, G.E. (1999). Partial melting of the Indarch (EH4) meteorite: A textural, chemical, and phase relations view of melting and melt migration. Meteoritics & Planetary Science, 34, 735-746. https://doi.org/10.1111/j.1945-5100.1999.tb01386.x.

McCoy, T. J., Keil, K., Bogard, D. D., Garrison, D. H., Casanova, I., Lindstrom, M. M., Brearley, A. J., Kehm, K., Nichols, R. H., & Hohenberg, C. M. (1995). Origin and history of impact-melt rocks of enstatite chondrite parentage. Geochimica et Cosmochimica Acta, 59(1), 161–175. https://doi.org/10.1016/0016-7037(94)00231-A

McCoy, T.J., Peplowski, P.N., McCubbin, F.M., Weider, S.Z., Solomon, S.C., Nittler, L.R. & Anderson, B.J. (2018). The geochemical and mineralogical diversity of Mercury. In: Mercury, the View After MESSENGER. Cambridge University Press, pp. 176–190.

McCubbin, F.M., Riner, M.A., Vander Kaaden, K.E., & Burkemper, L.K. (2012). Is mercury a volatile-rich planet? Geophysical Research Letters, 39. https://doi.org/10.1029/2012GL051711.

McCubbin, F.M., Vander Kaaden, K.E., Pelowski, P.N., Bell, A.S., Nittler, L.R., Boyce, J.W., et al. (2017). A Low O/Si Ratio on the Surface of Mercury: Evidence for Silicon Smelting? Journal of Geophysical Research: Planets, 122, 2053–2076. https://doi.org/10.1002/2017JE005367.

Milillo, A., Sarantos, M., Grava, C., Janches, D., Lammer, H., Leblanc, F., et al. (2023). Future Directions for the Investigation of Surface-Bounded Exospheres in the Inner Solar System. Space Science Reviews, 219(6), 49. https://doi.org/10.1007/s11214-023-00994-8.

Minitti, M.E., & McCoy, T.J. (2012). Assessing the longwave ultraviolet fluorescenct characteristics of martian meteorites. 43rd Lunar and Planetary Science Conference (2012).

Mitrofanov, I. G., Kozyrev, A. S., Konovalov, A., Litvak, M. L., Malakhov, A. A., Mokrousov, M. I., et al. (2010). The Mercury Gamma and Neutron Spectrometer (MGNS) on board the planetary orbiter of the BepiColombo mission. Planetary and Space Science, 58(1-2), 116-124. https://doi.org/10.1016/j.pss.2009.01.005.

Moores, E.M., & Vine, F.J. (1971). The Troodos Massif, Cyprus and other ophiolites as oceanic crust; evaluation and implications, A discussion on the petrology of igneous and metamorphic rocks from the ocean floor. Philosophical Transactions of the Royal Society of London, 268, 443–466. https://doi.org/10.1098/rsta.1971.0006.

Morlok, A., Klemme, S., Weber, I., Stojic, A., Sohn, M., & Hiesinger, H. (2017). IR spectroscopy of synthetic glasses with Mercury surface composition: Analogs for remote sensing. Icarus, 296, 123-138. https://doi.org/10.1016/j.icarus.2017.05.024.

Morlok, A., Renggli, C., Charlier, B., Namur, O., Klemme, S., Reitze, M.P., et al. (2023). A mid-infrared study of synthetic glass and crystal mixtures analog to the geochemical terranes on mercury. Icarus, 396, 115498. https://doi.org/10.1016/j.icarus.2023.115498.

Morlok, A., Renggli, C., Charlier, B., Reitze, M.P., Klemme, S., Namur, O., et al. (2021). Mid-infrared reflectance spectroscopy of synthetic glass analogs for mercury surface studies. Icarus, 361, 114363. https://doi.org/10.1016/j.icarus.2021.114363.

Morlok, A., Sehlke, A., Stojic, A.N., Whittington, A., Weber, I., Reitze, M.P., Hiesinger, H., & Helbert, J. (2024). Synthetic analogs for lava flows on the surface of Mercury: A mid-infrared study. Icarus, 425, 116078. https://doi.org/10.1016/j.icarus.2024.116078.

Morlok, A., Weber, I., Stojic, A.N., Sohn, M., Bischoff, A., Martin, D., Hiesinger, H., & Helbert, J. (2020). Mid-infrared reflectance spectroscopy of aubrite components. Meteoritics & Planetary Science, 55(9), 2080–2096. https://doi.org/10.1111/maps.13568.

Moroz, L., Baratta, G., Strazzulla, G., Starukhina, L., Dotto, E., Barucci, M.A., Arnold, G., & Distefano, E., (2004). Optical alteration of complex organics induced by ion irradiation: 1. Laboratory experiments suggest unusual space weathering trend. Icarus 170, 214–228. https://doi.org/10.1016/j.icarus.2004.02.003.

Murchie, S.L., Klima, R.L., Denevi, B.W., Ernst, C.M., Keller, M.R., Domingue, D.L., et al. (2015). Orbital multispectral mapping of mercury using the MESSENGER mercury dual imaging System: evidence for the origins of plains units and low-reflectance material. Icarus, 254, 287–305. https://doi.org/10.1016/j.icarus.2015.03.027.

Namur, O., & Charlier, B. (2017). Silicate mineralogy at the surface of Mercury. Nature Geoscience,10, 9–13. https://doi.org/10.1038/ngeo2860.

Namur, O., Charlier, B., Holtz, F., Cartier, C., & McCammon, C. (2016). Sulfur solubility in reduced mafic silicate melts: Implications for the speciation and distribution of sulfur on Mercury. Earth and Planetary Science Letters, 448, 102-114. https://doi.org/10.1016/j.epsl.2016.05.024.

Nesvorný, D., Jedicke, R., Whiteley, R.J., & Ivezić, Ž. (2005). Evidence for asteroid space weathering from the Sloan Digital Sky Survey. Icarus, 173, 132–152. https://doi.org/10.1016/j.icarus.2004.07.026.

Nittler, L.R., Chabot, N.L., Grove, T.L., & Peplowski, P.N. (2018). The chemical composition of mercury. In: Solomon, S., Nittler, L., Anderson, B. (Eds.), Mercury: The View after MESSENGER (Cambridge Planetary Science). Cambridge University Press, Cambridge, pp. 30–51.

Nittler, L.R., Starr, R.D., Weider, S.Z., McCoy, T.J., Boynton, W.V., Ebel, D.S., et al. (2011). The major-element composition of mercury's surface from MESSENGER X-ray spectrometry. Science, 333, 1847–1850. 10.1126/science.1211567.

Nittler, L.R., & Weider, S.Z. (2019). The surface composition of Mercury. Elements, 15, 33-38. https://doi.org/10.2138/gselements.15.1.33.

Noble, S.K., Pieters, C.M., & Keller, L.P. (2007). An experimental approach to understanding the optical effects of space weathering. Icarus, 192 (2), 629–642. https://doi.org/10.1016/j.icarus.2007.07.021.

Noguchi, T. et al. (2023). A dehydrated space-weathered skin cloaking the hydrated interior of Ryugu. Nature Astronomy, 7, 170–181. doi:10.1038/s41550-022-01841-6.

Noguchi, T. et al. (2011). Incipient Space Weathering Observed on the Surface of Itokawa Dust Particles. Science, 333, 1121. doi:10.1126/science.1207794.

Ohnenstetter, D., & Brown, W.L. (1992). Overgrowth Textures, Disequilibrium Zoning, and Cooling History of a Glassy Four-Pyroxene Boninite Dyke from New Caledonia. Journal of Petrology, 33, 231-271. https://doi.org/10.1093/petrology/33.1.231.

Okada, A., Keil, K., Taylor, G.J., & Newsom, H. (1988). Igneous History of the Aubrite Parent Asteroid: Evidence from the Norton County Enstatite Achondrite. Meteoritics, 23, 59-74. https://doi.org/10.1111/j.1945-5100.1988.tb00897.x.

Orsini, S., Livi, S., Torkar, K., Barabash, S., Milillo, A., Wurz, P., et al. (2010). SERENA: A suite of four instruments (ELENA, STROFIO, PICAM and MIPA) on board BepiColombo-MPO for particle detection in the Hermean environment. Planetary and Space Science, 58(1-2), 166-181. https://doi.org/10.1016/j.pss.2008.09.012.

Osozawa, S., Shinjo, R., Lo, C.-H., Jahn, B., Hoang, N., Sasaki, M., et al. (2012). Geochemistry and geochronology of the Troodos ophiolite: an SSZ ophiolite generated by subduction initiation and an extended episode of ridge subduction? Lithosphere, 4(6), 497–510. https://doi.org/10.1130/L205.1.

Patzer, A., Hill, D.H., & Boynton, W.V. (2001). Itqiy: A metal-rich enstatite meteorite with achondritic texture. Meteoritics & Planetary Science, 36(11), 1495–1505. https://doi.org/10.1111/j.1945-5100.2001.tb01841.x.

Pearce, J.A., Lippard, S.J., & Roberts, S. (1984). Characteristics and tectonic significance of supra-subduction zone ophiolites. Geological Society of London Special Publications, 16, 74–94. https://doi.org/10.1144/GSL.SP.1984.016.01.06.

Pearce, J.A., & Robinson, P.T. (2010). The Troodos ophiolitic complex probably formed in a subduction initiation, slab edge setting. Gondwana Research, 18, 60–81. https://doi.org/10.1016/j.gr.2009.12.003.

Penttilä, A. (2025). On the difference between internally or externally mixed darkening agent on regolith reflectance. EPSC Abstracts, Vol. 18, EPSC-DPS2025-1748, 2025. https://doi.org/10.5194/epsc-dps2025-1748.

Penttilä, A., Väisänen, T., Markkanen, J., Martikainen, J., Kohout, T., Videen, G., Muinonen, K., (2020). Rigorous light-scattering simulations of nanophase iron spaceweathering effects on reflectance spectra of olivine grains. Icarus 345, 113727. https://doi.org/10.1016/j.icarus.2020.113727.

Peplowski, P.N., Evans, L.G., Stockstill-Cahill, K.R., Lawrence, D.J., Goldsten, J.O., Mc- Coy, T.J., et al. (2014). Enhanced sodium abundance in mercury's north polar region revealed by the MESSENGER gamma-ray spectrometer. Icarus, 228, 86–95. https://doi.org/10.1016/j.icarus.2013.09.007.

Peplowski, P.N., Klima, R.L., Lawrence, D.J., Ernst, C.M., Denevi, B.W., Frank, E.A., et al. (2016). Remote sensing evidence for an ancient carbon-bearing crust on mercury. Nature Geoscience, 9, 273–276. https://doi.org/10.1038/ngeo2669.

Peplowski, P.N., Lawrence, D.J., Evans, L.G., Klima, R.L., Blewett, D.T., Goldsten, J.O., et al. (2015). Constraints on the abundance of carbon in near-surface materials on Mercury: results from the MESSENGER gamma-ray spectrometer. Planetary and Space Science, 108, 98–107. https://doi.org/10.1016/j.pss.2015.01.008.

Peplowski, P.N., Lawrence, D.J., Rhodes, E.A., Sprague, A.L., McCoy, T.J., Denevi, B.W., et al. (2012a). Variations in the abundances of potassium and thorium on the surface of Mercury: Results from the MESSENGER gamma-ray spectrometer. Journal of Geophysical Research: Planets, 117, E00L04. https://doi.org/10.1029/2012JE004141.

Peplowski, P.N., Rhodes, E.A., Hamara, D.K., Lawrence, D.J., Evans, L.G., Nittler, L.R., & Solomon, S.C. (2012b). Aluminum abundance on the surface of Mercury: Applications of a new background-reduction technique for the analysis of gamma-ray spectroscopy data. Journal of Geophysical Research: Planets., 117, E00L10. https://doi.org/10.1029/2012JE004181.

Pieters, C.M., Fisher, E.M., Rode, O., & Basu, A. (1993). Optical effects of space weathering: The role of the finest fraction. Journal of Geophysical research: Planets, 98 (E11), 20817-20824. https://doi.org/10.1029/93JE02467.

Pieters, C.M., & Noble, S.K. (2016). Space weathering on airless bodies. Journal of Geophysical research: Planets, 121 (10), 1865–1884. https://doi.org/10.1002/2016JE005128.

Pisello, A., Bisolfati, M., Poggiali, G., Tolomei, P., Braschi, E., Brucato, J.R., & Perugini, D. (2023). Mid-Infrared (MIR) Spectroscopy of Silicate Glasses as Analogs for Mercury's Surface: The Influence of Grain Size. Minerals, 13, 170. https://doi.org/10.3390/min13020170.

Pompilio, L., Sgavetti, M., & Pedrazzi, G. (2007). Visible and near-infrared reflectance spectroscopy of pyroxene-bearing rocks: New constraints for understanding planetary surface compositions. Journal of Geophysical research, 112, E01004. https://doi.org/10.1029/2006JE002737.

Potin, S., Beck, P., Schmitt, B., & Monyier, F. (2019). Some things special about NEAs: Geometric and environmental effects on the optical signatures of hydration. Icarus, 333, 415-428. https://doi.org/10.1016/j.icarus.2019.06.026.

Przylibski, T.A., Zagozdzon, P.P., Kryza, R., & Pilski, A.S. (2005). The Zakłodzie enstatite meteorite: Mineralogy, petrology, origin, and classification. Meteoritics & Planetary Science 40, Nr 9, Supplement, A185–A200.

Reddy V., Sanchez, J.A., Bottke W.F., Thirouin, A., Rivera-Valentin. E.G., Kelley, M.S., Ryan, W., Cloutis, E.A., Tegler S.T., Ryan, E.V., Taylor, P.A., Richardson, J.E., Moskovitz, N.M., & Le Corre, L. (2016). Physical characterization of ~2 m diameter Near-Earth Asteroid 2015 TC25: A possible boulder from E-type asteroid (44) Nysa. The Astronomical Journal, 152:162. doi:10.3847/0004-6256/152/6/162.

Reitze, M. P., Weber, I., Morlok, A., Hiesinger, H., Bauch, K. E., Stojic, A. N., & Helbert, J. (2021). Mid-infrared spectroscopy of crystalline plagioclase feldspar samples with various Al, Si order and implications for remote sensing of Mercury and other terrestrial Solar System objects. Earth and Planetary Science Letters, 554, 116697. https://doi.org/10.1016/j.epsl.2020.116697.

Renggli, C.J., Klemme, S., Morlok, A., Berndt, J., Weber, I., Hiesinger, H., & King, P.L. (2022). Sulfides and hollows formed on Mercury's surface by reactions with reducing S-rich gases. Earth and Planetary Science Letters, 593, 117647. https://doi.org/10.1016/j.epsl.2022.117647.

Renggli, C. J., Stojic, A. N., Morlok, A., Berndt, J., Weber, I., Klemme, S., & Hiesinger, H. (2023). Mid-infrared spectroscopy of sulfidation reaction products and implications for sulfur on Mercury. Journal of Geophysical Research: Planets, 128, e2023JE007895. https://doi.org/10.1029/2023JE007895.

Rider-Stokes, B.G., Branagan-Harris, E., Markus, K., Snape, J.F., Jackson, S.L., Russell, S.S., et al. (2025). Insights into pyroxene-dominated surfaces and implications for ongoing space exploration missions. Icarus, 441, 116713. https://doi.org/10.1016/j.icarus.2025.116713.

Rosticher, C., Chanéac, C., Bos, A.,Viana, B. (2016). Study on the persistent luminescence of diopside nanotracers $CaMgSi_2O_6$: $Eu^{2+}$, $Mn^{2+}$, $Pr^{3+}$. Proc. SPIE, 9749, Oxide-based Materials and Devices VII, 97490E (27 February 2016). https://doi.org/10.1117/12.2219992.

Rosticher, C., Viana, B., Laurent, G., Le Griel, P., & Chanéac, C. (2015). Insight into $CaMgSi_2O_6$:$Eu^{2+}$, $Mn^{2+}$, $Dy^{3+}$ Nanoprobes: Influence of Chemical Composition and Crystallinity on Persistent Red Luminescence. European Journal of Inorganic Chemistry, 2015, 3681-3687. https://doi.org/10.1002/ejic.201500257.

Rothery, D. A. (2015). Planet Mercury: From Pale Pink Dot to Dynamic World. Springer. https://doi.org/10.1007/978-3-319-12117-8.

Rothery, D.A., Massironi, M., Alemanno, G. et al., (2020). Rationale for BepiColombo Studies of Mercury's Surface and Composition. Space Science Reviews, 216(66). https://doi.org/10.1007/s11214-020-00694-7.

Rubin, A.E. (1983). The Adhi Kot breccia and implications for the origin of chondrules and silica-rich clasts in enstatite chondrites. Earth and Planetary Science Letters, 64(2), 201-212. https://doi.org/10.1016/0012-821X(83)90204-2.

Rubin, A.E. (2015). Impact features of enstatite-rich meteorites. Chemie der Erde, 75, 1-28. https://doi.org/10.1016/j.chemer.2014.09.001.

Rubino, S., Lantz, C., Baklouti, D., Leroux, H., Borondics, F., & Brunetto, R. (2020). Space weathering affects the remote near-IR identification of phyllosilicates. The Planetary Science Journal 1 (3), 61.

Rubino, S., Leroux, H., Lantz, C., Aleon-Toppani, A., Baklouti, D., Djouadi, Z., et al. (2024). Space-weathering induced changes in hydrated silicates: a multi-scale study combining visible/infrared spectroscopy and electron microscopy. Icarus, 116070. https://doi.org/10.1016/j.icarus.2024.116070.

Ruzicka, A., Grossman, J. N., & Garvie, L. A. J. (2014). The Meteoritical Bulletin, No. 100. Meteoritics & Planetary Science, 49(6), E1–E101. https://doi.org/10.1111/maps.12342.

Sears, D.W., Kallemeyn, G.W., & Wasson, J.T. (1982). The compositional classification of chondrites: II The enstatite chondrite groups. Geochimica et Cosmochimica Acta, 46, 597-608. https://doi.org/10.1016/0016-7037(82)90161-2.

Shackelford, A., Donaldson Hanna, K., Gillis-Davis, J., Rahman, Z., Cymes, B., Christoffersen, R. & Keller, L. (2025). Space Weathering Effects on Mercurian Surface Analogs: Insights from Coordinated Spectral, Microstructural, and Chemical Analyses. EPSC Abstracts, Vol. 18, EPSC-DPS2025-1078, 2025. https://doi.org/10.5194/epsc-dps2025-1078.

Sharma, S., Misra, A.K., Acosta, T.E., & Lucey, P.G. (2012). Time-resolved remote Raman and fluorescence spectrometers for planetary exploration. Proceedings Volume 8379, Laser Radar Technology and Applications XVII; 83790J (2012). https://doi.org/10.1117/12.920955.

Sherman, D.M., Burns, R.G., & Burns V.M., (1982). Spectral characteristics of the iron oxides with application to the martian bright region mineralogy. Journal of Geophysical Research, 87(B12), 10,169-10,180. https://doi.org/10.1029/JB087iB12p10169.

Sherman, D.M., & Waite, T.D. (1985). Electronic spectra of $Fe^{3+}$ oxides and oxide hydroxides in the near IR to near UV. American Minetralogist, 70, 1262-1269.

Schlemm, C. E., Starr, R. D., Ho, G. C., Bechtold, K. E., Hamilton, S. A., Boldt, J. D., et al. (2007). The X-Ray Spectrometer on the MESSENGER spacecraft. The Messenger Mission to Mercury, 393-415. https://doi.org/10.1007/s11214-007-9248-5.

Skinner, B.J., & Luce, F.D. (1971). Solid Solutions of the Type (Ca,Mg,Mn,Fe)S and their use as Geothermometers for the Enstatite Chondrites. American Mineralogist, 56 (7-8), 1269–1296.

Slade, M. A., Butler, B. J., & Muhleman, D. O. (1992). Mercury radar imaging: Evidence for polar ice. Science, 258(5082), 635-640. 10.1126/science.258.5082.635.

Solomon, S.C., McNutt Jr., R.L., Gold, R.E., Acuna, M.H., Baker, D.N., Boynton, W.V., et al. (2001). The MESSENGER mission to Mercury: scientific objectives and implementation. Planetary and Space Science, 49,1445–1465. https://doi.org/10.1016/S0032-0633(01)00085-X.

Solomon, S.C., Nittler, L.R., & Anderson, B.J. (2018). MERCURY: The View after MESSENGER. Cambridge University Press.

Sprague, A. L., Deutsch, L. K., Hora, J., Fazio, G. G., Ludwig, B., Emery, J., & Hoffmann, W. F. (2000). Midinfrared (8.1–12.5 μm) imaging of Mercury. Icarus, 147(2), 421-432. https://doi.org/10.1006/icar.2000.6447.

Srivastava, Y., Kumar, A., Basu Sarbadhikari, A., Ray, D., Nair, V.M., Das, A., Shukla, A.D., Sathiyaseelan, S., Ramachandran, R., Sivaraman, B., Vijayan, S., Panwar, N., Verma, A J., Srivastava N., Rani, A., Arora, G., Mahajan, R.R., & Bhardwaj, A. (2023). The Diyodar meteorite fall in India. Current science, 124, 152-154.

Stockstill-Cahill, K.R., McCoy, T.J., Nittler, L.R., Weider, S.Z., & Hauck II, S.A. (2012). Magnesium-rich crustal compositions on Mercury: implications for magmatism from petrologic modeling. Journal of Geophysical Research: Planets, 117, E00L15. https://doi.org/10.1029/2012JE004140.

Strazzulla, G., Dotto, E., Binzel, R., Brunetto, R., Barucci, M.A., Blanco, A., & Orofino, V., (2005). Spectral alteration of the Meteorite Epinal (H5) induced by heavy ion irradiation: A simulation of space weathering effects on near-Earth asteroids. Icarus 174, 31–35. https://doi.org/10.1016/j.icarus.2004.09.013.

Su, F., Lou, B., Ou, Y., Yang, Y., Zhou, W., Duan, C-K, & Liang, H. (2021). VUV−UV−vis Luminescence, Energy Transfer Dynamics, and Potential Applications of $Ce^{3+}$- and $Eu^{2+}$-Doped $CaMgSi_2O_6$. The Journal of Physical Chemistry C, 125, 5957-5967. https://doi.org/10.1021/acs.jpcc.1c01320.

Sunshine, J.M. & Pieters, C.M. (1998). Determining the composition of olivine from reflectance spectroscopy. Journal of Geophysical Research, 103(6), 13,675-13,688.

Sutton, S.R., Goodrich, C.A., & Wirick, S. (2017). Titanium, vanadium and chromium valences in silicates of ungrouped achondrite NWA 7325 and ureilite Y-791538 record highly-reduced origins. Geochimica et Cosmochimica Acta, 204, 313-330. https://doi.org/10.1016/j.gca.2017.01.036.

Szymczak M., Su K., Mei L., Runowski M., Woźny P., Guo Q., Lia L., & Marciniak L (2024). Investigating the Potential of $Cr^{3+}$-Doped Pyroxene for Highly Sensitive Optical Pressure Sensing. ACS Applied Materials and Interfaces 16, 60491−60500. http://doi.org/10.1021/acsami.4c12145.

Udry, A., Wilbur, Z.E., Rahib, R.R., McCubbin, F.M., Vander Kaaden, K.E., McCoy, T.J., Ziegler, K., Gross, J., DeFelice, C., Combs, L., & Turring, B.D. (2019). Reclassification of four aubrites as enstatite chondrite impact melts: Potential geochemical analogs for Mercury. Meteoritics & Planetary Science, 54(4), 785-810. https://doi.org/10.1111/maps.13252.

Taylor, R.N., Robert, W., Nesbitt, R.W., Harmon, R.S., Auvray, B., & Croudace, I.W. (1994). Mineralogy, chemistry, and genesis of the boninite series volcanics, Chichijima, Bonin Islands, Japan. Journal of Petrology, 35, 577–617. https://doi.org/10.1093/petrology/35.3.577.

Thomas, R.J., Hynek, B.M., Rothery, D.A., & Conway, S.J. (2016). Mercury's low-reflectance material: Constraints from hollows. Icarus, 277, 455-465. https://doi.org/10.1016/j.icarus.2016.05.036.

Thomas, R.J., et al. (2014). Mechanisms of explosive volcanism on Mercury: implications from its global distribution and morphology. Journal of Geophysical Research: Planets 119, 2239–2254. https://doi.org/10.1002/2014JE004692.

Trang, D., Lucey, P.G., & Izenberg, N.R. (2015), Radiative tranfer modeling of Messenger VIRS spectra of Mercury: Detection and mapping of submicroscopic iron and carbon, Abstract 2014 presented at Workshop on Space Weathering of Airless Bodies: Integration of Remote Sensing Data, Laboratory Experiments, and Sample Analysis, Lunar and Planet. Inst., Houston.

Vander Kaaden, K.E., & McCubbin, F.M. (2015). Exotic crust formation on Mercury: Consequences of a shallow, FeO-poor mantle. Journal of Geophysical Research: Planets., 120, 195–209, https://doi.org/10.1002/2014JE004733.

Vander Kaaden, K.E., & McCubbin, F.M. (2016). The origin of boninites on Mercury: an experimental study of the northern volcanic plains lavas. Geochimica et Cosmochimica Acta,173, 246–263. https://doi.org/10.1016/j.gca.2015.10.016.

Vander Kaaden, K.E., McCubbin, F.M., Nittler, L.R., Peplowski, P.N., Wieder, S.Z., Frank, E.A., & McCoy, T.J. (2017). Geochemistry, mineralogy, and petrology of boninitic and komatiitic rocks on the mercurian surface: insights into the mercurian mantle. Icarus, 285, 155–168. https://doi.org/10.1016/j.icarus.2016.11.041.

Van Niekerk, D., Keil, K., & Humayun M. (2014). Petrogenesis of anomalous Queen Alexandra Range enstatite meteorites and their relation to enstatite chondrites, primitive enstatite achondrites, and aubrites. Meteoritics & Planetary Science, 49(3), 295–312. https://doi.org/10.1111/maps.12248.

Vernazza, P., Brunetto, R., Binzel, R. P., Perron, C., Fulvio, D., Strazzulla, G., & Fulchignoni, M. (2009). Plausible parent bodies for enstatite chondrites and mesosiderites: Implications for Lutetia's fly-by. Icarus, 202(2), 477–486. https://doi.org/10.1016/j.icarus.2009.03.016.

Vernazza, P., Fulvio, D., Brunetto, R., Emery, J.P., Dukes, C.A., Cipriani, F., Witasse, O., et al. (2013). Paucity of Tagish Lake-like Parent Bodies in the Asteroid Belt and among Jupiter Trojans. Icarus, 225 (1), 517–525. https://doi.org/10.1016/j.icarus.2013.04.019.

Vilas, F., Domingue, D.L., Helbert, J., D'Amore, M., Maturilli, A., Klima, R.L. et al. (2016). Mineralogical indicators of Mercury's hollows composition in MESSENGER color observations. Geophysical Research Letters, 43(4), 1450-1456. https://doi.org/10.1002/2015GL067515.

Vilas, F., & Hendrix, A. (2015). The UV/blue effects of space weathering manifested in S-complex asteroids. I. Quantifying change with asteroid age. The Astronomical Journal, 150 (Issue 2), 12. 10.1088/0004-6256/150/2/64.

Watters, T.R. & Prinz, M. (1979). Aubrites: Their origin and relationship to enstatite chondrites. Proc. Lunar Planet. Sci. Conf. 10th,1073-1093.

Weber, I., Reitze, M.P., Morlok, A., Stojic, A.N., Hiesinger, H., Schmedemann, N., et al. (2023). Mid-IR spectral properties of different surfaces of silicate mixtures before and after excimer laser irradiation. Icarus, 404, 115683. https://doi.org/10.1016/j.icarus.2023.115683.

Weber, I., Stojic, A.N., Morlok, A., Reitze, M.P., Markus, K., Hiesinger, H., et al. (2020). Space weathering by simulated micrometeorite bombardment on natural olivine and pyroxene: A coordinated IR and TEM study. Earth and Planetary Science Letters, 530, 115884. https://doi.org/10.1016/j.epsl.2019.115884.

Weider, S.Z., Nittler, L.R., Murchie, S.L., Peplowski, P.N., McCoy, T.J., Kerber, L., et al. (2016). Evidence from MESSENGER for sulfur- and carbon-driven explosive volcanism on Mercury. Geophysical Research Letters, 43(8), 3653–3661. https://doi.org/10.1002/2016GL068325.

Weider, S.Z., Nittler, L.R., Starr, R.D., Crapster-Pregont, E.J., Peplowski, P.N., Denevi, B.W., et al. (2015). Evidence for geochemical terranes on Mercury: Global mapping of major elements with MESSENGER's X-Ray Spectrometer. Earth and Planetary Science Letters, 416,109–120. https://doi.org/10.1016/j.epsl.2015.01.023.

Weider, S.Z., Nittler, L.R., Starr, R.D., McCoy, T.J., & Solomon, S.C. (2014). Variations in the abundance of iron on mercury's surface from MESSENGER X-Ray spectrometer observations. Icarus, 235, 170–186. https://doi.org/10.1016/j.icarus.2014.03.002.

Weider, S.Z., Nittler, L.R., Starr, R.D., McCoy, T.J., Stockstill-Cahill, K.R., Byrne, P.K., et al. (2012). Chemical heterogeneity on Mercury's surface revealed by the MESSENGER X-Ray spectrometer. Journal of Geophysical Research: Planets, 117, E00L05. https://doi.org/10.1029/2012JE004153.

Weyrauch, M., Horstmann, M., & Bischoff, A., (2018). Chemical variations of sulfides and metal in enstatite chondrites—Introduction of a new classification scheme. Meteoritics & Planetary Science,53(3), 394–415. https://doi.org/10.1111/maps.13025.

Wheelock, M.M., Keil, K., Floss, C., Taylor, G.J., & Crozaz, G. (1994). REE geochemistry of oldhamite-dominated clasts from the Norton County aubrite: Igneous origin of oldhamite. Geochimica et Cosmochimica Acta, 58, 449-458. https://doi.org/10.1016/0016-7037(94)90476-6.

Wilbur, Z.E., Udry, A., McCubbin, F.M., Vander Kaaden, K.E., DeFelice, C., Ziegler, K., Ross, D.K., McCoy, T.J., Gross, J., Barnes, J.J., Dygert, N., Zeigler, R.A., Turrin, B.D. & McCoy, C. (2022). The effects of highly reduced magmatism revealed through aubrites. Meteoritics & Planetary Science, 57(7), 1387-1420. https://doi.org/10.1111/maps.13823.

Woelki, D., Regelous, M., Haase, K.M., Romer, R.H.W., & Beier, C. (2018). Petrogenesis of boninitic lavas from the Troodos Ophiolite, and comparison with Izu-Bonin–Mariana fore-arc crust. Earth and Planetary Science Letters, 498, 203–214. https://doi.org/10.1016/j.epsl.2018.06.041.

Zambon, F., Carli, C., Wright, J., Rothery, D.A., Altieri, F., Massironi, M., et al. (2022). Spectral units analysis of quadrangle H05-Hokusai on Mercury. Journal of Geophysical Research: Planets, 127, e2021JE006918. https://doi.org/10.1029/2021JE006918.

Zhang, P., Li, Y., Zhang, J., Li, S., Jin, Z., Han, H., et al. (2023). Compositional indication of E- and M-type asteroids by VIS-NIR reflectance spectra of meteorites. Astronomy & Astrophysics, 671, A77 (2023). https://doi.org/10.1051/0004-6361/202245207.

Zhang, P., Tai, K., Li, Y., Zhang, J., Lantz, C., Hiroi, T., Matsuoka, M., Li, S., Lin, Y., Wen, Y., Han, H., & Zeng, X., (2022). Diverse space weathering effects on asteroid surfaces as inferred via laser irradiation of meteorites. Astronomy & Astrophysics, 659, A78. https://doi.org/10.1051/0004-6361/202142590.

Zolotov, M.Y., Sprague, A.L., Hauck, S.A., Nittler, L.R., Solomon, S.C., & Weider, S.Z. (2013). The redox state, FeO content, and origin of sulfur-rich magmas on mercury. Journal of Geophysical Research: Planets, 118, 138-146. https://doi.org/10.1029/2012JE004274.

# Appendices

## A. Supportive information of Chapters 3,4, and 5

### Chapter 3

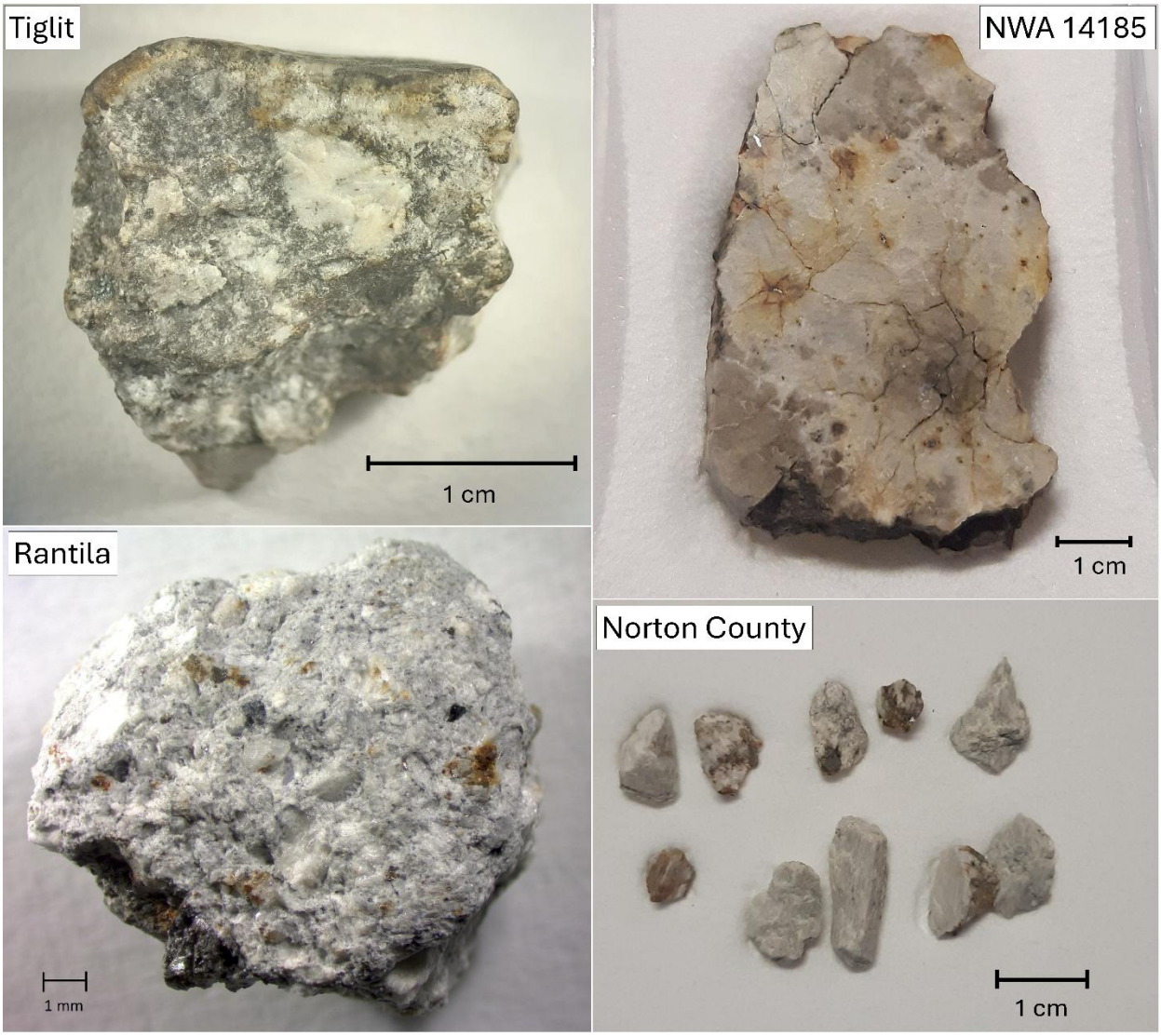


Figure S3.1. The four aubrites under investigation. A thin fusion crust can be observed on the top side of the Tiglit fragment.

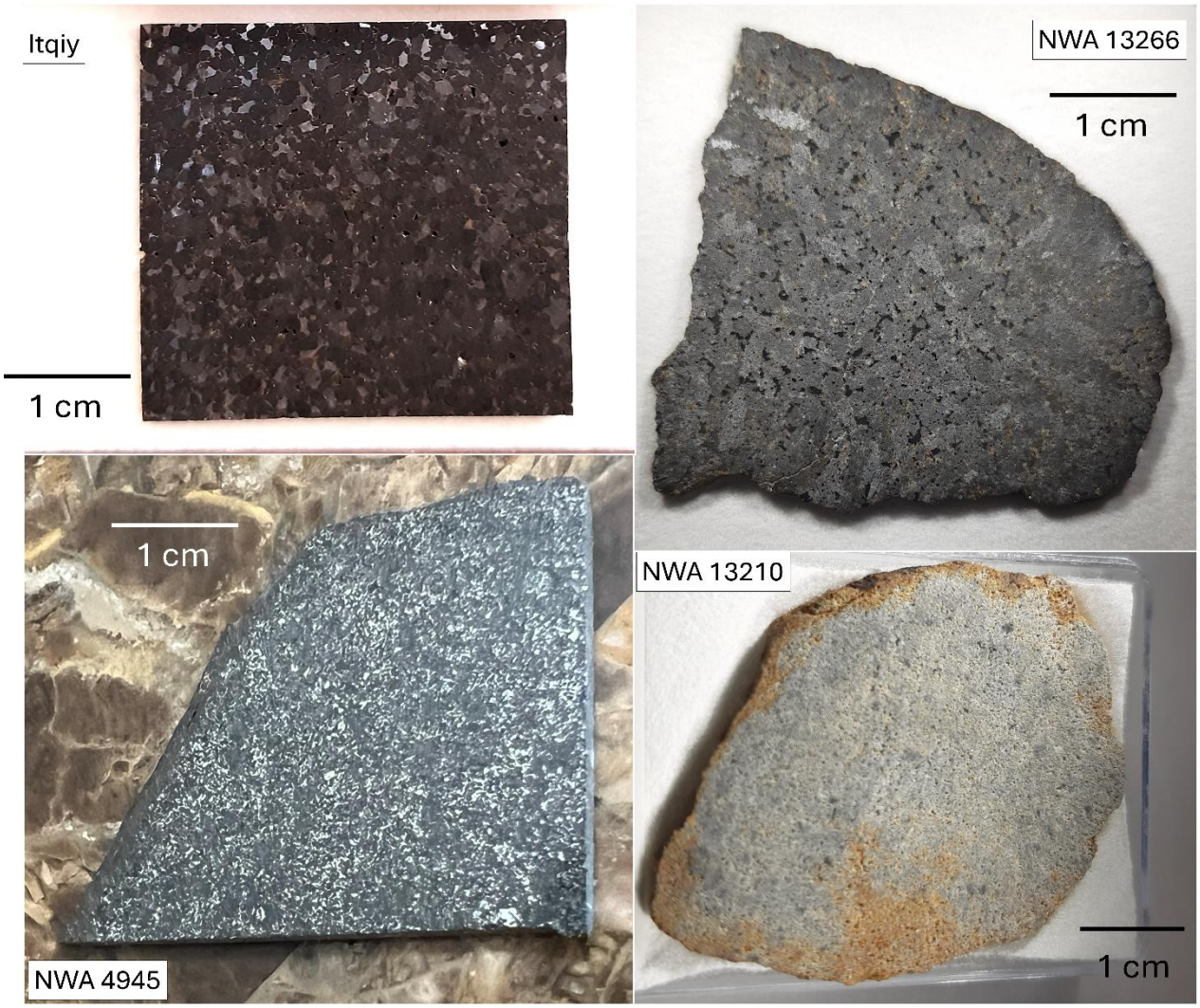


Figure S3.2. The four enstatite chondrites, achondrite and melt rock under investigation.

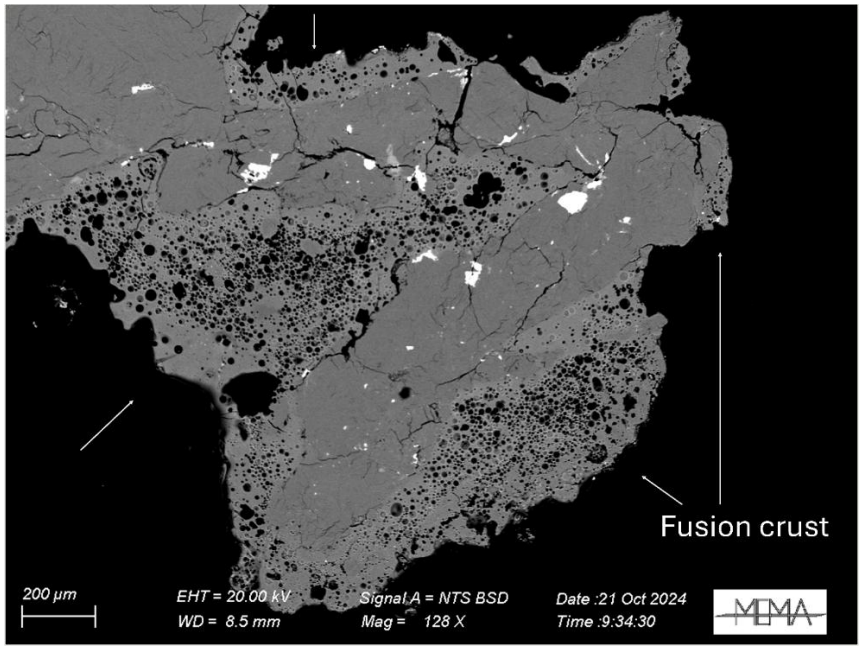


Figure S3.3. Fusion crust in Tiglit aubrite.

| | Accelerating voltage (kV) | Beam current (nA) | Beam size (µm) | Correction |
|---|---|---|---|---|
| Silicates | 15 | 20 | 3 | ZAF |
| Metals | 15 | 10 | 5 | ZAF |
| Sulphides | 20 | 10 | 3 | PRZ |
| Glasses | 15 | 10 | 10 | ZAF |

| **Investigated elements** | **Si** | **Mg** | **Fe** | **Ca** | **Na** | **K** | **Al** | **Mn** | **Cr** | **Ni** | **Ti** | **Cu** | **Co** | **V** | **S** | **P** | **Zn** |
|---|---|---|---|---|---|---|---|---|---|---|---|---|---|---|---|---|---|
| Silicates | Ab | Ol | Ilm | Di | Ab | San | Pl | Bus | Chr | Ni | Ilm | - | - | - | - | - | - |
| Metals | Si | - | Fe | - | - | - | - | Mn | Cr | Ni | Ti | Cu | Co | V | - | Ap | - |
| Sulphides | Ol | Mg | Ccp | Di | Ab | - | - | Mn | Chr | Pnt | Ti | Ccp | - | V | Ccp | Ap | Sph |
| Glasses | Ab | Ol | Ilm | Di | Ab | San | Pl | Bus | Chr | Ni | Ilm | - | Co | V | Cls | - | Wil |

Table S3.1. EPMA operating conditions and certified standards for every investigated element.
ZAF= Atomic Number (Z), Absorption (A), and Fluorescence (F) correction
PRZ= Phi-Rho-Z (φ(ρz)) correction, φ=ionization distribution, ρ=mass density, z=depth
Ab=albite, Ol=olivine, Di=diopside, Ilm=ilmenite, San=sanidine, Pl=plagioclase, Chr=chromite, Bus=bustamite, Ap=apatite, Ccp=chalcopyrite, Pnt=pentlandite, Sph=sphalerite, Cls=celestite, Wil=willemite

# Chapter 4

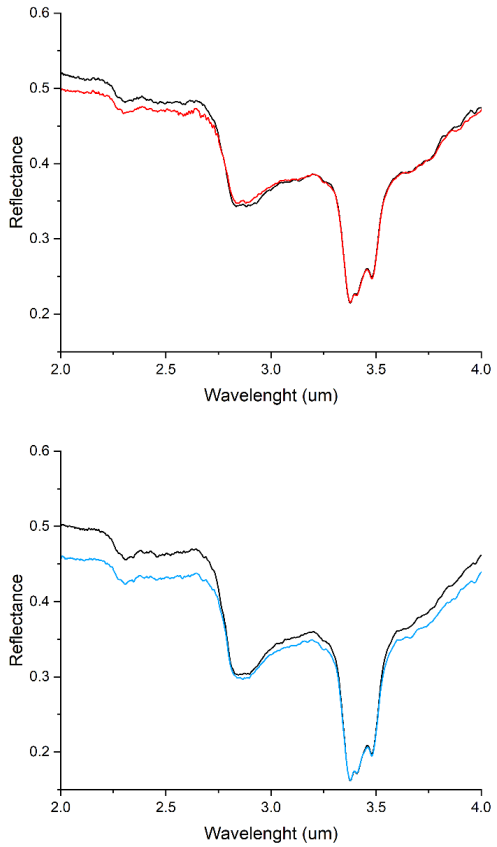


Figure S4.1. Organics features in PBS spectra. Top, black= spectrum before irradiation, red= spectrum after the last He irradiation dose; bottom, black= spectrum before irradiation, blue= spectrum after the last C irradiation dose.

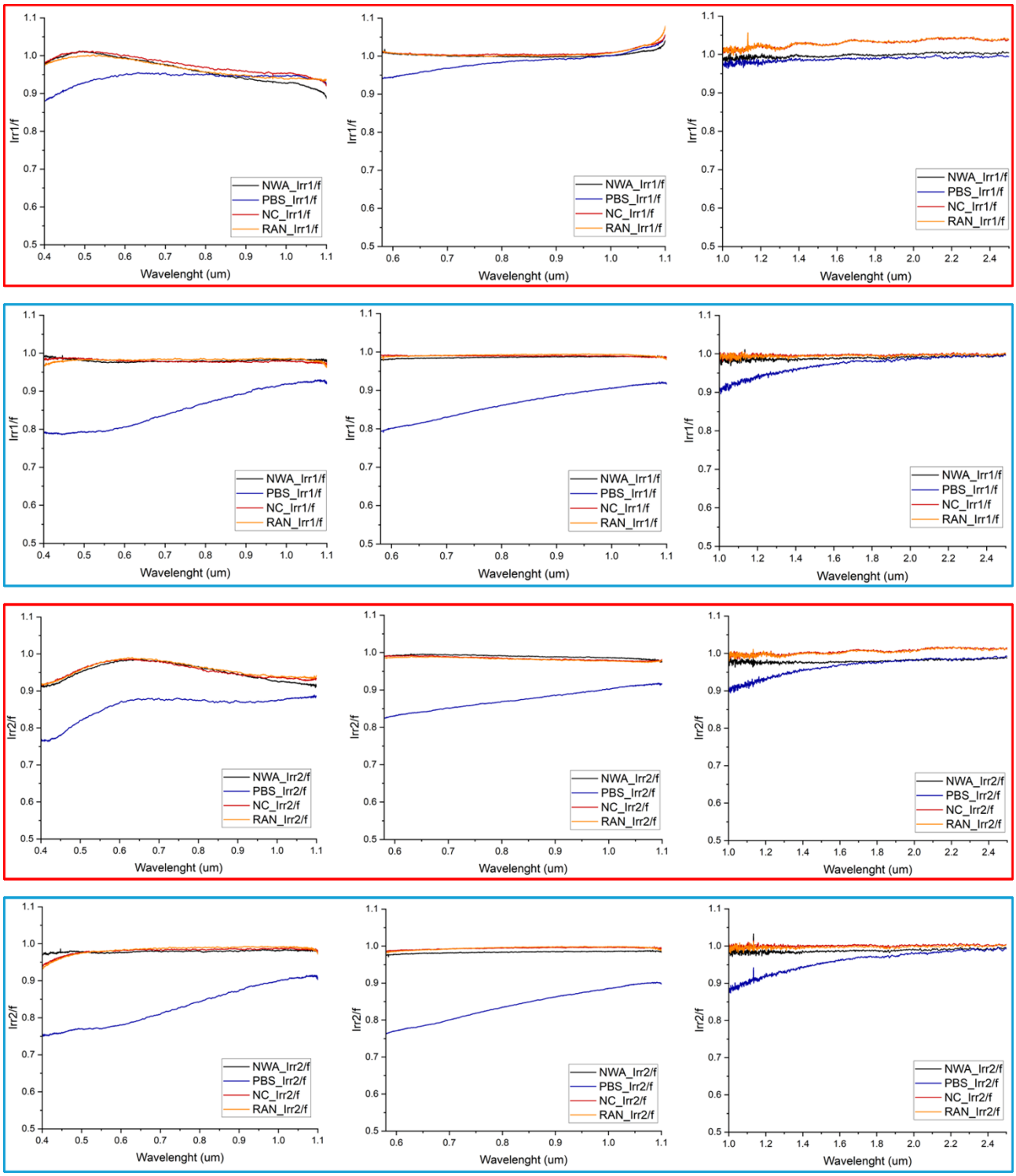


Figure S4.2. Ratio between irradiated sample spectrum and the fresh sample spectrum for the investigated ion fluences. Irr1= first fluence $1x10^{16}$ ions/cm$^2$; Irr2= second fluence $3x10^{16}$ ions/cm$^2$, Irr3= third fluence $6x10^{16}$ ions/cm$^2$, Irr4= fourth fluence $1x10^{17}$ ions/cm$^2$. Red frame= He irradiation; blue frame= C irradiation. The first panel in each frame represents the measurements in the VIS range; the second panel represents the "RED" measurements, meaning a measurement taken with the same spectrometer and configuration of the VIS spectra acquisition but with an IR light source, used to better constrain the merging of the spectra acquired in the VIS and IR spectral ranges; the third panel represents the measurements in the IR range. The different response of PBS to ion irradiation, compared to the other samples, is clearly observable.

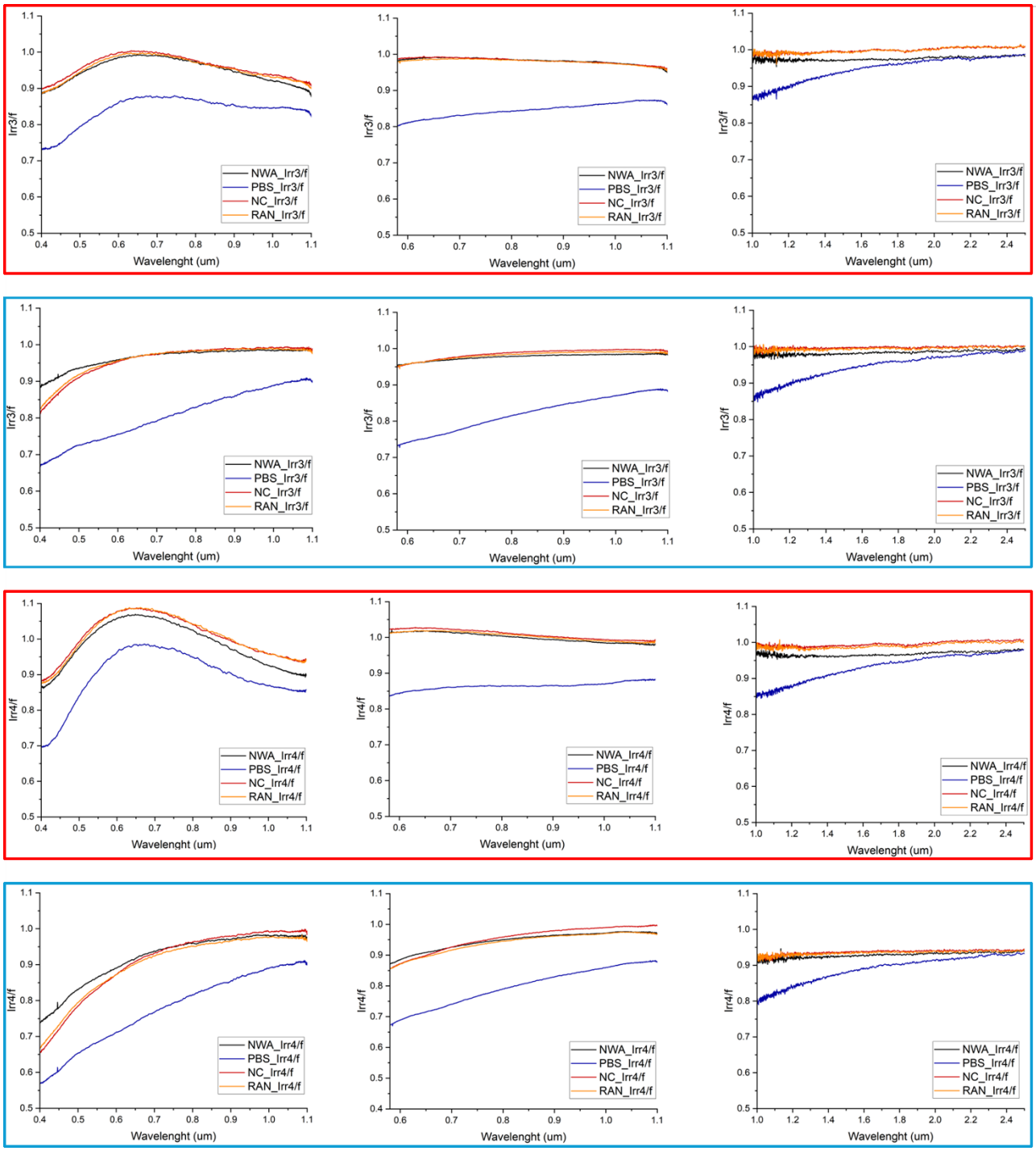


Figure S4.2. continue.

# Chapter 5

The supportive information of Chapter 5 corresponds to the supportive materials of the submitted papers.

The supporting information for this article concerns sample descriptions and additional details on some of the analytical methods. Specifically, we present here a picture of the investigated samples where it is possible to observe their macroscopic characteristics (**Figure S5.1**); and a more detailed description of measurement conditions for EPMA analysis and reflectance spectroscopy in the ultraviolet (UV), visible (VIS), near-infrared (NIR) and mid-infrared (MIR) spectral ranges.

**Text S5.1.**
Reflectance spectroscopy measurements taken at the S.LAB laboratory were made with illumination and collection field of view cones of ±3°, which approximate a bidirectional measurement. The spot size was 6 mm. The illumination source was a quartz tungsten halogen lamp. A Spectralon® optical standard 99% (registered trademark of Labsphere, Inc.) was used for calibration.
Reflectance spectroscopy measurements taken at PSL in the VIS and NIR ranges were made with a bidirectional configuration, using an InGaAs-diode detector and a $CaF_2$ beam splitter. The measurements consisted of 500 scans with a 4 $cm^{-1}$ spectral resolution and 4 mm aperture. MIR hemispherical reflectance was measured with a nitrogen-cooled MCT (Mercury Cadmium Telluride) detector and a KBr beam splitter. The measurements consisted of 1000 scans with a 4 $cm^{-1}$ spectral resolution.

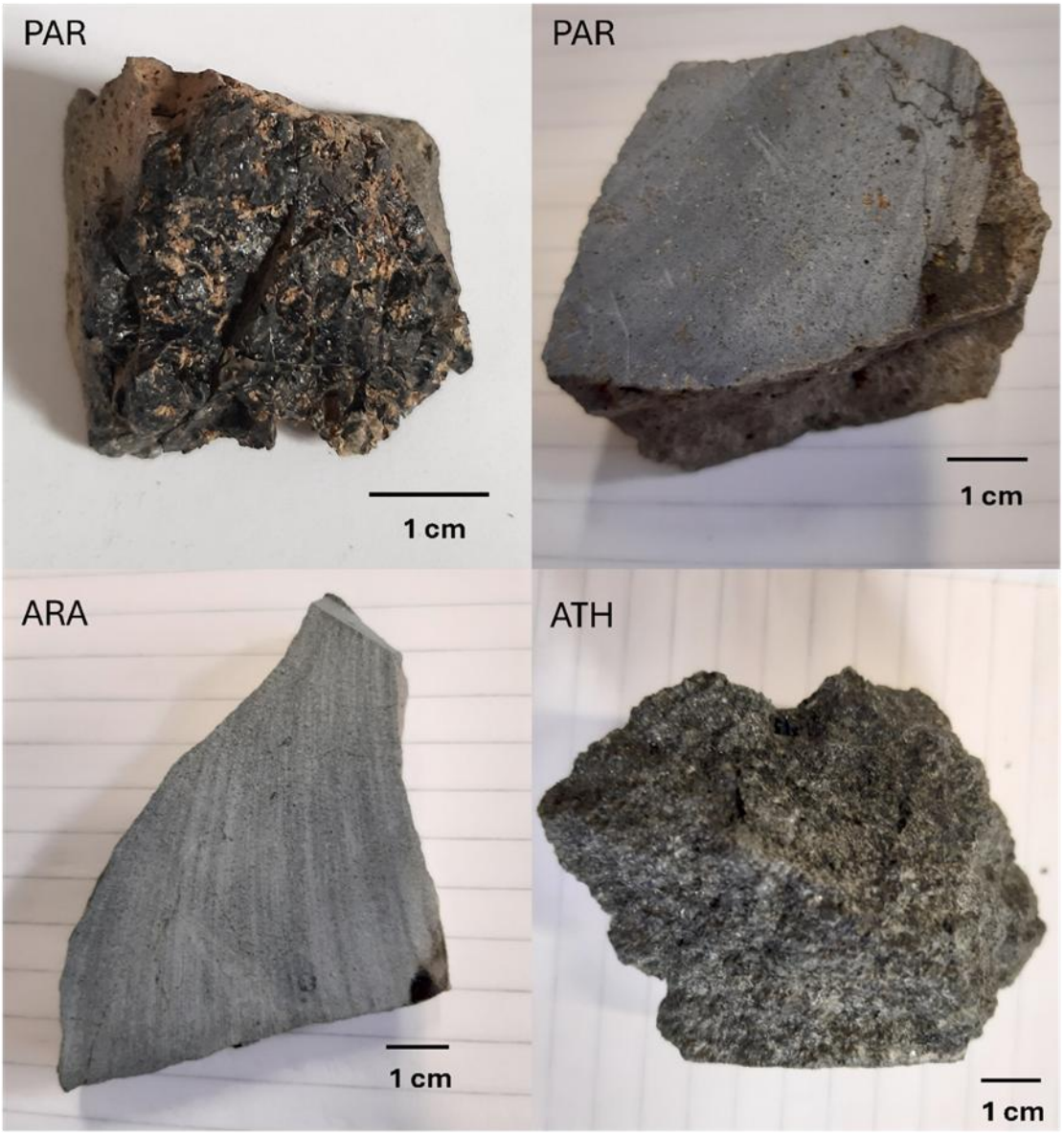


Figure S5.1. Hand specimens of the investigated boninites from the three localities. It is possible to observe the dark glass covering one side of the PAR sample (upper left panel) and the vesiculated aspect of the ATH sample (lower right panel).

| | Accelerating voltage (kV) | Beam current (nA) | Beam size (µm) | Correction |
|---|---|---|---|---|
| Silicates | 15 | 20 | 3 (5 for hydrated phases) | ZAF |
| Oxides | 15 | 20 | 5 | ZAF |
| Sulphides | 20 | 10 | 3 | PRZ |
| Glasses | 15 | 10 | 10 | ZAF |

| **Investigated elements** | **Si** | **Mg** | **Fe** | **Ca** | **Na** | **K** | **Al** | **Mn** | **Cr** | **Ni** | **Ti** | **Cu** | **Co** | **V** | **S** | **P** | **Zn** | **F** | **Cl** | **Ba** |
|---|---|---|---|---|---|---|---|---|---|---|---|---|---|---|---|---|---|---|---|---|
| Silicates | Ab | Ol | Ilm | Di | Ab | San | Pl | Bus | Chr | Ni | Ilm | - | - | - | Cls | - | - | Flr | Ttp | Brt |
| Oxides | Ab | Ol | Ilm | Di | - | - | Grt | Bus | Chr | Ni | Ilm | - | - | **V** | - | - | Wil | - | - | - |
| Sulphides | Ol | Mg | Ccp | Di | Ab | - | - | Mn | Chr | Pnt | Ti | Ccp | - | V | Ccp | Ap | Sph | - | - | - |
| Glasses | Ab | Ol | Ilm | Di | Ab | San | Pl | Bus | Chr | Ni | Ilm | - | Co | V | Cls | - | Wil | - | - | - |

Table S5.1. EPMA operating conditions and certified standards for every investigated element. ZAF= Atomic Number (Z), Absorption (A), and Fluorescence (F) correction. PRZ= Phi-Rho-Z (φ(ρz)) correction, φ=ionization distribution, ρ=mass density, z=depth. Ab=albite, Ap=apatite, Brt=barite, Bus=bustamite, Ccp=chalcopyrite, Chr=chromite, Cls=celestite, Di=diopside, Flr=fluorite, Grt=garnet, Ilm=ilmenite, Ol=olivine, Pl=plagioclase, Pnt=pentlandite.

## B. Ion irradiation on boninite glass sample

Ion irradiation with $He^+$ and $C^+$ performed on aubrites (**Chapter 4**) was performed also on the glass portion of one boninite rock fragment. The sample comes from Parekklisia locality (**Chapter 5**) and the appearance of the glass covering the rock can be observed in **Figure S5.1**. For details on the analytical procedures, the reader is referred to **Chapter 4, Section 4.2**.

Two areas of the sample were investigated, one irradiated with He and the other one with C.

The fresh sample spectra show very low albedo (0.1 absolute reflectance), slight blue slopes, broad and very weak absorption features around 1 μm (**Fig. B1**). Ion implantation does not produce great darkening nor reddening (**Fig. B2**).

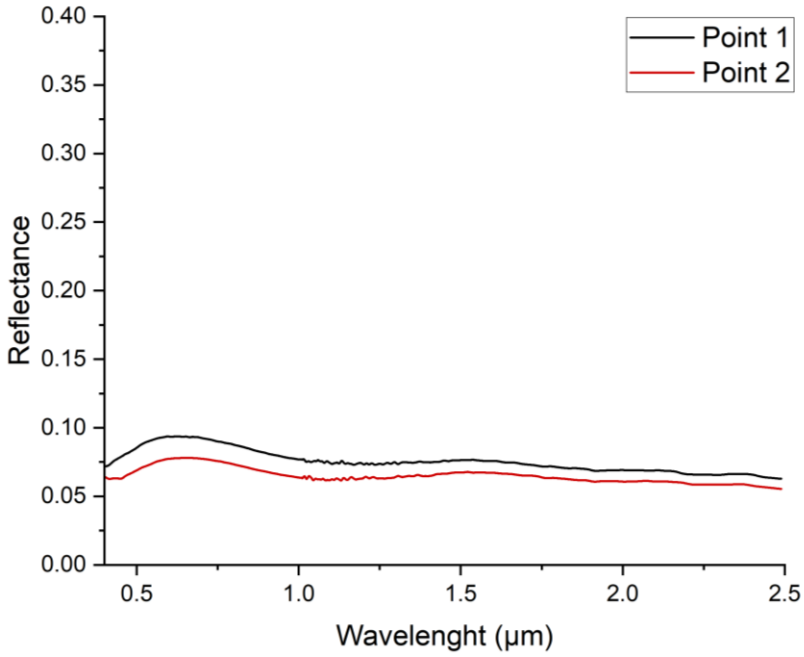


Figure B9. Fresh sample spectra acquired in different areas of the sample: Point 1, where He implantation was then performed; Point 2, where C implantation was then performed.

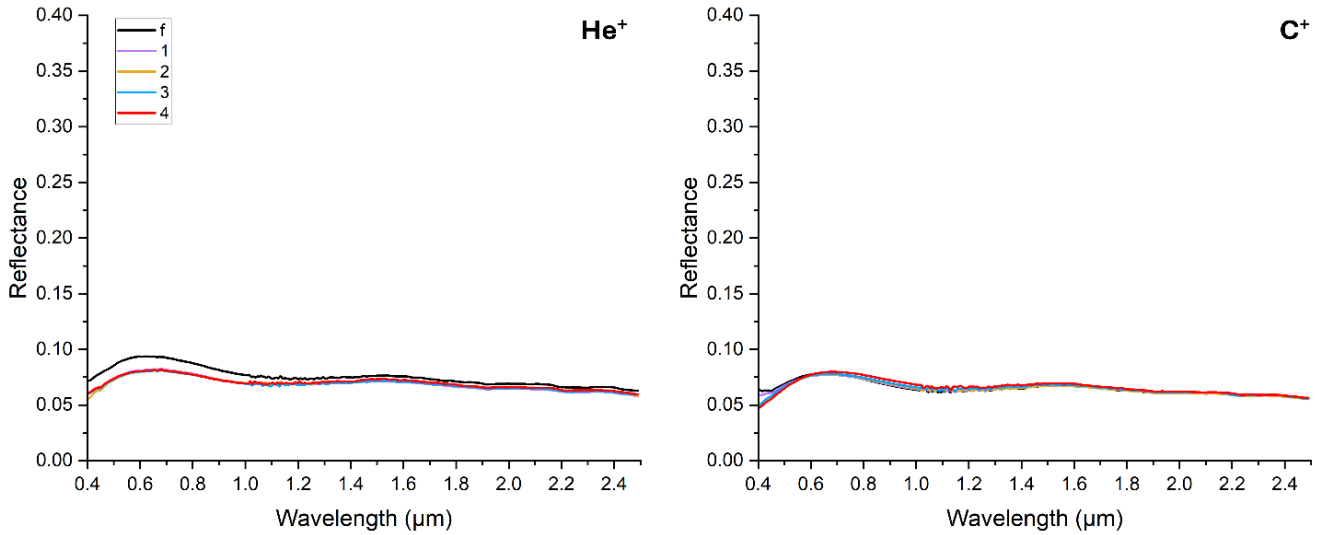


Figure B10. Ion implantation effects on VNIR spectra. f= spectrum on the fresh sample, 1= $1x10^{16}$ ions/cm$^2$, 2= $3x10^{16}$ ions/cm$^2$, $6x10^{16}$ ions/cm$^2$, $1x10^{17}$ ions/cm$^2$.

It is possible to observe an albedo decrease, especially in the VIS range, after the first He irradiation dose. Increasing fluence does not produce other spectral changes. The highest dose of ion implantation seems to cause a weak brightening effect form 0.6 μm on.

The spectral effects observed in the VNIR range after ion irradiation are quite different from those found for aubrites (**Chapter 4**) and from those found by ***Caminiti et al. (2024)*** for a boninite rock sample. The MIR spectral effects are currently under investigation and are expected to provide further insights into the type and extent of the irradiation effects on these glassy materials.

**References**

Caminiti, E., Lantz, C., Besse, S., Brunetto, R., Carli, C., Serrano, L., et al. (2024). Effects of ion irradiation on Mercury terrestrial analogues in the visible to mid-infrared. Icarus, 420, 116191. https://doi.org/10.1016/j.icarus.2024.116191.

# C. Gas mixing experiments: creation of synthetic glass under Mercury's conditions

During this PhD project, I carried out an experimental petrology study aimed at creating synthetic glass under controlled conditions simulating Mercury's surface reduced environment. The obtained synthetic glass is currently being used in the International Team project #552 "*Wide-ranging characterization of explosive volcanism on Mercury: origin, properties, and modifications of pyroclastic deposits*", supported by the International Space Science Institute (ISSI) in Bern, focused on the creation of synthetic analogues reproducing Mercury's regolith, for the study of pyroclastic deposits, mixing the glass with different synthetic silicates. For this project the glass is mixed with different synthetic silicates. The preliminary results are presented in ***Carli et al.* (*2025*)**.

The experiments were conducted using a gas-mixing furnace at the Laboratorio di Mineralogia Petrologia Sperimentali, Dipartimento di Scienze della Terra, Universtià degli Studi di Firenze.
The starting material for the experiment is a natural glass, an obsidian from Lipari.
To perform the experiments, the powders were put in Pt crucibles. After preliminary tests, five experimental runs were carried out to produce the required amount of material (30 g) for the project. We processed up to 7 g of powder per run. The samples were heated up to 1150°C at a rate of 5°C/min, with a dwell time of 20 min at the maximum temperature. The reducing atmosphere was reached adjusting CO and $CO_2$ gas fluxes. The oxygen fugacity and temperature during the experiments were monitored using a Sato-type oxygen fugacity and temperature probe. At the end of the dwell time the samples were quenched in water.
The resulting glass chips obtained after each run (**Fig. C1**), were powdered and analysed with X-ray diffraction at the Centro di Servizi di Cristallografia Strutturale (CRIST), Università degli Studi di Firenze, to make sure that the quenching was efficient and no crystallization occurred during the cooling (**Fig. C2**).

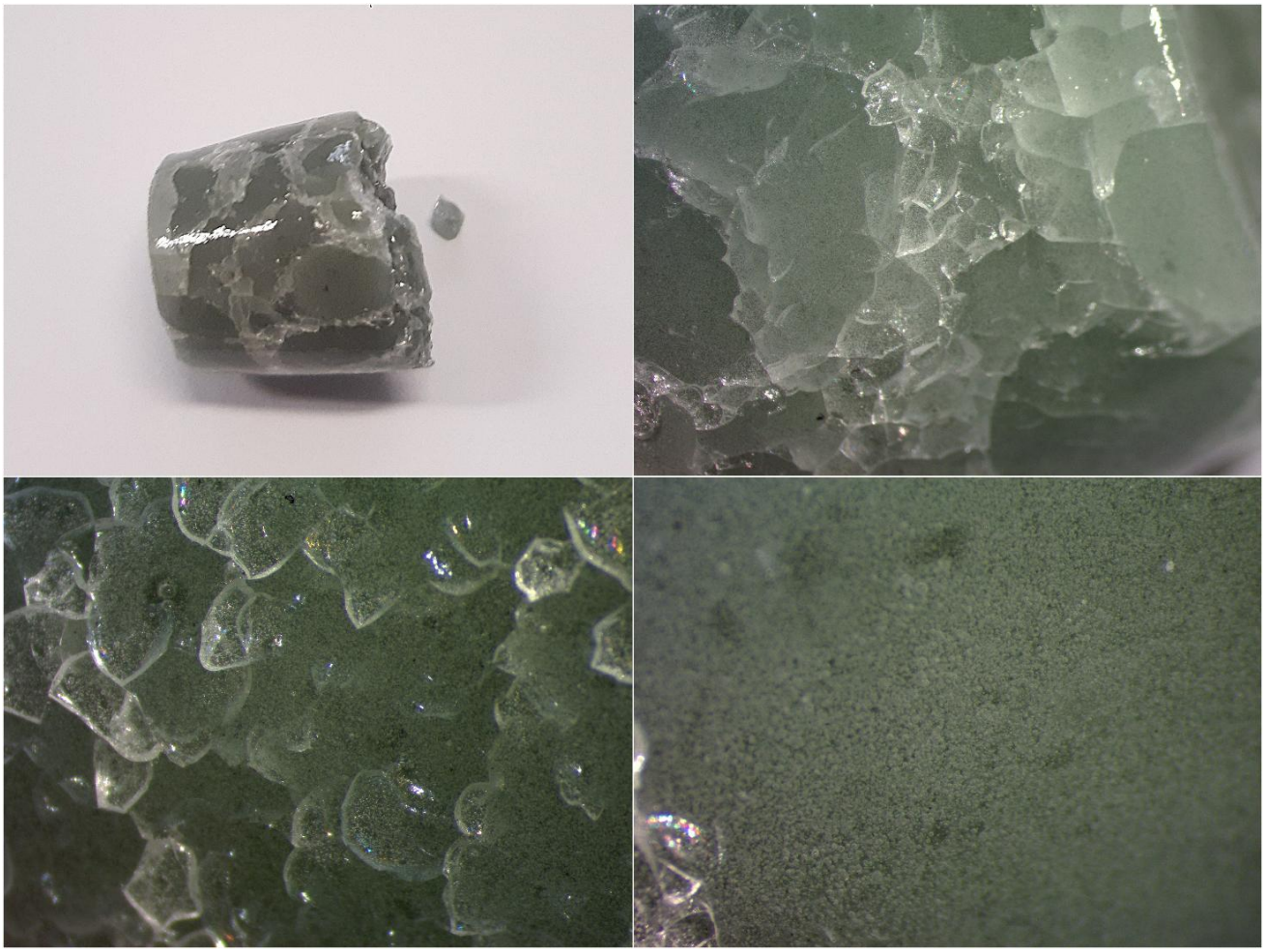

Figure C1. Example of one of the obtained glass chips (ca 1 x 1.5 x 1.5 cm) and their details viewed at the optical stereomicroscope.

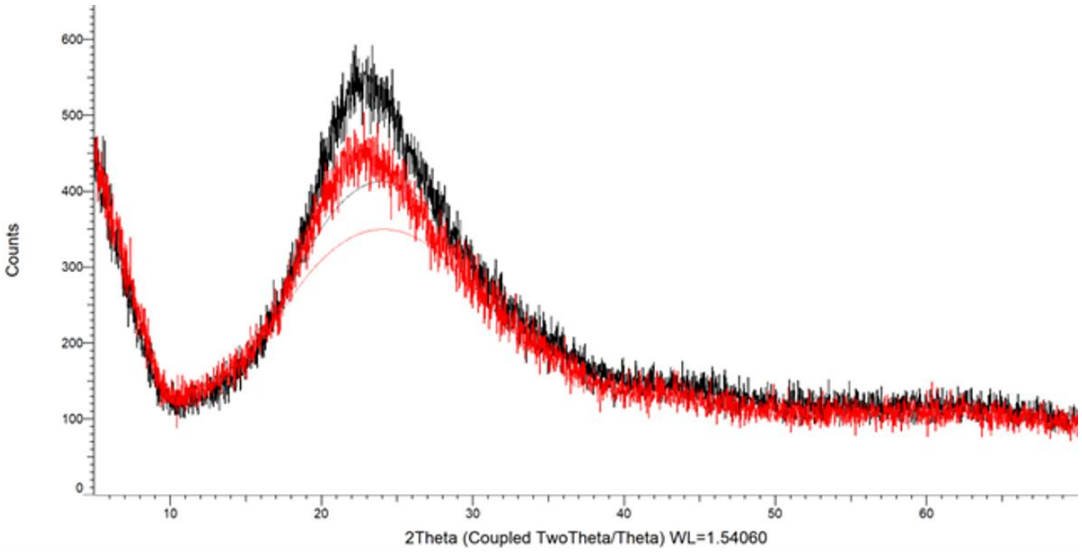


Figure C2. X-ray powder diffraction (XRPD) pattern of the glass obtained with gas-mixing experiments (red) compared to the XRPD pattern of the original natural obsidian (black). In both cases, a distinct amorphous hump can be observed, while diffraction peaks from crystalline phases are absent.

**References**

Carli, C., Maturilli, A., Galiano, A., Penttilä, A., Landi A.I., et al. (2025). Laboratory spectral measurements of mineral mixtures simulating pyroclastic material on Mercury. 56th LPSC (2025), n.1202.